Exploring attractively interacting fermions in 2D using a Quantum Gas Microscope

Debayan Mitra

A DISSERTATION
PRESENTED TO THE FACULTY
OF PRINCETON UNIVERSITY
IN CANDIDACY FOR THE DEGREE
OF DOCTOR OF PHILOSOPHY

RECOMMENDED FOR ACCEPTANCE
BY THE DEPARTMENT OF
PHYSICS
ADVISER: PROFESSOR WASEEM BAKE

November 2018

© Copyright by Debayan Mitra, 2018. All rights reserved.

Abstract

Recent advances in the field of ultracold quantum gases have played an important role in expanding our understanding of strongly-correlated quantum matter. These gases are isolated, clean and fully controllable systems, allowing bottom-up engineering of idealized condensed matter models. Interacting Fermi gases are particularly interesting because of their relevance to understanding systems ranging from high-temperature superconductors to neutron stars.

In this thesis, I describe the development of a quantum gas microscope for studying Fermi gases of lithium-6 in two dimensions. With this tool, we can probe 2D systems containing over a thousand fermions and measure the spin or density on each site as well as n-point correlations of these quantities. The design of our microscope introduces several new simplifying features, including a novel Raman cooling scheme for imaging that does not require confining the atoms in the Lamb-Dicke regime in all directions.

I report on two experiments we have performed using this instrument. First I present an exploration of attractive spin-imbalanced gases in two dimensions. We observe in-trap phase separation characterized by the appearance of a spin-balanced core surrounded by a polarized gas. In addition, we observe pair condensation in momentum-space measurements even for large polarizations where phase separation vanishes, indicating the presence of a polarized pair condensate.

In a second experiment, we explore fermions in an optical lattice, described by the Fermi-Hubbard model. Compared to the repulsive model, the attractive model has received less experimental attention despite its rich phase diagram, including a possible FFLO phase in the polarized system. Using the microscope, we directly image charge density wave correlations in our system and use them to put a lower bound on pairing correlations. We also demonstrate that these correlations constitute a sensitive thermometer that might be useful in the development of future cooling schemes.

These initial explorations with our fermion quantum gas microscope set the stage for future work that might shed insights on a wide variety of condensed matter problems, ranging from the microscopic mechanisms for pairing in high-temperature superconductors to Cooper pairing at non-zero momentum in large magnetic fields.

Acknowledgements

As is the case for summarizing my gratitude for my years as a graduate student, I do not know where to start. I think it is apt to begin by thanking my advisor, Professor Waseem Bakr, not only for giving me this opportunity to work with him, but also for being my guide and mentor through the entire process. Prior to starting my PhD at Princeton, my experience was largely concentrated in the field of experimental condensed matter physics. I was very generously offered to work on silicon qubits by Professor Jason Petta. While working there, I acquired important nanofabrication skills like photo and e-beam lithography. But when I found out that Waseem was joining the department, I was excited by the prospect of building my own experiment. I knew that I would be studying similar physics, but I would learn the new and powerful tools of laser cooling and trapping of atoms.

Building an experiment was the most educational experience where I not only had to think like an engineer but also like an electrician and a plumber. I learned a lot from Stan Kondov, the first postdoc who joined our group. We spent many hours assembling vacuum chambers, winding coils and discussing car problems. The second postdoc to join us, now Professor Peter Schauß, was indispensable to the science that we produced. I do not remember a time I asked him a question that he could not answer. My fellow graduate student, Peter Brown and I worked side by side for many years and he played a crucial role in ensuring the success of our experiments. The next graduate student in our group, Elmer Guardado-Sanchez will be the very capable hands to take care of the machine after the first generation of graduate students depart. I would also like to wish our newer graduate student, Lysander Christakis, success in the new experimental direction of our group.

Research cannot continue without all the administrative and technical assistance we receive. I would like to start with Geoff Gettelfinger, our department manager. The time and patience that he spared to deal with our day to day water cooling problems has been incredibly valuable. I would like to thank Steve Lowe for training me to use the student machine shop and always providing guidance and advice with every machining project. Additionally, I'm very thankful for Vinod Gupta and Sumit Saluja's IT help and support navigating the Feynman cluster. In the beginning, we had to place orders on a daily basis and sometimes deal with US customs delays. The purchasing and logistics department deserves a huge thank you for their patience and tireless help, especially Darryl Johnson, Julio Lopez, Ted Lewis, Lauren Callahan, Barbara Grunwerg and Claudin Champagne. I would like to thank our administrative assistant, Antonia Sarchi, for promptly resolving all financial queries. Lastly I would like to thank my graduate administrators Jessica Heslin, Barbara Mooring and Catherine Brosowsky for helping navigate different stages of grad school.

My graduate school experience would not be complete without thanking the professors who taught me in the classroom. My biggest thanks goes to Professor Herman Verlinde. Not only was he a great instructor to introduce quantum field theory to a layman, but he was also the most caring director of graduate studies. Next I thank Professor Ali Yazdani, Professor Frans Pretorius and Professor Andrei Bernevig for teaching the other courses I took. I extend my gratitude to Professor David Huse.

Although I never took a class under him, I enjoyed the conversations we had about our experiments and always learned a lot from his keen insights. I also thank him for being part of my committee. I thank Trithep Devakul for helping us navigate numerical simulations. In addition to taking classes, I also taught different courses for four semesters. I would like to thank Catherine Visnjic and Kasey Wagoner for introducing me to their new style of pedagogy. Finally I would like to thank Professor Michael Romalis for being a part of my committee and Professor Jeff Thompson for carefully reading my thesis.

Being in graduate school for six years, especially in a small town like Princeton, could be a laborious experience without friends. My experience was particularly memorable because I lived in the graduate college my first year. I spent countless nights at the Dbar with my friends Gustavo Joaquin Turiaci, Aitor Lewkowycz, Zach Sethna, Mike McKeown, Jose Zamalloa and many others. I made more friends as I moved along in grad school like Olya Krepchenko, Will Coulton and Mykola Dedushenko. Every summer I would participate in the softball league to proudly play for the Big Bangers. The team and all our triumphs will always be close to my heart. I also made many friends outside of grad school, mostly through my girlfriend. A special thank you to Alex Coulston, Audrey Jenkins and Angelika Hicks for being great housemates and for throwing unforgettable parties. Also thank you to Princeton in Asia for incorporating me as a member of their team.

At this point I would like to mention one of the most important moments of my time in Princeton. During my time here I met my girlfriend, Emily Eckardt. For the last three years, she has been both an inspiration and a motivation in research and personal life. Her positive outlook towards life has rubbed off on me and her drive to work towards a social good motivates me to become a better educator and not only a better researcher. In addition, her parents Bob Eckardt and Jane Shapiro, have been my family away from my own family. I am indebted to them for their kindness and generosity and for their endless curiosity and interest in people's lives. Her brothers even guest starred on the *Biq Banqers* every now and then.

Last but not the least, I owe an immense debt of gratitude to my parents for the sacrifices they made so that I could be here today. My mother, Susmita Mitra, left behind her career as a promising young engineer to ensure that my brother and I were raised well. She was not only my teacher but also my cheerleader who would lift me up when I was down. My older brother, Debkishore Mitra, was the person I could go to whenever I had difficulty in school and was a constant source of encouragement. This thesis is a culmination of thirty years of work and I am grateful to have the chance to thank each person who contributed to this accomplishment.

To my family

Contents

			roments	ii
			gements	iv
			les	X
1		oducti		1
2	Exp	erime	ntal Setup	7
	2.1		ım Chamber Design	7
	2.2		rant Vacuum Viewports	10
	2.3		IR coatings	12
	2.4	Bakeo		14
	2.5	Magne	etic Field Coils: Design and Winding	18
		2.5.1	Zeeman slower	18
		2.5.2	MOT coils	21
		2.5.3	Feshbach coils	23
		2.5.4	Coil Winding	25
	2.6	Water	Cooling	28
	2.7	671 nr	m Laser System	32
		2.7.1	⁶ Li Spectroscopy	32
		2.7.2	MOT and Zeeman slower	34
		2.7.3	Low and High Field Imaging	37
		2.7.4	Raman laser system	39
	2.8	Optica	al Potentials	41
		2.8.1	Optical Dipole Trap	41
		2.8.2	Light Sheet and Bottom Beam	43
		2.8.3	Accordion Lattice	45
		2.8.4	2D Square Science Lattice	50
3	Pat	hway t	to a Quantum Gas Microscope	55
	3.1		eto-optical trap	55
	3.2	_	oration	59
		3.2.1	Radio frequency sweeps	59
		3.2.2	Molecular Bose-Einstein condensates	62
	3.3	Single	site imaging	65
		3.3.1	Raman imaging	65

		3.3.2 3.3.3	Microscope objective	70 72		
4	Pha	ıse sep	paration and pair condensation in a spin-imbalanced 2D			
		mi gas		74		
	4.1	_	erate Fermi gases	74		
	4.2	Fermi	gas in 2 dimensions	78		
	4.3		BCS crossover in 3D and 2D	82		
	4.4	Superi	fluidity in 2D	84		
	4.5		mbalance: Phase separation and superfluidity	85		
		4.5.1	Creating 2D spin-imbalanced clouds	86		
		4.5.2	Imaging	90		
		4.5.3	Measuring temperature	93		
		4.5.4	Measuring condenstate fraction	95		
		4.5.5	Fitting in-situ profiles	96		
		4.5.6	Extracting critical polarization $P_{\rm c}$	99		
		4.5.7	Phase diagram	101		
5	Quantum gas microscopy of an attractive Fermi–Hubbard system 104					
	5.1	The F	ermi-Hubbard model	104		
	5.2	Attrac	etive $(U < 0)$ or Repulsive $(U > 0)$?	108		
	5.3	Quant	um gas microscopy	112		
		5.3.1	Calibrating Hubbard parameters	113		
		5.3.2	Measuring double occupancies	115		
		5.3.3	Charge density wave and s-wave pairing	117		
		5.3.4	Measuring correlations vs n	122		
		5.3.5	Measuring correlations vs U/t	126		
		5.3.6	Thermometry	128		
	5.4	Mappi	ing and further work	130		
6	Con	clusio	n	133		
	6.1	Future	e Work	133		
\mathbf{A}	Pro	perties	s of $^6\mathrm{Li}$	135		
	A.1	- Atomi	c properties	135		
	A.2	Zeema	n shifts	136		
	A.3	Scatte	ring lengths	137		
В	Ree	ntrant	vacuum viewport design	138		
\mathbf{C}	AR	/HR c	oatings	139		
D	Lattice description 1					
			-	141		
	D.2	Band	structure calculation	143		

E Objective specifications	145
Bibliography	147

List of Tables

2.1	Bakeout parameters	1
2.2	Water cooling parameters	29
2.3	Thermal expansion and Sellmeir parameters for PP-MgO:SLT	4
4.1	Calculated and measured 2D parameters	88
4.2	Mean field theory fitting results	98
A.1	Atomic properties of ⁶ Li	135

List of Figures

1.1	Quantum gas microscopy
1.2	Observation of spin canting in the repulsive Hubbard model
1.3	Conductivity versus temperature
2.1	Design of the experiment
2.2	Reentrant vacuum viewport design
2.3	Vacuum system bakeout
2.4	Zeeman slower design and testing
2.5	MOT Coils
2.6	Feshbach Coils
2.7	Coil Winding
2.8	Water cooling
2.9	Spectroscopy
2.10	MOT and Zeeman slower light
	Low and high field imaging
2.12	Raman laser system
2.13	Optical Dipole Trap
2.14	Light sheet and bottom beam
2.15	Second harmonic generation
	Accordion lattice
	Science lattice
	Pinning circuit
3.1	Properties of the MOT
3.2	RF antennas
3.3	Rabi oscillations
3.4	Bose-Einstein Condensation
3.5	Raman cooling scheme
3.6	Raman sideband cooling setup
3.7	Objective mount
3.8	Single atom reconstruction
4.1	Binding energy
4.2	BEC-BCS crossover
4.3	Phase separation in 3D and 1D
4.4	Experimental setup

4.5	Imbalancing calibration	88
4.6	Checking single accordion layer	89
4.7	Double imaging scheme	91
4.8	Average density profiles	92
4.9	Temperature fitting	94
4.10		96
4.11	Azimuthal averages	97
	Example mean field theory fits	99
	In-situ difference images	100
4.14	Central polarization and condensate fraction vs. global polarization .	101
	Phase diagram	102
5.1	Fermi-Hubbard model phase diagram	106
5.2	Single site images of a repulsive Fermi-Hubbard system	109
5.3	RF spectroscopy for Hubbard U calibration	114
5.4	Detecting double occupancies	116
5.5	DQMC simulations of pairing, total density and doublon density cor-	110
- 0	relators	118
5.6		120
5.7	Fitting to Quantum Monte Carlo	121
5.8	Observation of doublon density correlations	123
5.9 5.10		124
	system prepared using scheme 2	125
5.11	Nearest-neighbor and next-nearest neighbor doublon density correla-	
	tors versus filling as a function of U/t	127
	Thermometry of an attractive Hubbard system	129
	Mapping between the attractive and repulsive Hubbard model	130
5.14	Creating density excitations with a DMD	132
A.1	Zeeman shift for ⁶ Li ground state	136
A.2	Scattering lengths for ⁶ Li	137
B.1	Reentrant vaccum viewport	138
C.1	AR coating on side viewports	139
C.2	AR-HR coating on reentrant viewports	140
D.1	Lattice Band Structure	144
E.1	Objective design	145
E.2		146

Chapter 1

Introduction

The field of atomic quantum gases can trace its roots back to Einstein's prediction in 1924 that an ideal gas of particles of integer spins would thermodynamically occupy the ground state below a certain temperature, forming a so-called Bose-Einstein condensate. Superconductivity was discovered in 1911 and superfluidity of ⁴He was discovered in 1938 but there was no obvious link between them and Einstein's theory. In 1950, Ginzburg and Landau introduced a phenomenological theory of superfluidity in terms of a complex valued order parameter function, which was later interpreted as a macroscopic quantum wavefunction of the superfluid [1]. This was followed by the realization in 1957 that superconductivity could be understood as the Bose-Einstein condensation of pairs of fermions, known as Cooper pairs [2]. It was not until 1995 that a weakly-interacting Bose-Einstein condensate, in the sense envisioned by Einstein, was directly observed in a dilute gases of alkali atoms [3, 4]. The first degenerate gas of fermionic atoms took even longer, until 1999, because fermions proved to be notoriously harder to cool than bosons [5].

While early work in the field of atomic quantum gases centered on weakly interacting systems, two experimental advances allowed the field to quickly shift focus to strongly interacting systems in the early 2000s. The discovery of Feshbach resonances allowed for tunability of interatomic interactions and access to the unitary regime where the properties of the gas become scale invariant [6]. Alternatively, the kinetic energy of the atoms may be quenched using optical lattices, enhancing the effect of interactions [7].

Creating strongly interacting quantum gases using Feshbach resonances has been a particularly successful route in fermionic gases because of the suppression of three-body losses due to Pauli blocking [8]. Early experiments have mostly focussed on studying the crossover between Bose-Einstein condensates of real space molecules and fermionic superfluids of weakly bound Cooper pairs (BEC-BCS crossover) [9, 10]. Superfluidity was directly observed through the appearance of vortices in rotating Fermi gases [11]. Other experiments have studied other aspects including the equation of state of strongly interacting Fermi gases [12, 13, 14], solitons [15], lower dimensional Fermi gases [16, 17, 18, 19, 20, 21], fermion pairing [9, 22, 23, 24], polaron physics [25, 26, 27] and the Josephson effect in fermionic superfluids [28]. A particularly fruitful direction has been the study of spin imbalanced fermi gases [29, 30, 31, 32,

33, 34]. Previous work had mostly focused on 3D gases where intriguing phenomena have been observed including phase separation and the destruction of superfluidity at the Chandrasekhar-Clogston limit. For our first work, we chose to study a fermionic system in a "quasi" 2D configuration with variable spin imbalance [35]. We were able to study the phenomenon of phase separation in 2D across the BEC-BCS crossover and found that pair condensation persists beyond phase separation on the BEC side. This work will be described in detail in this thesis.

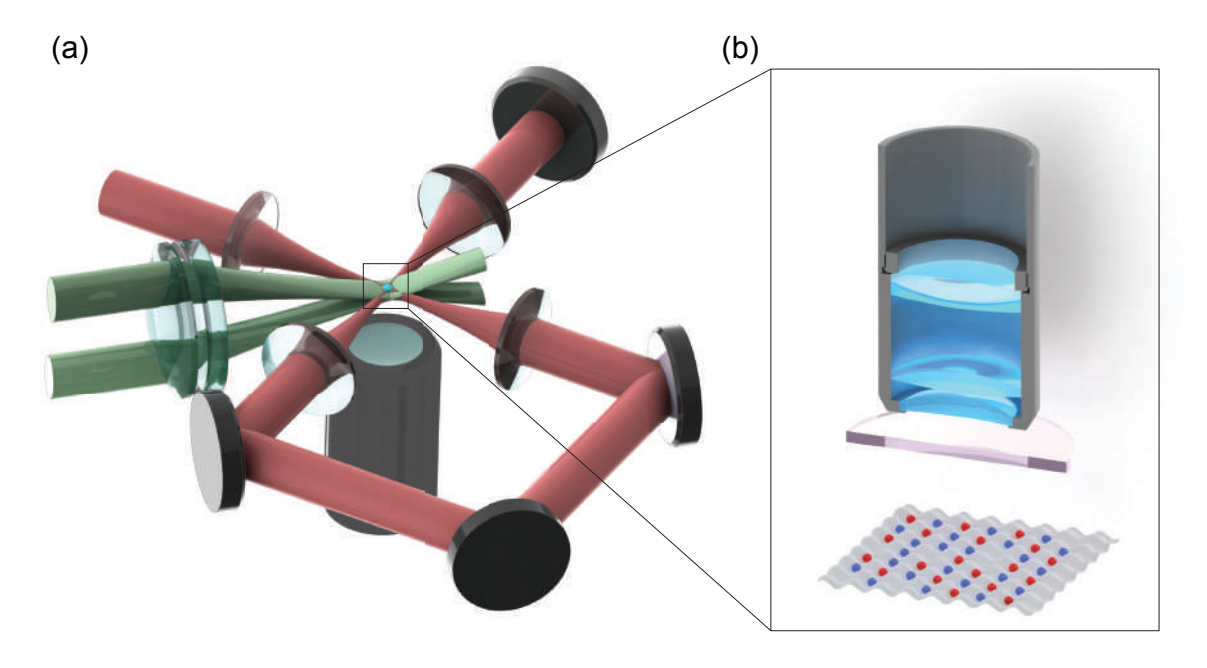


Figure 1.1: Schematic of our quantum gas microscope. (a) Depiction of the optical potentials. The atoms are confined in a single layer of an accordion lattice (green). The science lattice is formed by a 4-fold interference of retroreflected light (red). (b) Zoom-in on the atoms. This cartoon shows atoms of two different hyperfine sublevels (red and blue) occupying the lattice. The objective gathers fluorescence light from the atoms spontaneously emitted during the Raman sideband cooling stage.

Quantum gases in an optical lattice allows studying phenomena related to electrons in real solids. The introduction of a band structure can dramatically modify the physics compared to the continuum. For example, unlike an atom in free space, an atom in a lattice starts Bloch oscillating under an applied force [36]. Another interesting phenomenon that arises in lattices is the possibility of quantized topological invariants. The simplest example is the Zak phase (or Berry phase), a geometric phase acquired by a particle when it adiabatically makes a loop across the Brilluion zone in a 1D lattice. This phase has been recently measured in optical lattice experiments [37]. A related invariant in 2D, the Chern number, was explicitly measured in the case of a Harper-Hofstadter Hamiltonian [38]. In addition, compared to the continuum, optical lattices also allow for the study of a different class of strongly interacting models, known as Hubbard models. The single band Hubbard model for

fermions, known as the Fermi-Hubbard model, is one of the simplest models that is believed to contain the same phenomenology as high T_c cuprates, as first suggested by P. W. Anderson [39]. The Fermi-Hubbard Hamiltonian can be written as

$$\mathcal{H} = -t \sum_{\langle \mathbf{r} \mathbf{r}' \rangle, \sigma} \left(c_{\mathbf{r}, \sigma}^{\dagger} c_{\mathbf{r}', \sigma} + h.c. \right) + U \sum_{\mathbf{r}} n_{\mathbf{r}, \uparrow} n_{\mathbf{r}, \downarrow}$$
 (1.1)

where the first term denotes tunnelling between nearest neighbor sites and the second term is the interaction between two fermions on the same site. Despite its simplicity, it can only be solved exactly in 1D [40]. In higher dimensions, several numerical methods [41, 42, 43, 44] have been used to study the Hubbard model but its low temperature physics remains out of reach [45]. This has motivated the "quantum simulation" of the Hubbard model with cold fermions in optical lattices. Here "quantum simulation" is used in the sense originally proposed by Feynman [46], where one uses an accessible quantum system to emulate another, less accessible one. In our case, cold atoms are the well understood, controllable system, used to emulate the physics of high temperature cuprates.

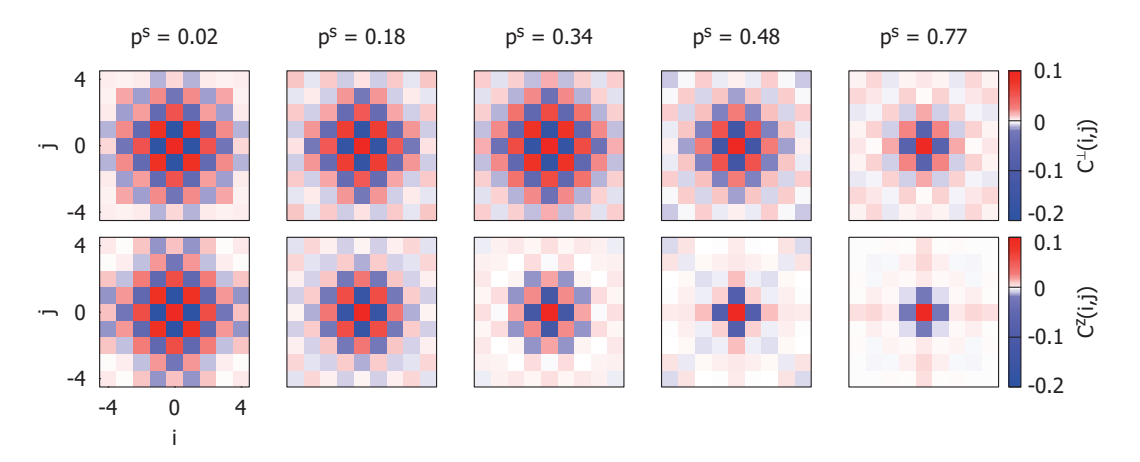


Figure 1.2: Observation of spin canting in the repulsive Hubbard model. Full spin correlation matrices for different site displacements $\mathbf{d} = (i, j)$, shown at half-filling for different local polarizations p^s . Top row shows S^{\perp} correlators, C^{\perp} , and bottom row shows S^z correlators, C^z . Correlators are defined as $C^{\alpha}(\mathbf{d}) = 4(\langle S_{\mathbf{i}}^{\alpha} S_{\mathbf{i}+\mathbf{d}}^{\alpha} \rangle - \langle S_{\mathbf{i}}^{\alpha} \rangle \langle S_{\mathbf{i}+\mathbf{d}}^{\alpha} \rangle)$ and their values are averaged over symmetric points. Each panel is calculated from ~ 50 images.

Quite recently, the tool of quantum gas microscopy, which allows for the detection of single atoms confined in lattice sites, has led to many breakthroughs in the understanding of the Hubbard model. When we started building our lab in 2013, the only existing quantum gas microscopes were for bosons [47, 48]. Using that tool, the superfluid to Mott insulator transition of the Bose-Hubbard model was studied [49]. Given the success of bosonic microscopes, it was not long before many groups started working on extending the tools of quantum gas microscopy to fermions. The first fermion microscopes were demonstrated in 2015 [50, 51, 52, 53, 54] and since then

enormous strides have been made in using them to probe Fermi-Hubbard systems, including observations of Mott insulators [55, 56] and long-range antiferromagnets [57, 58, 59]. Our first excursion with our own quantum gas miscroscope was to extend the understanding of the antiferromagnetic state in the presence of spin imbalance [60]. We prepared half-filled Mott insulators $\langle n \rangle = 1$ with a higher number of spin- \uparrow than spin- \downarrow . The local polarization is obtained from the local density of spins n_{σ}^{s} and is defined as $p^{s} = (n_{\uparrow}^{s} - n_{\downarrow}^{s})/(n_{\uparrow}^{s} + n_{\downarrow}^{s})$. We measured the spin correlations along and perpendicular to the effective magnetic field as a function of polarization. The main result is shown in Fig. 1.2.

When the system is unpolarized, we measure spin correlations that are equally strong along both directions. But as spin imbalance is introduced, the spins prefer to be in a "canted" state to minimize energy. This leads to stronger correlations orthogonal to the field versus along the field.

Next, we set out to explore the Hubbard model with attractive interactions. Although a few prior experiments were done with attractive interactions [61, 62, 63, 64], this work was the first to employ quantum gas microscopy to study a single band Hubbard system. We observed charge-density wave correlations expected for negative U and established that density can be employed as a thermometer at high temperatures while density correlators are a better thermometer at low temperatures [65]. This experiment will be presented in detail in this thesis.

Finally we have studied transport in the repulsive Hubbard model. Traditionally, fermionic transport experiments have looked at conductivity by studying mass flow through optically structured mesoscopic systems [66, 67] or by studying bulk transport in a lattice [68, 69, 70]. In our work, we explored the diffusion of charge in a Fermi-Hubbard system with density modulation in the linear response regime [71]. We created a spatial modulation using a digital micromirror device and observed how the density modulation evolves over time. By fitting the decay to a phenomenological model we obtained a current relaxation rate Γ and a diffusion constant D. Applying the Nernst-Einstein relation $\sigma = \chi_c D$, where χ_c is the compressibility, we were able to obtain the conductivity σ . Surprisingly we found that the resistivity $(\rho = 1/\sigma)$ is linear with temperature and shows no sign of saturation at the Mott-Ioffe-Regal (MIR) bound (Fig. 1.3). The MIR bound comes from the simple assertion that the mean free path of a quasiparticle cannot be less than the lattice spacing [72, 73]. These two observations are signatures of non-conventional transport in our system and a breakdown of Fermi liquid theory. Details of this publication and the one on spin imbalanced Hubbard physics will be provided in a future thesis by P. T. Brown from our group.

The outline of this thesis is as follows. I will describe in depth the experimental setup in chapter 2. Since I was the first graduate student on this experiment, it is important for me to lay out the details of the design and construction of the experiment. I describe the design of the vacuum system, the bakeout and assembly. I then describe the magnet coil design, their winding and the water cooling system. Next I focus on all the different laser systems that were built to cool and trap the Li atoms.

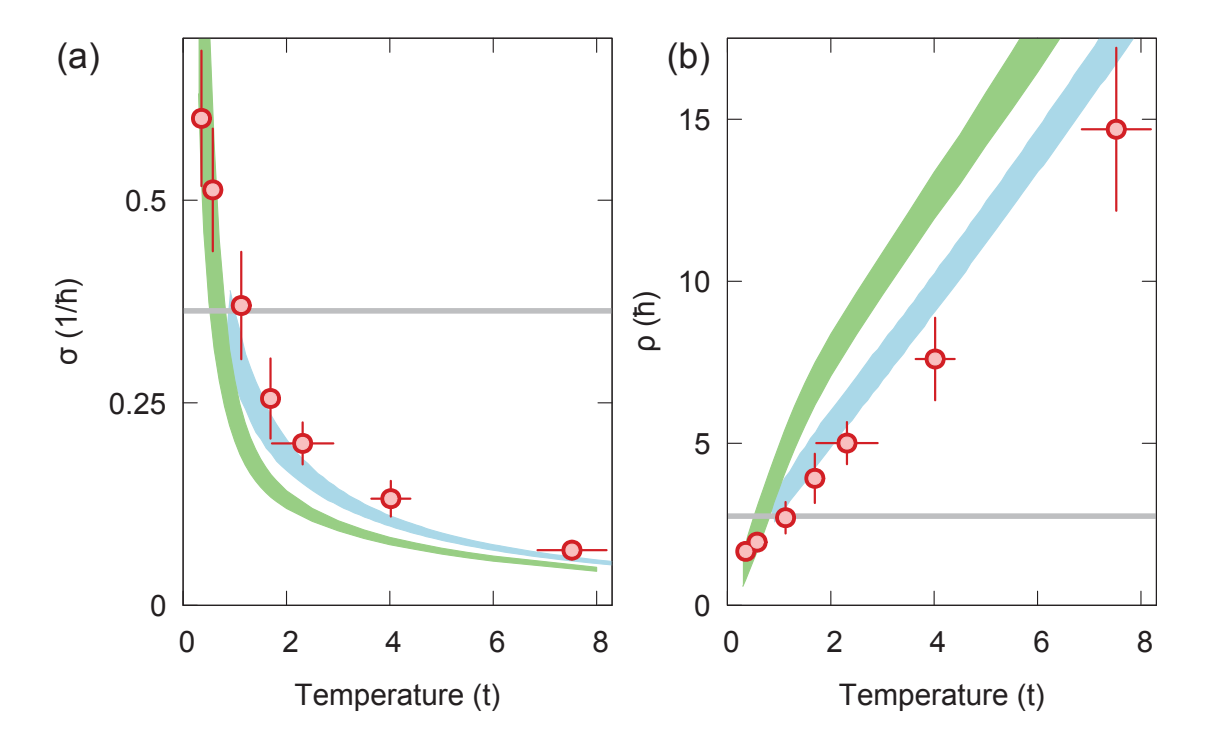


Figure 1.3: Conductivity versus temperature. (a) Results for the DC conductivity, σ . Experiment (red), 16-site finite-temperature Lanczos method for U/t = 7.5 and $\langle n \rangle = 0.8 - 0.85$ (light-blue band), single-site dynamical mean-field theory results for U/t = 7.5, $\langle n \rangle = 0.825$ (green band), and the lower bound on conductivity inferred from the Drude relation using the Mott-Ioffe-Regel limit, $\sigma_{\min} = \sqrt{\frac{n}{2\pi}} \left(\frac{1}{\hbar}\right)$ (grey). (b) Results for the resistivity, ρ , using the same color scheme. Experimental error bars sem.

In chapter 3, I describe in detail each step along the way to imaging ultracold fermions in an optical lattice. First I explain how we cool the atoms from the initial 700 K temperature out of the oven down to a few mK and trap them in the magneto-optical trap. Next I describe the process of loading the atoms into an optical dipole trap where, after evaporation, we achieve a quantum gas of fermions. Next, I present our scheme to produce Fermi gases in a "quasi" 2D geometry. Finally I explain how we image fermions with single site resolution in an optical lattice. It involves the development of a Raman sideband cooling scheme that works with a 2D lattice and a light sheet in the third direction where the atoms are not confined in the Lamb-Dicke regime.

In chapter 4, I describe the work surrounding our first publication [35]. Before exploring lattice gases, we embarked on a study of spin imbalanced Fermi gases in a "quasi" 2D geometry. We explored the in-situ density of majority and minority spins and saw that the density remained equal near the center of the trap even for large imbalances. We studied this phase separation effect across the BEC-BCS crossover. In addition, we observed condensation of fermions on the BEC side. Interestingly,

unlike 3D, condensation did not vanish when phase separation ended, pointing to the possibility of a polarized condensate.

In chapter 5, I describe the work published in [65]. It is the first study of fermions with attractive interactions in any quantum gas microscope. We observed the formation of charge density waves in our system by perfecting a technique to image only sites with double occupancies. We established that the density correlators were a better thermometer than densities at low temperatures. Finally we shed light on a mapping that exists between the repulsive and the attractive Hubbard models due to a particle-hole transformation.

In chapter 6, I summarize the important results from the experiments described in this thesis. Furthermore, I present an outlook on the research being performed in our lab and the exploration of many further aspects of fermions in lattices.

Chapter 2

Experimental Setup

2.1 Vacuum Chamber Design

The main components of our vacuum chamber are the science chamber, the oven and the Zeeman slower. A large part of our vacuum chamber design was based off a design by the Heidelberg group [74]. The science chamber is the spherical octagon from Kimball Physics (MCF600-SphOct-F2C8) that has eight viewports for optical access. It is made from 316 stainless steel. The viewports themselves were CF40 fused silica from Kurt J. Lesker Company (VPZL-275Q). The top and bottom viewports required a special design for reentrant windows that will be discussed later. The spherical octagon was sent to GSI Helmholtzzentrum für Schwerionenforschung GmbH in Darmstadt to get a Non-Evaporable Getter (NEG) coating. This coating helps in achieving ultra-high vacuum in our experiment. The coating process is a magnetron sputtering performed under vacuum with a TiZrV wire as cathode and the octagon as anode. Krypton is used as sputter gas. The NEG coating needs to be activated normally at 250°C for 24 hours. In case the coating needs to be reactivated, which can occur if the system needs to be vented, then it is recommneded to start the NEG activation at a lower temperature (220°C for 24 hours), which can be increased at each reactivation. In addition, the coating does not degrade if it is not under vacuum. We performed this activation process during the bakeout stage.

Our experiment required a number of custom parts. The main custom parts are the oven, a 4-way and a 6-way cross, a vacuum feedthrough and the Zeeman slower rod (Fig.2.1). The 6-way cross in sandwiched between the Lithium oven and the Zeeman slower. On the inside, it houses a motorized atomic shutter mounted through the vacuum feedthrough and a Titanium sublimation cartridge (Varian Model 9160050) mounted on a CF100 to CF40 reducer flange (Kurt Lesker RF600X275). In addition, the 6-way cross provides optical access through two CF40 extensions that can also be used to mount an all metal angle valve (VAT 54132-GE02-0001) and an ion pump. The 4-way cross is designed to be very similar to the 6-way cross except it is placed after the science chamber.

The Lithium oven consists of a CF16 flange leading up to a 25 mm diameter reservoir through a narrow neck of 10 mm inner diameter. We fill the reservoir

with isotopically purified ^6Li (95% isotopic purity provided by Cambridge Isotope Lab and then cleaned and repackaged under inert gas in a sealed ampule by Ames laboratory) and with a band heater wrapped outside, we are able to generate sufficient vapor pressure by heating up to 350°C. In stand-by mode, we keep the oven at a temperature of 250°C where the vapor pressure is very low but it allows us to reach high temperature faster during start-up. Usually we fill the oven with 1 gram of ^6Li which has a life span of $\sim 8,200$ hours of continuous use.

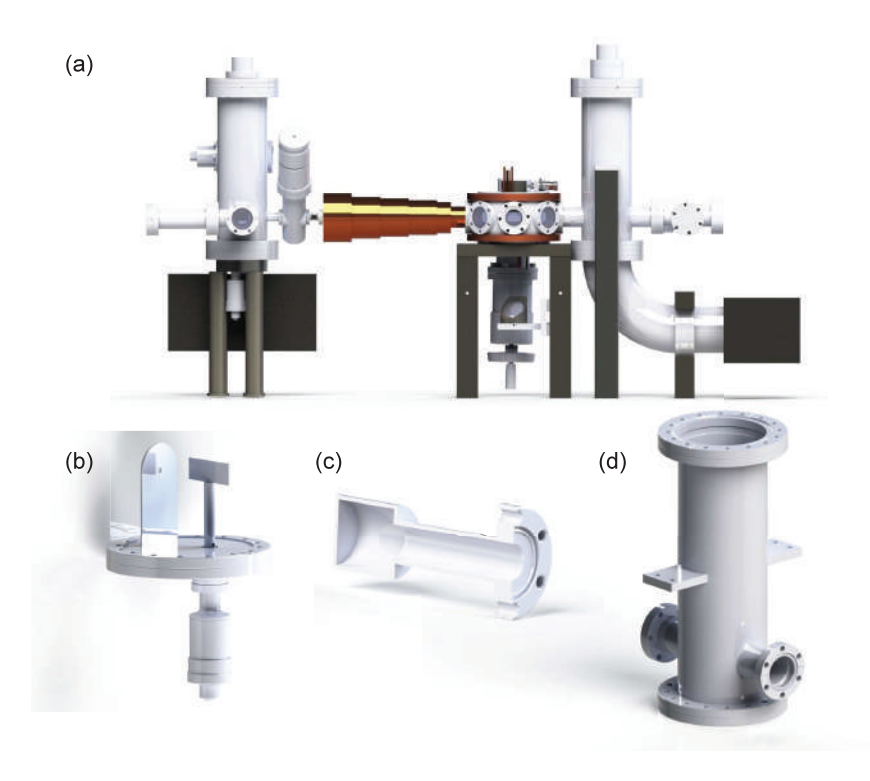


Figure 2.1: SolidWorks rendering of the experiment design. (a) The full vacuum chamber assembly showing from the left to right, the oven, the 6-way cross, the Zeeman slower, the science chamber and the 4-way cross. (b) Schematic of the atomic beam shutter attached to an external motor, along with a 5 mm aperture connected to the feedthrough. (c) Cross-section of the oven. (d) Schematic of the 4-way cross with the two brackets on the sides to support the structure.

The vacuum feedthrough is essentially a modified CF100 flange intended to be attached to the bottom of the 6-way cross. It has an extension with a CF16 flange offset from the center. We attach a motor connected to a vacuum feedthrough (MDC670000-01) through this extension which in turn connects to a barrier for the atomic beam. In addition, the feedthrough also holds an aperture of 5 mm diameter intended to limit the solid angle of the atoms coming out of the oven.

The Zeeman slower tube has a CF16 flange on one end and a CF40 on the other. Although the outside is cylindrical with a diameter of 19.05 mm, the internal structure is conical with the diameter increasing from 5 mm (at the entry point for atoms) to 16 mm (at the exit point). The total length of the slower tube is 300 mm. All the custom designed parts were manufactured by Sharon Vacuum using 304 stainless steel. Both 304 and 316 stainless steel have similar non magnetic properties with 316 stainless steel being less prone to becoming magnetic when cold worked and more resistant to corrosion. However the cost and availability of 304 stainless steel makes that a more preferable choice.

To connect the oven side of the experiment to the science side, we added an all metal gate valve (VAT 48124-CE01-0001) with CF16 flange connectors on both sides. The idea is to separate the two sections so that whenever we would need to replace lithium in the over, we could avoid breaking vacuum on the experiment side. In addition, we introduced a bellow (Kurt Lesker MEW0750251C1) in between the gate valve and the Zeeman slower in order to mechanically decouple the two sides and it also helps in aligning the atomic beam to the MOT center.

On the experiment side, we added a CF40 all metal gate valve (VAT 48132-CE01-0002) to one of the optical accesses on the spherical octagon through a closed coupler (Kimball Physics MCF275-ClsCplr-C2-700) for flexibility with orientation. The purpose of this valve is to keep open the possibility of a future expansion of the science chamber to a science cell where atoms could be transported. This valve was also placed upside-down to decrease clutter on top of the science chamber. The experiment side is also fitted with the same angle valve as the oven side for turbo pump connection.

2.2 Reentrant Vacuum Viewports

The reentrant viewports that go on top and on the bottom of the spherical octagon were custom designed especially keeping in mind that the crucial aspect of a quantum gas microscope is the placement of a high numerical aperture (NA) objective. To determine the vertical spacing between the top and bottom reentrant viewports, we factored in that the diameter of the MOT beams passing in between the viewports is ~ 25 mm. The vertical thickness of the spherical octagon is 38.1 mm and the viewports on the sides (Kurt J. Lesker Company VPZL-275Q) have an aperture of 35.6 mm, sufficiently larger than the MOT beam diameter.

For the aperture of the reentrant viewport itself, the maximum available diameter is quite large at 110 mm. But the constraint of placing the Feshbach coils close to the atoms meant that we would only be able to use a small fraction of the available space. The Feshbach coils have an inner diameter of 55 mm and outer diameter of 90 mm.

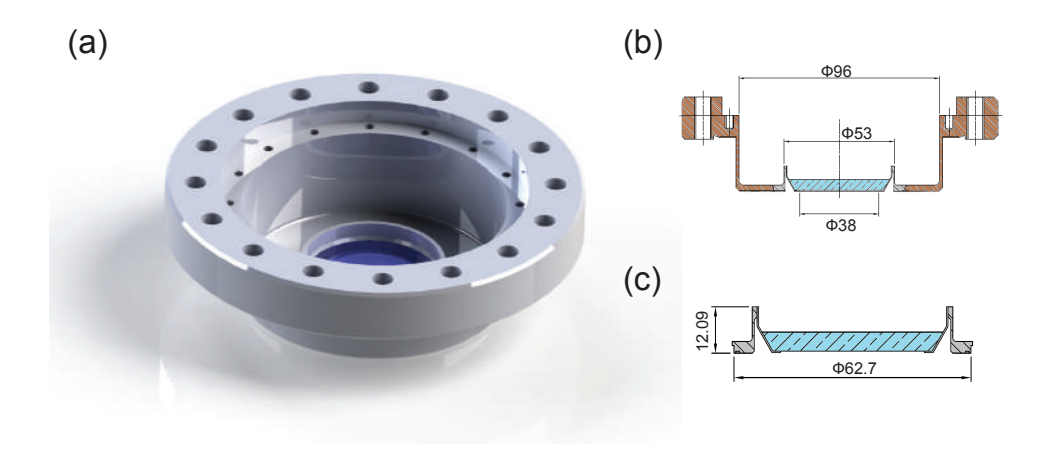


Figure 2.2: Design of reentrant vacuum viewports (a) Solidworks rendering of the viewport. The outermost through holes are meant for connecting to the spherical octagon while the inner tapped holes are for securing the Feshbach coils. (b) Cross-section of the assembly showing the important dimensions and the aperture of the viewport. (c) Cross-section of the sub-assembly that was sent around for AR/HR coating and ultimately welded to the larger sub-assembly. All dimensions are in mm.

To achieve the highest possible resolution with our microscope, the quantity that matters is the numerical aperture (NA) that we can obtain from this system. For a distance of 11 mm from the atoms to the reentrant viewport and an aperture of 38 mm, one can get an NA $(\sin(\theta))$ in excess of 0.5. The distance between the reentrant viewports of 22 mm would also allow for sufficiently large MOT beams.

The reentrant viewports were manufactured by the UK Atomic Energy Authority. The material used was 316 stainless steel. The viewport was manufactured in multiple stages. First a fused silica disk (Spectrosil 2000) of thickness 5 ± 0.03 mm, flatness of $\lambda/10$ and polished to a scratch/dig of 20/10 was bonded to a stainless steel ring (Fig.2.2(b)). Although the substrate flatness was sufficient for our applications, the bonding process can lead to warping of the glass. So this subassembly was then sent to Fineoptix GmbH in Germany for MRF polishing. Upon testing for the surface flatness with reflection interferometry, each surface individually was measured to be 5λ in flatness. However when measured for transmission through both surfaces against a mirror as reference, the relative flatness was around 0.02λ . Since we care more about the relative flatness of the surfaces, we decided to skip the MRF polishing step.

At the end of this stage, the subassemblies were shipped back to Spectrum Thin Films in the US for AR/HR coating (see section 2.3). After that, the subassemblies were shipped back to the UK AEA to be welded on to the rest of the reentrant viewport.

2.3 AR/HR coatings

For the purpose of our experiment and for 6 Li, we designed the coatings to be optimal at the following wavelengths. At 671 nm for the MOT and Raman light, at 1064 nm for the dipole trap and the 2D lattice, at 532 nm for the accordion lattice and at 323 nm for a possible UV MOT in the future. The viewports on the 6-way cross on the oven side of the experiment were left uncoated because we only need that optical access for diagnostics. The 6 viewports on the side of the spherical octagon along with the one viewport on the 4-way cross for the Zeeman slower beam were all anti-reflection coated for the four wavelengths. All transmissions were optimized for normal incidence. The coating company (Laseroptik GmbH) performed the coating process at 200°C based on the viewport manufacturer's recommendation. The resulting measured coating curve is shown in Fig. C.1. Below are the measured transmission at the design wavelengths and for an angle of incidence of 0° :

1. 671 nm : $T \sim 95\%$

2. $1064 \text{ nm} : T \sim 92\%$

3. 532 nm : $T \sim 92\%$

4. $323 \text{ nm} : T \sim 80\%$

The reentrant viewports had a slightly different set of requirements than the side viewports. Although the bottom viewport needs to be anti-reflection coated like the rest, the top one would need to be high transmission at 671 nm for the MOT beams, while high reflection at 1064 nm only on the inside vacuum surface. The reason for that is to enable the retro-reflection of a laser beam to form a lattice in the vertical direction. As we will see later, we ended up not using the HR coating. High reflection coatings are more complicated for a variety of reasons:

- Usually HR coatings require more layers than AR coatings leading to adhesion problems on polished surfaces.
- High-reflection at a given wavelength λ can lead to moderate reflection (30-40%) at $\lambda/2$.
- HR coatings require higher temperatures. Depending on the type, post coating treatments at temperatures up to 380°C may be required.
- The same problem of higher temperature requirements mean that mounted or bonded viewports might be susceptible to damage.
- Any mounted optic would be effected by shadowing during the deposition process. For HR coatings, this effect could be more pronounced due to their greater thickness.

The HR coating was performed by Spectrum Thin Films. In addition they performed the AR coating on the other side of the top reentrant viewport and both sides of the bottom viewport. The resulting measured coating curves are shown in Fig. C.2. Below are the measured transmissions at the design wavelengths and for an angle of incidence of 0° for the two coatings separately:

- 1. 671 nm : AR (T $\sim 99\%$); HR (T $\sim 95\%$)
- 2. $1064 \text{ nm} : AR (T \sim 99.5\%); HR (T < 1\%)$
- 3. 532 nm : AR (T $\sim 99\%$); HR (T $\sim 35\%$)

We realized after the bakeout of the vacuum chamber that the HR coating actually got damaged (see section 2.4 for details). We considered breaking vacuum to remove the HR coating but we were told by the company that it was a very durable coating. They had tried to chemically remove the coating in the past with poor results. The only way to completely remove the coating would be to polish the fused silica. Given the complexity of the process, we decided to continue with the partially damaged coating.

Another coating that we needed for the experiment was an HR coated dot of 2 mm diameter on top of an AR coated quarter-wave plate of 30 mm diameter. The purpose of this piece was to act as the retro-reflection for the vertical MOT beam after it goes through the objective (see section 2.7.2). This coating was also performed by Spectrum Thin Films using a mask. The specs for the coating is R > 99% @ 671 nm for an angle of incidence of 0° .

2.4 Bakeout

In order to achieve ultra-high vacuum (UHV) inside our vacuum chamber, one needs to remove the largest source of background gas - hydrogen. Although a vacuum pump can easily remove other gases from the chamber, it is the hydrogen atoms that are bound to interstitial sites of the stainless steel surface or that satisfy dangling bonds that desorbs at a very slow rate - a process known as outgassing. But even before reaching UHV pressures, there are other sources of outgassing that need to be taken into account like fingerprints, oil/grease from machining, water vapor, etc. In this section, I will describe the entire process that started with design considerations and ended with a UHV system.

The material of choice is stainless steel. The various components were cleaned in the following order:

- 1. First all items were inspected by eye for any visible signs of dirt or gunk. The knife edges on the flanges were checked for damage.
- 2. For the vacuum parts that were manufactured by Sharon vacuum, we first sonicated them with the soap Alconox mixed with tap water for 15 minutes. Then we drained the soap water and sonicated again for 15 minutes in tap water. To sonicate the large 4-way and 6-way crosses, we employed a large size sonicator (Quantrex Q650H).
- 3. For all vacuum components except the vacuum windows, we sonicated them first in acetone inside of a fume hood for 15 minutes and then in isopropyl alcohol (IPA) to remove any residues left by acetone. The viewports were never sonicated nor were they treated with soap or acetone to prevent damage to the AR or HR coatings. The only cleaning process performed was using lens cleaning paper and methanol.
- 4. The items were then placed in UHV grade aluminum foil (All Foils inc) and allowed to dry in air. Thereon after the parts were kept completely wrapped in UHV foil till they were ready to be assembled.

We assembled and baked out the oven side of the experiment first since it required fewer custom parts, no special coatings on the viewports and a less stringent vacuum requirement. The various flanges were mated using copper gaskets except for the lithium oven, for which a nickel gasket (Kurt Lesker GA-0133NIA) was used to withstand possible degradation due to the high lithium flux. We used standard silver plated hex bolts and nuts which were themselves sonicated in acetone and IPA. They were tightened in a star pattern using a torque ratchet up to the recommended torque values. We used an anti-seize (Kurt Lesker VZTL-4OZ) to ensure that the bolts are removable in the event that we need to break vacuum in the future.

The next step is to check for leaks in the vacuum system. We did not use a leak detector for this but instead just started the pumping process. We connected the turbo pump (Varian Turbo V 81-M) to the angle valve and connected the outlet port

of the turbo to a roughing pump (Varian SH01101UNIV) through a 4 feet long bellow with NW25 KF ends (Kurt Lesker MHT-QF-B48). To measure the pressure, we installed ion gauges (Varian UHV-24P) within standard straight CF40 nipples (Kurt Lesker FN-0275S). This ion gauge is sensitive in a wide range from 10^{-3} down to 5×10^{-12} Torr. We attached another gauge (ConvecTorr L9090305) to measure a pressure range from atmospheric down to 10^{-4} Torr. We started the evacuation process while keeping the angle valve closed and turning on the roughing pump while keeping the turbo off. The roughing pump can reach an ultimate pressure of 5×10^{-2} Torr. After a few minutes of roughing when the pressure is low enough on the outlet of the turbo, it is safe to turn on the turbo pump. The turbo pump was mounted to avoid any stress and unwanted vibrations. Once the turbo reached its maximum speed of 1350 rpm, we opened the angle valve. We can start measuring a readout of the ion gauge when the ConvecTorr gauge bottoms out at a value close to $\sim 10^{-4}$ Torr. At this point we can perform a crude leak check by spraying compressed air and/or methanol around all the flanges and joints while looking for a pressure spike on the ion guage. We never found any leaks in our system.

After reaching close to the base pressure of the turbo, we closed the angle valve and turned off first the turbo and then the roughing pump (after the turbo came to a complete stop). The sealed and partly evacuated vacuum system was then wrapped with regular aluminum foil which inturn was wrapped with heating tape (HTS/Amptek AWH-051-060DM-MP) to cover as much of the surface as possible. The viewports were covered with a copper cap that ensured the heating tape or aluminum foil could never make direct contact with the glass or any coating on it. We placed thermocouples (Omega Engineering SA1XL-K-200-SRTC) at different locations around the setup, sometimes using two thermocouples in sensitive areas like in the vicinity of viewports. The setup was then wrapped over with another layer of aluminum foil.

Each side of the experiment is in addition equipped with an ion pump. The oven side has a smaller pump (Varian VacIon Starcell Plus 40) which has a CF40 flange connector and a pumping speed of 36 l/s while the experiment side is larger (Varian VacIon Starcell Plus 75) with a CF100 flange connector and a pumping speed of 65 l/s. In order to bake them out, we removed their outer cover and the magnets and wrapped the rest with foil and heating tape. The pumps can't be operated without the magnets but they won't be turned on anyway until the end of the bakeout process.

Through the process of baking out, the temperatures in different sections of the vacuum system was monitored and incremented at a rate of ~ 1 °C/min to reach the final values using variacs connected to the heating tapes. Bakeout continued as long as the pressure did not reach a steady state with all temperatures held steady. Following is a list of vacuum parts, the recommended bakeout temperatures and actual temperatures at which they were baked.

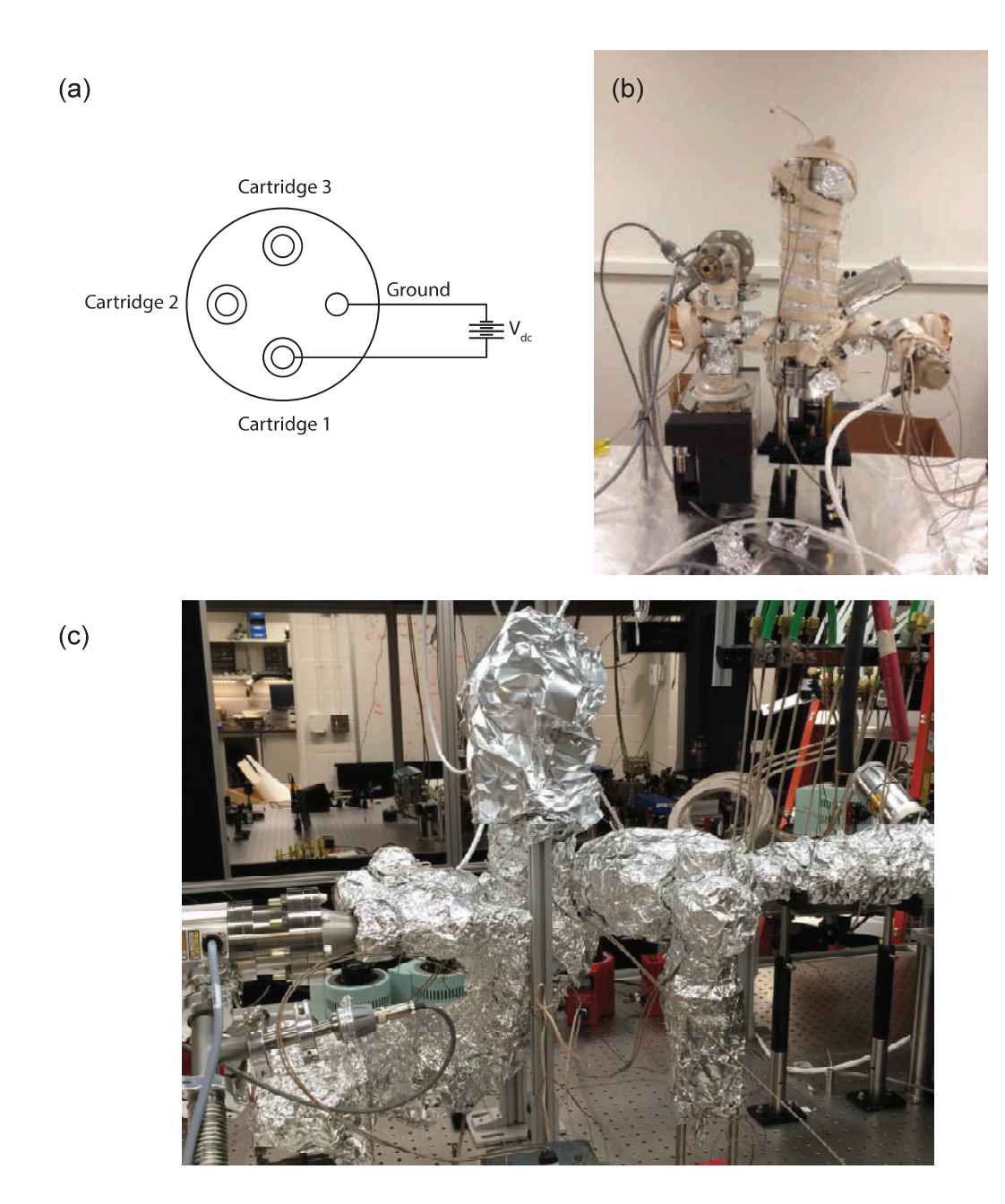


Figure 2.3: Vacuum system bakeout. (a) Connector diagram for Titanium sublimation filament. We connect one cartridge at a time to a 50 A DC power supply. In normal mode of operation, we supply 30 A through a cartridge that requires a voltage drop of 2.8 V. (b) Bakeout of the oven side of the experiment. This part was baked first before assembling the rest of the experiment. In this picture one can see the heating tapes wound around the different parts already covered with aluminum foil. (c) Bakeout of the rest of the experiment.

Table 2.1: Bakeout parameters

Vacuum Part	Recommended Max Bakeout T (°C)	Actual Bakeout T (°C)
4-way and 6-way cross	450	360
Lithium oven	-	270
Angle valves	300	220
Gate valves	300	120
Ion pumps	350	300
Zeeman slower	150	80
Spherical octagon (NEG)	220	160
Reentrant viewports	250	200
Ion gauges	450	260
AR/HR coatings	< 200	180

The only exception to the bakeout process was the Zeeman slower tube. Since the slower coils need to be slid in place before sealing the flanges and since the coil insulation can't be subject to very high temperatures, the slower tube was separately air baked at 350 °C before being installed.

At the end of the first stage of bakeout, the ion pump magnet was replaced and the ion pump turned on. To prolong the life of these pumps, they should only be turned on after the pressure has reached values below 10^{-6} Torr. The temperatures of the various vacuum parts were held constant for several hours, now with the ion pump turned on. Once the pressure was around 10^{-7} Torr, we turned off the ion gauge and applied a current of 25 A for 60 mins to degas the titanium-sublimation filaments. The bakeout process is complete and the temperatures can now be gradually decreased to room temperature.

After the whole system was cooled down, we again applied 30 A to the titanium-sublimation filaments. The heating due to the high currents causes titanium atoms to sublimate and settle on the comparatively colder stainless steel. Hence it was also important in the design to avoid any line-of-sight between the sublimation element and the viewports. To ensure that, one must take into account the fact that the rods elongate by several millimeters when hot. In our design of the 6-way cross, we left a space of oonly 1.5 mm between the bottom of the titanium-sublimation filament and the atomic shutter. So to avoid the expanding filament from hitting the shutter, we had to keep the shutter in the "open" position where they would not touch. To avoid line-of-sight from occuring on the 4-way cross due to expansion, we added an extra double sided CF40 flange of 25.4 mm thickness (Kurt Lesker DFF275X150SS) to connect the filament to the top of the 4-way cross. After firing the filaments, the pressure in the vacuum system declined sharply to about 10^{-11} Torr. In normal operation, the pressure on the experiment side is about 5×10^{-12} Torr and the oven side about 3×10^{-10} when the oven is hot.

2.5 Magnetic Field Coils: Design and Winding

Magnetic fields play an important role in ultra-cold atom experiments, starting with a spatially varying field for the Zeeman slower, an anti-Helmholtz field for the MOT to a uniform field to tune the scattering length around a Feshbach resonance. Thus it becomes paramount to design these field coils after performing accurate simulations. The description of the design and implementation of each coil is laid out in the subsequent sections. All the coils were wound using the same hollow core copper wire. The wire itself was seamless Oxygen-free Copper alloy 101 (Small Tube Products). This alloy is suitable for magnetic coils because of its very low resistance and its soft temper makes it highly malleable for winding purposes. In addition, the wire had a hollow square cross-section with outer dimension 3.18 mm and inner dimension 1.59 mm. The wire was, however, not insulated. So the spool of wire was coated with Double Dacron glass insulation (Express Wire Services Inc.). Dacron glass is specially well suited for our purposes because it is abrasion resistant, increases flexibility and prevents overload burnout. The epoxy used to bind the coil was nonmagnetic (Duralco NM 25-1 sold by Cotronics Corp.). The total outer dimension including the insulation and the epoxy was ≈ 3.5 mm.

2.5.1 Zeeman slower

The first stage of a typical cold atom experiment is the process of Zeeman slowing. The basic idea of slowing is that an atom that posseses a cycling transition of energy $\hbar\omega_a$ can repeatedly absorb a resonant photon of momentum $\hbar k$ and get a recoil in its momentum. This would imply effectively slowing down the velocity of the atom and since the transition is cycling, the process can occur several times. The spontaneously emitted photon after each absorption does not, on average, impart momentum to the atom because of equal emission probability in all directions. The one caveat though is in its rest frame, an atom moving with a velocity v sees an incoming photon frequency to be Doppler shifted. So even if the photon was initially resonant to the atom frequency, it ceases to be so as it gets slowed down. The Doppler shift in frequency is given by $\omega' - \omega_a = \omega_a v/c$.

There are many strategies to account for this Doppler shift. One approach is to chirp the frequency of the incoming photons at a suitable rate. Another approach more suitable for implementation in our experiment is using a magnetic field gradient (B(z)). We designed the slower in a decreasing field configuration. In the presence of this field gradient, the atoms experience a Zeeman shift leading to a total shift in detuning of

$$\delta_{eff} = \delta_0 + \omega_a \frac{v}{c} - \frac{\mu_B B(z)}{\hbar} \tag{2.1}$$

Where, δ_0 is the bare detuning between the atomic transition and the laser frequency (ω_l) and μ_B is the Bohr magneton. We start out by first estimating the average velocity of lithium atoms coming out of the oven. For a temperature of $\sim 400^{\circ}\text{C}$, the RMS velocity is given by the Boltzmann formula $v_{RMS} = \sqrt{3K_BT/m} \sim 1300 \text{ m/s}$,

where K_B is the Boltzmann's constant and m is the mass of a lithium atom. We want to calculate a B-field profile of the form $B = B_0 \sqrt{1 - z/z_0}$ using Newtons law to obtain a uniform deceleration. z_0 is the length of the slower. At the end of this length, we want to slow down most atoms in the ground state to around 50 m/s which is the capture velocity of the MOT. At a given location z within the slower, suppose that the velocity of an atom in v(z) and the field is B(z). One can calculate the Zeeman shift in the ground and excited hyperfine states using the Breit-Rabi formula. For any given ground hyperfine state, the detuning $(\Delta E(F, m_F, F', m'_F, B(z))/\hbar)$ to the excited manifold can be calculated.

Then the force the atom experiences due to absorption of a photon is

$$\mathcal{F} = m\frac{dv}{dt} = -\hbar k_l \frac{s\Gamma/2}{(1+s+4\delta(z)^2/\Gamma^2)}$$
 (2.2)

Where, $s = I/I_{sat}$ is the saturation parameter amd I_{sat} is the saturation intensity of the transition, Γ is the transition linewidth and $\delta(z)$ is the effective detuning at the location z given by $\delta(z) = \delta_0 + \omega_a v(z)/c - \Delta E(F, m_F, F', m'_F, B(z))/\hbar$. Knowing this, one can calculate the final velocity after accounting for deceleration through the entire length of the slower.

In Fig. 2.4(a), one can see the result of the simulation for a slower of length 398 mm (from center of the MOT to entry point of slower). We assume a saturation parameter s=4 and a maximum field strength of 750 G. We see that for the highest energy ground state, one can slow atoms with speeds less than 750 m/s down to 50 m/s over the length of the slower. In comparison, atoms with speeds less than 850 m/s in the third highest energy state can be slowed down to ~ 150 m/s.

With the theoretical B-field profile calculated, we now turn to simulating currents in the coils of the slower to produce the required profile. For that we used a 3D modelling package in conjugation with Mathematica called Radia [75]. We split the slower into 6 parts. The first part is the coil that is closest to the chamber. It is composed of a single layer of 8 turns and it has its own power supply and a single input and output port for water cooling. The rest of the coils carry the same current but have variable number of turns (layers). Starting from the second to the sixth, the number of turns (layers) are 8 (3), 16 (4), 16 (5), 16 (6) and 16 (8). There are in total five input and output ports for water cooling. To determine the currents required in the coils, we simulated the coil geometry and fit I_{first} and I_{rest} to best fit the theoretical field profile $(B = B_0 \sqrt{1 - z/z_0})$. We obtain $I_{first} = 42$ A and $I_{rest} = 30$ A. The fit required us to include the field due to the MOT coils such that the total axial field smoothly reduced to 0 in the center of the science chamber.

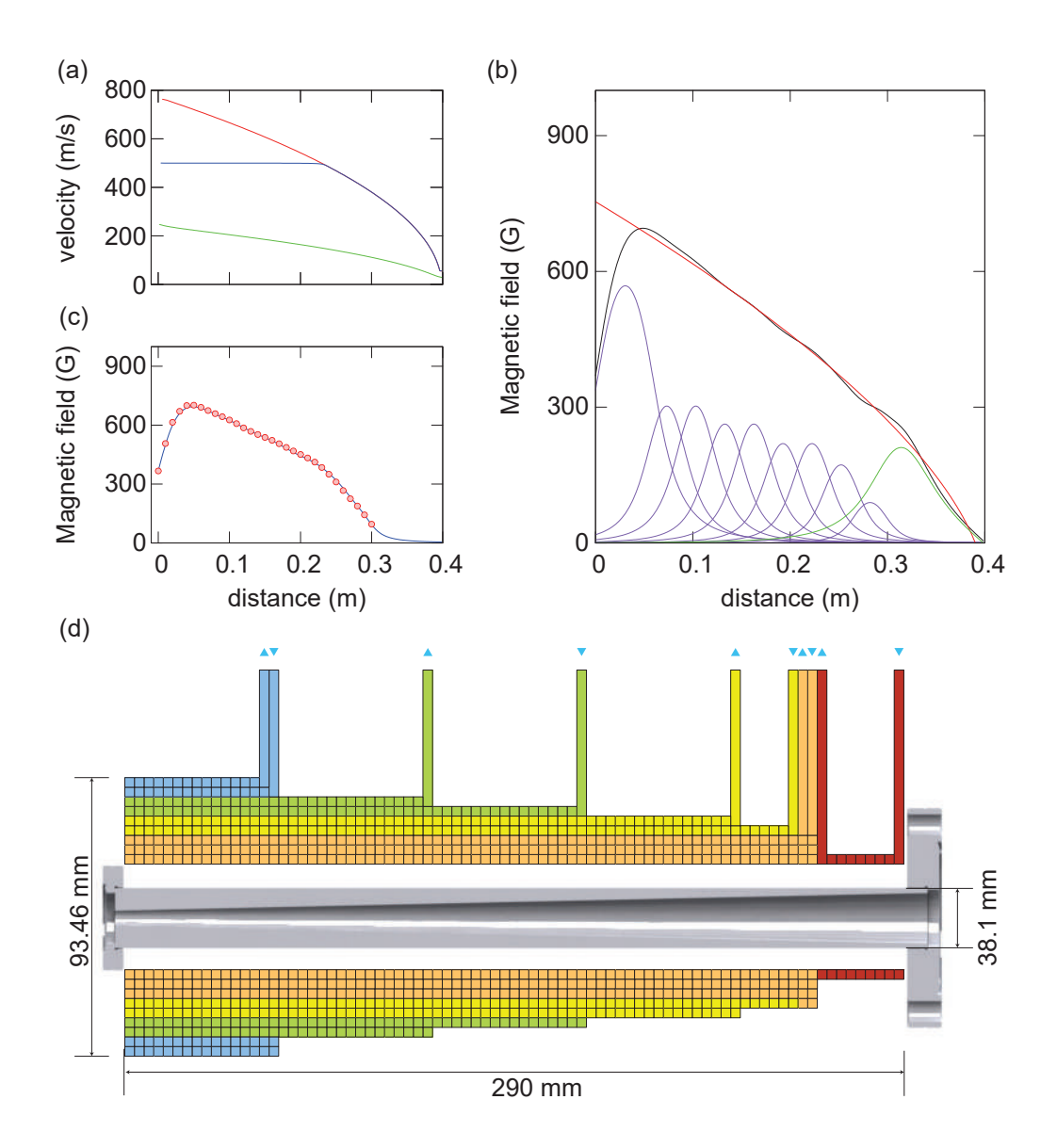


Figure 2.4: Zeeman slower design and testing. (a) The velocity profile for an atom in state $|6\rangle$, starting out with a velocity of 500 m/s (blue) and the maximally slowable 765 m/s (red). Similarly for an atom in $|1\rangle$ starting out with the maximally slowable velocity of 250 m/s (green). (b) Radia simulation of field profile for each slower coil (purple), MOT coil (green), total (black) and theoretical field profile (red). Distance on the x-axis ends at the position of the center of the MOT. (c) Simulated total field due to all 6 slower coils (minus the MOT coils) (blue line) and the corresponding measured values (red circles) after the slower was built. (d) Schematic of the slower design. Number of turns and layers are accurate although not to scale. Space between tube and coils is filled with air. The first coil (red) is electrically isolated from the rest. The rest of the coils have the same current flowing through each wire. Blue arrows depict direction of water cooling input/output. Color coding shows sections supplied by a single cooling water input/output.

2.5.2 MOT coils

Even during the design of the Zeeman slower coils, we took into account the anti-Helmholtz field that would eventually trap the atoms. The simplest configuration to achieve that is to use two cylindrical coils carrying currents in the opposite direction to achieve $\vec{B}=0$ at the geometric center. Since we wanted to separate the MOT and Feshbach coils, we chose the location to be on top of the spherical octagon around the reentrant viewports (Fig. 2.5(a)). The limiting constraint for us is the outer diameter of the reentrant vacuum viewports because the MOT coils would be placed around them. The chosen inner diameter was thus fixed at 154.4 mm and the distance between the inner surfaces was fixed at 70.6 mm. The target gradient for operation of the magneto-optical trap is ~ 20 G/cm near the center of the trap.

The simulation of the MOT coils was also carried out using the Radia package. The final configuration has 6 concentric turns and 4 lateral layers in each of the two MOT coils. Each coil in addition has three sets of leads for both electrical contact and for cooling water. According to the simulations, we need to run a current of 112.2 A to obtain the desired field gradient of 20 G/cm.

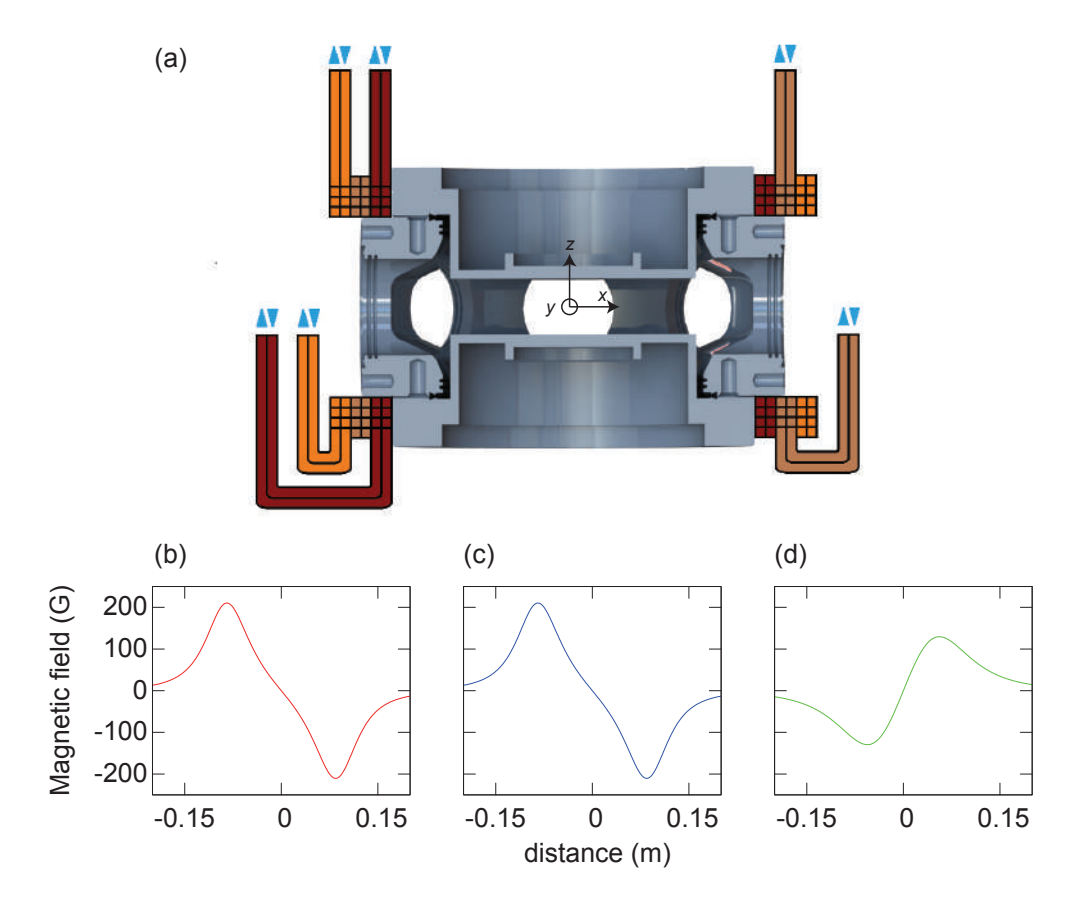


Figure 2.5: MOT coils. (a) Schematic of MOT coils with reference to the vacuum system. The inner diameter of the coils is constrained by the reentrant vacuum viewports. The distance between the coils is contrained by the spherical octagon. Color coding signifies the extent of the coils cooled by a single pair of leads. All coils are electrically connected to the same power supply and carry current in opposite directions between the top and the bottom. (b) Simulation of the x-component of \vec{B} along the x-axis for a current of 112.2 A. (c) The y-component of \vec{B} along the y-axis. (d) The z-component of \vec{B} along the z-axis. The origin is defined as the geometric center of the spherical octagon.

2.5.3 Feshbach coils

Probably the most crucial magnetic field in the experiment is the Feshbach field. This field allows us to tune the interactions between $^6\mathrm{Li}$ atoms by using the magnetic field dependence of the s-wave scattering length (a_s) . It is important for this field to be uniform over the size of the atomic cloud. For this reason we employ two coils in Helmholtz configuration, unlike the MOT coils. One of the initial challenges is to design a water cooled coil that can produce fields in excess of 1000 G. That is since the $|1\rangle - |2\rangle$ Feshbach resonance occurs at 832 G, one would need to go to sufficiently higher field to access the weakly interacting regime.

In order to reduce the requirement for current, we placed the Feshbach coils at a location closest to the atoms yet outside the vacuum system. The reentrant vacuum viewports were designed with this in mind, to utilize the region right next to the window. We simulated the field due to the Feshbach coils also using the package Radia. The inner diameter of the coil is 55 mm while the outer diameter is 90 mm. We would also want the magnetic field to be uniform over a distance of a few millimeters. The final configuration we used consisted of 5 concentric turns stacked in 4 layers. The field profile is shown in Fig. 2.6. For a current of 200 A, we produce a field of 911 G with a curvature of 0.16 G/mm² at this field at the center. The curvature of the Feshbach field also produces magnetic confinement for the atoms, although it is much smaller than the confinement produced by the trapping lasers.

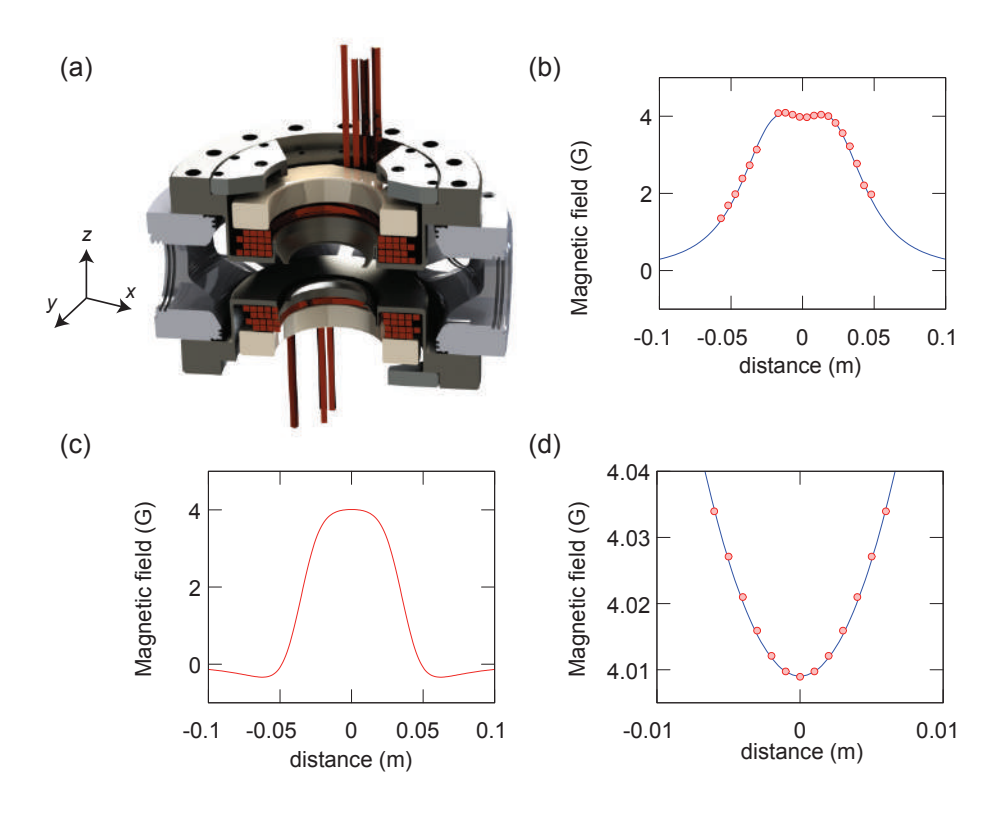


Figure 2.6: (a) Solid works rendering of the Feshbach coils and their placement relative to the reentrant vacuum viewports. The coils (red) are sandwiched between the viewport and a piece of Macor (white). There are two sets of input and output for water cooling for each coil. (b) Simulation of B_z along z-axis over a range of 100 mm (blue line) and actual measurements (red circles) for a current of 0.88 A (c) Simulation of B_z along the y or x-axis for 0.88 A. (d) The curvature of the field (B_z) along the z-axis around the geometric center in a smaller range of 10 mm. Simulation (red circles) and quadratic fit (blue line) for a current of 0.88A.

2.5.4 Coil Winding

In order to facilitate the winding of the Zeeman slower coils and also to avoid twisting of the hollow core wire during winding, we designed a wire feedthrough (Fig. 2.7(b)) machined from Teflon. The feedthrough can be mounted on a standard lathe and has a square channel of side 3.18 mm running through the whole length. The reason we avoided using metal to make the feedthrough was to prevent scratching the Dacron insulation on the wire at any sharp edges. In addition, the added friction from the feedthrough also increased the tension on the wire, making it easier to ensure close packing. The whole setup was mounted on a lathe as shown in Fig. 2.7(a). The lathe was used to rotate the tube at the slowest speed (20 rpm) while the epoxy was spread on the wire with a brush after the feedthrough. Along with the rotation, the feedthough was translated by hand. Once each layer was complete, about half a meter of extra coil length was retained for connections before the wire was cut with a saw to make sure the hollow opening was not constricted. Then once the layer had dried out, the next one was layed over in the same fashion. The slower coils were the hardest ones to wind and took several days to complete.

The MOT and Feshbach coils comprised of fewer turns and layers but were wound on the lathe in a similar fashion. One difference, however, was that for the slower, the extra length of wires for connections were tangential to the windings while for the MOT and Feshbach coils, they needed to be bent out of plane to make them accessible. This bending needs to be done carefully to avoid pinching and constriction of the coil. In addition, these connections had to be meticulously placed out of the way of other essential optics like the objective.

In order to make electric contacts, we stripped the insulation on the wire about 5 cm below the end. Then we silver soldered a custom made part out of copper that contains a channel wide enough for the wire to slide through (Fig. 2.8(b)). This piece had a circular hole to attach it with 1/4-20 bolts. Next to make connections with the water cooling system, we used a standard swagelok compatible fitting with a square hole (Fig. 2.8(c)). The wire was silver soldered after passing through the hole.

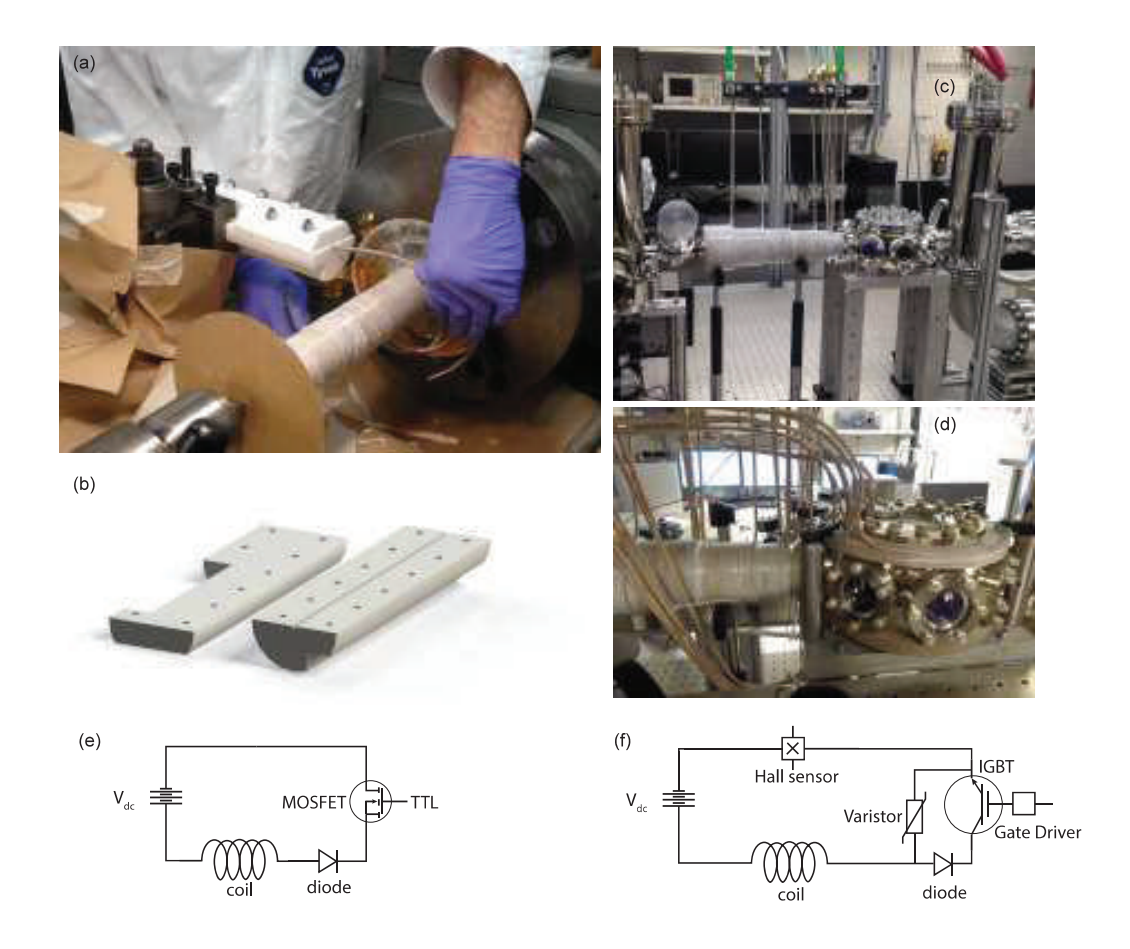


Figure 2.7: Magnet coil winding. (a) Image of the Zeeman slower coils being wound using a lathe. (b) Rendering of the wire guide designed to prevent twisting of the hollow core wire during the winding process. (c) Image of the completed Zeeman slower depicting the water connections on top. (d) Image of the MOT coils and their placement. (e) Schematic of the electrical circuit to switch on and off and protect the circuit carrying currents up to 100 A. A simple MOSFET based switch and a diode are employed. (f) Schematic of the circuit for switching on and off and also serve for the current in the Feshbach coils (MOT coils are the same without the Hall sensor). We use an IGBT instead and also have a varistor added for overvoltage protection.

The current in the magnet coils were produced using standard power supplies. Since current stability is not crucial for the slower and MOT coils, we used refurbished DC power supplies: EMS 40 V-50 A for the slower last coil, Power Ten 50 V-50 A for the rest of slower coils and Lambda EMS 13-200-2-D (13 V, 200 A) for the MOT coils. The above supplies were run in constant current mode. In addition, we added a simple 0-5 V analog current control for the MOT coil power supply to be used for varying a magnetic gradient. The Feshbach coils need a better power supply because we need to be able to stabilize the field to much better accuracy. We use the Delta Elektronika SM 18-220 power supply with a passive current stability of 10^{-4} .

The Zeeman slower currents were switched using a simple mosfet and a diode was added to prevent damage to the power supply due to a negative voltage (D06D100 and R5021213LSWS rated up to 100 A) (Fig. 2.7(e)-(f)). The MOT coils were switched using an IGBT (CM600HA-24H), a varistor (V321DA40) was added to protect the IGBT from high voltage inductive spikes when switching the current rapidly and a diode (VS-400UR120D) to protect the power supply. The low field shim coils were sent through another set of mosfets and diodes (D1D40 and 1N2128A rated up to 40 A). The low current mosfets were mounted on heat sinks while the high current IGBTs were additionally provided with water cooling. The Feshbach coils are essentially the same setup as the MOT coils but in addition we add a Hall sensor (Danisense DS200UBSA-10) on the current return path to read out the current and to stabilize the same with a servo. The IGBTs in addition require high currents at the gate for a fast switch on. So we added a driver (BG1A-KA) that is capable of providing up to 20 A of current to the gate.

2.6 Water Cooling

Since the Zeeman slower, MOT and Feshbach coils are designed to run at currents of 30 A, 112 A and up to 200 A respectively, heating of the coils due to Joule heating during the continuous operation of several seconds can be significant. To mitigate that, we used a hollow core copper wire with square cross-section. Knowing the total length of wire, the resistivity of Cu ($\rho = 1.68 \times 10^{-8} \Omega m$), the cross section area ($a = 7.56 \times 10^{-6} m^2$) and the current flowing through, we can calculate the total power dissipated ($P = \rho I^2 l_{tot}/a$):

- Zeeman slower, $l_{tot} = 74$ m and P = 152 W
- MOT coils, $l_{tot} = 32 \text{ m}$ and P = 893 W
- Feshbach coils, $l_{tot} = 13$ m and P = 1126 W

Hence a combined power dissipation from all our coils would be 2.2 kW. In order to calculate the pressure drop and flow rate required to keep the coils from heating up too much, we make use of the Hazen-Williams equation:

$$\frac{dV}{dt} = \left(\frac{C^{1.85}d^{4.87}\Delta P}{4.52L}\right)^{0.54} \tag{2.3}$$

Where, dV/dt is the flow rate in gallons per minute (gpm), ΔP is the pressure drop over the length of the pipe in pounds per square inch (psi), C is a pipe roughness coefficient (~ 140 for Cu), d is the inside diameter of the pipe in inches and L is the length of the pipe in feet. Using this equation, we can estimate the volume flow rate of water through the hollow-core wires for a given maximum pressure differential and then estimate the temperature rise in the wire knowing the power dissipated in the coils due to Joule heating, the specific heat capacity of water ($C_V = 4.15 \text{ kJ/kg}^{\circ}\text{C}$ at 20 °C) and the density of water ($\bar{\rho} = 998 \text{ kg/m}^3$). We use:

$$P = \frac{dQ}{dt} = \bar{\rho} \frac{dV}{dt} C_V \Delta T \tag{2.4}$$

Using the above relation and the aforementioned power dissipated in the coils, we get the following flow rates and temperature increase in our coils for a maximum pressure drop of 500 psi:

- Zeeman slower, dV/dt = 0.06 gpm and $\Delta T = 10$ °C
- MOT coils, dV/dt = 0.1 gpm and $\Delta T = 35$ °C
- Feshbach coils, dV/dt = 0.2 gpm and $\Delta T = 27$ °C

The values above are for continuous operation of current in the coils. In the actual experiment, currents are kept on for only a few seconds after every 16-18 seconds, allowing the coil temperatures to reach an intermediate steady state value. Although higher pressure drops than 500 psi would allow for better cooling, we were limited

by maximum pressure ratings on pumps and other plumbing parts like tubes and connectors. The total flow rate that would flow through all the coils combined is ~ 0.4 gpm, which is a rather small value.

In order to generate the high pressure, we decided to use a booster pump (Webtrol EZ Series H15B40-1 5HP). The advantage of this particular pump is that it can provide 500 psi of discharge pressure at a flow rate of up to 5 gpm through the pump, much more than what we need. Next, we needed a heat exchanger that would also be able to sustain the required flow rate through the booster pump for safe operation. Our choice was Neslab System II (2 PD2). This heat exchanger is rated to discharge at a pressure of 60 psi and a flow of 6 gpm. In addition, the maximum cooling capacity is 34 kW for a temperature difference of 10 °C which is higher than the load due to our coils. In normal operation and in steady state, we have the following typical parameters:

Table 2.2: Water cooling parameters

Property	Value	Units
Building Chilled Water Supply Pressure	80	psi
Building Chilled Water Supply Flow Rate	4	gpm
Building Chilled Water Supply Temperature In		$^{\circ}\mathrm{C}$
Building Chilled Water Supply Temperature Out	14	$^{\circ}\mathrm{C}$
Neslab Heat Exchanger Discharge Pressure	60	psi
Neslab Heat Exchanger Discharge Flow Rate Neslab Heat Exchanger Temperature Setpoint Steady-State Water Temperature		gpm
		$^{\circ}\mathrm{C}$
		°C
Booster Discharge Pressure	550	psi
Booster Discharge Flow Rate	4	gpm

The heat exchanger is connected to chilled water from the building at the input and its output is split between the booster and the low power load in the experiment like beam dumps (Fig.2.8). The output of the booster is inturn connected to all high power load in the experiment like the magnet coils. Since the total flow out of the booster (4 gpm) is much higher than the flow through all the coils combined (0.4 gpm), we introduced a low resistance channel in parallel to the load to have the excess flow go through.

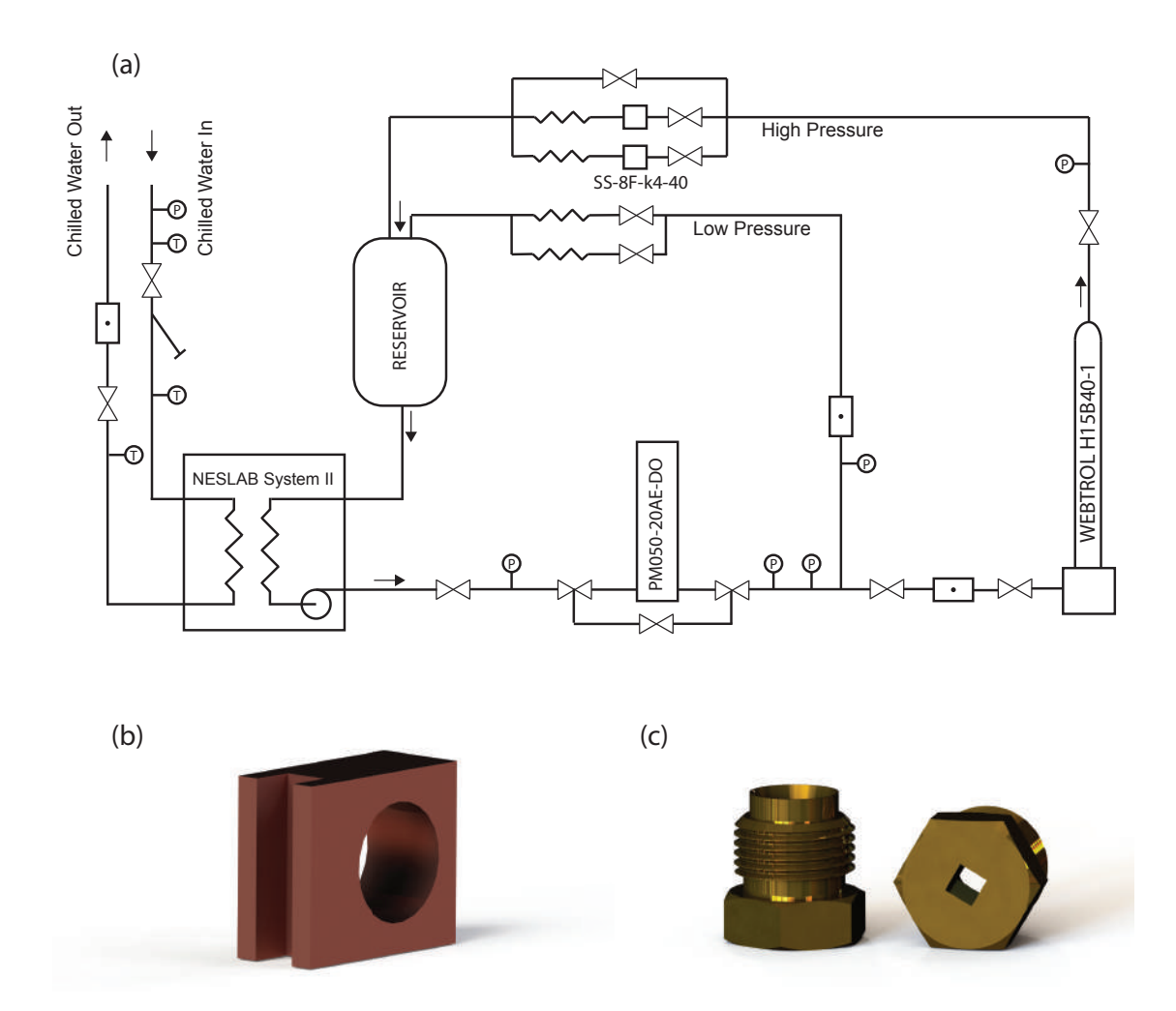


Figure 2.8: (a) Schematic of the water cooling system for the magnet coils. (b) The copper lug used to make electrical contact with the square cross-section magnet coil wire and to enable its mounting. (c) Brass Swagelok pieces used to make a connection for cooling water flow in the wires. Notice that the standard part has been modified by punching a square hole in the bottom for the wire to pass through.

Since the water used for cooling is part of a closed loop, we added ways of preventing dirt and algae buildup that could lead to clogging of the heating coils. The water used to fill the reservoir is deionized with a small amount of algae control fluid added to it. There is a 50 μ m filter after the chiller (Parker PM050-20AE-DO) that acts as a first stage filtration. Then the high pressure path is further filtered by a 40 μ m high pressure filter (Swagelok SS-8F-K4-40). In the beginning we used aluminum gaskets that would completely disintegrate in the time that the filters would need to be replaced (usually 2-3 months). So we switched to the stainless steel version (Swagelok SS-8TF-K2) that tend to be essentially reusable.

In addition, we added temperature interlocks to the coil power supplies in the event that either the chiller or the booster pump should stop working. The booster itself is interlocked to the chiller to avoid dry operation. We attached thermocouples (Omega Engineering SA1XL-K-200-SRTC) on each individual coil using Kapton tape and used a standard digital temperature switch (Dwyer Instruments 40T-10). The triggering of any one of the temperature switches would turn off the current on all power supplies. But even after the temperatures have lowered to within acceptable range, the system would not be restored without a manual button press. This would ensure that the event of cooling failure does not escape the user's attention.

It was also important to choose pipings and connectors that were appropriately suited for high pressure operation. To go from the wall manifold to the experiment table, we used a high pressure water hose (McMaster Carr 53115K29). Close to the experiment, we used brass manifolds (McMaster Carr 5627K553) to split the flow from one hose to many smaller diameter tubes that would carry the cooling water to and from the coils. The tube used was a flexible nylon tube (McMaster Carr 9685T3) capable of withstanding 800 psi of pressure and had an outer diameter of 0.25 in. In order to couple this tubing to the square cross section hollow core copper wires, we used a Swagelok tube cap (Swagelok B-400-C Fig. 2.8(b)). On the cap side of the fitting, we pressed a square hole of side 3.18 mm such that the copper wire with its insulation removed would snugly slide through. Then with enough length fed through, we silvered soldered the junction to obtain a water tight seal. The rest of the connections were done through standard Swagelok sleeves or with pipe thread sealant tape for NPT type connections.

2.7 671 nm Laser System

2.7.1 ⁶Li Spectroscopy

The first step of designing the laser system we use for laser cooling of lithium is to define a frequency reference. We do that by dedicating a laser to be locked to the D2 transition of ⁶Li using modulation transfer spectroscopy. The spectroscopy cell was designed to be a simple straight nipple with CF40 flange ends, a small bucket in the center to add lithium to and a CF16 extension to connect an angle valve (MDC 314001) for pumping (Fig. 2.9(a)). The cell was manufactured by Sharon Vacuum using 304 stainless steel. The two ends have been fitted with viewports with the same AR coating as the experiment chamber (Fig. C.1). The bucket is covered with a band heater (Tempco NHL00112) of 38.1 mm inner diameter. The band heater is connected to a variac and a thermocouple. The temperature of the cell is kept fixed at 190 °C. The lithium inside the bucket evaporates and creates a vapor in the center of the cell that the laser beams can probe. However, if the vapor reaches the viewports, then it would lead to coating by deposition. To avoid that, we introduced some Argon in the cell and in addition, we water cool the ends of the cell to ensure that the vapor condenses before reaching the viewports.

Since we do not need high vacuum conditions inside the cell, we use a cheaper source of lithium (Sigma Aldrich 340421-10G) which is 95% isotopically purified ⁶Li and is packaged in a bottle under oil. The oil prevents the oxidation of lithium in air. Before placing the chunks of lithium inside the cell, we cleaned it by scraping on the surface while immersed in a mixture of methanol and dry ice. Then we evacuated the sealed cell using only the scroll pumps to reach base pressure and then slowly introduced a small amount of Argon. To generate the spectroscopy light, we use a tunable diode laser (Toptica DL PRO).

Modulation transfer spectroscopy is a pump-probe method of sub-Doppler spectroscopy. The advantages of this type of spectroscopy over saturated absorption spectroscopy is two fold. Firstly, the error signal produced with this method is offset free (Fig. 2.9(e)) while in regular spectroscopy, the error signal contains an intensity dependent offset. Secondly, the absence of a linear background absorption leads to a lower sensitivity to beam intensity and cell temperature. This feature eliminates long time offset drifts of the error signal, which cannot be corrected by laser locks. Ultimately this laser is locked to the D2 cooling transition $(2S_{1/2} F=3/2 \rightarrow 2P_{3/2})$.

In this scheme (Fig. 2.9(b)), we generate a sideband at 4.75 MHz using an EOM designed using a LiTaO₃ crystal (Castech J7116-1) on the pump beam that then is overlapped with the un-modulated probe beam in a Doppler-free counter-propagating way. At resonance, the modulation can be efficiently transferred to the probe beam if the light-atom interactions are sufficiently non-linear by a process known as 4-wave mixing [76]. This signal can be extracted through homodyne detection to produce an error signal. Unlike saturated absorption spectroscopy where one looks for probe beam absorption, the error signal is zero away from a resonance. We employed two different channels of an RF generator (Rigol DG1022) to generate the sideband and use for homodyne detection.

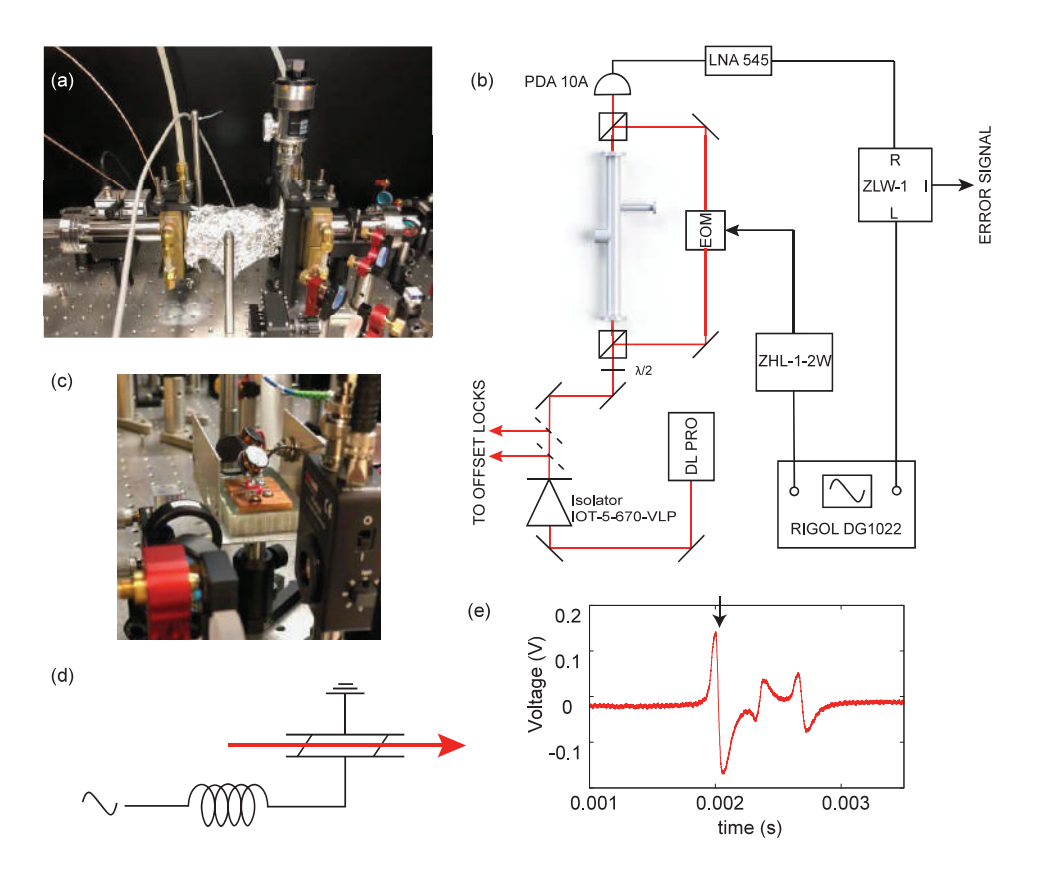


Figure 2.9: The setup for modulation transfer spectroscopy of the D2 line of lithium for MOT and imaging light. (a) Photograph of the setup. The bucket with the band heater is wrapped in foil. Two brass cooling blocks are visible. (b) Schematic of the modulation transfer spectroscopy. (c) Image of the electro-optic modulator (EOM). (d) An EOM consists of a resonant LC circuit where the LiTaO₃ crystal between two Cu plates forms a capacitor. (e) The error signal generated by this spectroscopy process. Black arrow denotes the lock point which is the $2S_{1/2}$ F=3/2 $\rightarrow 2P_{3/2}$ transition.

2.7.2 MOT and Zeeman slower

Light for the MOT beams and the Zeeman slower beam were generated using a second DL PRO diode laser. The principle of operation of the magneto optical trap will be discussed in section 3.1. The laser is offset locked to the spectroscopy laser as depicted below. The detuning (δ) of the laser with respect to the D2 transition can be tuned from -11 Γ to 2 Γ . The free running linewidth of the laser is 10 kHz, much smaller than the linewidth of the transition ($\Gamma = 5.87$ MHz). The laser head outputs ~ 25 mW of power which is not sufficient for efficient trapping of atoms. So we used tapered amplifiers to amplify the laser power before being sent through other optical elements.

The tapered amplifier chips are designed for amplification up to 500 mW at 670 nm (Eagleyard EYP-TPA-0670-00500-2003-CMT02-0000). The mount design was based off of the design by the Harvard group [77] and was machined out of copper (Fig. 2.10(d)-(e)). Temperature stabilization was performed by adding two peltier coolers (Thorlabs TEC3-6) sandwiched between the mount and heat sinks, and a thermistor (Thorlabs TH10K) connected to a temperature controller (Thorlabs TED200C). In addition, the DC current required to drive the TA chip was provided by a laser diode current controller (Thorlabs LDC220C) through a protection circuit (Fig. 2.10(f)) designed to avoid any electrical damage to the chip. To improve thermal contact, a single layer of 50 μ m thick, 99.99% indium foil was placed between the chip and the mount.

The incident beam was focused down and the output beam collimated with aspheric lenses (Thorlabs C230TME-B for input and Melles Griot 06 GLC 001 for output) placed on translation stages (Thorlabs SM1Z) for focus alignment. The lateral alignment however was performed only once and fixed with epoxy. The normal operating current of the amplifiers is around 0.9 A. After initial setup, we were able to output ~ 350 mW of power from the TAs for ~ 30 mW input power but after a few years, the output degraded to ~ 200 mW.

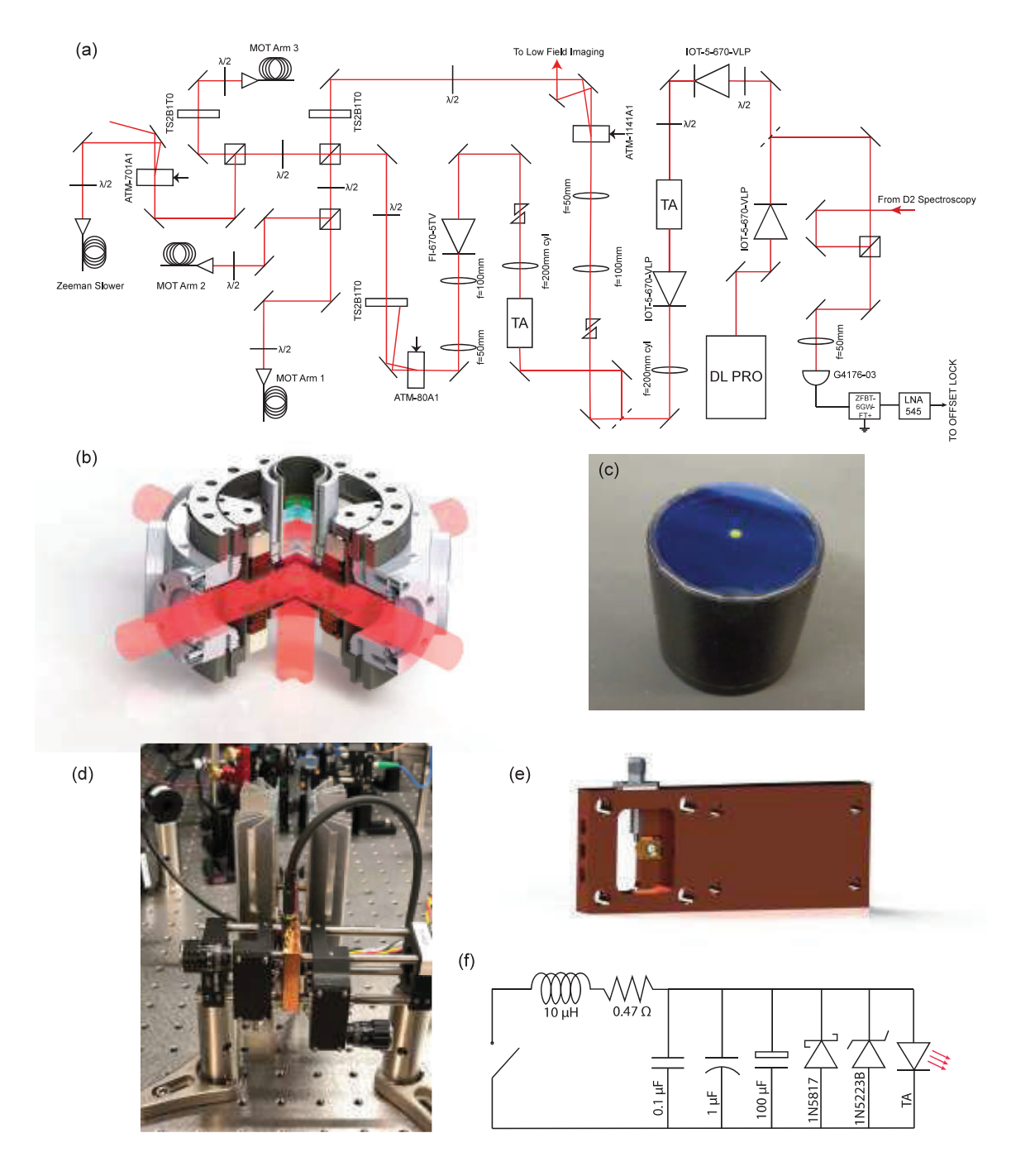


Figure 2.10: MOT and Zeeman slower light. (a) Schematic of the laser setup. All MOT and slower light is derived from a single DL PRO laser offset locked to the spectroscopy laser and two separate tapered amplifiers (TAs). Light for the Zeeman slower is a combination of cooling and repump light passed through another AOM. (b) Rendering of the MOT beams with respect to the science chamber. Notice that the vertical beam passes through the high resolution objective and gets retroreflected by a HR dot on a quarter-wave plate (shown in (c)). (d) Image of a full TA setup with heat sinks. (e) Rendering of the TA mounted on its copper mount. (f) TA protection circuit.

The output of the first TA is used to generate the repump light and to seed a second TA to generate the cooling light. The repump light is passed through an acousto-optic modulator (AOM, Intraaction ATM-1141A1) to increase its frequency by 114 MHz and the cooling light is passed through another AOM (Intraaction ATM-80A1) to decrease its frequency by 114 MHz. Both AOMs have a first order diffraction efficiency of 70-80%. Each beam is split into 4 parts, three of which are used for the MOT beams in the three directions. The fourth beam is passed through another AOM (Intraaction ATM-701A1) which decreases its frequency by 70 MHz to generate the Zeeman slower beam. The beams were then fiber coupled and sent via polarization maintaining optical fibers (OZ Optics PMJ-3A3S-633-4/125-3-20-1) to the experiment table.

The MOT beams are first-passed through the science chamber, then the polarization is rotated by passing through a quarter-wave plate and retroreflecting the beams to create a $\sigma^+ - \sigma^-$ beam configuration required for the operation of the MOT. The vertical direction MOT beam, however, has to be retroreflected after passing through the objective. We retroreflect the beam at the Fourier plane of the obective. We HR coated a 2 mm diameter dot on a quarter wave plate (Spectrum Thin Films). This QWP was mounted on a plastic tube (Fig. 2.10(c)) and placed at the correct depth. The effect of the HR dot on the point spread function in the fluorescence imaging will be discussed in section 3.3.2.

2.7.3 Low and High Field Imaging

The principle of absorption imaging is to extract the number of atoms from the intensity of resonant light absorbed in a very short pulse. This method of imaging requires the ability to adjust the detuning of an imaging laser very close to resonance. But the resonance corresponding to the D2 transition depends on the DC magnetic field applied. The difference between the zero-field and high field values ($\sim 1000~\rm G$) could be as high as a gigahertz. Hence we designed two different imaging lasers, one for low field and the other for high field imaging. The low field imaging light is derived from the zeroth order diffraction after the repump AOM. Next it is passed through an AOM (Intraaction ATM-801A1) being run at 55 MHz and we use the negative second order. The light is subsequently split in two separate imaging paths.

For high field imaging, we dedicated a laser that was homemade using a Littrow ECDL design [78]. The laser head outputs about 18 mW of 671 nm light. laser is also offset locked to the spectroscopy laser, but to be able to tune the laser by a gigahertz, we used a photodiode (Hamamatsu G4176-03) and amplifier (RF-Bay LNA-2500) with a larger bandwidth. One of the challenges with the Littrow design is that frequency tuning needs to be done by adjusting the angle of the grating (Richardson Gratings 33003FL01-059H). But that inadvertently leads to a shift in the output beam pointing. To avoid power fluctuations on the experiment side, we fiber coupled the light right after the laser head and then sent the output of the fiber to the AOM (Intraaction ATM901A1). The AOM was set up in a cat's-eye configuration to be able to perform a fast switch in imaging light detuning without loss in alignment. Details of that setup will be discussed in the section on spin imbalance in a 2D Fermi gas (section 4.5.2). Next, the output of the AOM was split in two parts and fiber coupled through the same horizontal and vertical axes used for low field imaging. We are able to scan the lock point from 550 MHz to 1120 MHz corresponding to a field range of roughly 400 G.

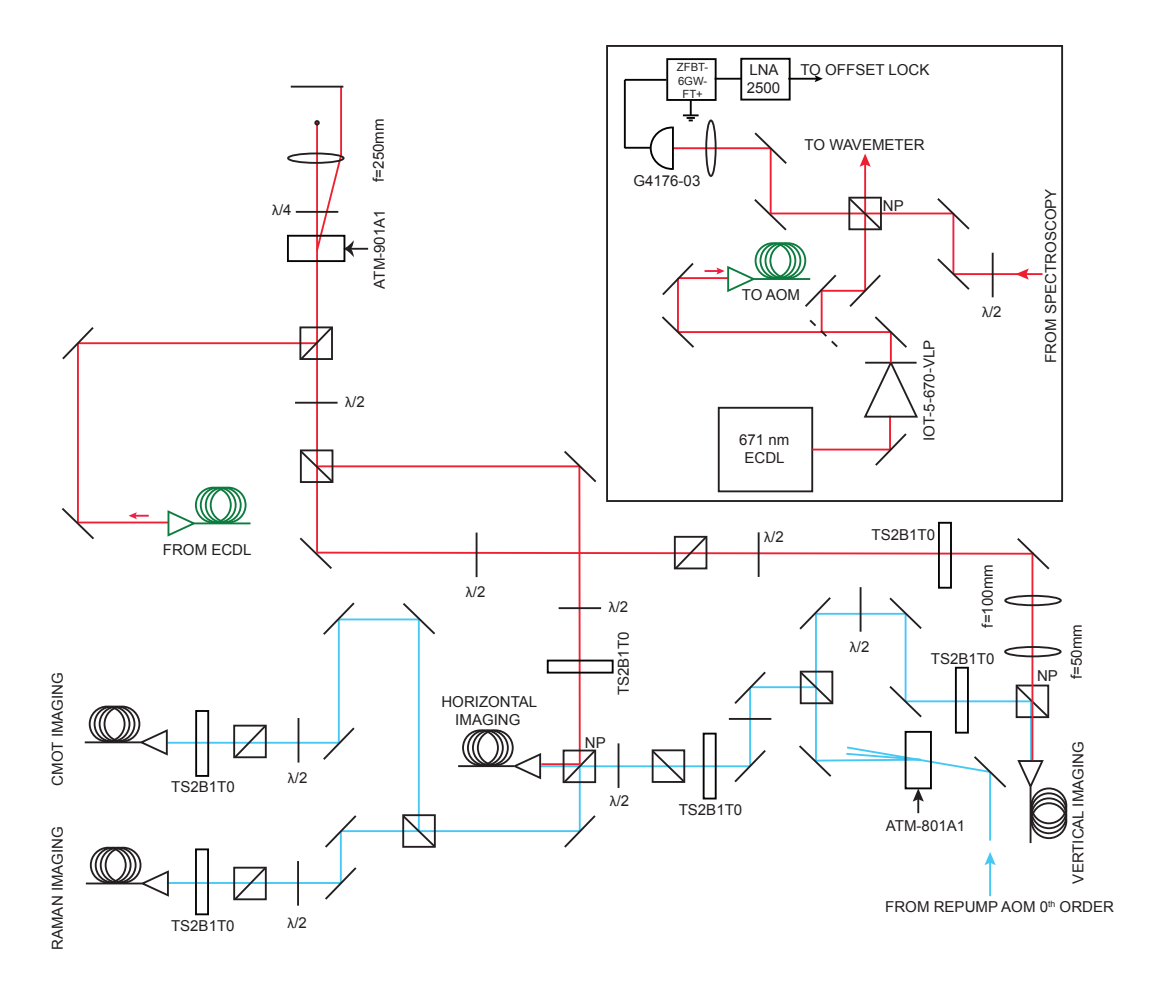


Figure 2.11: Schematic of low (blue) and high (red) field imaging. Boxed inset shows the generation of light for high field imaging and the offset lock with spectroscopy laser. The light is redirected via an optical fiber (green) to the AOM in double pass cats-eye configuration. Both low and high field imaging light is coupled to the same fibers and sent to the experiment.

2.7.4 Raman laser system

In order to image single atoms in a lattice, we perform Raman sideband cooling [53]. This method relies on the two hyperfine ground states of ^6Li ($2\text{S}_{1/2}$ F=1/2 and F=3/2) and an excited state. Our Raman beams are red detuned by 5.6 GHz from the D1 line. The details of the Raman cooling scheme can be found in section 3.3.

We dedicate two lasers for this purpose. We first take a homemade Littrow ECDL laser [78] and lock it to the D1 ($2S_{1/2}$ F=3/2 \rightarrow $2P_{1/2}$) transition using modulation transfer spectroscopy (Fig. 2.12(b)). We generate a sideband at 6.31 MHz using an EOM and use the same spectroscopy cell used for the D2 master laser. This laser serves as a reference to offset lock the Raman laser. In addition, this laser serves as the pump laser that transfers atoms in the $2S_{1/2}$ F=1/2 state to the $2P_{1/2}$ state. This requires us to detune the laser by 228 MHz from the lock point. We achieve that by double passing the beam through an AOM driven at 114 MHz using a cat's-eye configuration (Fig. 2.12(a)). In practice, the detuning of the pump beam is tuned experimentally and will be discussed later. The Raman beam is obtained from another Toptica DL PRO system. It is offset locked 5.6 GHz red detuned from the $2S_{1/2}$ F=3/2 \rightarrow $2P_{1/2}$ transition. The Raman beam is sent through an AOM operating at 88.3 MHz, which is used as a fast switch.

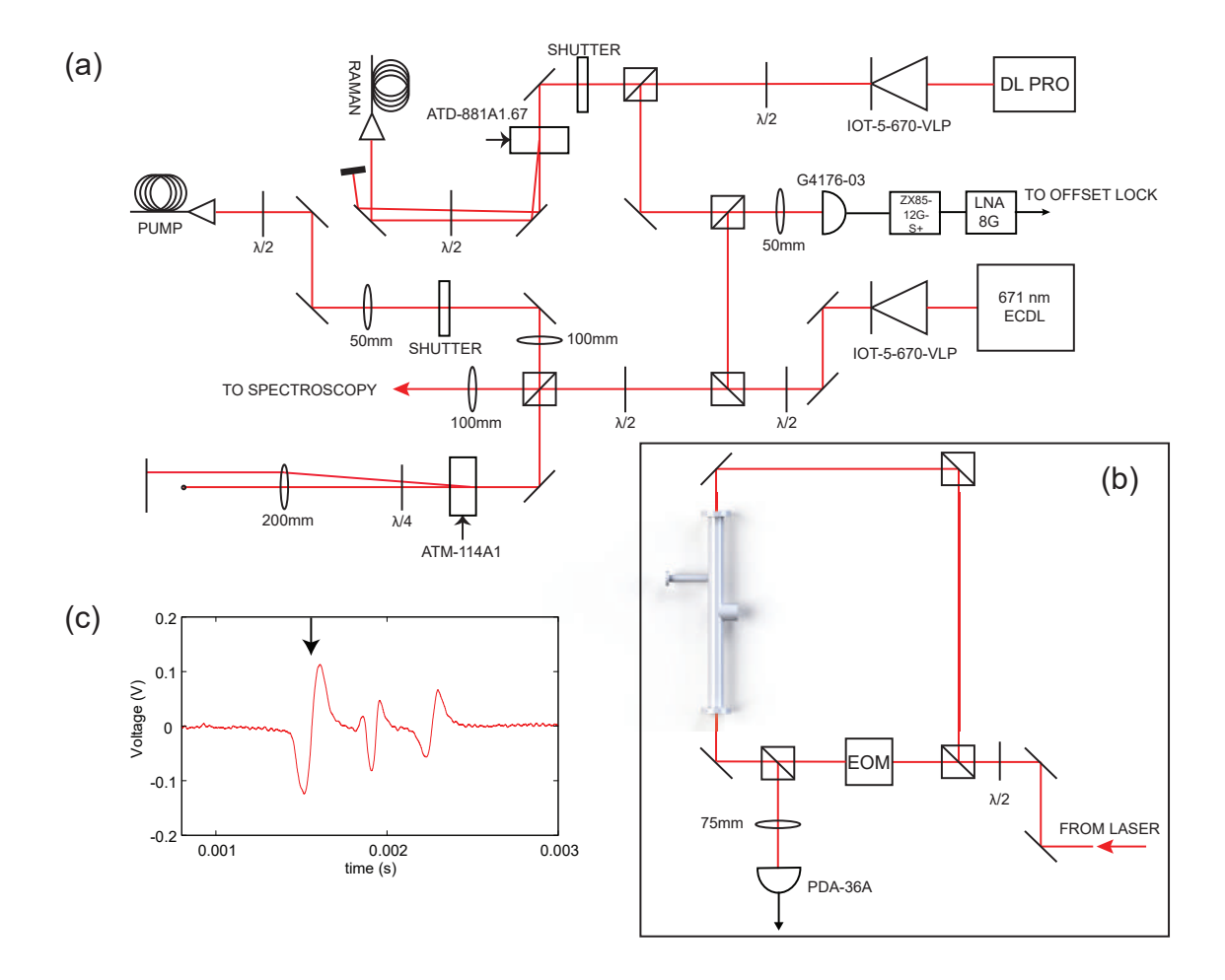


Figure 2.12: Raman laser system. (a) Schematic of the Raman laser setup. A homemade ECDL is used to lock to the D1 transition of $^6\mathrm{Li}\ (2\mathrm{S}_{1/2} \to 2\mathrm{P}_{1/2})$. A second laser (Toptica DL PRO) is offset locked to the first laser. (b) Modulation transfer spectroscopy setup for locking to the D1 transition. (c) The error signal obtained from this setup. The two main features are due to the hyperfine structure of the ground state and are separated by 228 MHz. The central feature is due to crossover. The arrow indicates the location where the laser is locked $(2\mathrm{S}_{1/2}\ \mathrm{F=}3/2 \to 2\mathrm{P}_{1/2})$.

2.8 Optical Potentials

2.8.1 Optical Dipole Trap

The atoms of lithium can be trapped in the intensity maximum of a red-detuned laser beam [79]. The dipole potential experienced by an atom in the presence of a drive is given by

$$U(\vec{r}) = -\frac{3\pi c^2}{2\omega_0^3} \left(\frac{\Gamma}{\delta} + \frac{\Gamma}{\omega_0 + \omega}\right) I(\vec{r})$$
 (2.5)

where, ω_0 is the frequency of the transition while ω is the frequency of the drive, Γ is the transition linewidth and $\delta = \omega_0 - \omega$ the detuning of the drive from the transition. In addition, the rate at which photons belonging to the laser are scattered by the atoms is given by

$$\hbar\Gamma_{sc} = \frac{3\pi c^2}{2\omega_0^3} \left(\frac{\omega}{\omega_0}\right)^3 \left(\frac{\Gamma}{\delta} + \frac{\Gamma}{\omega_0 + \omega}\right)^2 I(\vec{r})$$
 (2.6)

So for a far red detuned beam ($\delta < 0$ and $|\delta| \gg \omega_0$), we see that the potential is attractive where intensity is maximum and the scattering rate is negligible, leading to the potential being almost conservative. In such conservative potentials, trapped atoms can have very long lifetimes, essentially limited by background gas scattering. In our experiment, we generate the optical dipole trap (ODT) using an Ytterbium fiber laser (IPG Photonics YLR-200-LP-AC-Y11). The laser outputs up to 200 W of multimode light centered around 1070 nm. We focus a beam of 112 W down to 70 μ m waist. Then the beam is retro-reflected and overlapped with a perpendicular polarization at the focus at a shallow angle of 11°. Due to the polarization, no substantial interference effects occur at the intersection, leading to a trap of 1.7 mK depth at the cross. This trap is cigar shaped with the tight trapping frequency of (2π) 7 kHz and shallow trapping frequency of (2π) 24 Hz.

The intensity of the ODT is modulated by sending it through a high power AOM (Gooch and Housego AOMO 3110-197). These AOMs require over 2 W of RF power to reach saturation, unlike the Intraaction AOMs that only need about 1 W.

The evaporation process imposes two requirements on the control of the intensity of the trapping laser: the intensity needs to be tunable over several orders of magnitude and especially at the lowest intensities, it is important to have low intensity noise. For this purpose, we designed a special intensity lock electronics with handover. The setup as depicted in Fig. 2.13(b). The idea of handover is to use a comparator (AD790), a latch (Quad NOR SN74LS02N) and two different photodiodes (PDs), one dedicated to high power operation and the other to low power. The lock always starts out at maximum power, where the low power PD is saturated. A comparator compares that PD voltage to a voltage reference and is in logic 0 state in the beginning. The latch is connected to the output of the comparator and an external override. As the power of the laser is decreased, the low power PD voltage eventually falls below the reference and the comparator switches to logic 1. This causes the latch to switch

to logic 1 and it stays in that state unless it is reset by passing logic 1 on the override. The output of the latch controls an SPDT analog switch (MAX4544). The normally open (NO) port is connected to the low power input while the normally closed (NC) port to the high power input. The switch output then connects to a single OPAMP (OP27) P-I feedback loop.

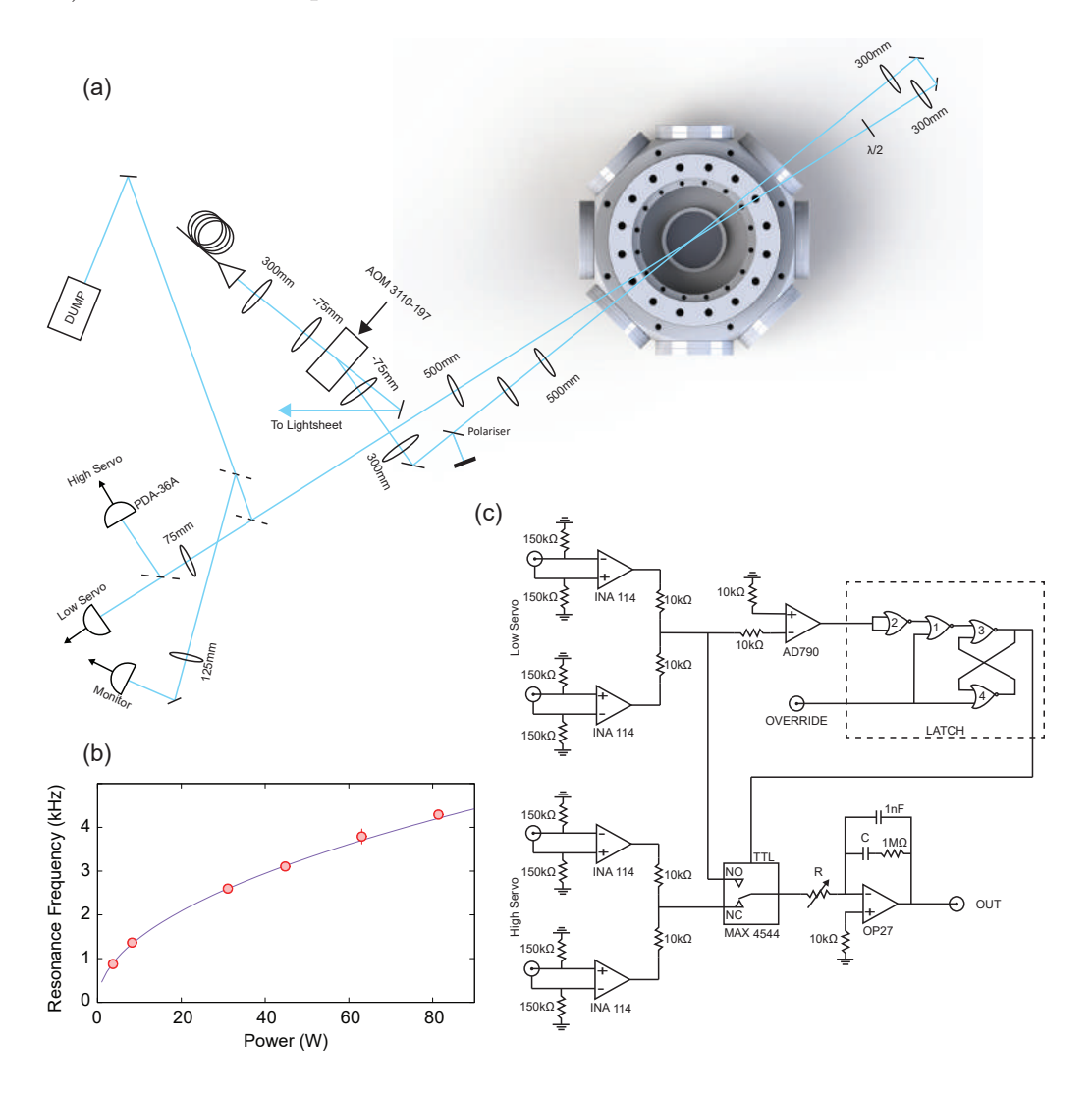


Figure 2.13: Optical dipole trap. (a) Layout of the optical dipole trap created at the intersection of two beams focussed to a waist of 71 μ m and at a shallow angle of 11°. The zeroth order of the AOM is recirculated for the lightsheet. (b) Measurement of the single beam trapping frequency by amplitude modulation of the ODT as a function of power. (c) Circuit diagram of the handover servo used for the intensity stability as well as control over two orders of magnitude.

2.8.2 Light Sheet and Bottom Beam

The same light used to form the ODT is recycled at different stages of the experiment to produce two more optical potentials. The first one is a dimple trap that is meant to increase the confinement along the vertical direction and hence load the atoms after evaporation into a highly anisotropic trap. This is achieved by using a telescope system made out of a 30 mm focal length cylindrical lens and a 1000 mm lens in conjuction with a high NA aspheric lens of 150 mm focal length and 50 mm diameter (Thorlabs AL75150-C) to focus an elliptical beam down at the atoms. At the atoms, the beam has waists of 5 μ m and 50 μ m. The power in the beam is stabilized by an intensity servo and the maximum power available is \sim 12 W. To allow for absorption imaging along the same axis as the light sheet, we used a dichroic (Thorlabs DMSP805L) which reflects 1070 nm while transmitting 671 nm, right before the aspheric lens. At the output end, the beam expands in the tight direction due to the short Raleigh range. To be able to dump this beam effectively, we added another 250 mm collimating achromatic lens (also used for absorption imaging), a dichroic and an aspheric lens on the output side of the chamber.

We measured the trapping frequency of the light sheet at a power of 1.6 W using modulation spectroscopy. The trapping frequencies in the three directions were 1 kHz, 4 kHz and 40 kHz, consistent with the measured waist (Fig. 2.14(c)). The AOM controller for the light sheet was also equipped with a pinning circuit. The purpose of this circuit is to bypass the intensity servo and run the AOM at maximum RF power. The circuit is able to switch to maximum power in $\sim 100~\mu s$. This is required to pin the motion of atoms down in a lattice during fluorescence imaging and will be discussed in detail later.

The bottom beam is a single circular beam focussed down to 100 μ m waist at the atoms. It is also derived from the ODT light. Because of the highly anisotropic shape of the light sheet, the atoms reside in a flat cigar shaped trap. In order to realize more uniform 2D potentials, we need a uniform radial confinement that the bottom beam can provide. The power of this beam is also stabilized with a servo and can go up to 4 W, leading to a confinement up to ~ 400 Hz in the radial direction. To avoid retroreflection of this beam by the top viewport which is high reflection coated at this wavelength, we send the beam up at a tilt such that the reflection does not coincide with the position of the atoms.

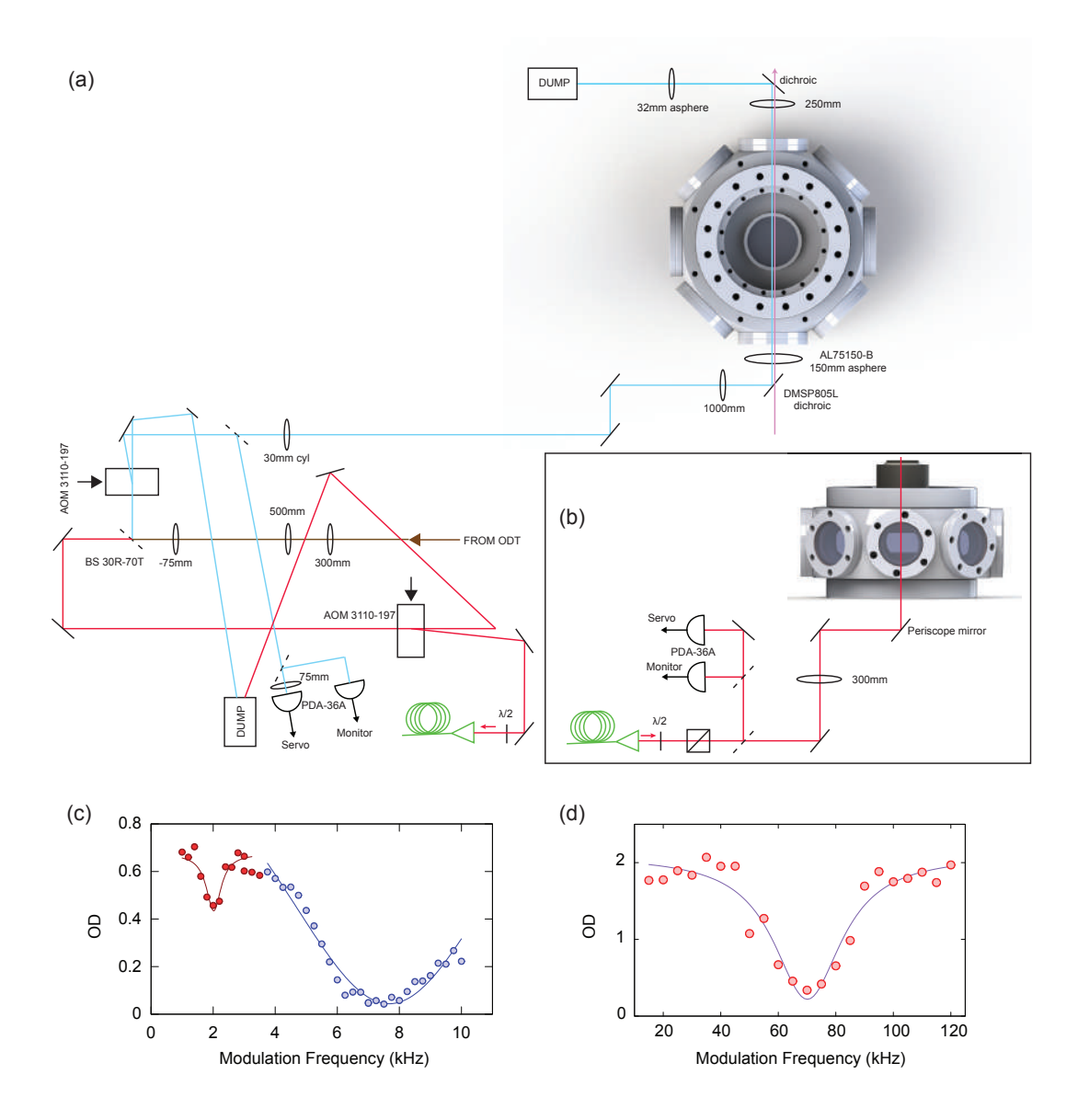


Figure 2.14: Schematic of light sheet and bottom beam. (a) Light from the 0th order of the ODT AOM is recirculated (brown) and split between two arms. The first one is used for the light sheet (blue) while the second one is used for the bottom beam (red). The highly anisotropic light sheet is created using a cylindrical lens telescope and a high NA aspheric lens. The use of dichroic mirrors allow us to perform absorption imaging along the light sheet direction (pink). The bottom beam is coupled into an optical fiber (green) to be sent below the main chamber. (b) The bottom beam path under the main chamber. (c) Light sheet trapping frequency measured using modulation spectroscopy for the two shallower of the three confinements. (d) Light sheet trapping frequency along the tight axis measured separately.

2.8.3 Accordion Lattice

Even after the evaporated atoms are loaded into a light sheet, the confinement that the atoms feel does not qualify as "quasi" 2D. So there is a need for even higher trapping frequency in the vertical direction. Although that can be achieved by increasing the power of the light sheet, the anisotropy in the radial direction would prevent from having a uniform radial trap. To address this, we designed a deconfining accordion lattice [80, 53]. The idea of an accordion lattice is to be able to change the lattice spacing dynamically. We achieve that by using an acousto-optic deflector (AOD) and a high numerical aperture lens.

To generate the light for the accordion, we recirculate light from the lattice laser (Mephisto MOPA 50 W at 1064 nm) and frequency double it to 532 nm. Since this wavelength is blue detuned compared to the D2 transition of lithium, the potential formed using it would be deconfining. We used a periodically poled MgO-doped (1 mol%) stoichiometric litium tantalate crystal (PP-MgO:SLT) with high single pass frequency doubling efficiency (HC Photonics 1BKSSTP10797020010100Y001) [81]. The crystal has a cross section of 1 mm×1 mm and a length of 20 mm. The poling grating has a spacing of $\Lambda_0 = 7.97~\mu m$.

The quasi phase match (QPM) configuration in a periodic poled ferroelectric crystal is when the phase mismatch between the fundamental wave, the second harmonic and the crystal grating is zero.

$$\Delta k = 2k_{\lambda} - k_{\lambda/2} + \frac{2\pi m}{\Lambda} \tag{2.7}$$

where m is the harmonic order which is 1 in our case. In addition, the wavelengths (due to the refractive index) and the grating spacing depend on temperature. This leads to a QPM condition

$$\frac{4\pi}{\lambda} \left(n(\lambda, T) - n\left(\frac{\lambda}{2}, T\right) \right) + \frac{2\pi}{\Lambda(T)} = 0 \tag{2.8}$$

The grating spacing depends essentially on the coefficients of linear and quadratic expansion $\Lambda(T) = \Lambda_0(1 + \alpha T + \beta T^2)$ and T = T - 25°C. The values of α and β are given in Table 2.3. Next, the refractive index as a function of wavelength and temperature is given by the Sellmeir equation [82]

$$n^{2}(\lambda, T) = A + \frac{B + b(T)}{\lambda^{2} - (C + c(T))^{2}} + \frac{E}{\lambda^{2} - F^{2}} + \frac{G}{\lambda^{2} - H^{2}} + D\lambda^{2}$$
 (2.9)

The parameters above are given in Table 2.3. Combining Eqs. 2.8, 2.9 and the temperature dependence of Λ , one can calculate the QPM temperature. For our crystal and seed wavelength, we get that $T_{QPM} \sim 55^{\circ}\mathrm{C}$.

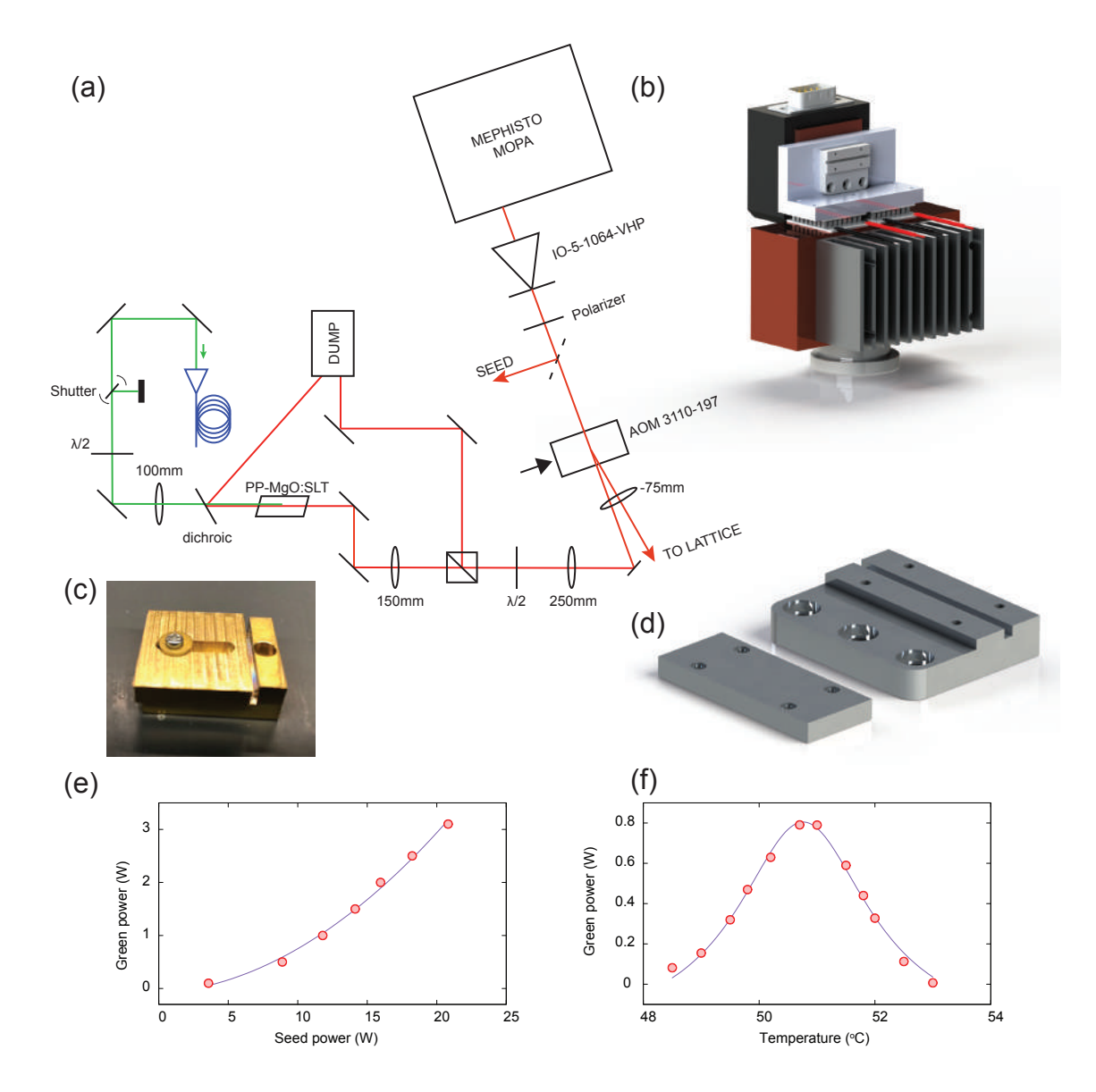


Figure 2.15: Second harmonic generation, (a) Schematic for redirecting the 0th order from the lattice AOM to seed the SHG crystal. The picked off part of the beam labelled SEED could be used as input to a fiber amplifier. The half-wave plate after the 250 mm lens is used to adjust the seed power as needed. The shutter is a D-mirror mounted on a timed mechanical relay. (b) Full oven mount for the crystal depicting the additional heat sinking added for efficient heat extraction from the crystal. (c) Original mount for SHG crystal with poor heat rejection. (d) New crystal mount with thermal contact on all 4 sides. (e) Green power as a function of seed power at a temperature of 50.7°C. Line is a quadratic fit as expected for SHG with parameters -0.1(2), 0.02(3) and 0.006(1). (f) Temperature dependence of second harmonic power at a smaller seed power of 5 W. The optimal value obtained is 50.7°C.

The initial mount provided by the manufacturer (Fig. 2.15(c)) only made contact on three surfaces of the crystal. To enhance thermal contact we added Indium foil in between. The seed beam is focussed down to a waist of 30 μ m and aligned to be coincident with the geometric center of the crystal. The first crystal used broke into two pieces at the location of the waist for a seed power of 35 W. We realized that the crystal mount was not capable of extracting heat from within the crystal. The manufacturer provided us with a new mount (Fig. 2.15(d)) that made contact with the crystal on all 4 surfaces. In addition, we designed a base of copper with Peltier coolers and a heat exhanger fins (Fig. 2.15(b)). We realized later on that we were extracting heat sufficiently well that we did not need to cool it further with Peltier coolers.

We measured the QPM condition for our system at a smaller seed power of 5 W by changing the temperature set-point. We measure a maximum at 50.7° C which is less than the expected 55° C. The discrepancy likely arises because temperature is not measured close to the position of the waist. In addition, we measured the second harmonic power as a function of seed power. The maximum second harmonic power that we operate at is 3 W obtained at a seed power of 21 W (Fig. 2.15(e)) leading to a conversion efficiency of $\sim 14\%$.

After the SHG crystal, we place a dichroic to separate the fundamental from the second harmonic and fiber couple it through a standard optical fiber (Throlabs P3-488PM-FC-2). To avoid damaging the fiber, we used a timed reflective shutter which is a D-mirror attached to a mechanical relay. The relay was connected to a 555-timer circuit which would automatically turn off after 10 seconds. We observed minimum thermal effects on the fiber due to the incident intensity being over the damage threshold.

Table 2.3: Thermal expansion and Sellmeir parameters for PP-MgO:SLT

Property	Value	Units
α	1.6×10^{-5}	$^{\circ}\mathrm{C}^{-1}$
β	7×10^{-9}	$^{\circ}\mathrm{C}^{-2}$
A	4.502483	_
В	0.007294	-
С	0.185087	-
D	-0.02357	_
\mathbf{E}	0.073423	_
F	0.199595	_
G	0.001	_
Н	7.99724	_
$b(T^{\circ}C)$	$3.483933 \times 10^{-8} (T + 273.15)^2$	-
$c(T^{\circ}C)$	$1.607839 \times 10^{-8} (T+273.15)^2$	_

On the output end of the fiber, we send the beam through a 300 mm focal length cylindrical lens that focuses the beam down to a waist of 65 μ m × 750 μ m. We align

the position of this focus to coincide with the center of an acousto-optic deflector (Intraaction ATD-805AD5). The AOD is positioned in such a way that the plane of beam diffraction is vertical. We block the zeroth order beam and make a factor of 4 demagnifying imaging system to the position of the atoms. Along the way, the beam is split evenly into two beams by using a polarizing beam splitter cube along with a quarter wave plate. We designed a monolithic structure (the tower) to hold this mechanism in place (Fig. 2.16(c)). Finally the two beams are focused on to the position of the atoms using a high NA aspherical lens.

The working principle of the accordion lattice is the following (Fig. 2.16(b)). When the RF drive frequency on the AOD is changed within a range of 99.8 MHz to 88.3 MHz, the diffracted first order only changes angle in the vertical plane with minimal change in intensity. This angular variation is converted into a variation in beam height in the Fourier plane of the 600 mm lens. This beam height variation, in turn, is converted to a vertical separation between two beams after the tower. These two beams then fall parallel on the asphere and are focused down and interfere at the position of the atoms. The result of this interference are 2D pancakes in the vertical direction with variable separation. This separation can be varied from 12 μ m down to 3.5 μ m.

The advantage of variable spacing is that we can load a cigar shaped cloud into a single layer of the 2D pancakes at maximum separation and then compress the pancake adiabatically to reach a more "2D" regime. We measured the vertical confinement in the case of minimum spacing using modulation spectroscopy and get 21-23 kHz (Fig. 2.16(d)). The radial deconfinement in the central layer produced by this accordion lattice has an effect on the confinement due to the bottom beam. We can measure this combined radial trapping frequency through modulation spectroscopy for a setting we use for the experiments described later in the thesis. We measure $\omega_x = (2\pi)95$ Hz and $\omega_y = (2\pi)125$ Hz (Fig. 2.16(e)).

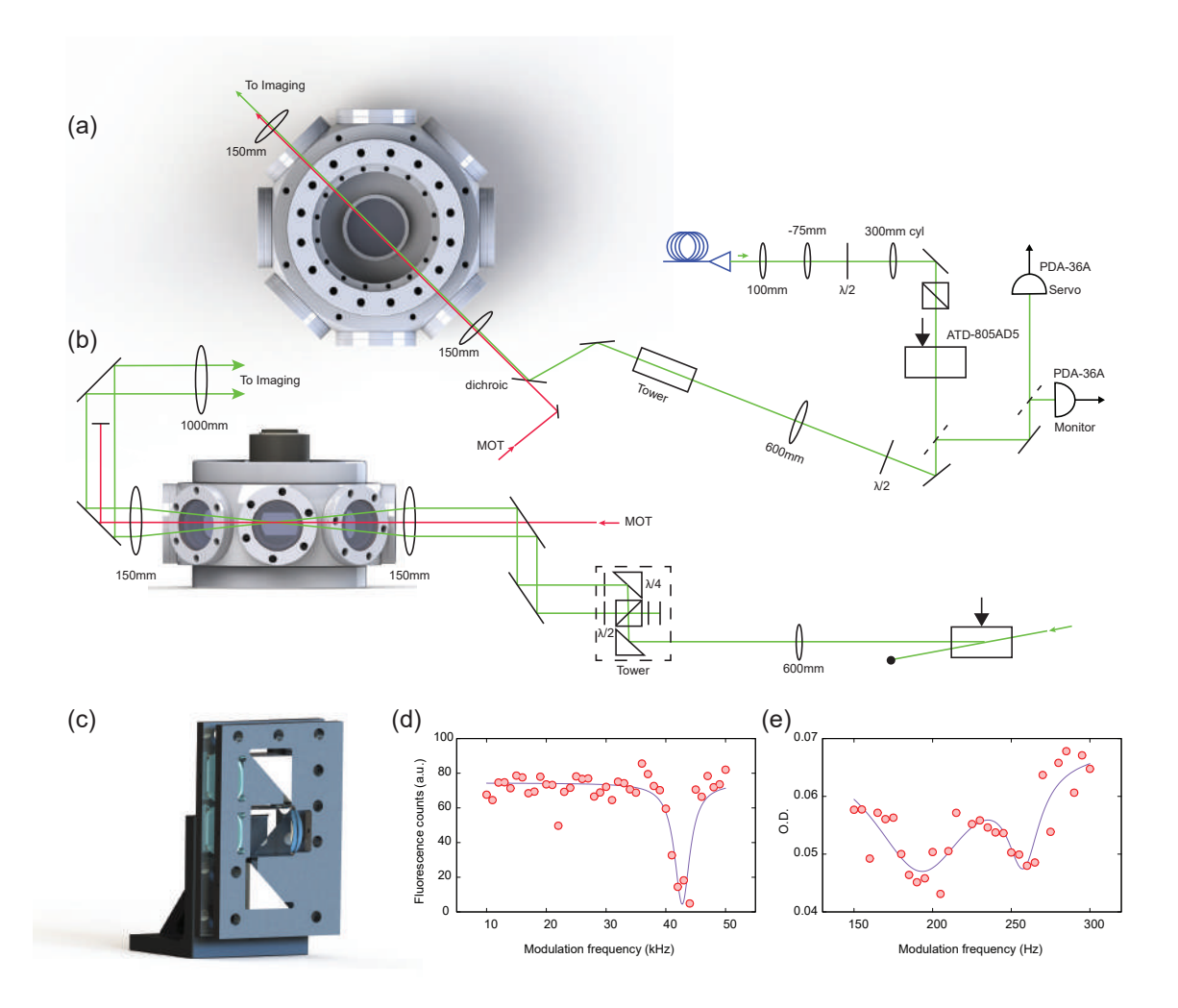


Figure 2.16: Accordion lattice. (a) Schematic of the experimental setup. 532 nm light is transmitted through a fiber after second harmonic generation and passed through an acousto-optic deflector mounted such that the diffracted order lies in the vertical plane. The center of the AOD is imaged on to the position of the atoms through a 4f system. Along the way, the beam is split into two parallel beams through the tower. The red beam is MOT light that is passed through the same path after a dichroic. (b) Same schematic but viewed in the vertical plane. (c) Rendering of the tower which consists of mirrors and a polarizing cube along with a quarter-wave plate. (d) Modulation sprectroscopy of a gas trapped in a single layer of the accordion lattice while the bottom beam provides radial confinement. We see a prominent breathing mode at twice the trapping frequency but a slight dip at the trapping frequency can be attributed to some sloshing of the cloud. (e) Same modulation spectroscopy at lower frequencies to obtain the radial confinement of the combined trap.

2.8.4 2D Square Science Lattice

The 2D lattice that we implemented in our experiment is a square lattice formed by the 4-fold interference of a single beam of coherent red-detuned light at 1064 nm. Details of the design and implementation of this scheme can be found in [83].

To understand the intensity profile of the lattice, we need to write down the electric fields in each pass of the lattice beam. The four passes can be enumerated as $\mathbf{E_i}$ where $\mathbf{i} = \mathbf{1}, \mathbf{2}, \mathbf{3}, \mathbf{4}$. The interference property of the lattice is also dependent on the polarization \hat{e}_i of each beam. Let us assume that the lattice beams are travelling along the x and y axes, then

$$\mathbf{E_{1}} = E_{1}e^{i(kx-\omega t)}e^{-\frac{y^{2}+z^{2}}{w^{2}}}\hat{e}_{1}
\mathbf{E_{2}} = E_{2}e^{i(-ky-\omega t)}e^{-\frac{x^{2}+z^{2}}{w^{2}}}\hat{e}_{2}
\mathbf{E_{3}} = E_{3}e^{i(ky-\omega t)}e^{-\frac{x^{2}+z^{2}}{w^{2}}}\hat{e}_{3}
\mathbf{E_{4}} = E_{4}e^{i(-kx-\omega t)}e^{-\frac{y^{2}+z^{2}}{w^{2}}}\hat{e}_{4}$$
(2.10)

where, E_i is related to the beam intensity as $I \sim |E|^2$. The waist of each beam is given by w and is $\sim 70~\mu\mathrm{m}$ for our setup. Lastly, k is the wave-vector $2\pi/\lambda$ where $\lambda = 1064~\mathrm{nm}$. Let us first consider the case where the beams are polarized in the z-direction. In this case $\hat{e}_i = (0,0,1)$ and all 4 beams interfere to form a non-separable lattice with electric field

$$\mathbf{E}_{\text{tot}}^{\perp} = \left[(E_1 e^{ikx} + E_4 e^{-ikx}) e^{-y^2/w^2} + (E_3 e^{iky} + E_2 e^{-iky}) e^{-x^2/w^2} \right] e^{-z^2/w^2} e^{-i\omega t} \hat{z} \quad (2.11)$$

The intensity profile can be obtained by calculating $\mathbf{E_{tot}}.\overline{\mathbf{E_{tot}}}$ and the lattice potential experienced by the atoms can be calculated using Eq. 2.5. The lattice spacing in this configuration is 752 nm $(a = \lambda/\sqrt{2})$. The recoil due to a lattice photon is give by $E_R = \hbar^2 (\pi/a)^2/2m = h \times 14.66$ kHz, representing the natural energy scale in the lattice.

The other configuration of the lattice is when the polarizations \hat{e}_i are in the x-y plane. In this case, only the pairs of beams with polarizations $(\pm 1, 0, 0)$ and $(0, \pm 1, 0)$ interfere to form a separable lattice of spacing $\lambda/2$ (Fig. 2.17(c)-(d)). The associated electric field is

$$\mathbf{E_{tot}}^{\parallel} = \left[(E_1 e^{ikx} - E_4 e^{-ikx}) e^{-y^2/w^2} \hat{y} + (-E_3 e^{iky} + E_2 e^{-iky}) e^{-x^2/w^2} \hat{x} \right] e^{-z^2/w^2} e^{-i\omega t}$$
(2.12)

The lattice formed in this scheme is shallower by a factor of four from the case of vertical polarization. In practice, the angle between the lattice passes is not exactly 90° but is around 91.6°. This leads to an anisotropy in the lattice spacing in the two directions and hence in the tunnelling rate. To mitigate this effect, we employ a variable retroreflection attenuation using a polarizing beam splitter (Thorlabs PBSW 1064) and a quarter-wave plate mounted on a motorized rotation mount (Fig.

(2.17(b)). The effect of an attenuation in the electric field by a factor r leads to a modification of the potential by

$$V(x,y) = V_0 \left(1 - \frac{1 + r^2 + 2r\cos(2kx\cos(\theta/2))}{1 + 2r + r^2} \cdot \frac{1 + \cos(2ky\sin(\theta/2))}{2} \right)$$
(2.13)

where V_0 is the full lattice depth. For simplicity, we have taken the lattice principal axes as the x and y axes and the beams propagate at an angle θ to the x-y direction (for detailed treatment, see Appendix D). In the case of r=1 we retrieve the unattenuated lattice, while in case of full attenuation (r=0), we are left with a 1D lattice along the y-axis.

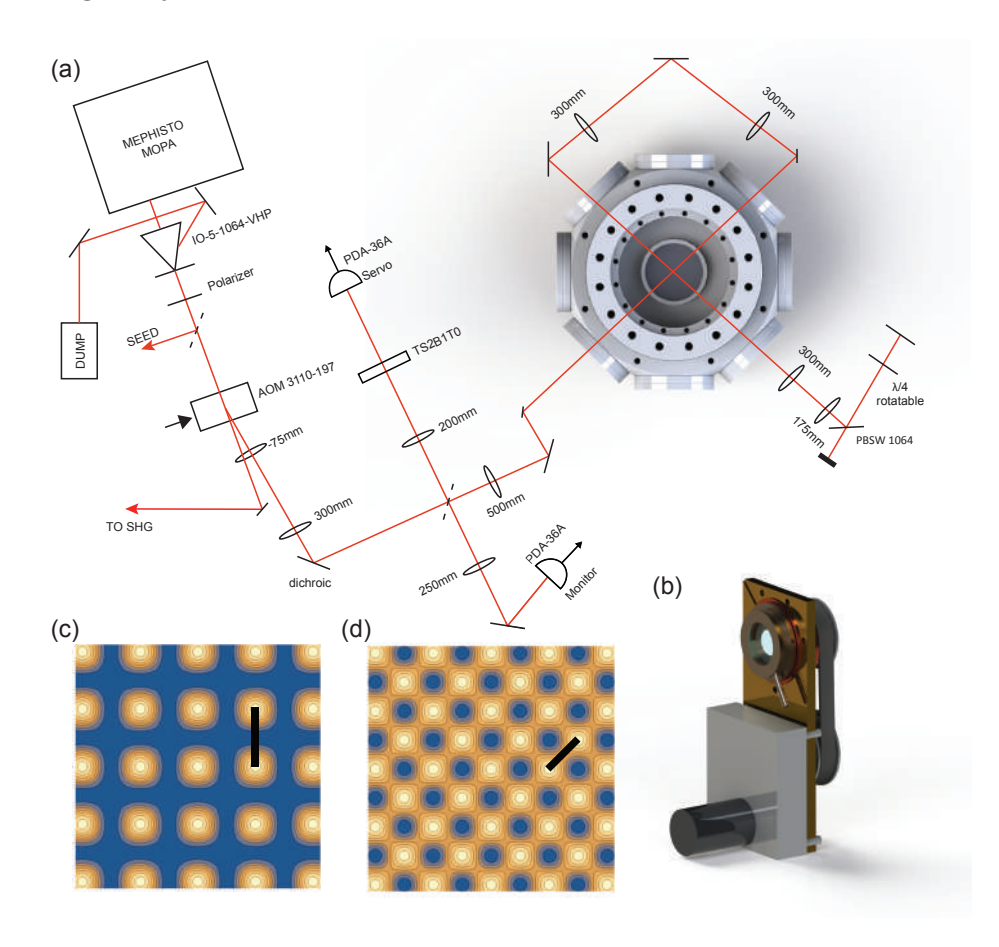


Figure 2.17: Science lattice. (a) Schematic of the lattice setup. Light from a 42 W MOPA at 1064 nm undergoes 4-fold interference with a polarization pointing out of plane. The attenuation of the reto-reflection is performed to adjust for a slight asymmetry along the two lattice directions. (b) The rotation mount that houses a quarter-wave plate used to tune the attenuation factor r. (c) Lattice potential contour plot for vertical beam polarization with maximum depth V_0 and spacing 752 nm. (d) Lattice potential contour plot for horizontal beam polarization leading to a maximum depth of $V_0/4$ and spacing 532 nm.

Light for the lattice is obtained from a single laser in master oscillator power amplifier (MOPA) configuration (Coherent Mephisto MOPA). The laser can maximally output 42 W of 1064 nm light. Its coherence length is specified to be greater than a kilometer. In addition, the laser is equipped with active intensity noise reduction (Noise Eater) that is capable of reducing intensity noise by over 10 dB/Hz over a range from 10 kHz to 1 MHz. Due to the efficiency of the AOM and losses at the isolator and other surfaces, we get about 28 W at full power in the first pass of the lattice beam. The beam is retroreflected at the very end. In order to make the retroreflection alignment easier, we focus down the beam with a 175 mm focal length lens and place a mirror at the Fourier plane to reflect it back. This mirror has a high damage threshold (Thorlabs NB1-K14). To adjust the intensity of the retroreflected beam, the beam is double passed through a quarter-wave plate on a rotatable mount (Fig. 2.17(b)). The angle of rotation is fixed by placing stops on the mount and the motor takes 1.98 s to make one full rotation. For loading atoms into the science lattice, the QWP position is such that the retro intensity is smaller by r^2 of about 0.24. The retro-reflected beam retraces its path backwards until it reaches the isolator. At this point, the light rejected through the isolator is redirected to a beam dump.

Before imaging of the atoms in the lattice, we need to pin the atoms to their position in the lattice in a time much shorter than the tunelling time. In general, our tunnelling rate is about 1 kHz, which means we need to ramp up the depth of the lattice in a time much smaller than 1 ms. However ramping up the lattice too fast could lead to excitations to higher bands. A moderate value for the ramp time is about 100 μ s. But we can not perform this ramp entirely using the intensity servo because it is only calibrated to operate up to a depth of 60 E_R . The maximum depth that we can achieve is $\sim 2500~E_R$. To ramp up to this depth fast, we implemented a pinning circuit (Fig. 2.18(a)). The purpose of the circuit is to smoothly switch between the servo voltage (usually a few 100 mV) and a voltage setpoint ($\sim 3 \text{ V}$) that leads to a saturation RF power on the AOM. When the TTL is in low state, the two SPDT switches allow only the servo voltage to reach the mixer. The transistor is introduced to provide the current needed to drive the mixer (Mini-Circuits ZLW-3+). The 330 Ω resistance is added to limit the current to below 40 mA, which is the maximum current rating for the mixer. Also during this time, the 0.1 μ F capacitor gets charged to the servo voltage. When the TTL is turned to high, the capacitor starts charging to the voltage setpoint at a rate given by a variable resistance and a capacitance. But at the same instant, the output voltage starts out at the servo value, leading to no discontinuity.

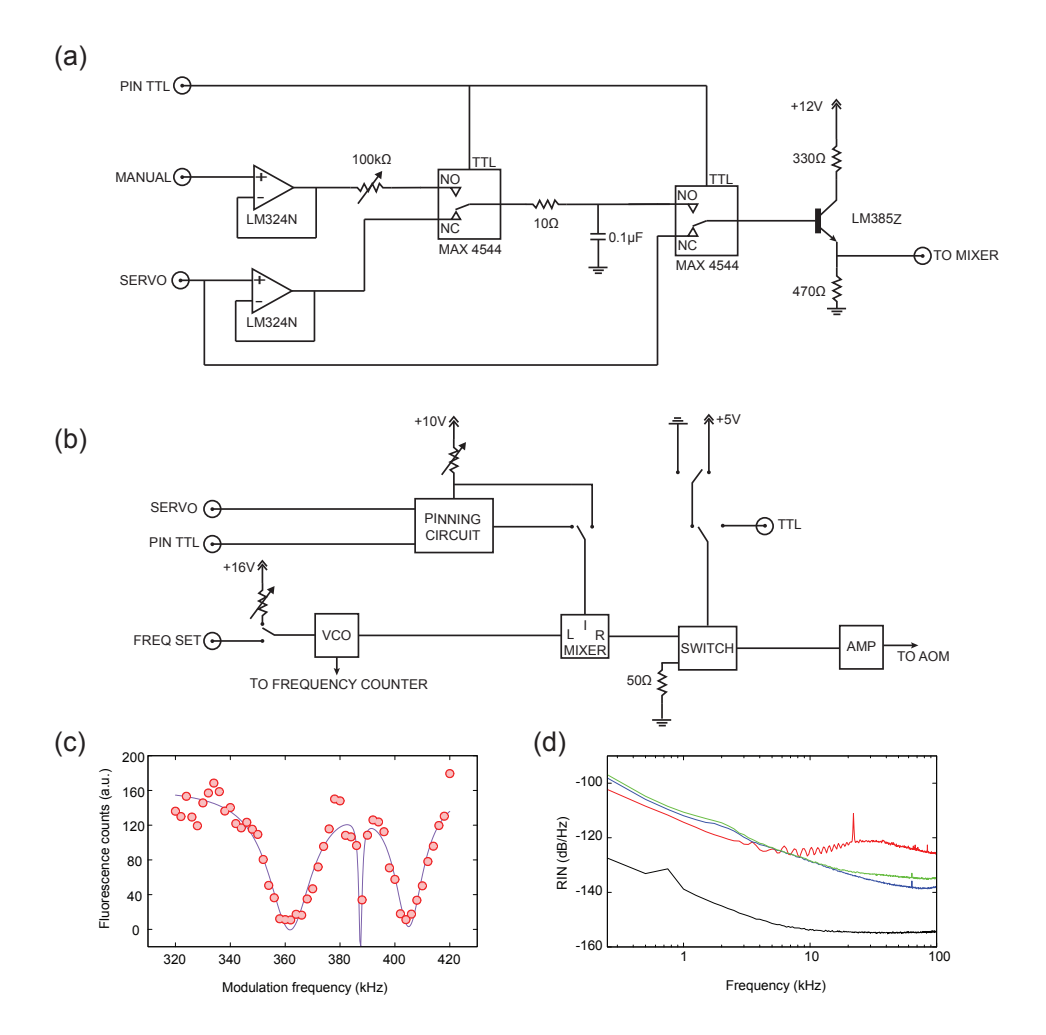


Figure 2.18: Pinning Circuit. (a) Schematic for the pinning circuit which allows us to ramp up the lattice intensity from a low science value to a high pinning value in $\sim 100 \ \mu s$. We use a capacitor which gets charged to the servo voltage while Pin TTL is low and when the TTL is switched to high, the SPDT switches change to manual input while the immediate output is still the servo voltage. From thereon, the capacitor charges at a variable rate to give the final pinning voltage. (b) Schematic of the entire AOM driver. The same schematic without the pinning circuit is used for driving all other AOMs. All the parameters can also be controlled manually by flipping three mechanical SPDT switches. (c) Amplitude modulation spectroscopy of the lattice at a depth of 60 E_R . The three dips visible here are due to excitations from the ground band to the lowest three d-bands of the lattice. Fitting to the location of these dips can be used to calibrate the depth and attenuation factor r for the lattice. (d) Relative intensity noise (RIN) of the lattice measured using SR770 network analyzer. Black line is the photodiode noise floor measured using a flashlight to produce the same voltage as lattice light. Green is the noise on the laser head without noise eater active and blue is with noise eater active. Red is the noise on the lattice servo.

The general scheme of the AOM driver is described in Fig. 2.18(b). A radio frequency (RF) waveform is produced through a voltage controlled oscillator (Mini-Circuits ZOS-150+) where the frequency is set by a manually adjustable potentiometer. Next, the RF is sent to a mixer where the signal is mixed with a DC voltage. The DC voltage can either be manually adjusted with a potentiometer, can be set by a servo directly or through a pinning circuit. Next, the RF is sent to a switch which can also be manually or externally controlled. We use two types of switches. For purposes where switching time is irrelevant, we use Mini-Circuits ZX80-DR230-S+ which has a 2 μ s switching time but needs only a unipolar voltage supply. But for faster switching, we use Mini-Circuits ZYSWA-2-50DR which has a 10 ns switching time, but requires a bipolar voltage supply. Finally the output of the switch is sent to an amplifier (Mini-Circuits ZHL-1-2W-S+) the output of which can be sent directly to the AOM. We use two separate AC-DC converters for supplying the amplifier and for the rest of the electronics.

To calibrate the depth of the lattice, we perform amplitude modulation spectroscopy. We modulate the lattice intensity with an external waveform generator and observe losses while imaging fluorescence. A relatively high lattice depth (around $60 E_R$) is used for this spectroscopy to ensure that we can work in a tight-binding regime. We scan a range of frequency where we see three dips associated with atoms getting excited from the ground band to the three d-bands of the lattice. Excitation to the lower lying p-bands is prohibited due to parity. Once atoms get excited to the higher bands, they are either lost from the system or they do not participate in Raman sideband cooling leading to a reduction in fluorescence counts (Fig. 2.18(c)). To obtain a lattice depth from spectroscopy, we calculate the band structure for our lattice with the depth V_0/E_R and the attenuation factor r as free parameters. The band structure is obtained numerically using a plane wave expansion for a reasonable number of reciprocal lattice vectors. We fit the position of the three dips and extract the depth and r. Subsequently, we estimate the tunnelling rate of our lattice at the science depth (usually between 5-10 E_R) by calculating the bandwidth of the ground band for a depth estimated from the ratio of light intensities. The tunnelling rate is given as W/(4d), where W is the bandwidth and d is the dimensionality of the system [84, 85, 86] and can be calculated for the two directions by taking cuts along them.

In addition, we can estimate the on-site interaction U that two atoms of opposite spins would experience in the absence of tunnelling. This interaction is s-wave in nature and occurs due to the proximity to a Feshbach resonance. In the tight binding model, we assume that the Wannier functions of the fermions in the lattice are sufficiently localized. We calculate the real space Wannier function of the lattice from the Bloch wavefunctions or by using the projection method [87], [88]. Once the Wannier functions w(x, y) are known, then the on-site interaction can be calculated (see Appendix D.2).

Chapter 3

Pathway to a Quantum Gas Microscope

3.1 Magneto-optical trap

There are 3 characteristic temperature scales associated with the cooling of neutral atoms:

1. The first temperature scale is defined by choosing the atomic speed to be large enough such that the Doppler shift in the atomic reference frame matches the atom's linewidth. The velocity in that limit would be $\sim \Gamma/k \sim 1~m/s$, where Γ is the natural linewidth of the absorption line and k is the photon wave-vector. The lowest achievable temperature of the order of several mK in this regime is given by:

$$k_B T_c = m\Gamma^2/k^2 \tag{3.1}$$

2. The next scale corresponds to the actual linewidth of the atomic transition, Γ . This temperature is called the Doppler limit and is $\sim 140~\mu \text{K}$ for the D2 line of ^6Li ($\Gamma = (2\pi)~5.87~\text{MHz}$) given by :

$$k_B T_D = \hbar \Gamma / 2 \tag{3.2}$$

Note however, that one can instead use the $2S_{1/2}$ to $3P_{3/2}$ transition at 323 nm and obtain a much lower Doppler limit due to the narrower linewidth of the transition ((2 π) 754 kHz) [89].

3. The next scale is determined by the lowest attainable energy due to one photon recoil. This temperature is only dependent on the photon momentum $\hbar k$ and is $\sim 3.5~\mu {\rm K}$ for the D2 line of $^6{\rm Li}$.

$$k_B T_R = \hbar^2 k^2 / m \tag{3.3}$$

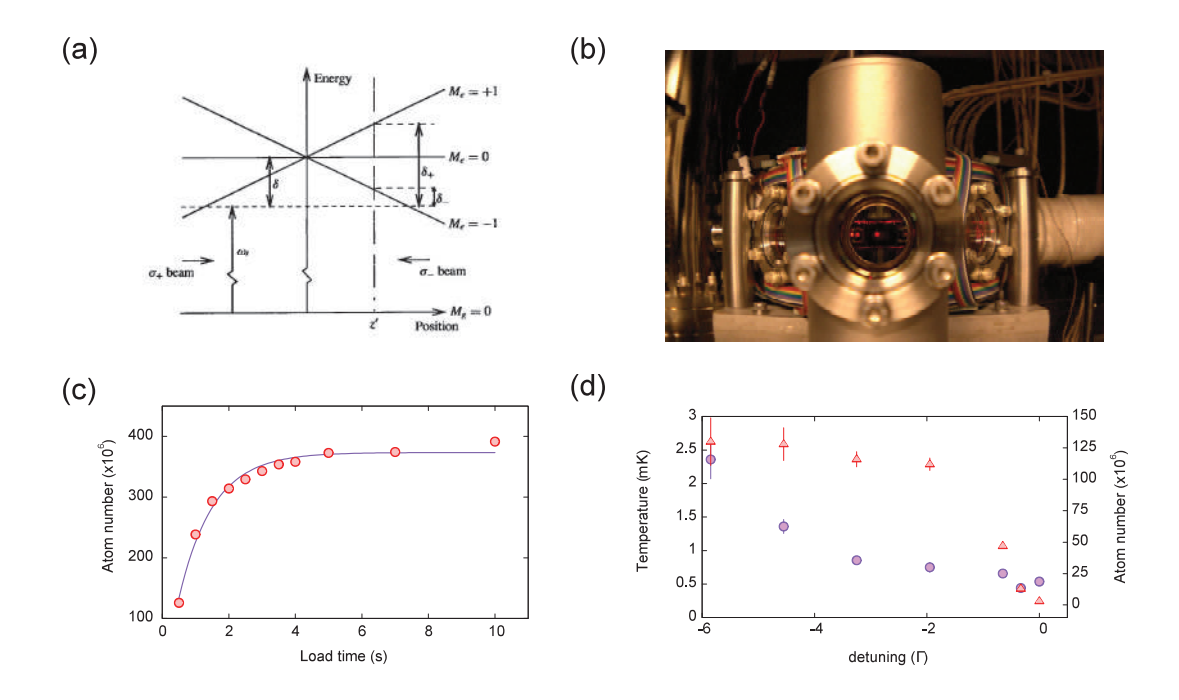


Figure 3.1: Properties of the magneto-optic trap. Schematic of operation of a MOT taken from [90]. An atom experiences a state specific Zeeman shift as it moves away from the center. In turn the atom only absorbs photons that are counter-propagating, providing a restoring force back towards the center. (b) A picture of the MOT in our setup and can be seen as a red dot near the center of the chamber. (c) Typical MOT loading rate in our system. We usually load the MOT for 5 seconds which leads to ~ 400 million atoms trapped at about 1.5 mK. (d) Plot of the detuning dependence of the atom number (red triangles) and the temperature (purple circles) after a stage of compression. During this cMOT stage, we ramp the intensity of cooling and repump light down to 1 % in 5 ms and simultaneously decrease the detuning (δ) from -5.4 Γ to -0.7 Γ . Notice that we successfully cool the atoms down at a cost of number of atoms. The final operating point is chosen by maximum loading into the optical dipole trap.

The magneto-optical trap, or MOT, is where the atoms are loaded after being slowed down in the Zeeman slower. It is important to note that the although we are slowing the atoms down, they still are not localized in space. According to Liouville's Theorem [90], the phase space density defined as the probability of finding a system near a particular point in phase space $(r_1, r_2, ..., p_1, p_2...)$ at a given time t, is conserved as long as the forces acting on the system are only position dependent. Cooling only occurs when one combines the squeezing of the velocity distribution as well as the position distribution of all atoms.

The MOT is our first stage of cooling of the $^6\mathrm{Li}$ gas. The design of the MOT consists of a pair of circular coils in an anti-Helmholtz configuration (Fig. 2.5). The idea of the MOT is to combine confinement in velocity space achieved by optical molasses with confinement in real space obtained by a restoring force due to the magnetic field. At the center of the trap, the field is 0 and it linearly increases at a rate of ~ 20 G/cm as one moves outwards.

Three retroreflected laser beams are used for cooling and trapping the atoms. Each beam consists of cooling light, red detuned by -5.4 Γ from resonance and a small fraction of repump light, usually $1/5^{th}$ in intensity of the cooling beam. The total beam intensity is usually set around $5I_{sat}$ (The saturation intensity of the D2 line of ⁶Li is 2.54 mW/cm²) The incoming beam is circularly polarized and has the opposite handedness to the retro-reflected beam.

In order to understand the trapping mechanism of a MOT, consider a 1D configuration (Fig. 3.1(a)) for an atom with a simple level structure where the ground state has 0 magnetic quantum number ($J_g = 0$ so $M_g = 0$) and the excited state has $J_e = 1$ and $M_e = 0$, ± 1 . Consider z = 0 as the center of the trap. Due to the linearly changing magnetic field, the states with a non-zero magnetic moment get Zeeman shifted. Now as an atom moves outwards from the center in the positive z direction, it finds itself closer to resonance with the $M_e = -1$ state and hence absorbs a photon from the σ^- beam since $\Delta M = -1$. Since this photon is counter-propagating, it kicks the atom back towards the center of the trap, hence confining it. In a similar fashion, an atom wandering out in the negative z direction, would absorb a σ^+ photon which in turn would kick it back towards the center of the trap.

To cool the atoms, the light beams must also provide a viscous force on the atoms. The spontaneous force experienced by an atom due to the absorption of a photon is simply $\hbar \vec{k} \gamma_p$, where γ_p is the scattering rate of the atoms in steady state. The net force due to the two counter-propagating photons is given by:

$$\Delta \vec{F} = \frac{8\hbar k^2 \delta s_0 \vec{v}}{\Gamma (1 + s_0 + (2\delta/\Gamma)^2)^2} = -\beta \vec{v}$$
 (3.4)

Where δ is the detuning and s_0 is the saturation parameter ($s_0 = I/I_{sat}$). Notice that for red detuning ($\delta < 0$), this force is like a viscous force that opposes the motion of the atom; hence the name optical molasses. Combined with the spatial confinement provided by the magnetic field and the laser beams, one achieves a reduction in phase space density.

After about 5 seconds of loading into the MOT at a detuning of -5.4 Γ , we obtain ~ 400 million atoms in the trap center at about 1.5 mK. The temperature of a cloud is measured from time-of-flight (TOF). We let the cloud expand for increasing time and image the atomic distribution in absorption. Then we fit the cloud profiles to 2D Gaussians. The cloud shape could be non-symmetric in trap but after sufficiently long times of flight when the atoms have travelled a large distance compared to the initial cloud size, it tends to be more symmetric. From the radius σ obtained from the Gaussian fit, we can perform a temperature fit knowing

$$\sigma^{2}(t) = \sigma^{2}(0) + \frac{k_{B}T}{m}t^{2} \tag{3.5}$$

In order to further reduce the phase space density, we perform what is known as a compressed MOT or a cMOT. After the MOT loading stage is complete, the Zeeman slower fields are turned off along with the corresponding laser beam. Almost simultaneously, we decrease the detuning of the MOT beams and bring them closer to resonance at -0.7 Γ in 2 ms. At the same time, we also reduce the intensities of the cooling and repumper laser beams to 1 % of their maximum values. This process leads to an increase in the phase space density at the cost of losing a fraction of the atoms and we end up with \sim 100 million atoms at a temperature of \sim 400 μ K (Fig. 3.1(c)-(d)).

3.2 Evaporation

After the initial preparation in a cMOT, atoms are transfered into the crossed dipole trap in 5 ms. The depth of the initial trap is 1.7 mK. We load about 300,000 atoms in the ODT and we measure the temperature to be $\sim 400~\mu\text{K}$, similar to the temperature in the cMOT. Atoms are in a mixture of the two lowest ground hyperfine states. Since we want the atoms to be in a mixture of states $|1\rangle$ and $|2\rangle$, we apply a short 100 μ s pulse of cooling light to transfer the leftover atoms in state $2S_{1/2}$ F=3/2 to F=1/2. But even then, we don't have an equal mixture in the two states. In order to achieve that we rely on a combination of RF pulses with decohering processes to obtain an equal spin mixture, as is described in more detail in the next section.

3.2.1 Radio frequency sweeps

The first step of this process is to ramp up the magnetic field to reach the Paschen Back limit where the Zeeman shift of the energy levels becomes linear with field. We ramp the Feshbach field to 528 G. At this field, the energy difference between |1| and $|2\rangle$ is (2π) 75.61 MHz. To drive coherent oscillations between the two hyperfine sublevels, we designed resonant RF antennas. The antennas themselves are flexible insulated copper wire made into the shape of a kidney bean ~ 10 mm across (Fig. 3.2(a)) and are placed as close to the bottom reentrant viewport as possible without significantly clipping the MOT beam. The two coils were designed to be resonant over a field range of 300-1000 G to the transitions between $|1\rangle - |2\rangle$ (74-77 MHz) and $|2\rangle - |3\rangle$ (91-81 MHz) resonances. The circuit diagram for the resonant antennas is given in Fig. 3.2(b) and is composed of a matching capacitance (C_M) and a tuning capacitance (C_T) . We chose $C_M = 10$ pF (surface mount) and $C_T = 100$ pF (mica) and tuned the resonance frequency by adjusting the shape of the coil. Both coils are driven by a single 100 W RF amplifier (Minicircuits ZHL-100W-52-S+) since they never operate at the same time. But to ensure that we could quickly switch between the two antennas, we added a high power SPDT RF switch (Pasternack PE71S6053, 0-18 GHz, 240 W and 10 ms switch time). The circuit diagram of the RF path is shown in Fig. 3.2(c). Since the amplifier running continuously at 100 W could damage the antennas, we added a timer circuit based on LM555 that would automatically switch the RF off after 110 ms.

We measured the response of the antennas at their final positions by measuring the pick-up of RF through a general broadband antenna placed in proximity to both coils. The resonance frequency of the coils were thus measured to be 76.5 MHz and 85 MHz (Fig. 3.2(d)), within the desired range. We characterized the antennas by measuring the Rabi frequency of driving coherent oscillations. The frequency of these oscillations depends on the amplitude of the magnetic field and the dipole matrix element. Consider first the two lowest hyperfine states. We start out in a spin polarized system where all atoms are in state $|1\rangle$, we apply an RF pulse of maximum amplitude for a variable time τ and at the end of the pulse we blow all atoms in state $|1\rangle$. The resulting curve is shown in Fig. 3.3(a) for a frequency of 75.561 MHz at a

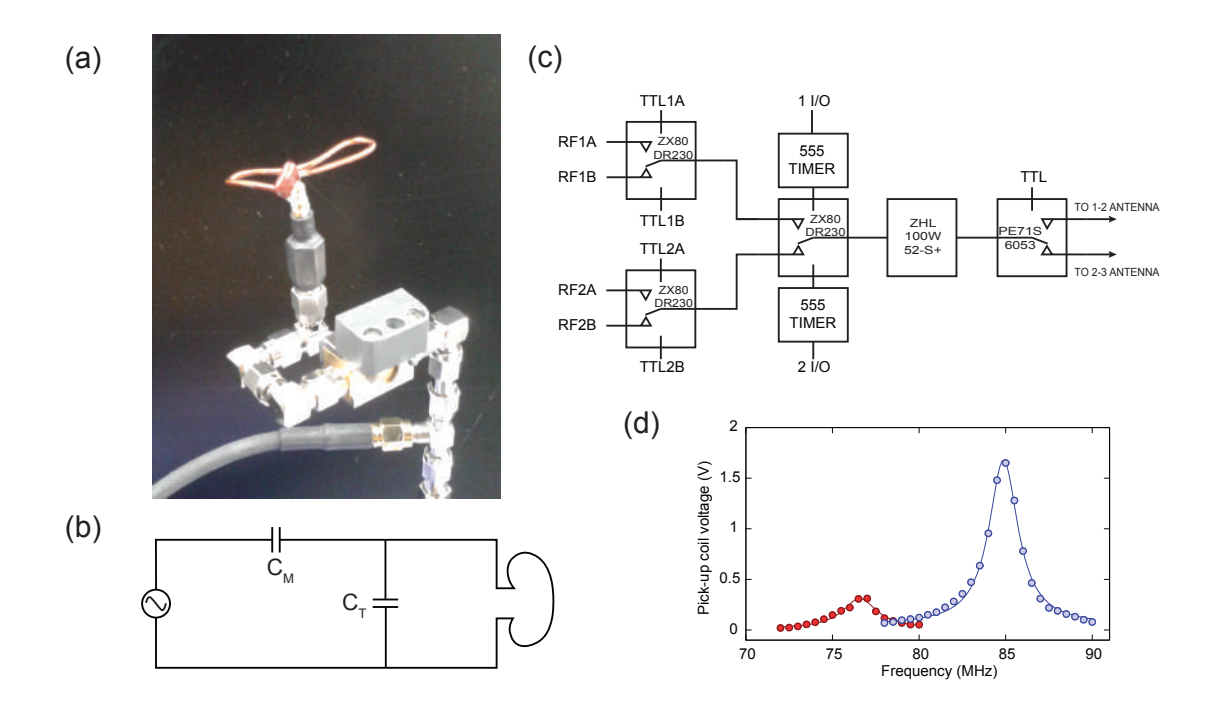


Figure 3.2: RF antennas. (a) Image of the resonant antenna. (b) Schematic of the same antenna. The matching capacitance C_M is 10 pF while the tuning capacitance C_T is 100 pF. (c) Schematic of the circuit that is used for driving the two antennas. Four separate RF generators are connected at the input of a multiplexer and a combination of 7 TTL signals are used to send the amplified RF signal to the antenna. The amplifier is rated up to 100 W and the switch after the amplifier up to 240 W. The timer circuits ensure high power is never on for more than 110 ms. (d) Voltage on a pick-up coil as a function of RF frequency. Red is $|1\rangle - |2\rangle$ antenna resonant around 76 MHz and blue is $|2\rangle - |3\rangle$ antenna resonant around 85 MHz.

field of 541 G. The Rabi frequency that we can obtain from our $|1\rangle - |2\rangle$ antenna is $\sim (2\pi)$ 14 kHz for fields beyond the Pashen Back limit.

In order to create an equal spin mixture in states $|1\rangle$ and $|2\rangle$, we apply 10 consecutive Landau-Zener (LZ) pulses. The Landau-Zener transfer is a way to diabatically transfer population from one state to another. We start out with negative detuning δ from resonance and sweep the detuning across resonance at a rate $\dot{\delta}$, then the excitation probability from $|1\rangle$ to $|2\rangle$ is given by [91]

$$P_{a \to e} = 1 - e^{-2\pi\Omega^2/\dot{\delta}} \tag{3.6}$$

where Ω is the Rabi frequency. So the excitation probability is maximized when δ is ramped from and to far off-resonant values in a very long time. In practice, however, it is sufficient to make $\delta \gg \Omega$. But we want to equalize the number in each state, so we picked parameters where $P_{g\to e} \to 1/2$. We perform the LZ sweep at a field of

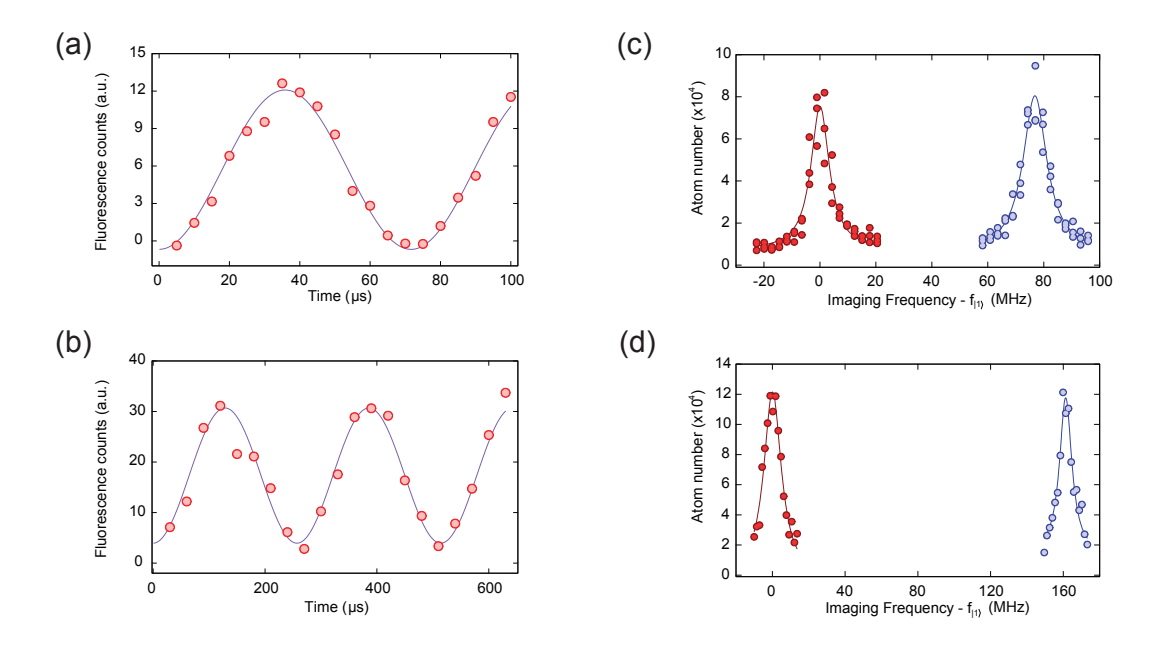


Figure 3.3: (a) Rabi oscillation at maximum RF power for the $|1\rangle - |2\rangle$ transition. The resonance frequency is 75.651 MHz at a field of 541 G and the Rabi frequency is (2π) 14 kHz. (b) Rabi oscillation at maximum RF power for the $|2\rangle - |3\rangle$ transition. The resonance frequency is 83.689 MHz at a field of 594 G and the Rabi frequency is (2π) 4 kHz. (c) Result of population balancing in states $|1\rangle$ and $|2\rangle$ after 10 Landau-Zener pulses of 2 ms each at 528 G, with center frequency of 75.607 MHz and a span of 300 kHz. X-axis is imaging detuning from the resonance for state $|1\rangle$. (d) Result of population balancing in states $|1\rangle$ and $|3\rangle$ obtained after a single LZ sweep to transfer the entire population in $|2\rangle$ to $|3\rangle$ at a field of 776 G. The duration of the sweep is 50 ms at a frequency of 82.054 MHz and a span of 500 kHz.

528 G, where the resonance frequence is 75.607 MHz. We ramp the detuning linearly over a span of 300 kHz centered about the resonance in 2 ms. To further enhance the equalization, we repeat this sweep ten times, spaced by 1 ms. After decoherence, we obtain equal mixture of $|1\rangle$ and $|2\rangle$ to very good accuracy. The result is shown in Fig. 3.3(c).

In addition, we can create a balanced mixture in states $|1\rangle$ and $|3\rangle$ by employing the second resonant antenna. We transfer the entire population in state $|2\rangle$ to $|3\rangle$ with a single LZ sweep. This sweep is performed at a field of 776 G where the resonance frequency is 82.054 MHz. The highest Rabi frequency we can get from this antenna is $\sim (2\pi)$ 4 kHz. We perform the sweep in 50 ms over the span of 500 kHz. The results of the process are shown in Fig. 3.3(b) and (d). After this stage, we blow away any atoms left in state $|2\rangle$ with a resonant light pulse.

3.2.2 Molecular Bose-Einstein condensates

At the start of evaporation, we have a phase space density of atoms in the trap of about 10^{-5} . The phase space density ρ is calculated from the optical depth, cloud size in trap and the temperature of the atoms. We fit cloud images to a 2D Gaussian $(\sim e^{-(x-x_0)^2/2S_x^2-(y-y_0)^2/2S_y^2})$. If the fit gives a peak optical depth (OD) and Gaussian sigma of S_x and S_y , then the volume density n is given by

$$n = \frac{OD}{\sigma(\sqrt{2\pi S_y^2})} \tag{3.7}$$

where we have assumed that the cloud is cylindrically symmetric, i.e. it is cigar shaped with S_x measuring the long axis and S_y measuring the short axis. σ is the resonant cross section given by $3\lambda^2/2\pi$. The thermal deBroglie wavelength of the cloud is defined as

$$\lambda_{dB} = \sqrt{\frac{h^2}{2\pi m k_B T}} \tag{3.8}$$

Finally, the phase space density ρ is defined as $\rho = n\lambda_{dB}^3$. It is a useful measure of the degree of degeneracy of an atomic cloud. For example, in order for a gas of non-interacting bosons to condense, the interparticle spacing must be of the order of the thermal deBroglie wavelength ($\rho \geq 2.6$). To increase our phase space density, we perform a phase of evaporative cooling of the atoms trapped in the ODT. The idea of evaporative cooling is to allow the highest energy atoms to escape from the trap upon which the remaining atoms rethermalize to a Boltzmann distribution at a lower temperature. This process is carried out at a variable rate until the leftover atoms have a sufficiently large ρ . Naturally, in order for the atoms to thermalize, they must be interacting. To achieve this interaction, we perform the evaporation at a field where the $|1\rangle - |2\rangle$ scattering length a_{12} is sufficiently large. One such place is near the broad Feshbach resonance located around B = 832 G for a $|1\rangle - |2\rangle$ mixture and one around B = 689 G for a $|1\rangle - |3\rangle$ mixture.

For evaporation to a molecular condensate, we ramp down the intensity of the ODT from the start value down to value that is 0.02% of the initial value in 6 seconds (for degenerate Fermi gas, the final value only needs to be 2% of the initial value). The ramp is exponential with a decay constant between 1 and 2 seconds. The handover servo allows us to stabilize the intensity over the 4 orders of magnitude. At the end of evaporation at 800 G, near the $|1\rangle - |2\rangle$ Feshbach resonance, we are left with a cloud of mostly Feshbach molecules. These bosonic molecules can further Bose condense to form a molecular Bose-Einstein condensate (mBEC) that we detect as a bimodality in the time-of-flight atom density (Fig. 3.4 (a)). In general we produce 20,000 - 30,000 molecules.

One of the uses of an mBEC is to calibrate the lattice spacing and depth [92]. Just as the diffraction of light waves on a periodic grating produces many equally spaced diffraction orders, the same would occur if a coherent matter wave would interact with an optical grating. An mBEC is essentially matter with a macroscopic wavefunction

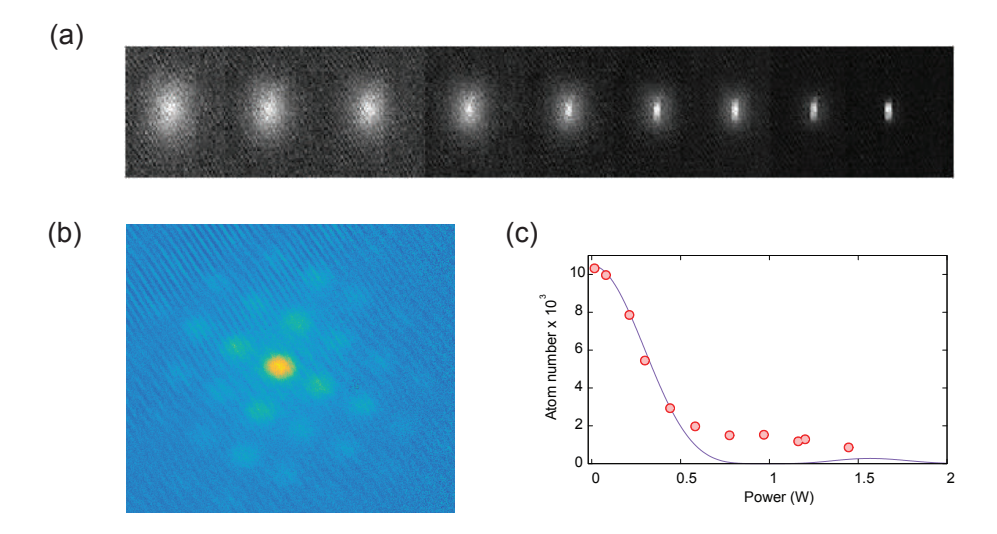


Figure 3.4: Bose-Einstein Condensation of $^6\text{Li}_2$ molecules. (a) Time of flight images of a cloud after different stages of evaporation. The final evaporation depth varies from 0.023 to 0.015% of the start value from left to right. The appearance of an mBEC can be spotted in the bimodality of the density profile. The decrease in the thermal cloud indicates a higher condensate fraction. (b) Example of the Kapitza-Dirac scattering of an mBEC when the lattice is pulsed on for 500 ns and the cloud is allowed to expand for 4 ms. The closest order is a momentum imparted of $2\hbar k$ in the two lattice directions. (c) Number of atoms in the 0^{th} order as a function of power in the lattice beams. The number decreases and can be fit to a Bessel functions (blue line). The argument of the Bessel function can be used to estimate the depth of the lattice.

and an optical grating can be produced by forming a standing wave of two retroreflected laser beams. There are two possible scenarios, one where the atoms diffract only when a momentum conservation criterion is met (Bragg diffraction) and the other where the atoms simply diffract off the grating (Raman-Nath diffraction). To see the difference between the two scenarios, consider first the total momentum transfer of an atom interacting with far off resonant photons. The atoms absorb from one direction and emit in the other, leading to a net momentum transfer of $2\hbar k$, where k is the photon wave-vector. Let τ be the interaction time between the matter and light, then the uncertainty principle states that the atoms sample a photon energy spread of $\Delta E = \hbar/2\tau$. When ΔE is much smaller than the recoil energy $E_R = \hbar^2 k^2/2m$, then diffraction is only possible when the Bragg condition is satisfied. On the other hand, if the interaction time is very short, $\Delta E \gg E_R$ and many diffraction orders are possible. This is diffraction in the Raman-Nath regime.

It is straight forward to solve the single particle time-dependent Schrodinger equation the Raman-Nath regime (the kinetic term can be ignored because of a very short τ). Consider the lattice configuration in Eq. 2.10 and for simplicity that the electric field in all directions is the same E_0 . The non-separable lattice potential is simply

$$V(x,y) = \frac{V_0}{2} \left[\cos(2kx) + \cos(2ky) \right] + V_0 \cos(kx + ky) + V_0 \cos(kx - ky)$$
 (3.9)

where, $V_0 = 4|E_0|^2$ is the amplitude of the cosine standing wave formed by the lattice and we have subtracted off a constant offset. Because of the above form, each term can be treated separately in the expansion of $\exp(-iV(x,y)\tau/\hbar)$. The final state is given by

$$|\psi\rangle \propto |\psi_0\rangle e^{-\frac{iV_0\tau}{2\hbar}\cos(2kx)} e^{-\frac{iV_0\tau}{2\hbar}\cos(2ky)} e^{-\frac{iV_0\tau}{\hbar}\cos(kx+ky)} e^{-\frac{iV_0\tau}{\hbar}\cos(kx-ky)}$$
(3.10)

Using an identity for Bessel functions of the first kind $e^{\alpha \cos(\beta)} = \sum_{n=-\infty}^{\infty} i^n \mathcal{J}_n(\alpha) e^{in\beta}$, one can write the probability of detecting a particle in the 0^{th} diffraction order as

$$P_0 = \mathcal{J}_0^4 \left(\frac{V_0 \tau}{\hbar}\right) \mathcal{J}_0^4 \left(\frac{V_0 \tau}{2\hbar}\right) \tag{3.11}$$

The population in the 0^{th} order decays with the power in the lattice beams while the population in the higher orders increase. In the experiment (Fig. 3.4(c)), we prepare an mBEC and after a 300 μ s time of flight, we pulse the laser forming the non-separable lattice for 500 ns at variable power. After another 4 ms time of flight, we image the number of atoms in the 0^{th} order. We fit the data to the function $A\mathcal{J}_0^4(bx)\mathcal{J}_0^4(bx/2)$, where x is the power in Watts. From the fit parameter b which is related to the depth per Watt, we obtain the maximum lattice depth as

$$V(P_{max}) = \frac{4\hbar b P_{max}}{\tau} \tag{3.12}$$

where, P_{max} is the maximum power in our lattice beams and is ~ 25 W. The factor of 4 is the enhancement due to the four-fold interference in our lattice. When aligned, we obtain $b \approx 2.2$ leading to a depth of ~ 1.6 mK (or $\sim 2300E_R$) for atoms trapped in the lattice. In addition, the distance between the 0^{th} and 1^{st} order can provide information about the momentum kick. In a time of 4 ms, the distance between the orders is 179.5 μ m taking into account a magnification of our imaging system. Now in time τ and after a momentum of $2\hbar k$ imparted, one would expect the atoms to travel a distance $2\hbar k\tau/2m$. Here we divide by 2m because the cloud is composed of molecules. Equating the two, we get that $a = \pi/k = 739$ nm. Here a is the lattice spacing formed by the 4-fold interference and is expected to be $1064/\sqrt{2}$ nm = 752 nm. So we can also verify the lattice spacing is what we expect.

3.3 Single site imaging

3.3.1 Raman imaging

To image the atoms in an optical lattice, one could employ absorption imaging by shining near resonant light on to the atoms in a deep lattice and collect the scattered photons. But each photon scattered would impart a kick on the atom and cause it to move around or escape from the deep well before enough photons have been collected to resolve the atom. So the signal to noise is limited and the atomic movement can blurr the image. Hence one requires a technique that scatters enough photons from a single atom without heating it up. In addition, by cooling the atoms in a deep lattice where the atoms do not move, one can achieve single site resolution. One such technique is electromagnetically induced transparency (EIT) cooling [93, 50]. The other more widespread technique is called sideband resolved Raman cooling. This technique was originally developed to cool ions to the vibrational ground state in a radio frequency trap [94] and later demonstrated for atoms in optical lattices [95]. Raman cooling was introduced as an imaging technique in quantum gas microscopes in experiments with ⁴⁰K and ⁶Li [52, 53, 56]. This was a departure from previous ⁸⁷Rb quantum gas microscopes which used polarization gradient cooling, which does not work as well for these species. As the name suggests, we drive transitions between resolved vibrational states of atoms on individual isolated sites of an optical lattice (Fig. 3.5 (a)) using a coherent two photon process.

In order to drive stimulated transitions of atoms from a higher vibrational state ν to $\nu-1$, we follow the scheme shown in Fig. 3.5(b). An atom starts out in the $2S_{1/2}$ F=3/2 manifold in vibrational state ν . A two photon Raman transition takes the atom to the $2S_{1/2}$ F=1/2 manifold and in the vibrational state $\nu-1$. This is achieved by using two beams, first a Raman beam detuned by 5.6 GHz from the $2S_{1/2} \rightarrow 2P_{1/2}$ transition and a retro-reflected beam detuned by $(228.2 + \omega_{latt}/(2\pi))$ MHz. Then the atom experiences a near resonant pump beam which excites the atom to the $2P_{1/2}$ state. The cooling cycle is closed when the atom spontaneously decays back to the $2S_{1/2}$ F=3/2 manifold while conserving the vibrational state $\nu-1$. Thus we have effectively lowered the vibrational energy of the atom by 1 $\hbar\omega_{latt}$ and the photon emitted during optical pumping is used for imaging.

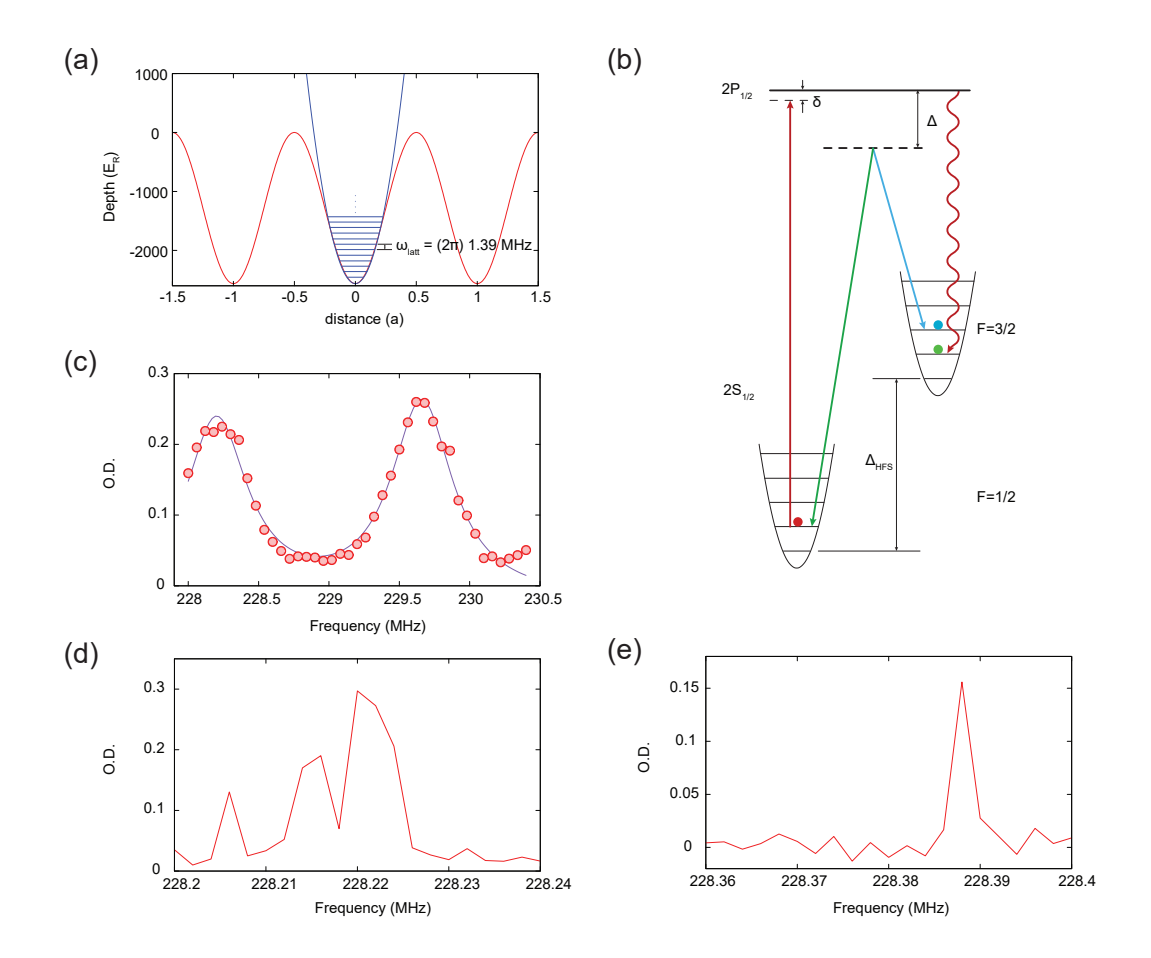


Figure 3.5: Raman cooling scheme.(a) 1D cut of our lattice potential at maximum depth (red). X-axis is distance in units of the lattice spacing (a = 752 nm). Maximum depth as obtained from a tight binding calculation. Fit of a single lattice site to a harmonic potential (blue) to obtain the spacing between vibrational levels $(\omega_{latt} \sim (2\pi) 1.39 \text{ MHz})$. (b) Schematic of the Raman cooling process. An atom in the $2S_{1/2}$, F=3/2 state starts out in an excited vibrational state (blue) of the lattice. A beam (blue) red-detuned to the $2S_{1/2} \rightarrow 2P_{1/2}$ by $\Delta = 5.6$ GHz and a counterpropagating beam (green) frequency detuned from the first one by $\Delta_{HFS} = 228.2 +$ $\omega_{latt}/(2\pi)$ MHz are incident on the atomic cloud. A third beam (red) near resonant with the $2S_{1/2}$, $F=1/2 \rightarrow 2P_{1/2}$ transition ($\delta \sim 10 \Gamma$) is also incident on the atoms. (c) Raman spectra at a field of $\sim 10\text{-}30$ mG. The first peak at 228.2 MHz is the carrier peak while the second one at 229.65 MHz is the blue Raman sideband. The energy difference between the two gives the lattice vibrational spacing of 1.45 MHz. (d) Radio-frequency (RF) spectroscopy at the lowest achievable magnetic field. Peaks at 228.206, 228.215, and 228.222 MHz correspond to a residual field of 10 mG. (e) RF spectroscopy at the magnetic field where we perform Raman cooling. The peak at 228.388 MHz corresponds to a field of 195 mG.

An important factor for the above scheme to be efficient is that the spontaneous emission process conserves the vibrational state. The recoil of the atom when it emits a photon is given by the operator $e^{-ik\hat{x}}$, where k is the photon momentum. It causes the momentum of the atom to change by $\hbar k$. Now in the basis of harmonic oscillator states $|\nu\rangle$, the probability of transition is given by

$$P_{\nu \to \nu'} = \langle \nu | e^{ik\hat{x}} | \nu' \rangle = \langle \nu | e^{ikx_0(\hat{a} + \hat{a}^{\dagger})} | \nu' \rangle$$
 (3.13)

where, the position operator \hat{x} can be written in terms of the harmonic oscillator creation and annihilation operator a and a^{\dagger} . $x_0 = \sqrt{\hbar/(2m\omega_{latt})}$ is the harmonic oscillator length. We define the Lamb-Dicke parameter η as

$$\eta = kx_0 = \sqrt{\frac{\hbar k^2}{2m\omega_{latt}}} \tag{3.14}$$

And we perform Taylor expansion in orders of η to obtain

$$P_{\nu \to \nu'} \sim \langle \nu | \left(1 + \eta (\hat{a} + \hat{a}^{\dagger}) + \mathcal{O}(\eta^2) \right) | \nu' \rangle \tag{3.15}$$

So we see that for a small Lamb-Dicke parameter η the branching ratio to decay into $\nu \pm 1$ is $\sim \eta^2/(1+\eta^2)$ and to even further vibrational states is strongly supressed. Hence obtaining the smallest possible η is crucial for Raman sideband cooling. For our lattice directions in plane, we have $\eta \approx 0.22$, while in the third direction, where we do not have a lattice but only confinement due to the lightsheet of about 70 kHz, we have $\eta_z \approx 1$. So we are in the Lamb-Dicke regime only in the lattice plane but we were still capable of performing single atom imaging. The reason for that is we do not need to be able to cool the atoms very efficiently to be able to image them. As long as an atom is capable of participating in the cooling process without being ejected from a lattice site, we can cycle photons through it.

The beam setup for Raman sideband cooling is shown in Fig. 3.6(a). Light from the Raman laser system (Fig. 2.12) is sent through optical fibers to the experiment. The Raman beam is linearly polarized and it passes at 45° to the lattice principal axes (so along one of the lattice beams). The beam is not coplanar with the lattice beam to allow coupling to the vertical direction. It runs at an angle of $\sim 10^{\circ}$ to the lattice plane. After passing through the chamber, it is double-passed through an acousto optic modulator set at 114.557 MHz. The polarization of the retro-reflected beam is linear and perpendicular to the incoming beam. The beam waist at the atoms is 75 μ m and the first pass power is 2.5 mW. The retro-reflected power is smaller by a factor of 0.77 due to AOM efficiency. The pump beam is also sent at an angle (shallower than the Raman beam), colinear with a lattice beam and has a waist of about 1 mm. The polarization of the pump beam is circular. The intensity and the detuning of the pump beam are tuned while optimizing the rate of hopping and loss in our system and are of the order of 50 μ W and 10 Γ relative to the free space resonance. We estimate the Rabi frequency of the 2-photon Raman transition to be (2π) 180 kHz by measuring power broadened Raman spectra for different powers.

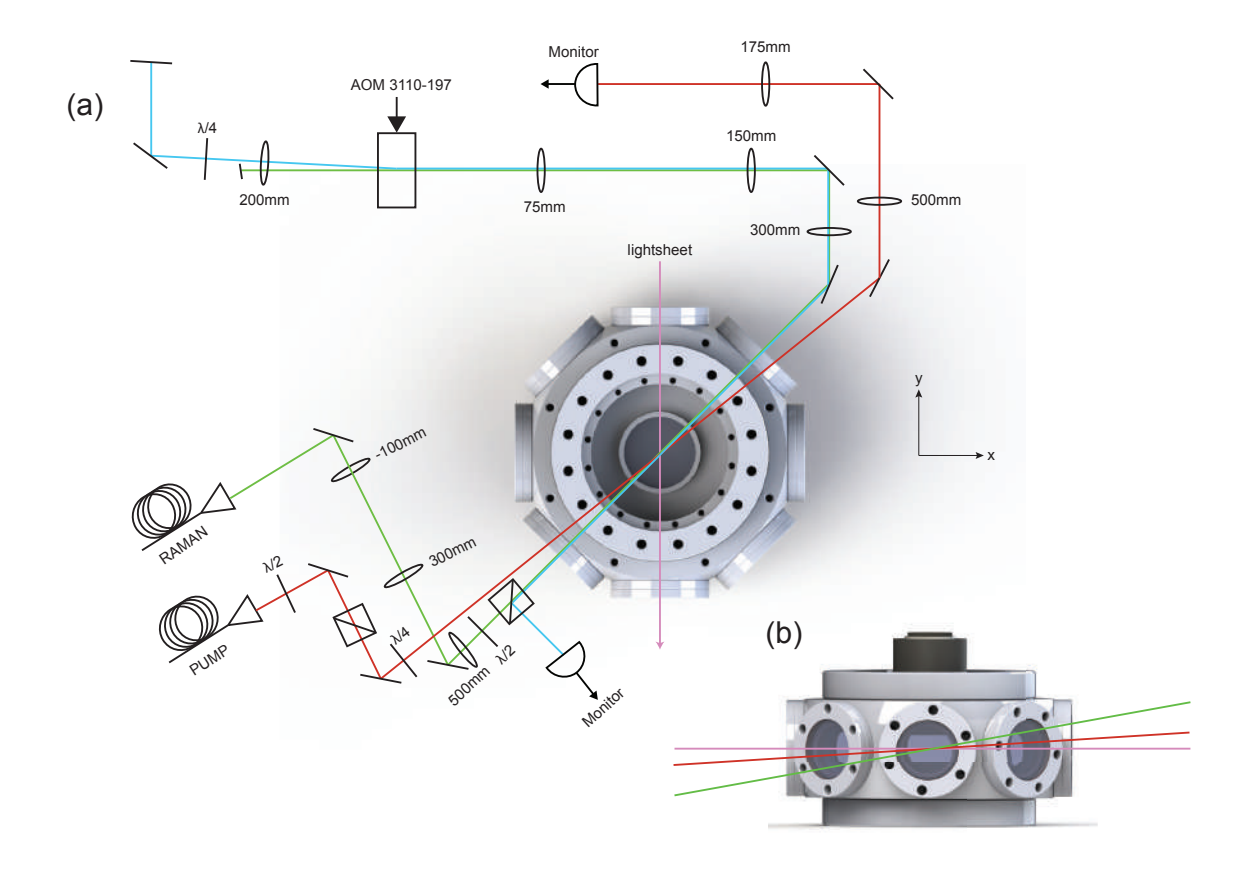


Figure 3.6: Raman sideband cooling setup. (a) Top view of the Raman beams. The pink arrow shows the direction of the lightsheet beam. The first Raman beam (green) is linearly polarized. It propagates at 45° to the lattice principle axes (x and y axes). It is also out of the plane formed by the lattice. It is double passed through an acousto-optic modulator to shift the frequency by 229.114 MHz. The quarter wave plate is adjusted so that this retro-reflected beam (blue) has a linear polarization perpendicular to the incident beam. A polarizing beam splitter cube placed near the end reflects out the second Raman beam which is monitored through a photodiode. The pump beam follows a similar path. It also runs at 45° to the lattice axes but makes a shallower angle out of plane. Its polarization is circular and depends on the direction of the applied magnetic field. After the chamber, the beam is directed to a photodiode to monitor the power. None of these beams are intensity stabilized. (b) Beam propagation in the y-z plane. The Raman beams (green) are at an angle of $\sim 10^{\circ}$ to the lattice axis (pink). The pump beam (red) is at a shallower angle.

To perform Raman spectroscopy, we prepare a spin polarized cloud in state $2S_{1/2}$ F=1/2 m_F=1/2 (or state $|1\rangle$) loaded in the lattice. When the atoms are pinned to their lattice sites, we turn off the Feshbach current and cancel the magnetic field due to the Earth using shim coils. To measure how well we can null our fields, we separately perform RF spectroscopy in a 3D trap. We start out with a spin polarized system in state $|1\rangle$ and apply an RF pulse at variable frequency. Due to the selection rule $\Delta m_F = 0, \pm 1$, transitions from $|1\rangle \rightarrow |3\rangle$ are forbidden. We then perform absorption imaging of atoms in state $2S_{1/2}$ F=3/2 and all values of m_F . We observe three peaks (Fig. 3.5(d)) at 228.206 MHz ($|1\rangle \rightarrow |4\rangle$), 228.215 MHz ($|1\rangle \rightarrow |5\rangle$) and 228.222 MHz ($|1\rangle \rightarrow |6\rangle$). At truly zero field, all these transitions would be degenerate at 228.205 MHz. The best field nulling we can achieve thus is ~ 10 mG. Now Raman spectroscopy can be performed at this field by varying the frequency difference between the Raman beam and its retro-reflection. Since the atoms start out in $|1\rangle$ and a vibrational state ν , they can end up in $|2\rangle$, $\nu' = \nu, \nu \pm 1, \nu \pm 2$, etc. The first one for which $\Delta \nu = 0$ is called the carrier transition. The transitions for which $\Delta \nu > 0$ are called blue sideband transitions or heating transitions, while the ones for which $\Delta \nu < 0$ are called red sideband or cooling transitions. We normally see the carrier and the first blue sideband (Fig. 3.5(c)) in Raman spectroscopy. We also see some transfer in the first red sideband because not all atoms are in the ground vibrational state. The splitting between the carrier and the first sideband gives the harmonic oscillator spacing ($\omega_{latt} = (2\pi) 1.45 \text{ MHz}$) which is the same in the two horizontal directions.

Although we initially attempted Raman cooling at ~ 10 mG, we found the Raman imaging process to be more efficient at a finite field. For this scheme, the magnetic field is non zero and this causes the hyperfine sublevels of the atom to shift in energy due to the Zeeman effect. The advantage of that is we can select the states which provide the largest coupling. We concluded that we mostly drive transitions between states $|3\rangle$ and $|2\rangle$ at an offset field of 195 mG. We measure the value of this offset field from RF spectroscopy (Fig. 3.5(e)). We observe a peak due to $|1\rangle \rightarrow |5\rangle$ at 228.388 MHz and one at 228.572 MHz for $|1\rangle \rightarrow |6\rangle$ transition.

3.3.2 Microscope objective

In order to image single atoms, we need an objective capable of resolving the distance between neighboring lattice sites. That distance in our experiment is 752 nm. We purchased a custom designed objective from Special Optics (Navitar) that suited our needs. The objective (54-25-25-671&800nm) (see Appendix E) has the following specifications:

- Effective focal length = 25 mm
- Working distance = 12 mm in air + 5 mm in fused silica
- Numerical aperture = 0.5
- Field of view in object plane = 150 μ m
- Anti-reflection coated at 671 nm and 800 nm
- Diffraction limited up to 120 μ m defocus
- Non-magnetic Ultern casing of 36 mm outer diameter

Due to the diffraction limited performance at the D1 transition wavelength, we can resolve features as small as 800 nm given by the Rayleigh criterion $(0.61\lambda/\text{NA})$, comparable to the lattice spacing. A 750 mm lens after the objective leads to a magnification of 30. We employ an Andor Zyla 4.2 sCMOS camera for fluorescence imaging. The quantum efficiency of the sensor is about 75% at 671 nm with 0.9 e^- readout noise and the pixel size is 6.5 μ m.

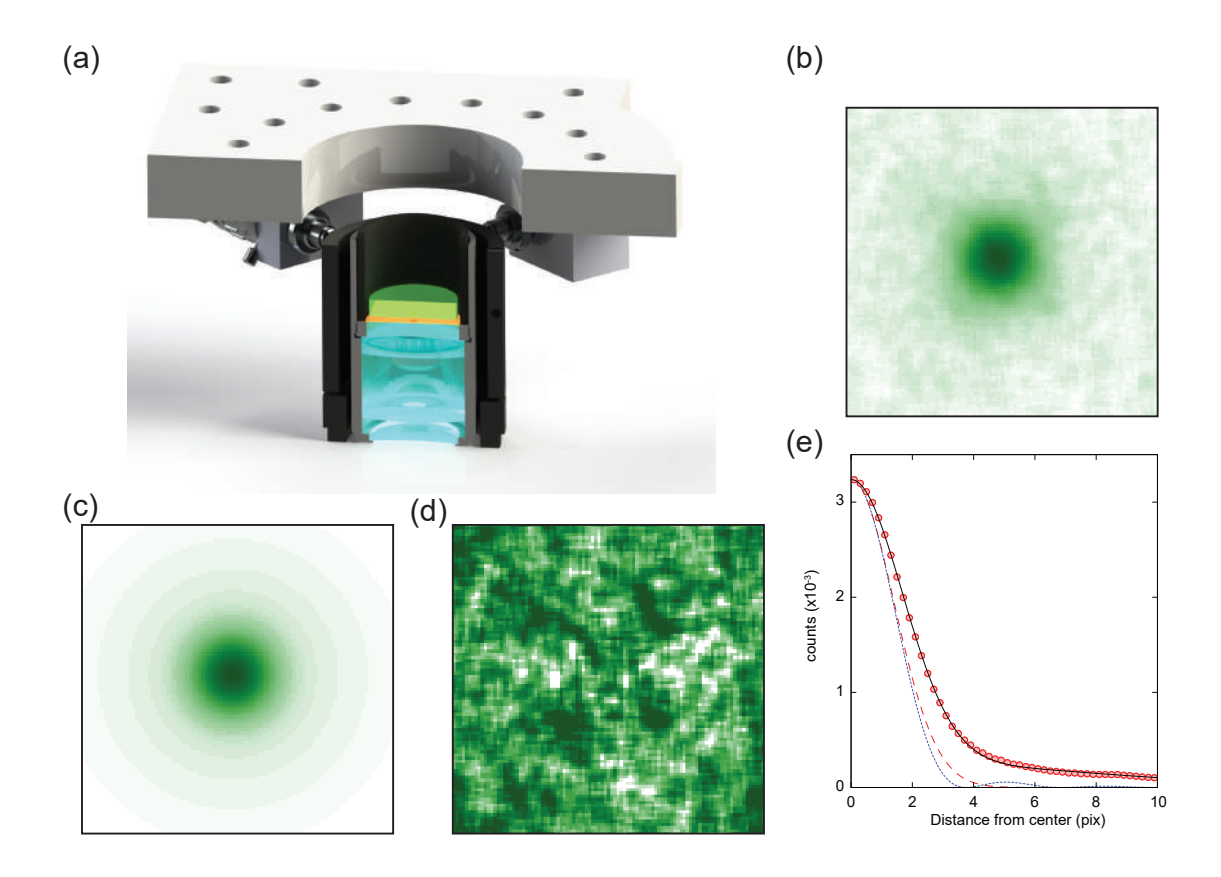


Figure 3.7: Objective mount and point spread function. (a) Shows the mounting of the objective. The objective is composed of 4 lenses (blue). On top of the objective and freely sliding is a mount carrying a quarter-wave plate (brown). On the top surface, there is a high reflection coated dot of 2 mm diameter which is placed at the Fourier plane of the objective. The vertical MOT beam gets focussed down and retro-reflected by the dot and the polarization changes sign because of double passing through the quarter wave plate. On top of the waveplate rests a $-\lambda/2$ correction plate (green) to eliminate spherical abberation of the point spread function. The bottom part of the objective mount is snugly fit to the reentrant viewport and the two micrometer screws allow for variation of tilt. The white ceramic piece on top allows for mounting of imaging optics. (b) Point spread function as obtained from averaging several single atom images. (c) Gaussian fit to the average point spread function. (d) Residual after subtracting the gaussian fit from the average point spread function. (e) Azimuthal average of the point spread function (red circles) and its gaussian fit (black). Ideally expected point spread function (blue dots) with a σ of 1.39 pix for our imaging system. Expected gaussian (red dashed) with the same σ as the ideal point spread function. The measured σ (black solid) of our point spread function is 1.65(5) pix.

3.3.3 Reconstructing single atoms

Our standard imaging technique involves taking two 1200 ms long exposures. The first exposure is pretriggered by 1225 ms from the start of Raman imaging. This frame only collects stray light from the MOT beams and serves as a global clear for the camera before starting an actual exposure. This frame is discarded. During the 1.2 s exposure, we collect about 1000 photons per atom.

We reconstruct the atom distribution in the lattice following the image reconstruction procedure described in [96, 48]. Reconstruction allows us to reduce the data from the fluorescence pictures to binary matrices that are the basis for all further data processing. The point spread function (PSF) of an imaging system is the response of the system to a point source. In principle, the diffraction limited PSF of an ideal microscope is an Airy disk which has the form

$$PSF(z) \sim \left(\frac{2J_1(z)}{z}\right)^2 \tag{3.16}$$

where, $z = 2\pi x \text{NA}/\lambda$ and $J_1(z)$ is the 1st order Bessel function. For an NA of 0.5, $\lambda = 671$ nm and an imaging system magnification of 30, we expect the width (2σ) of the PSF to be ~ 600 nm. We estimate the PSF of our imaging system by analyzing images with sparse atomic density distributions. The average of many of these single atom images is shown in Fig. 3.7(b). We can estimate the width of the PSF by performing a 2D gaussian fit to the average. We notice that the resulting radial distribution is wider than expected. We also notice that aberration and coma effects are minimal by subtracting the gaussian fit from the average. The final measured 2σ width of our PSF is 715(20) nm which is larger than expected but still smaller than the lattice spacing (752 nm) ensuring our ability to resolve two atoms on neighboring lattice sites.

We perform calibrations of our lattice angle and spacing by using very sparse images of pinned atoms. The images are fit to a 2D grid with four free parameters, the angles θ_1 and θ_2 that the grid makes with the x and the y axis defined by the camera pixels and the spacings a_1 and a_2 that are the spacing between sites on this grid along the two axes. These fit values are in turn used to define the lattice grid for reconstruction. The fit values can change based on any modification done to the imaging system, so they are measured every few weeks. For the stable working condition of the experiment, the average values of these parameters are $\theta_1 = -54(1)^{\circ}$, $\theta_1 = -36(1)^{\circ}$, $a_1 = 3.5(1)$ pixels and $a_2 = 3.4(1)$ pixels (1 pixel = 217 nm).

An example of reconstruction is shown in Fig. 3.8. We make a histogram of detected photons on each site for a given image. Usually the histogram is bimodal, with a peak near zero photons corresponding to empty sites and a peak at a higher photon count corresponding to sites with a single atom. Due to strong light assisted collisions, atoms in sites with more than one atom are lost and these sites appear empty. Next we fit gaussians to these peaks and identify a threshold between them. Any site with more counts than the threshold is identified as occupied. It is important for reconstruction to work properly that the peaks associated with empty and occu-

pied sites be well separated. If it is not the case, either recalibrating lattice angles or refocusing the camera must be performed.

We estimate fidelity errors due to Raman imaging imperfections by taking 40 consecutive images with our standard imaging time of 1200 ms of the same atom cloud and determine the shot-to-shot differences. This leads to a hopping rate during one picture of 0.4(2)% and a loss rate of 1.6(3)%. In addition, while holding the atoms in a deep lattice for spin manipulations or doublon hiding/detection, we lose 2(1)% of the atoms, leading to a net detection efficiency of 96%.

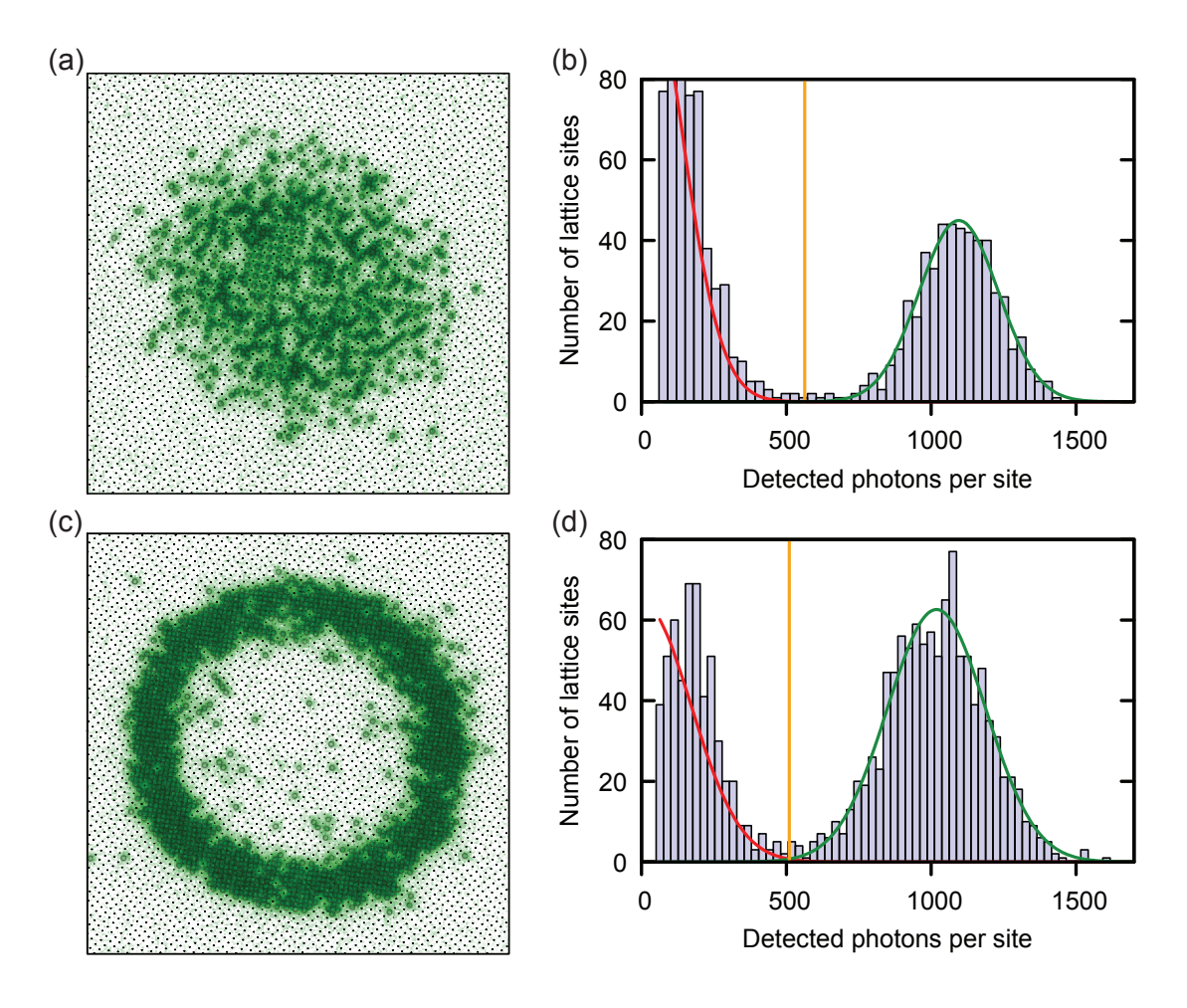


Figure 3.8: Reconstruction visualization. (a) A fluorescence image with lattice sites overlaid, showing occupied sites (circles) and unoccupied sites (points). Field of view is 46 μ m. (b) Histogram of detected photons on each site for panel (a). We identify the lower peak with unoccupied sites and the upper with occupied sites. By fitting gaussians to these peaks, we identify a threshold value (orange line). Any site with more counts than the threshold we count as an atom. (b) Fluorescence image showing a band insulator in the center of the cloud, surrounded by a Mott insulator region. (d) Histogram of detected photons for panel (c).

Chapter 4

Phase separation and pair condensation in a spin-imbalanced 2D Fermi gas

4.1 Degenerate Fermi gases

Degenerate Fermi gases are omnipresent in the universe. From the semiconductor transistors located within our computers to the cores of neutron stars, the physics of fermions dictates many important phenomena in our daily life. Fermi-Dirac statistics describes the thermodynamics of an ideal gas of fermions [97]. The essential ingredient is the Pauli exclusion principle [98], which states that two identical fermions can not occupy the same quantum state simultaneously. Our experiments are motivated by the understanding of exotic phenomena that appear in strongly interacting systems of fermions.

As was described in the previous sections, we start with fermionic lithium atoms in a $|1\rangle - |2\rangle$ mixture and evaporate near the Feshbach resonance at 832 G to create a molecular BEC. Alternatively, it is possible to produce a degenerate gas of fermions, where the atoms do not pair and form molecules. I will describe first the simplest of such cases, a non-interacting gas of fermions in a 3D harmonic trap.

It is more difficult to cool down fermions to quantum degeracy than bosons through evaporative cooling. Efficient evaporative cooling requires atoms to scatter off one another and thermalize. Identical fermions can not scatter off one another in the s-wave channel. One needs fermions of opposite spins. But even with fermions of opposite spins, as the temperature approaches zero, Pauli blocking drives collision rates down to zero as well. Despite the challenge of evaporative cooling, the first degenerate gas of fermionic potassium was observed in 1999 [5] four years after the first observations of BEC in rubidium and sodium in 1995 [3, 4].

Non-interacting fermions can be readily created in our experiments by using a spin polarized gas or by working at a magnetic field where the s-wave interactions between fermions vanish. In the limit of large N, many single particle fermionic states

are occupied and one can safely apply a semiclassical treatment to the system. The semiclassical distribution function in such a system is given by

$$f(\vec{k}, \vec{r}) = \left(e^{\beta \left(\frac{\hbar^2 k^2}{2m} + V(\vec{r}) - \mu\right)} + 1\right)^{-1} \tag{4.1}$$

where, $\beta=1/k_BT$, $V(\vec{r})=m\omega^2r^2/2$ is the harmonic potential assumed to be symmetric here and μ is the chemical potential. In most situations, however, the harmonic potential is only cylindrically symmetric. The potential then can be written as $V(r,z)=m\omega_r^2r^2+m\omega_z^2z^2$ with $\omega_z=\lambda\omega_r$. This distribution tends to a Maxwell-Boltzmann distribution at high temperatures and low particle density. The chemical potential can be implicitly calculated from the particle number using [99]

$$N = \int \frac{g(\epsilon)d\epsilon}{e^{\beta(\epsilon-\mu)} + 1} \tag{4.2}$$

where $g(\epsilon)$ is the single particle density of states given by $\epsilon^2/(2\lambda\omega_r^3)$ for a cylindrically symmetric potential and N is the number of particles in each non-interacting spin state. If the harmonic oscillator potential is not cylindrically symmetric, one can replace $\lambda^{1/3}\omega_r$ with the geometric mean $(\omega_x\omega_y\omega_z)^{1/3}$. From the knowledge of the Fermi function and the density of states, all other thermodynamic quantities can be calculated. The energy scale of the system is given by the Fermi energy given by

$$E_F = \hbar \omega_r (6\lambda N)^{1/3} \tag{4.3}$$

In the same way, the temperature scale of the system is called the Fermi temperature and is given by $E_F = k_B T_F$. The Thomas-Fermi radius of the cloud can be calculated from $m\omega_r^2 R_{TF}^2/2 = E_F$.

To understand interactions between cold fermions in 3D, consider the Schrodinger equation of two colliding particles in their center of mass (COM) frame

$$\left(-\frac{\hbar^2 \nabla^2}{2\mu} + V(r)\right) \psi_k(r) = E_k \psi_k(r) \tag{4.4}$$

where, in COM coordinates, the reduced mass $\mu = m/2$ and U(r) is the interaction potential. The above equation can be rewritten as

$$(\nabla^2 + k^2)\psi_k(r) = v(r)\psi_k(r) \tag{4.5}$$

where, the momentum k is given by $E_k = \hbar^2 k^2 / 2\mu$ and the modified potential $v(r) = 2V(r)\mu/\hbar^2$. Rewriting the above in spherical coordinates and rearranging one gets

$$(kr)^{2} \frac{d^{2}\psi_{k}(r)}{d(kr)^{2}} + 2(kr) \frac{d\psi_{k}(r)}{d(kr)} + ((kr)^{2} - v(r))\psi_{k}(r) = 0$$
(4.6)

Notice that the above equation is the Bessel differential equation of second order in the variable kr. The solution of the above equation in the far field limit (i.e. $r \gg r_0$, where r_0 is the range of the interaction potential) can be written as

$$\psi_k(r) = e^{ikz} + \frac{e^{ikr}}{r} \int v(r')\psi_k(r')e^{ikr'}d^3r' = e^{ikz} + f(k)\frac{e^{ikr}}{r}$$
(4.7)

where, f(k) is known as the scattering amplitude and it depends on the form of the interaction potential. The direction of propagation of the plane wave is the z axis. The simplest approximation to make here is that the collisions happen predominantly in the s-wave or spherically symmetric channel. Hence the scattering amplitude has no angular dependence. This can be achieved by integrating over the spherically symmetric part of the plane wave. In addition, the process of scattering only adds a phase shift δ to the incoming wave. Combing the two, one obtains

$$\psi_k(r) \sim e^{ikr} + \frac{e^{ikr}}{r} \frac{e^{i\delta} \sin \delta}{k}$$
 (4.8)

Thus the scattering amplitude in the case of s-wave scattering is

$$f(k) = \frac{e^{i\delta}\sin\delta}{k} = \frac{1}{k\cot\delta - ik} \tag{4.9}$$

Now the calculation of the phase shift δ requires knowledge of the interaction potential V(r). Let us consider a simple example of an attractive potential well. Below r_0 , the well has a depth $-V_0$ and above r_0 , the depth V(r) = 0. We assume that the wavefunction inside the well and outside are both sinusoidal but with a phase difference δ . But they have different momenta because of the potential. So

$$\psi_k(r) = \begin{cases} A\sin(k'r), & r < r_0 \\ B\sin(kr + \delta), & r > r_0 \end{cases}$$

$$\tag{4.10}$$

where, $\hbar^2 k'^2/2\mu - V_0 = \hbar^2 k^2/2\mu$. Now the wavefunction must be continuous and differentiable at $r = r_0$ giving

$$k'\cot(k'r_0) = k\cot(kr_0 + \delta) \tag{4.11}$$

Solving for δ after expanding in powers of kr_0 , one gets

$$k \cot \delta = -\frac{1}{a_s} + \frac{r_e k^2}{2}$$

$$a_s = r_0 - \frac{\tan q r_0}{q}$$

$$r_e = \left(\frac{1}{q} - r_0^2 q\right) \cos(q r_0) + r_0 \sin(q r_0) + \frac{q^2 r_0^3 \cos^2(q r_0/3)}{\sin q r_0 - q r_0 \cos(q r_0)}$$
(4.12)

where, $q = \sqrt{2mV_0}/\hbar$, r_e is the effective range of the interaction and a_s is the swave scattering length. Although the attractive well is only a pedagogical tool, it is a close approximation to a real inter-atomic scattering potential like the Lennard-Jones potential. In the limiting case of the effective range $r_e \to 0$, which is true for point interactions, one gets $k \cot \delta \approx -1/a_s$. Hence the scattering amplitude at momentum k approximately equals

$$f(k) \approx \frac{-a_s}{1 + ika_s} \tag{4.13}$$

In addition, the scattering amplitude is maximum when $a_s \to \pm \infty$, which is the case of being at the Feshbach resonance for our atoms. When $a_s > 0$ and close to this resonance, molecular bound states or dimers can form with a binding energy

$$E_b^{3D} = \frac{\hbar^2}{2ma_s^2} \tag{4.14}$$

These dimers are weakly bound near the Feshbach resonance and the binding energy increases as one moves to the BEC side (Fig. 4.1). Above the resonance, however, where $a_s < 0$, no dimers can form and no bound states exist.

4.2 Fermi gas in 2 dimensions

Dimensionality is very important in nature. Many interesting properties appear when fermions are confined in a plane like the Quantum Hall Effect [100, 101]. Another example is high temperature superconductivity in the cuprates, where the lower dimensionality is believed to play an important role [102]. Yet another example is the FFLO phase theorized in spin-imbalanced attractive Fermi gases, which can be enhanced in 1D and 2D due to Fermi surface nesting [103, 104]. These examples motivate us to study strongly interacting atomic Fermi gases in 2 dimensions. A simple way to change the dimensionality of a system is to increase the harmonic confinement in the axial direction.

As a measure of the extent of 2 dimensionality, we can compare the Fermi energy and the temperature to the harmonic oscillator level spacing in the axial direction. If $E_F, T \gg \hbar \omega_z$, then the fermions occupy many axial states and the gas in 3D. However if $E_F, T \ll \hbar \omega_z$, then only the ground state in the axis direction is occupied and the gas is purely 2D. In our experiment, ω_z is about (2π) 22 kHz for the accordion lattice. The radial trapping frequency geometric mean ω_r is about (2π) 135 Hz. In the case of $\omega_z \gg \omega_x, \omega_y$, one finds that the density of states is given instead by [105]

$$g(\epsilon) = \frac{\epsilon}{(\hbar\omega_r)^2} \tag{4.15}$$

where, if the trap is not uniform in plane, one can replace ω_r with the geometric mean $\sqrt{\omega_x \omega_y}$. From this, the Fermi energy is

$$E_F = \hbar \omega_r \sqrt{2N} \tag{4.16}$$

N is the number of particles in each non-interacting spin state. We have about 9×10^3 atoms giving a Fermi energy of $(2\pi\hbar)$ 18 kHz which puts us in a "quasi" 2D regime.

Collisions in 2D are a little different compared to Eq. 4.7. Suppose that the incident wave is a plane wave travelling in the z direction. In the asymptotic limit $(r \to \infty)$, the scattered wavefunction can be written as [106, 107]

$$\psi_k(r) \sim e^{ikz} - \sqrt{\frac{i}{8\pi kr}} f(k)e^{ikr} \tag{4.17}$$

To understand why the scattered wave has a e^{ikr}/\sqrt{r} dependence in 2D compared to the e^{ikr}/r dependence in 3D, consider the conservation of $|\psi_k(r)|^2$ before and after scattering. The probability current j is defined as

$$j = \frac{\hbar}{i2m} \left(\psi_k(r)^* \nabla \psi_k(r) - \psi_k(r) \nabla \psi_k(r)^* \right)$$
(4.18)

The divergence of j should be 0 for conservation of probability, i.e.

$$\psi_k(r)^* \nabla^2 \psi_k(r) = \psi_k(r) \nabla^2 \psi_k(r)^*$$
(4.19)

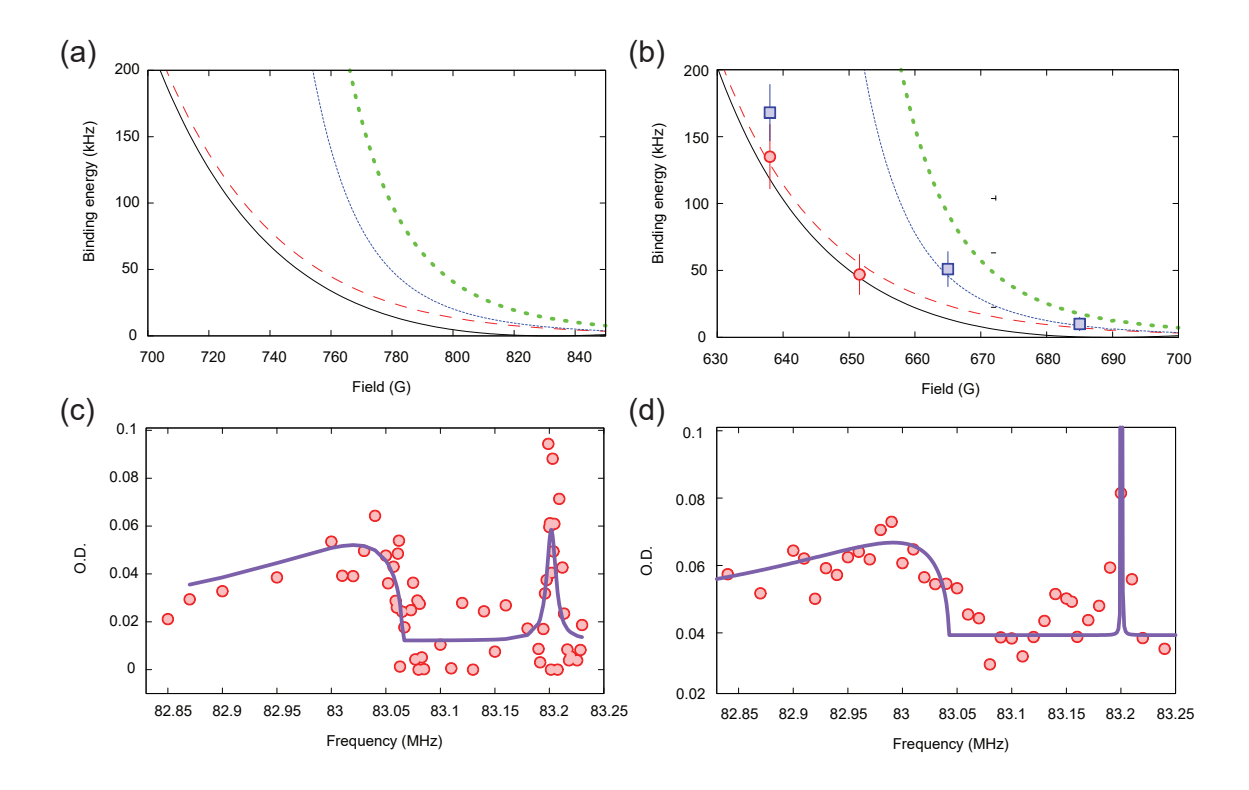


Figure 4.1: Binding energy and RF spectroscopy. (a) Theoretical calculations for the binding energy for a $|1\rangle - |2\rangle$ mixture versus field. E_b^{3D} (solid black line) is 0 beyond the Feshbach resonance at 832 G, confinement induced E_b^c (red dashed line), $E_b^{2D(0)}$ (dotted blue line), E_b^{2D} exact (dotted green line). (b) same as (a) but for a $|1\rangle - |3\rangle$ mixture. In addition, measured value of binding energies from RF spectroscopy in 3D (red circles) and in our "quasi" 2D system (blue squares). (c) RF spectroscopy of $|1\rangle - |3\rangle$ bound state to $|1\rangle - |2\rangle$ free state transition at 637 G in a 3D trap. The narrow peak corresponds to unpaired $|3\rangle$ singles while the broad feature corresponds to the bound to free transition. A fit (blue line) to the spectra gives the binding energy of $h\times 135$ kHz. (d) RF spectroscopy of the same system but in a "quasi" 2D trap. The binding energy from fit is $h\times 168$ kHz.

Now using the expression for the laplacian in polar coordinates $\nabla^2 = 1/r\partial/\partial r(r\partial/\partial r)$, one can verify that the above condition is satisfied when $\psi \sim e^{ikr}/\sqrt{r}$. Similar to the 3D case, one can derive the expression for f(k) in terms of a phase shift δ in the s-wave channel

$$f(k) = -\frac{4}{\cot \delta - i} \tag{4.20}$$

For low energy elastic scattering, one can compute the phase shift to get [108]

$$\cot \delta = -\frac{2}{\pi} \log \left(\frac{1}{k a_{2D}} \right) + \mathcal{O}(k^2) \tag{4.21}$$

where, a_{2D} is the s-wave scattering length in 2D. This leads to the expression for the scattering amplitude in a 2D system

$$f(k) = -\frac{4\pi}{2\log(ka_{2D}) - i\pi} \tag{4.22}$$

In this case, the scattering amplitude is maximum when $ka_{2D} \rightarrow 1$, different from the 3D case. Also different from the 3D case, in 2D, the scattering length is a more complex quantity to define and compute. First of all, a realistic 2D system can be thought of an asymmetric 3D system with an additional length scale $l_z = \sqrt{\hbar/m\omega_z}$ that is given by the axial confinement ω_z . Consider now the bound state of two fermions in such a confined system. Far in the BCS limit, the bond length is large compared to l_z and the dimers are essentially confined in plane. But far on the BEC side, tightly bound dimers form where the bond length could be much smaller than l_z . In that limit, the dimers experience no confinement and behave as if in 3D. So one would expect the dimer binding energy far in the BEC limit to converge to E_b^{3D} . In addition, confinement leads to the existence of a weakly bound dimer state even above the Feshbach resonance [109]. The scattering amplitude obtained for the case when the temperature k_BT and E_F are comparable to or smaller than $\hbar\omega_z$ is given by [110]

$$f(r) = \frac{4\pi}{\sqrt{2\pi} \frac{l_z}{a_z} + w(k^2 l_z^2/2)}$$
(4.23)

where, the quantity w(x) is given by

$$w(x) = \lim_{J \to \infty} \left(\sqrt{\frac{4J}{\pi}} \log \left(\frac{J}{e^2} \right) - \sum_{j=0}^{J} \frac{(2j-1)!!}{(2j)!!} \log(j-x-i0) \right)$$
(4.24)

For $x \ll 1$, we get $w(x) = \Delta w(x) - \log(2\pi x/0.905) + i\pi$. If, in addition l_z is sufficiently small, $\Delta w(x) \to 0$ and we are left with

$$a_{2D}^{(0)} = l_z \sqrt{\frac{\pi}{0.905}} \exp\left(-\sqrt{\frac{\pi}{2}} \frac{l_z}{a_s}\right)$$
 (4.25)

And similarly we can define the 2D binding energy in this limit as

$$E_b^{2D(0)} = \frac{\hbar^2}{2ma_{2D}^{(0)}} \tag{4.26}$$

Outside of this limit, one needs to calculate the correction $\Delta w(x)$ and obtain the full 2D expression for the scattering length

$$a_{2D} = l_z \sqrt{\frac{\pi}{0.905}} \exp\left(-\sqrt{\frac{\pi}{2}} \frac{l_z}{a_s}\right) \exp\left(-\frac{1}{2} \Delta w \left(\frac{k^2 l_z^2}{2}\right)\right)$$
(4.27)

And accordingly obtain the full 2D binding energy E_b^{2D} [111]. To calculate its value for all other values of kl_z , we need to solve for the limit of w(x). Numerically,

the calculation can be sped up if the double factorial is calculated iteratively for every j as $J \to \infty$. We generated a look-up table of all integers up to 1,000,000 and the corresponding $\ln(n!!)$. We found J=500,000 to be sufficiently large such that the numerical sum converges. The other important factor is approaching 0 from above in the logarithm. For practical purposes, it seems like 0.01i was sufficient to get convergence, but to be sure a value of 0.001i was used. We calculate w or Δw , which is independent of a_{3D} and find that for experimentally reasonable values of kl_z , we might need to correct $a_{2D}^{(0)}$ by a factor of about 0.6-0.7.

Note that $\ln(ka_{2D})$ only weakly depends on k. This can be understood as the dependence being logarithmic instead of algebraic. The effect of the correction on binding energy can be very significant on both sides of resonance. Only far on the BEC side, where the inter-molecular spacing is negligible compared to l_z does $E_B \to E_B^{(0)}$. Thus for calculating interaction parameter, we should use a_{2D} while for the binding energy, it is better to use $E_B^{(0)}$, as verified by our measurement using RF spectroscopy (Fig. 4.1). Finally, the confinement induced bound state energy E_b^c can be obtained by solving the transcendental equation

$$\frac{l_z}{a_s} = \int_0^\infty \frac{du}{\sqrt{4\pi u^3}} \left(1 - \frac{e^{E_b^c u/\hbar\omega_z}}{\sqrt{(1 - e^{-2u})/2u}} \right)$$
(4.28)

2D Fermi gases were first reported by [17] by loading a 3D gas to a 1D lattice with a large lattice spacing. The criteria for such a system to satisfy 2D kinematics is that the axial states are weakly populated [112]. RF spectroscopy on 2D Fermi gases was performed in [18] and [26]. A dimensional crossover from 3D to 2D Fermi gases was studied in [19] for weakly interacting Fermi gases and in [20] for strongly interacting Fermi gases. In our experiments, $l_z = 270$ nm. The different binding energies in 2D and 3D are plotted in Fig. 4.1 for the $|1\rangle - |2\rangle$ mixture (a) and for the $|1\rangle - |3\rangle$ mixture (b). In order to measure the binding energy, we perform RF spectroscopy in the trap. We prepare a $|1\rangle - |3\rangle$ mixture at a given field and apply RF pulses to transfer atoms from $|3\rangle$ to state $|2\rangle$ and finally we image the population in $|2\rangle$. The first peak is the transition of $|3\rangle$ singles to $|2\rangle$. But the paired atoms require not only the energy difference between the states but also the binding energy to transition to a $|2\rangle - |3\rangle$ free state. We perform this spectroscopy in the light sheet potential for 3D and in our final trap for 2D. We notice that in general, the higher axial confinement leads to a higher binding energy of pairs.

4.3 BEC-BCS crossover in 3D and 2D

In 3D, molecular dimers formed at scattering lengths $a_s > 0$ are real space dimers with decreasing pair size as one moves away from resonance. At resonance, a_s diverges and the atoms enter a unitary regime. In this regime, the phase shift due to scattering becomes $\pi/2$, the largest value it can have and the scattering amplitude becomes $f(r) \approx i/k$. In this regime, thermodynamic properties of the system become universal. On the other side where $a_s < 0$, no bound states exist in 3D (but they are possible in 2D). Due to the weak but attractive interaction, there is Cooper instability in the system. This means that fermions with opposite spin and momenta on the Fermi surface can pair up to form a Cooper pair that can further lead to superfluidity [2]. There is no sharp phase transition between the BEC and BCS regimes. They are smoothly connected by a crossover.

Experiments in 3D demostrated superfluidity by creating vortices [11]. In a different experiment, RF spectroscopy was performed on the pairs across the crossover [9]. In the BEC limit, the measured energy difference in spectroscopy matches the two-particle binding energy calculations. But as one crosses over to the BCS side, the difference between the two increases indicating many-body effects. Other experiments include measuring the decay rate of atoms from the trap as a function of $1/k_F a_s$ [10] and measuring the release of energy across the crossover [113]. The 3D equation of state was measured in [13] and [33].

More recently experiments were performed in a "quasi" 2D system [114] where the equation of state was measured. The boundary between the BCS and BEC regimes in 2D is given by $k_F a_s = 1$, so it is different from the unitary regime in 3D. Calculations for superfluidity and weakly bound dimers in a "quasi" 2D geometry were done in [115, 116]. The pairing pseudogap in a 2D Fermi gas was measured through momentum resolved photoemission spectroscopy in the strong coupling regime ($\log(k_F a_s)=0$) [24].

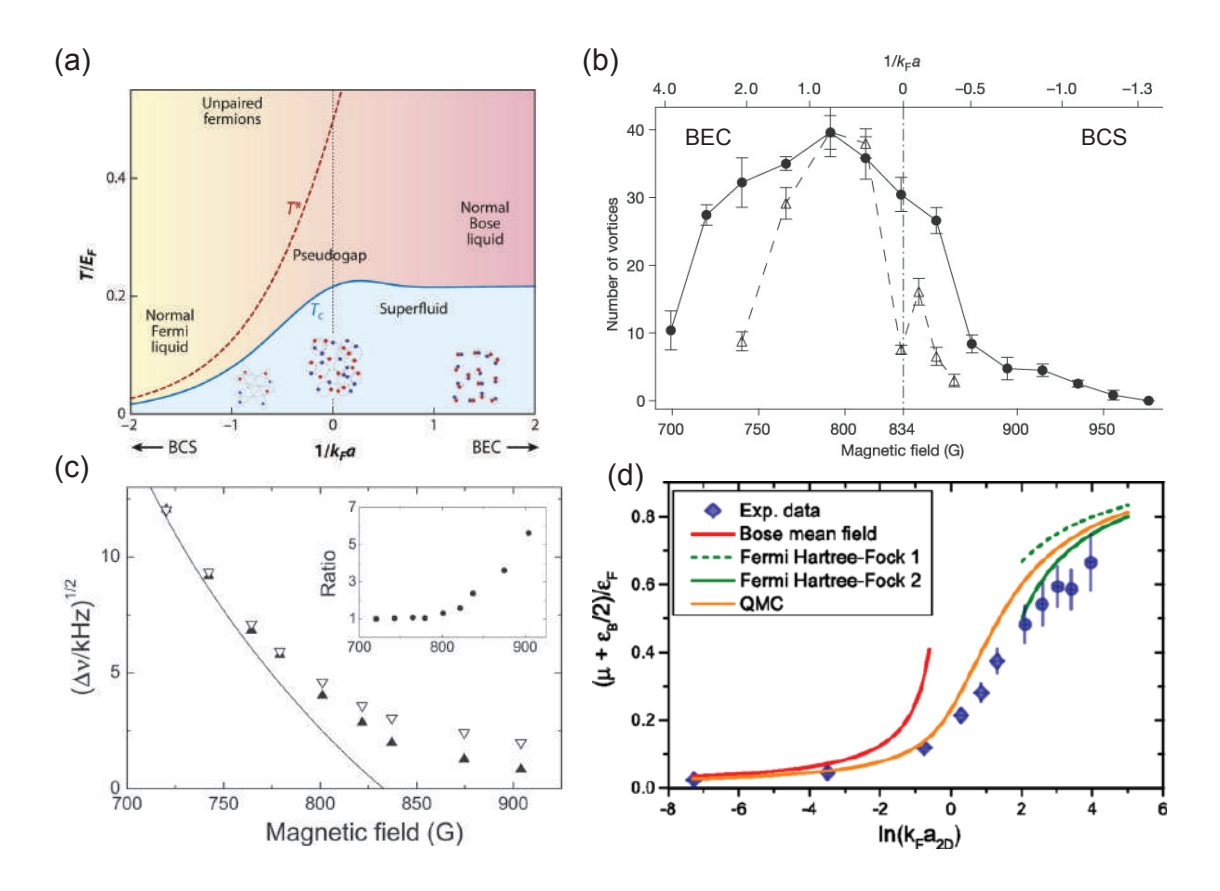


Figure 4.2: BEC-BCS crossover. (a) Schematic of the crossover in 3D taken from [117]. The onset of pairing temperature T^* and the critical temperature for superfluidity T_c as a function of $1/k_F a_s$. Unitarity is given by the condition $k_F a_s \to \infty$. On the BEC side, the real space pairs bose condense while on the BCS side Cooper pairs of fermions condense. (b) Vortex number versus magnetic field through the crossover taken from [11]. Vortices are a signature of superfluidity. (c) Measurement of the pairing gap as a function of field taken from [118]. In the BCS regime, the deviation from the binding energy of pairs is related to the superfluid pairing gap. (d) Low temperature equation of state across a 2D BEC-BCS crossover taken from [114].

4.4 Superfluidity in 2D

Unlike in 3D, lower dimensional Fermi gases can not have long range order due to the Mermin-Wagner theorem [119]. According to the theorem, phase fluctuations at long wavelengths play a dominant role at finite temperatures preventing long range order to establish in the system. As a consequence, a true BEC can not exist in a 2D at $T \neq 0$ [120, 121]. But quasi-condensation can still occur where no true long range order exists but the system is superfluid nevertheless.

The superfluid transition in 2D is known as a Berezinskii-Kosterlitz-Thouless (BKT) transition [122, 123, 124, 125]. The BKT transition is associated with the pairing of vortices with opposite circulation. A key signature of this transition is the algebraic decay of the order parameter below T_c as opposed to the usual exponential decay above. In addition, the theory predicts a finite jump in the superfluid density at T_c . Many of its key features have been detected in experiments with 2D Bose gases [126]. Recently, experiments in 2D Fermi gases [21] have seen evidence of BKT transitions.

Another intriguing aspect of spin imbalanced Fermi systems is the mechanism of fermion pairing. We know that the usual BCS mechanism requires two fermions with opposite spins and Fermi wave-vectors interacting via an infinitesimally attractive interaction. These Cooper pairs have zero center-of-mass momentum. But when the population is imbalanced, not all fermions can find a pairing partner. One mechanism that was suggested to explain pairing for imbalanced Fermi seas is the Fulde-Ferrell-Larkin-Ovchinnikov pairing mechanism [127, 128]. In such a pairing scheme, two fermions of opposite spin but finite center-of-mass momenta can pair. In addition, by looking at Fermi surface nesting, it was concluded that this pairing mechanism is expected to be enhanced in lower dimension [129]. The crossover from 3D to 1D and the enhancement of FFLO was theoretically studied in [103] and the finite temperature 3D phase diagram was calculated in [130]. The effect of harmonic trapping including the shell structure with phase boundaries on the FFLO state in lower dimensions was studied in [104]. The effect of strong interactions across the BEC-BCS crossover in 2D on the FFLO phase was also extensively studied [131, 132, 133]. Finally the effect of quantum fluctuations on the mean field phase diagram in 2D, including the effect of the FFLO instability on the BKT transition has been studied [134, 135].

4.5 Spin Imbalance: Phase separation and superfluidity

Pairing in both BEC and BCS regimes relies on fermions of two different spin states. In the BEC limit, the two spin fermions form real space dimers that can Bose condense while in the BCS limit, the fermions of opposite spin state and momenta on the Fermi sea can form momentum space pairs. These mechanisms work if there are an equal number of fermions in either spin state. But if there is an excess of one spin state compared to the other, there will be some unpaired fermions left behind. The first question that was posed is whether a system with spin imbalance can support superfluidity [29]. Pair condensation was observed as a sudden deformation in the cloud shape near the trap center [136]. The unpaired spin polarized fermions compete with the condensate and can lead to phase separation. Such a separation of phases was first observed in 3D fermi gases [30]. In this case, the paired atoms tend to occupy the trap center while the unpaired atoms occupy the edge of the trap. The crossover from BEC to BCS in 3D with spin imbalance was further studied in [137]. Spin imbalance in 3D has also been studied theoretically quite extensively [138, 139, 140, 141].

An interesting aspect that ultracold atoms bring to the table is that most gases are trapped in a harmonic potential, i.e. are not homogenous. This added complexity allows for different phases to exist in different parts of the trap. When the fermion populations in the two spin states are the same, then the position of the trap only determines the local Fermi energy. But in the presence of imbalance, the variable chemical potential in the trap can lead to a shell structure where the trap center is superfluid and the edge is in the normal phase [142]. This was studied in depth [143] in the context of trapped 3D Fermi gas experiments performed in [29] and [10]. One other aspect of measurement of spin imbalance is to study the limit of superfluidity in the system. It was observed that small amounts of population imbalance, equivalent to an external magnetic field in traditional condensed matter experiments, do not destroy superconductivity. But as the imbalance is increased, at some point superfluidity is suppressed. This limit is known as the Chandrasekhar-Clogston limit [144]. This limit of a critical polarization was studied for 3D systems both experimentally and theoretically [145].

Similar experiment were performed in near 1D chains [32]. Phase separation in 1D is expected to be inverted, i.e. the condensed phase prefers to occupy the trap edge while the unpaired phase prefers the trap center.

Our first experiment was motivated by the limited understanding of pairing and superfluidity in spin-imbalanced "quasi" 2D systems. We observed the separation of phases in the trap across the BEC-BCS crossover and measured it as a function of population imbalance in the system. To establish pairing, we performed time-of-flight expansion of the cloud on the BEC side and observed bimodality. We were able to represent our data as a phase diagram. The paper can found in [35] and the following sections describe the different aspects of the experiment in detail.

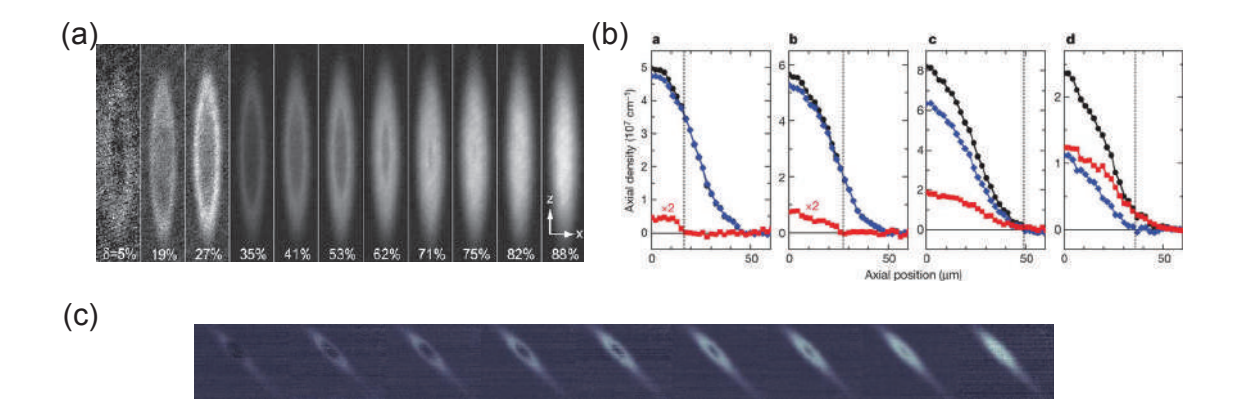


Figure 4.3: Phase separation in 3D and 1D. (a) Phase separation observed in a 3D gas at unitarity taken from [30]. Images are phase contrast that gives the difference density between the two states. (b) Phase separation in 1D chains taken from [32]. The reconstructed radial profiles show that the density difference between the two species tend to decrease to zero near the trap edge while they are higher near the trap center effectively inverting the 3D profile. (c) Phase separation in 3D observed in our experiment for lithium atoms trapped in the lightsheet. The population imbalance ranges from < 10% for the leftmost frame to roughly 90% for the rightmost frame.

4.5.1 Creating 2D spin-imbalanced clouds

We start our experiment in the optical dipole trap discussed previously. After optically pumping the atoms to the lowest two hyperfine states $|1\rangle$ and $|2\rangle$, we produce a balanced mixture of these states using ten consecutive diabatic Landau-Zener sweeps at 537 G, with a sweep rate chosen to approximately transfer 50% of the atoms from one state to the other (see Fig. 3.3). We then imbalance the mixture by transferring a fraction of the atoms from state $|2\rangle$ into a third hyperfine state $|3\rangle$ using another diabatic Landau-Zener sweep. We subsequently remove the atoms in state $|3\rangle$ with a resonant pulse. We control the amount of imbalance using the sweep rate. By varying the duration of the RF sweep, we were able to continuously vary the global polarization of the cloud $P = (N_{\uparrow} - N_{\downarrow})/(N_{\uparrow} + N_{\downarrow})$, where $\uparrow = |1\rangle$ and $\downarrow = |2\rangle$ (Fig. 4.5).

The imbalanced mixture is then evaporatively cooled at 800 G close to degeneracy. We load the atoms into the lightsheet trap to compress the atoms axially in preparation for loading them into a single well of the accordion lattice. To independently control the radial confinement, we ramp up the bottom beam. The spacing of the different layers of the accordion can be changed by controlling the angle at which the lattice beams intersect, allowing us to load a single layer reproducibly at large spacing (12 μ m) and then adiabatically reduce the lattice spacing to 3.5 μ m to reach a "quasi"-2D geometry (Fig. 4.4). At this stage, we turn off the light sheet confinement and all of the axial confinement is provided by the accordion lattice.

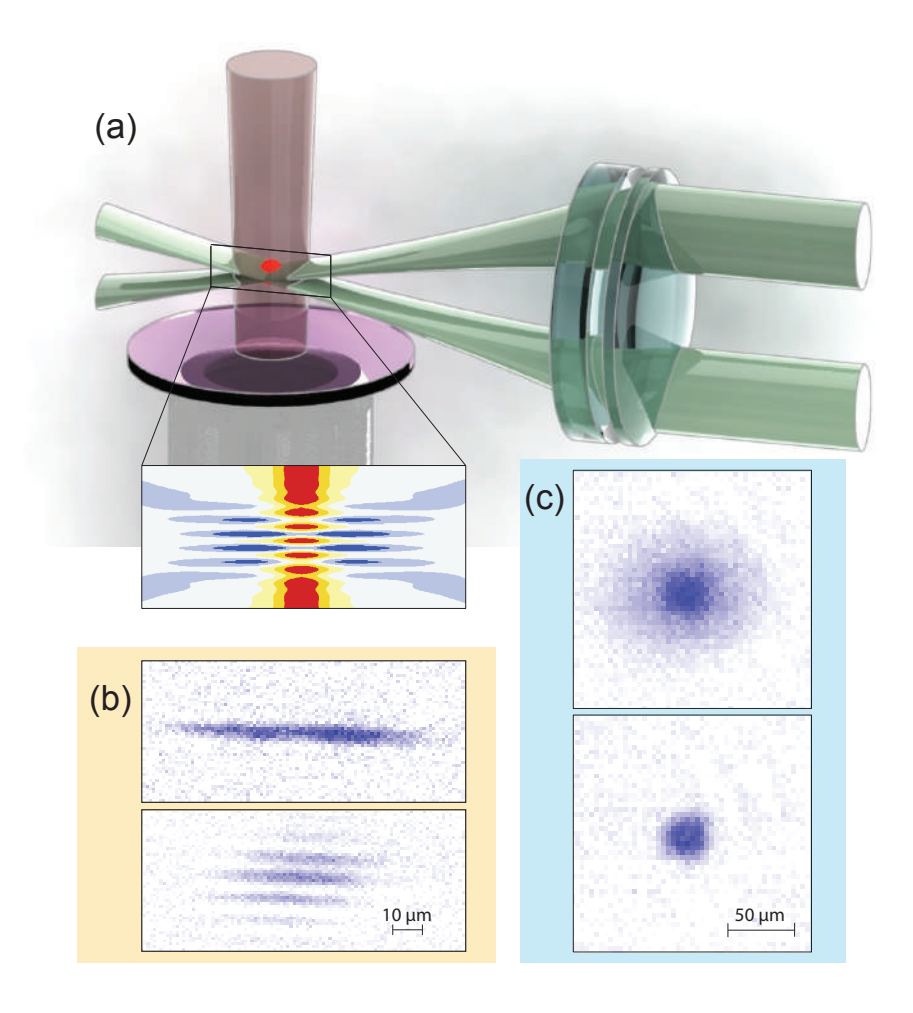


Figure 4.4: Experimental setup. (a) A 1D optical lattice is formed at the intersection of two interfering blue-detuned beams (green), providing axial confinement. The lattice spacing can be dynamically tuned by changing the angle between the beams. The atoms are radially confined by a red-detuned beam (brown) in the vertical direction. A high-NA objective (grey) is used to image the in-plane density distribution. The inset shows a section of the optical potential with color scale from red (attractive) to blue (repulsive). (b) Side absorption images illustrating our capability to load and resolve single (above) and multiple pancakes (below) after adiabatically increasing the lattice spacing to $\sim 12~\mu m$. (c) In-situ absorption images of majority (above) and minority (below) clouds along the vertical direction at 755 G and polarization P=0.6.

B(G)	$a_{2D}(\mu\mathrm{m})$	$E_b^c(\mathrm{kHz})$	$\mu_{0\uparrow}(\mathrm{kHz})$	$k_F(\mu m^{-1})$	$\ln(k_F a_{2D})$	T (nK)
730	0.0261	104.37	11.68	3.73	-2.33	179.31
755	0.0598	51.56	12.39	3.84	-1.47	157.90
780	0.1215	24.80	11.66	3.73	-0.79	137.69
830	0.3090	5.84	12.59	3.87	0.18	145.41
920	0.8994	0.83	12.27	3.82	1.23	111.75

Table 4.1: Calculated and measured parameters for the experiment. The 2D scattering length a_{2D} is obtained from Eq. 4.27. The confinement induced binding energy E_b^c is calculated by solving Eq. 4.28. The majority chemical potential $\mu_{0\uparrow}$ is obtained from Fermi-Dirac fits to the tail of the majority radial profile in Eq. 4.32.

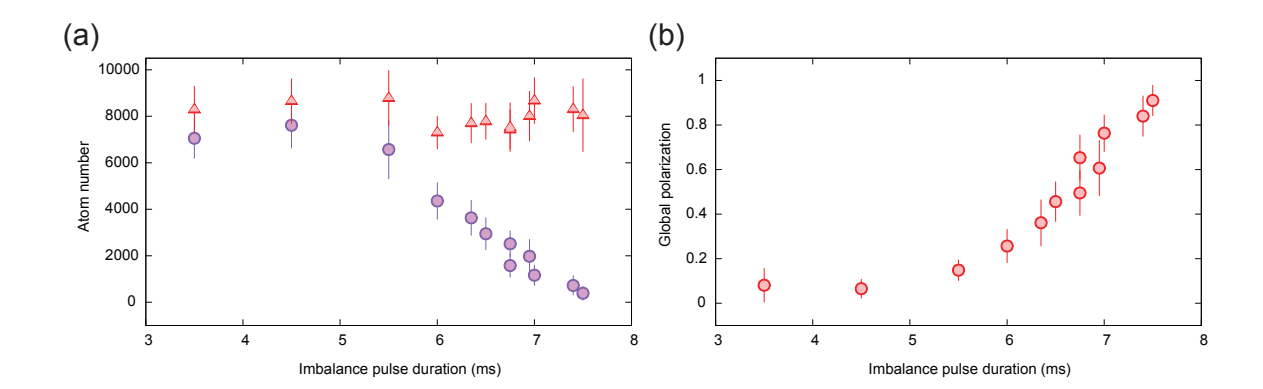


Figure 4.5: Calibrating the pulse length for imbalancing. (a) The number of atoms in the majority state ($\uparrow = |1\rangle$, red triangles) and the minority state ($\downarrow = |2\rangle$, purple circles) as a function of the duration of the imbalance pulse. Imbalancing is performed at a field of 776 G for all final fields. Error bars are s.e.m. of 30 experimental shots. (b) Global polarisation $P = (N_{\uparrow} - N_{\downarrow})/(N_{\uparrow} + N_{\downarrow})$ obtained from the data in (a). Note that we span the range from spin balanced to fully polarized by scanning a single parameter. This particular calibration was used to obtain the data at a final field of 755 G.

Finally, we perform a second evaporation in the combined 2D trap by ramping down the radial confinement to its final value in 200 ms. The trapping frequencies of our combined trap are $\omega_x = (2\pi)$ 95 Hz, $\omega_y = (2\pi)$ 125 Hz and $\omega_z = (2\pi)$ 22.5 kHz. The final number of atoms in state $|1\rangle$ is held constant while the number in state $|2\rangle$ is varied. The magnetic field is then ramped to its final value in 50 ms to set the interactions in the 2D gas.

To ensure that the gas is in the "quasi"-2D regime the chemical potential of the majority atoms, $\mu_{0\uparrow}$, is kept below the axial vibrational level spacing $\hbar\omega_z$. This condition is satisfied by keeping the majority atom number fixed to $\sim 9\times10^3$, resulting in $\mu_{0\uparrow}/\hbar\omega_z < 0.7$ over the full parameter regime. Our ability to load a single layer is confirmed by taking an absorption image of the cloud on-edge through an auxiliary

imaging system (Fig. 4.6). We perform an adiabatic ramp of the accordion lattice spacing back up to $12 \mu m$ and image to see the occupation in fully resolved layers.

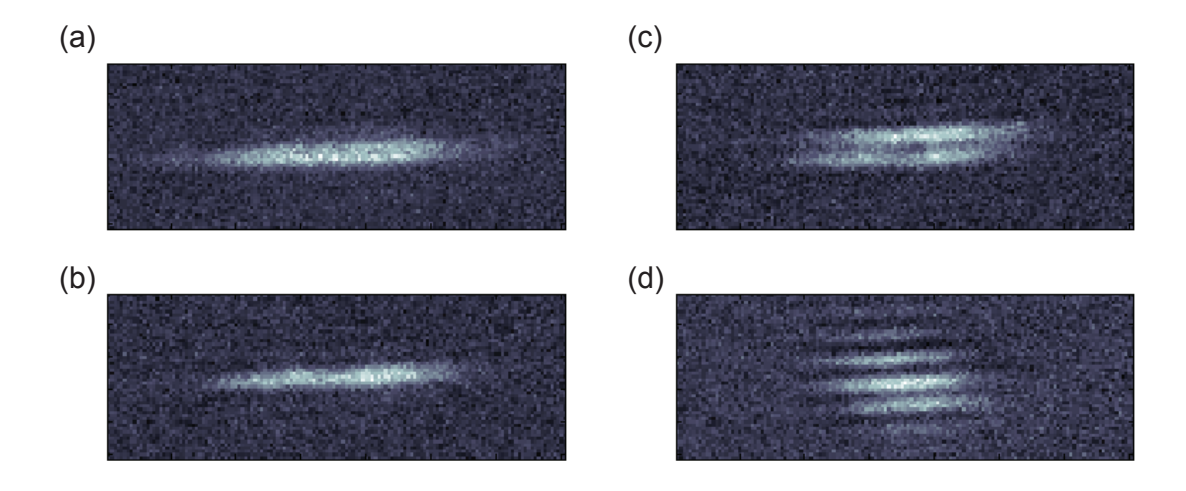


Figure 4.6: Absorption images of the majority density in the accordion lattice taken along the auxilliary imaging axis after the accordion lattice spacing has been adiabatically ramped up to the maximum of 12 μ m, greater than the imaging resolution of the system. (a) An example of when a single layer of the accordion is occupied at a field of 780 G. When uncompressed, they still appear as a single layer. (b) The same but taken at 830 G. (c) A scenario when two layers of the accordion were loaded. (d) A scenario when multiple layers were loaded. We could also intentionally misalign the accordion to deterministically load a certain number of layers.

The experiment was performed for 5 magnetic fields 730 G, 755 G, 780 G, 830 G and 920 G spanning the BEC-BCS crossover in 2D. 830 G also marks the 3D Feshbach resonance of a $|1\rangle - |2\rangle$ mixture. We expect the strongly interacting regime in 2D to lie somewhere between 780 G and 830 G. The details of the calculated and measured experimental parameters is given in Table 4.1.

4.5.2 Imaging

At a given interaction and for each polarization, we study the in-situ density distribution as well as the momentum distribution after a time of flight of 3 ms of releasing the gas from all optical potentials simultaneously. Since we are interested in observing if the majority density in the trap center equals that of the minority, we would ideally want to image the two states simultaneously. But imaging them together will make it impossible to discern absorption due to each spin state separately. The other option is to image one spin state and repeat the experiment to measure the other spin state. The problem with the latter is that atom number fluctuations can only be accounted for after repeating the experiment many times and requires twice the amount of data collection. So the most efficient solution was to image both states in the same experimental run, but separated by a short time.

In order to perform double imaging, we used a camera (Andor Neo 5.5 sCMOS) that has a special feature called the overlap mode with global shutter where the exposure for a frame begins while the previous frame is being read out (Fig. 4.7(a)). The camera runs at a readout rate of 200 MHz which means that the exposure time is set to 55.3 ms. We set the number of frames to 7 in the external exposure mode which means that the camera waits for seven external triggers each cycle. The first trigger starts exposure and the frame starts reading out half way through the exposure time. The first frame is discarded. The second trigger starts exposure for frame 2 and the imaging light resonant to state $|1\rangle$ is pulsed on for 10 μ s at the end of the exposure. At this time, a pulse is sent to the second switch (Minicircuits ZYSWA-2-50DR) which has a short switching time of 20 ns and changes to the second VCO that is running at the resonance for state $|2\rangle$. Thanks to the cat's-eye setup for the high field imaging beams (Fig. 2.11), this change in frequency of ~ 80 MHz of the AOM does not change the beam intensity and position. Finally the RF signal is sent through a voltage variable attenuator (Minicircuits ZX73-2500M-S+) and the main I/O switch 1 to the amplifier. After only 6.4 μ s from the end of the first imaging pulse, a second imaging pulse hits the atoms. The very short time between the two pulses ensures that no significant heating or displacement of the cloud occurs. The second frame gets read out while the third one is exposed. Next, all traps are turned off and after waiting for 1 s to allow for the atoms to completely escape, the same cycle is repeated to obtain beam images for the two beams separately. Finally a seventh trigger in the absence of the imaging light gives the frame with dark counts.

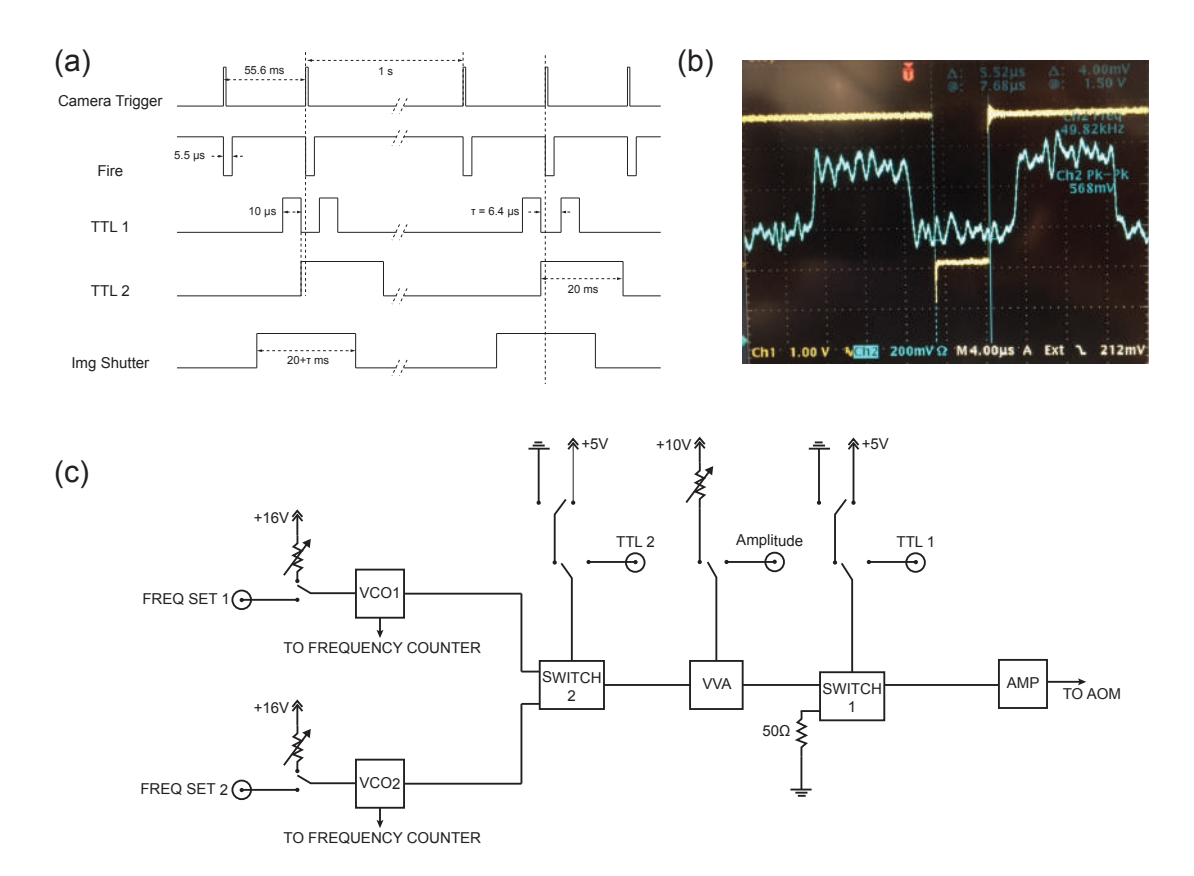


Figure 4.7: Double absorption imaging scheme. (a) Pulse sequence to achieve double imaging. The camera (Andor Neo 5.5 sCMOS) is triggered by the computer. The camera is running in overlap mode. Every time this trigger changes state, it causes the camera to start firing at a predetermined rate (exposure time) for a certain number of images (7). The first and fourth images are discarded. TTL 1 turns on the general imaging light and the first pulse is resonant to state $|2\rangle$. The next pulse is delayed by 6.4 μ s during which switch 2 changes state and the output becomes resonant to state $|1\rangle$. Also exposure for the previous frame ends and its readout begins while simultaneously exposure for the next frame begins. After these three images are taken and after an arbitrary long time (1 s), the same process is repeated without atoms to get the beam images for absorption imaging. Finally a seventh image without any light is taken to obtain the dark counts. (b) Synchronisation of the Fire output of the camera (yellow) with the actual imaging pulses (blue) measured on a fast photodiode. (c) Modified AOM driver designed to operate with two fast switches to choose between two different frequency VCOs.

We noticed that if $|1\rangle$ was measured first, there was an effect of optically pumping some atoms to $|2\rangle$ leading to a systematically 10-15% higher number in the second image. To avoid that we switched the order and imaged $|2\rangle$ first. After that, imaging of the first state had a systematic effect of $\sim 5\%$ lower atom number of the second state, well within the experimental fluctuations, hence it was not accounted for. To calibrate the optical depth of the gas to the absolute density, we use the known density of a band insulator in our optical lattice with 752 nm spacing. Examples of in-situ and time-of-flight cloud images can be found in Fig. 4.8.

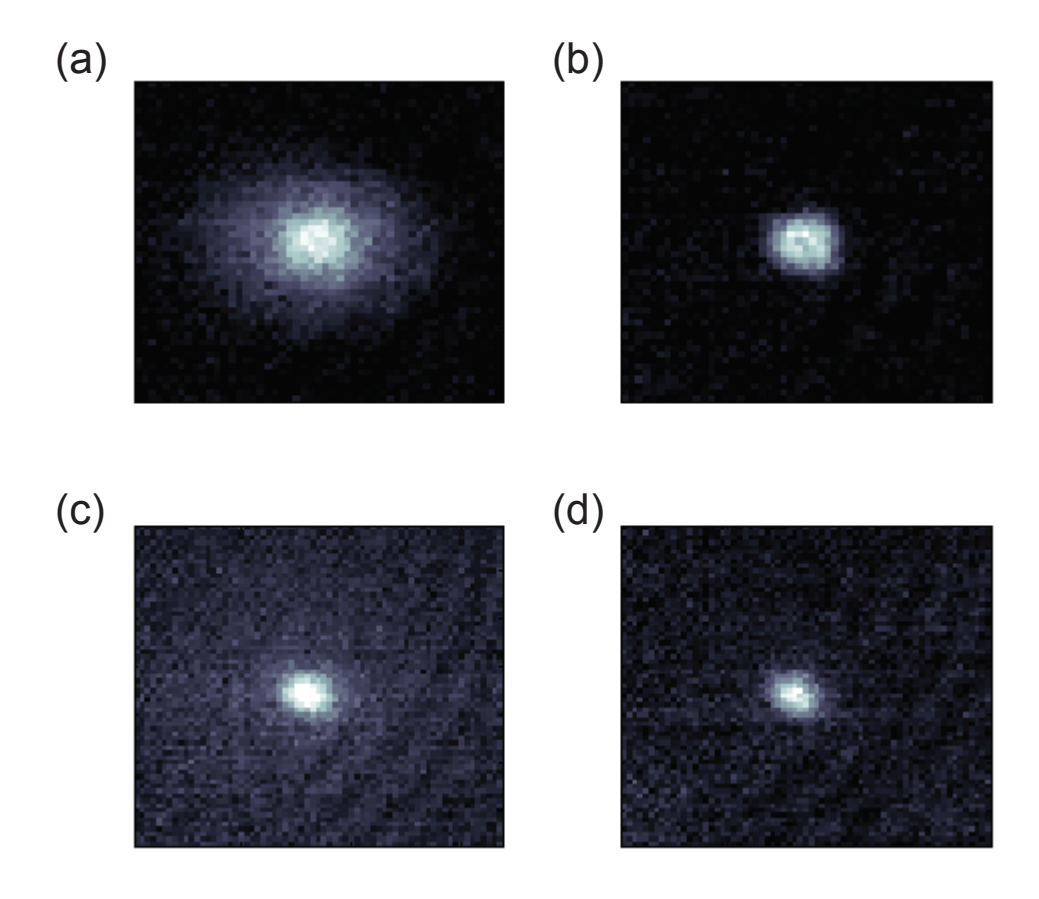


Figure 4.8: Example of an average of ~ 30 images for both in-situ and time of flight data at 60% polarization and at a field of 755G. The top two figures are the majority (a) and minority (b) in-situ profiles scaled to emphasize on the bimodality in the in-situ profile due to phase separation. The bottom two figures show the TOF data after 3 ms. The majority (c) on the left shows a clear thermal cloud which is difficult to discern for the minority (d).

4.5.3 Measuring temperature

Measuring the temperature of a Fermi gas is challenging if there are interactions. In the absence of interactions and at zero temperature, linear density in a trap after integrating over one direction is given by the Thomas-Fermi distribution for $r < R_{TF}$ [146]

$$n(r) = \frac{8N}{3\pi R_{TF}} \left(1 - \frac{r^2}{R_{TF}^2} \right)^{3/2} \tag{4.29}$$

where, $R_{TF} = \sqrt{2E_F/m\omega_r^2}$ is the Thomas-Fermi radius. Above R_{TF} , n=0. Now at finite temperatures, if the gas is nearly an ideal Fermi gas, then the density profile can be written as

$$n(r) = -\sqrt{\frac{m\omega_r}{2\pi\hbar}} \left(\frac{k_B T}{\hbar\omega_r}\right)^{3/2} \operatorname{Li}_{3/2} \left(-e^{\beta\left(\mu - \frac{m\omega_r^2 r^2}{2}\right)}\right)$$
(4.30)

where, $\text{Li}_3/2$ is the polylog function of order 3/2. Finally for an interacting Fermi gas at finite temperature, one can use a virial expansion of the phase space density [147, 114, 148, 149].

$$n(r)\lambda_{dB}^{2} = \log(1 + e^{\beta(\mu - V(r))}) + 2b_{2}e^{2\beta(\mu - V(r))} + 3b_{3}e^{3\beta(\mu - V(r))} + \dots$$
 (4.31)

where, λ_{dB} is the thermal de-Broglie wavelength $\sqrt{2\pi\hbar^2\beta/m}$ and b_i 's are the virial coefficients. If we focus on the tail of the distribution where the density of fermions is small and the interactions negligible, then the higher orders can be neglected and one finds

$$n(r) = \frac{m}{2\pi\hbar^2 \beta} \log \left(1 + e^{\beta \left(\mu - \frac{m\omega_r^2 r^2}{2}\right)} \right)$$
 (4.32)

If the cloud is non interacting by virtue of being spin polarized, then one can perform a fit on the local density n(r) starting at the tail of the distribution to obtain the two unknown quantities, β and μ . In our experiment, we vary the polarization of the cloud from balanced (P=0) to almost fully polarized $(P\to 1)$. We take the majority density for the cases with high polarization and perform the above mentioned fit to only the tail (Fig. 4.9(a)). We notice that a Fermi-Dirac fit to the tail when extrapolated to the entire cloud, deviates significantly from the actual density. This is the reason why a balanced cloud can not be used to measure temperature unless the virial coefficients $(b_i$'s) have been taken into account.

A Fermi-Dirac fit to the tail of the radial majority density profile yields $T/T_F = k_B T/\mu_{0\uparrow} = 0.18(5)$ independent of polarization, and only weakly dependent on the Feshbach field (Fig. 4.9(b) and (c)). An alternate definition of a temperature scale is employed in [148]. Instead of using the non-interacting tail of the atomic density, it employs the central density of the majority atoms in the trap (n_0) and is defined as

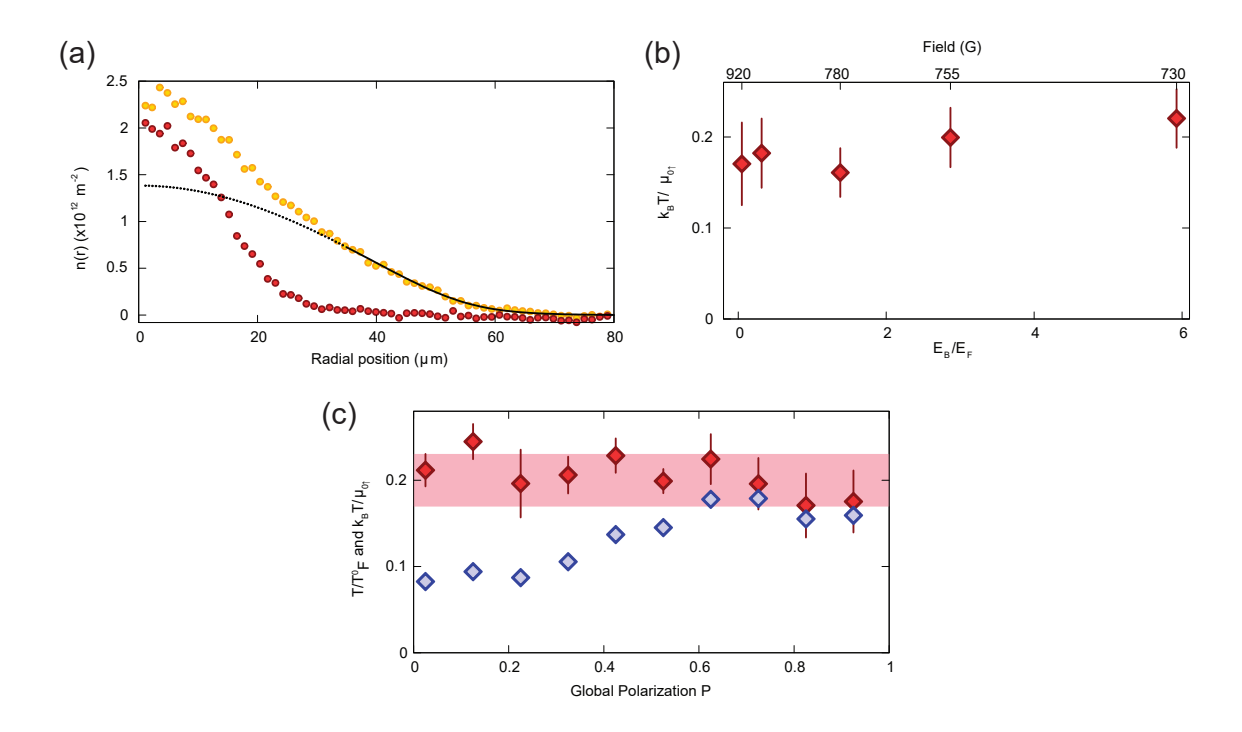


Figure 4.9: Obtaining temperature from tail fit to cloud. (a) Fermi-Dirac fit to the fully-polarized tail of a majority profile to obtain temperature. Data depicted for P=0.48 at 780 G. The majority density $n_{\uparrow}(r)$ is shown in yellow and the minority density $n_{\downarrow}(r)$ in red. The black solid line is the fit to the majority density using the expression in Eq. (4.32) beyond the Thomas-Fermi radius of the minority cloud. The black dotted line is the fit extrapolated to the trap center. (b) Interaction dependence of $k_B T/\mu_{0\uparrow}$. The temperature (T) and the majority chemical potential $(\mu_{0\uparrow})$ are obtained from a Fermi-Dirac fit to the fully-polarized region of the cloud. (c) Polarization dependence of $k_B T/\mu_{0\uparrow}$ (red diamonds) and T/T_F^0 (blue diamonds) for the 755 G dataset. $k_B T/\mu_{0\uparrow}$ stays essentially constant over the whole polarization range while T/T_F^0 drops towards the balanced regime due to increased density in the center of the cloud.

 $T_F^0 = \frac{2\pi n_0 \hbar^2}{mk_B}$. This definition of the Fermi temperature is not well defined for a spin imbalanced system as the central density of the majority cloud changes with global polarization. Hence our definition of T_F deviates from this definition via the central density. For our balanced data on the BEC side, we get $T/T_F^0 = 0.10(3)$.

4.5.4 Measuring condenstate fraction

In addition to measuring the in-trap real space density profile, we can also access the momentum space profile by imaging after a time-of-flight. We measure momentum space profiles by releasing the cloud from the trap and allowing a time of flight of 3 ms during which the cloud expands only in the magnetic field confinement. Due to the tight confinement in the axial direction, the cloud expands fast along that axis and the interactions are effectively quenched. We verified that after 3 ms of time of flight, the cloud expands to ~ 3.5 times its in-trap size in the radial plane (Fig. 4.10(a)), ensuring access to a reliable momentum space distribution. We were limited in the expansion time by magnetic gradients and the rapid ballistic expansion of the cloud in the vertical direction due to the strong confinement. However, this expansion along the axial direction of the 2D gas leads to a rapid reduction of the density during time of flight, and the pair center of mass momentum distribution is not significantly affected by scattering events. For the data at 730 G, 755 G and 780 G, we see clear signatures of bimodality in the minority density after time of flight. We quantify this bimodality by fitting the azimuthal average of the minority density after time of flight to a sum of two Gaussians. The narrow Gaussian fits the slowly expanding condensate while the broader Gaussian fits the rapidly expanding thermal cloud (Fig. 4.11(d)-(f)). The standard deviation of the two Gaussian modes are shown in Fig. 4.10(a). From the size of the thermal cloud, we extract a kinetic energy per particle of ~ 70 nK. The condensed fraction is the ratio of the number of minority atoms in the condensate to the total minority atom number.

For the fields 730 G, 755 G and 780 G, the 3D binding energy is non zero. This means that any pairs in the system are not broken by the rapid expansion in the axial direction. This is not true, however, for 830 G and 920 G, where the 3D binding energy is nearly zero. As expected, we do not see bimodality at those fields in time of flight. In other experiments like [148], the pairing of atoms is measured after performing a rapid ramp to the BEC side. If the field is changed fast compared to E_F , the momentum space pairs on the BCS side convert to real space pairs that appear as bimodality in time of flight. But in our experiments, we found that ramp time had a non-negligible effect on the measured condensate fraction even for the fastest ramp time of 60 μ s (Fig. 4.10(b)). Thus we decided to avoid any rapid field ramps in our experiment.

The existence of a spin-balanced core strongly suggests the presence of a condensate in that region of the trap. Examples are shown in Fig. 4.11(d)-(f) corresponding to the same parameters as the in-situ images. The paired nature of the condensate is confirmed by the observation that both the optical density and the width of the narrow mode match between majority and minority clouds.

To compare the measured condensate fraction for a balanced gas with ref. [148], we calculate T/T_F^0 as defined in this reference. This yields $T/T_F^0 = 0.10(3)$ for 730-780 G, where T_F^0 has been defined previously. For the calculated values of $\ln(k_F a_{2D}) = -2...-0.5$ for our data we find a condensate fraction of 0.25(5) consistent with ref. [148] for the given temperature.

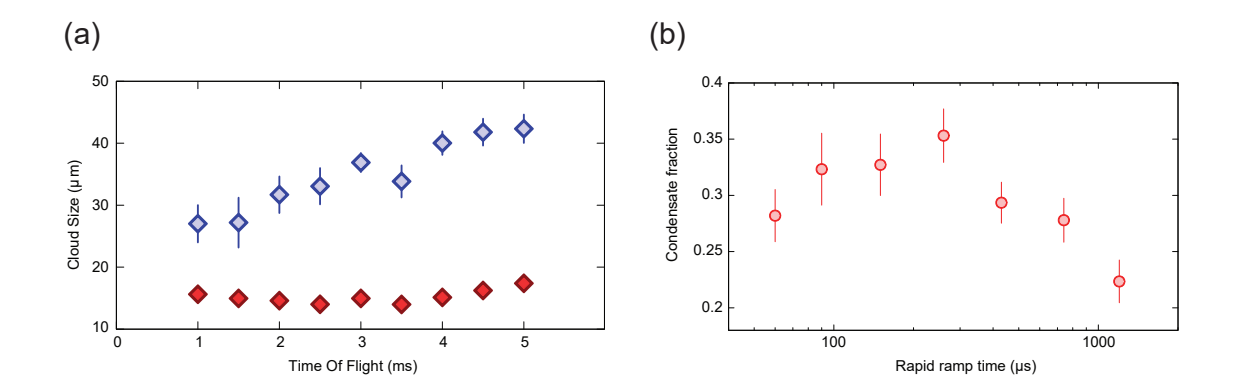


Figure 4.10: (a) Minority cloud size versus time of flight. Data displayed for 780 G and P=0.3. The time of flight data is fit to the sum of two Gaussians. Blue diamonds are the Gaussian width of the thermal part while the red diamonds are the Gaussian width of the condensate. The thermal cloud expands much more rapidly than the central mode during time of flight. (b) Majority condensate fraction obtained after a rapid ramp from 830 G to 760 G for variable ramp times. Condensate fraction is obtained from a double gaussian fit of the time of flight images. The ramp time is varied from 60 μ s to 1.2 ms. Notice that the condensate fraction first increases and then decreases with ramp rate. We do not see a saturation in condensate fraction for our shortest available ramp time.

4.5.5 Fitting in-situ profiles

The in-situ data that we obtain by near simultaneously imaging both spin states shows regions in the cloud where majority and minority densities are equal even at high polarizations. To quantify this region we average each image azimuthally over the elliptical contour lines of the trap. The resulting profiles are fit to the sum of a one-dimensional Gaussian and the Thomas-Fermi profile (Eq. 4.29). The fits give us the atom number in each species. We post-select each in-situ profile to be averaged with other profiles within a range of P=0.05. This leads to 20 global polarization bins, starting at P=0.025 up to P=0.975, each containing 5-15 images. We calculate the optical depth (OD) of the image using

$$OD = -\log\left(\frac{I_{atoms} - I_{dark}}{I_{beam} - I_{dark}}\right) \tag{4.33}$$

where, I_{atoms} is the image of atoms either in state $|2\rangle$ (second frame) or $|1\rangle$ (third frame). I_{beam} is the image of only the beam without atoms and I_{dark} is the image without any imaging light. From the OD, we can directly obtain the local density of each spin component as

$$n_{\uparrow,\downarrow}(r) = \frac{2\pi O D_{\uparrow,\downarrow}(r)}{3\lambda_0^2} \tag{4.34}$$

where, $\lambda_0 = 671$ nm. Using this local density, one can also define the local polarization as

$$p(r) = \frac{n_{\uparrow} - n_{\downarrow}}{n_{\uparrow} + n_{\downarrow}} \tag{4.35}$$

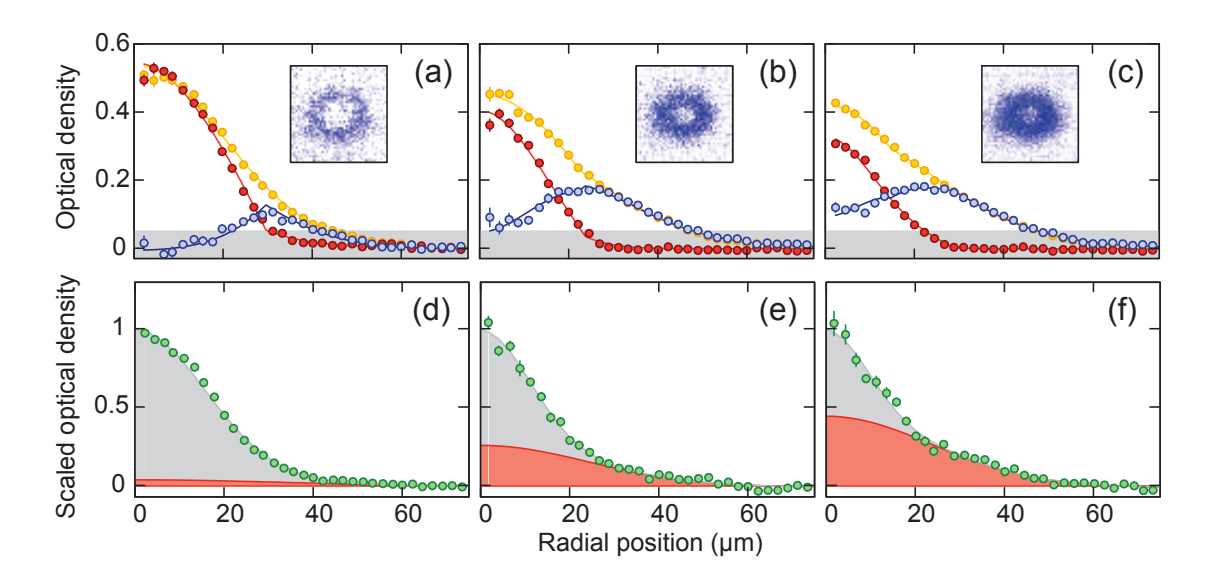


Figure 4.11: Phase separation and condensation versus global polarization. (a)-(c) Azimuthal average of in-situ OD of majority (yellow) and minority (red) clouds, and of their difference (blue) for $P=0.25,\,0.55,\,$ and 0.75 respectively taken at a field of 780 G, with fits to the sum of a Gaussian and a Thomas-Fermi profile. The insets show the corresponding two-dimensional OD difference. The gray shaded region represents the systematic error in the determination of OD differences. The radial position is measured along the minor axis of the elliptical contour lines used for azimuthal averaging. (d)-(f) OD of the minority cloud after 3 ms time of flight normalized to its peak value, with a double Gaussian fit to the data. The thermal component is shaded in red, while the condensate is shaded in gray. Error bars represent the standard deviation of the mean in evaluating the azimuthal average. All distributions represent an average of 30 experimental realizations.

Fig. 4.11(a)-(c) shows in-situ density profiles for three different polarizations at 780 G. For all shown polarizations we observe a dip in the center of the difference OD. For P=0.25 the central polarization is consistent with zero, while for P=0.75 we observe a clear difference in central density for minority and majority components. These spatially varying profiles can be understood in the local density approximation. While the difference between the chemical potentials of the two species remains fixed throughout the trap, the average chemical potential is scanned by the trap. Thus one can expect shells of coexisting phases in the trap. The insets in Fig. 4.11 show an example of such structure where a balanced phase exists in the trap center, surrounded

Feshbach field	730 G	755 G	780 G
$\mu_{\rm f}$ in kHz	14.5(2)	14.5(2)	14.0(2)
$ ilde{g}_{ m bb}$	2.54(3)	2.46(4)	2.78(4)
$ ilde{g}_{ m bf}$	2.71(5)	2.69(5)	2.79(6)
$a_{\rm bb}$ in a_0	3710(100)	3580(110)	4050(120)
$a_{\rm bf}$ in a_0	3220(110)	3200(120)	3320(140)
$a_{\rm bb}$ in $a_{\rm ff}$	1.46(4)	0.93(3)	0.63(2)
$a_{\rm bf}$ in $a_{\rm ff}$	1.27(4)	0.83(3)	0.52(2)

Table 4.2: Mean field theory fitting results. The scattering length is comparable to the axial harmonic oscillator length for all magnetic fields. See text for definition of parameters.

by a partially polarized gas which is, in turn, enclosed by a shell of fully polarized gas of majority atoms.

In the BEC regime it is possible to employ a simple zero-temperature mean field model [150, 151]. Here we limit our focus on a 2D Fermi gas with effective density-independent 3D scattering, that is approximately valid for 730 G and 755 G and describes our data well for these datasets. At 780 G the scattering length becomes larger than the harmonic oscillator length in z-direction and it would be required to take into account corrections to the scattering. The mean field model describes the gas as a mixture of bosons with mass $m_{\rm b}=2m$ and fermions with mass $m_{\rm f}=m$ with the assumption that all minority atoms are paired. Under the minimization condition of the total Gibbs free energy function of fermion density (n_f) and boson density (n_b) , one obtains the following coupled linear equations for the chemical potentials.

$$\mu_{\rm f0} = \frac{2\pi\hbar^2}{m_{\rm f}} n_{\rm f} + g_{\rm bf} n_{\rm b} + V_{\rm f}(r) \tag{4.36}$$

$$\mu_{b0} = g_{bb}n_b + g_{bf}n_f + V_b(r) \tag{4.37}$$

with
$$g_{\rm bf} = \frac{\sqrt{8\pi}\hbar^2 a_{\rm bf}}{m_{\rm bf}l_{\rm z,bf}} = \frac{\hbar^2}{m}\tilde{g}_{\rm bf}, g_{\rm bb} = \frac{\sqrt{8\pi}\hbar^2 a_{\rm bb}}{m_{\rm b}l_{\rm z,b}} = \frac{\hbar^2}{m}\tilde{g}_{\rm bb}$$
, with $m_{\rm bf} = \frac{2m_{\rm b}m_{\rm f}}{m_{\rm b}+m_{\rm f}}$ and $l_{\rm z,b} = \sqrt{\frac{\hbar}{m_{\rm b}\omega_z}} = 3650a_0$ and $l_{\rm z,bf} = \sqrt{\frac{\hbar}{m_{\rm bf}\omega_z}} = 4470a_0$ the effective harmonic oscillator lengths and a_0 is the Bohr radius. $V_{\rm b,f}$ is the effective Gaussian trapping potential for bosons and fermions, respectively.

These equations can be solved analytically for all r independently under local density approximation and directly give the radial density profiles of minority and majority spin component as a function of the global chemical potentials μ_{f0} and μ_{b0} . We note that this model shows perfectly matching minority and majority densities in the center of the trap as well as partially polarized regions in the trap over a wide parameter range [Fig. 4.12].

We observe deviations from the predicted boson-boson and boson-fermion scattering lengths which were calculated for 3D to be $0.6a_{\rm ff}$ and $1.18a_{\rm ff}$ for boson-boson and boson-fermion interactions respectively [152, 115, 116]. These may be because

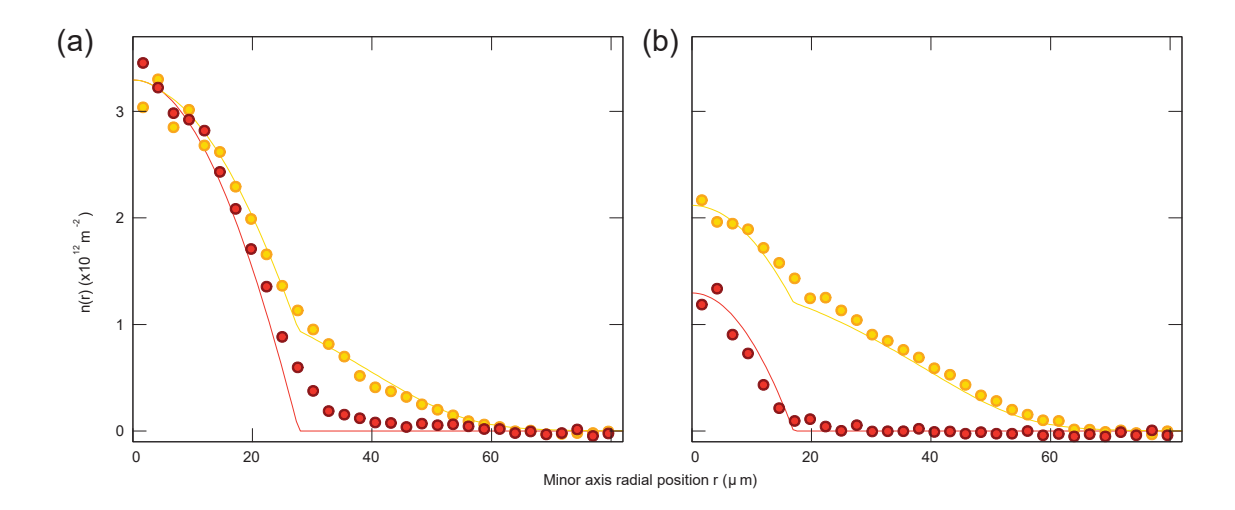


Figure 4.12: Example mean field theory fits. Data displayed for 755 G and P = 0.2 (a) and P = 0.8 (b) with interaction parameters given in table 4.2. The majority $(n_f + n_b)$ is shown in yellow and the minority (n_b) in red, points and line are experiment and theory, respectively.

we are not fully in the 3D scattering regime. Furthermore, Ref [151] which studied phase separation in 3D imbalanced clouds found that beyond mean field corrections can be significant. We find reasonable agreement with our data at 730 G, 755 G and 780 G when using simultaneous fitting of all data for each Feshbach field to determine consistent effective scattering parameters ($a_{\rm ff}$ from [153]). Here the only polarization-dependent fit parameter is $\mu_{\rm b0}$. In the model function we replace the non-interacting Fermi tail by the exact finite-temperature solution.

4.5.6 Extracting critical polarization P_c

Fig. 4.13 displays in-situ OD difference profiles in two-dimensions as a function of interactions (rows) and global polarization (columns). The central polarization p(0) is defined as the local polarization p(r) averaged over a 5 μ m radius central disk of the trap. It can be viewed as an indicator of phase separation in an imbalanced cloud. The chemical potential of the fermions in the trap can be written as

$$\mu_{\uparrow,\downarrow} = \mu_{0\uparrow,\downarrow} - \frac{1}{2} m \omega_x \omega_y r^2 \tag{4.38}$$

where, $\mu_{0\uparrow,\downarrow}$ is the chemical potential in the trap center and $\omega_{x,y}$ arw the radial confinements due to the trap. Now since the two spin states \uparrow and \downarrow experience the same trap frequency, the chemical potential difference between the two states is

$$\Delta \mu = \mu_{0\uparrow} - \mu_{0\downarrow} \tag{4.39}$$

and is constant throughout the trap. In other words, for a given global polarization P, the difference in chemical potential $\Delta \mu$ throughout the trap is a constant. This

implies that for a completely non interacting gas of two-spin fermions, the central polarization p(0) would be proportional to the global chemical potential difference $\Delta \mu$, which in turn will be proportional to P. Hence, for a non interacting system, one would expect a plot between p(0) and P to be a straight line of unit slope going through the origin. This however is not true when interactions are present.

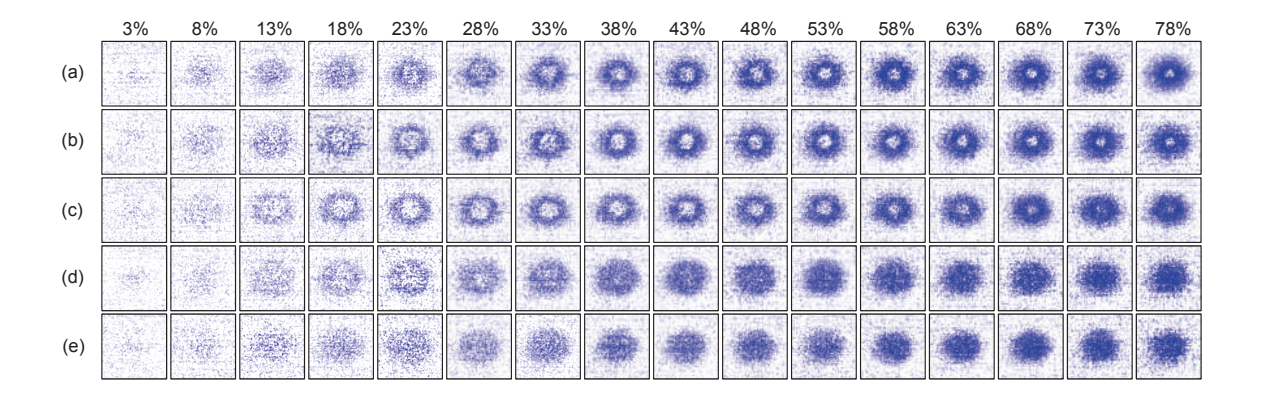
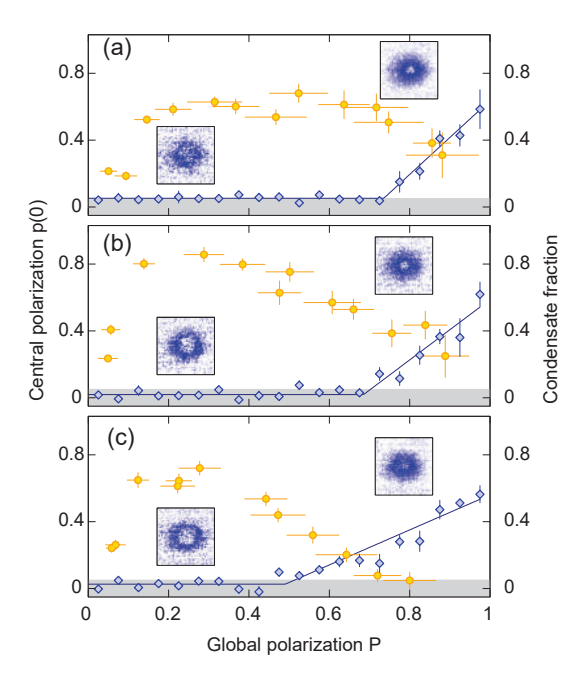


Figure 4.13: Two dimensional *OD* difference images for varying global polarization (columns) and magnetic fields (rows). The magnetic fields are (a) 730 G, (b) 755 G, (c) 780 G, (d) 830 G and (e) 920 G. The global polarization is labelled at the top of each column.

In the presence of interactions, we see that the central density continues to be balanced even when the global polarization is as high as 0.8. In terms of cloud profile, we see that the minority cloud is compressed to occupy the trap center and the majority cloud has a thermal tail beyond the radius where the minority density becomes negligible. This feature also has a strong dependence on interactions. The central polarization of the gas p(0) is shown in Fig. 4.14 vs. P for Feshbach fields of 730 G, 755 G, 780 G, 830 G, and 920 G along with the minority condensate fraction obtained for fields on the BEC side. We find that p(0) is consistent with zero within experimental uncertainty for a range of P less than a field-dependent critical polarization P_c . For $P > P_c$, central polarization p(0) grows linearly like a non interacting system. This critical polarization is akin to the Chandrasekhar-Clogston limit of superconductivity. However, we notice that the condensate does not disappear at P_c .

We observe pair condensation that persists to high values of P at 730 G, 755 G and 780 G [Fig. 4.14(a)-(c)], even beyond P_c , pointing to a polarized condensate. For B=830 G and 920 G, no bimodality is observed. This can be anticipated for expansion in 3D since there is no bound state beyond the Feshbach resonance and the fragile dimers that exist in the trapped system break after release. The measured condensate fraction for a balanced gas is compatible with the fraction that has been measured in a different experiment [148] for comparable T/T_F^0 . Similar to experiments in 3D [29], we find that the condensate fraction does not drop monotonically with increasing P as one would expect naively, but rather peaks at a non-zero P. The harmonic confinement



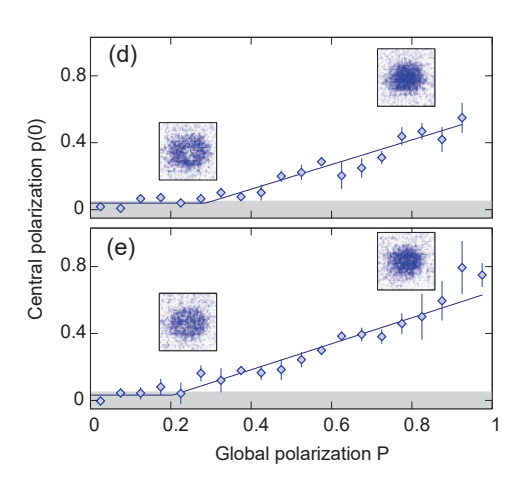


Figure 4.14: Central polarization and condensate fraction vs. global polarization. Central polarization (blue diamonds) and condensate fraction (yellow circles) are shown for the Feshbach fields of (a) 730 G, (b) 755 G, (c) 780 G, (d) 830 G and (e) 920 G. The points represent the average of 5-15 experimental realizations, and error bars are the standard deviation of the mean. The gray region indicates the experimental uncertainty in the determination of the central polarization. The blue line is a bilinear fit to the data to determine $P_{\rm c}$. For condensate fraction data, each point is obtained from a bootstrap analysis of 30 experimental shots. Error bars represent the standard deviation of the bootstrap distribution. The insets show the OD difference at P=0.25 and 0.75

of the clouds may explain this observation. Although the absolute temperatures we measure are independent of P, increasing P leads to a shrinking minority cloud whose wings experience a higher majority density, and therefore a higher local critical temperature.

4.5.7 Phase diagram

We studied the stability of the spin-balanced condensate to chemical potential imbalance across the BEC-BCS crossover. The tight confinement of the gas along the axial direction allows for a confinement induced two-body bound state with binding energy E_B even above the Feshbach resonance, unlike the 3D case. As was described earlier, the unitarity point in the quasi-2D case occurs when $\log(k_F a_{2D}) = 0$. This leads to a less clear distinction between the BEC and BCS regimes unlike in 3D where the Feshbach resonance clearly marks unitarity. Hence, we choose to characterize the interaction strength using the ratio E_B/E_F , where $E_F = \hbar \sqrt{2\omega_x \omega_y N_{\uparrow}}$ is the Fermi

energy of the majority atoms in the non-interacting gas and is ~ 18 kHz in our experiment. We identify the BEC regime with $E_B/E_F \gg 1$ and the BCS regime with $E_B/E_F \ll 1$. The respective values of E_B/E_F are $\sim 6(1)$, 2.9(7), 1.4(3), 0.32(7) and 0.05(2). In the BEC regime, the gas may be thought of as an interacting Bose-Fermi mixture of deeply bound dimers and excess majority atoms, with strong atom-dimer repulsion leading to the observed profiles. This picture is supported by comparison of the mean field model with the data in the BEC regime (see Fig. 4.12). In the BCS regime, the superfluid gap prevents fermionic quasiparticles from entering the superfluid below the Chandrasekhar-Clogston limit. We find that P_c decreases as the BCS limit is approached as summarized in Fig. 4.15(a). Our observed critical polarization is consistent with a previous measurement [34] for comparable values of E_B/E_F .

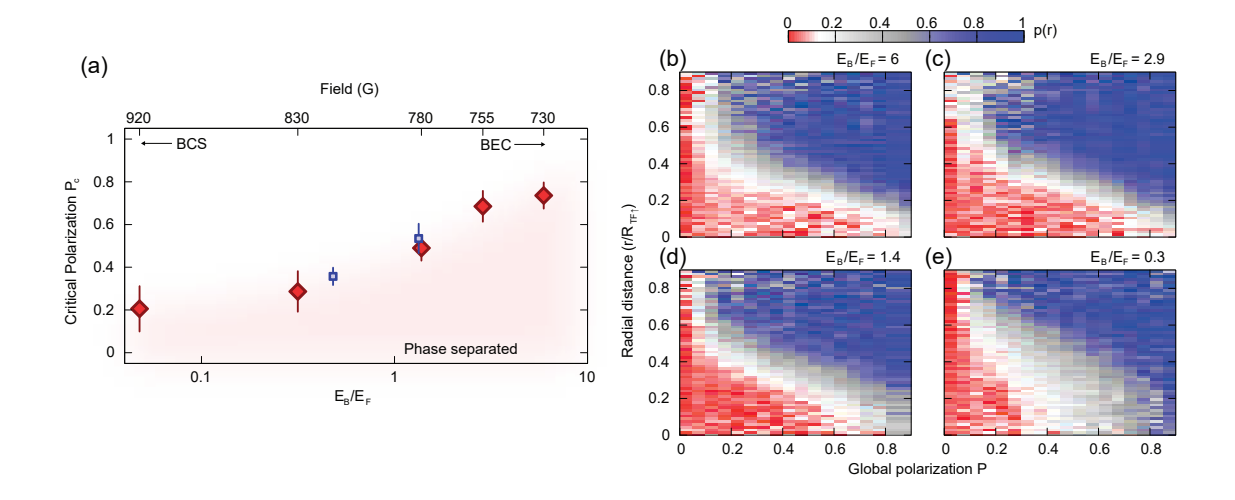


Figure 4.15: (a) Critical polarization (P_c) for phase separation vs. E_B/E_F (log-scale). The global polarization at which phase separation ends is extracted from a bilinear fit to the central polarization data in Fig. 4.14 (red diamonds). Corresponding magnetic fields for these points are shown on the secondary x-axis. For comparison, we extracted two points from the data of ref. [34] (blue squares). The error bars are given by the fit uncertainty. Phase diagram of an imbalanced 2D Fermi gas for four different interactions determined by the Feshbach fields (b) 730 G, (c) 755 G, (d) 780 G and (e) 830 G. The corresponding interaction strengths E_B/E_F are shown in the top-right corner of each panel. The color indicates the local polarization of the gas in the trap p(r) as a function of the scaled position in the trap $r/R_{TF\uparrow}$ and the global polarization P. We distinguish three different phases: a balanced condensate (red), a partially polarized phase (white to gray) and a fully polarized normal gas (blue).

Fig. 4.15(b)-(e) shows an experimental phase diagram of a spin-imbalanced 2D Fermi gas for four different values of the interaction strength E_B/E_F . These phase diagrams show the local polarization p(r) as a function of the global polarization P and the position in the trap r scaled by the Thomas-Fermi radius of a fully polarized

gas $R_{TF\uparrow}$, defined as $m\omega_x\omega_yR_{TF\uparrow}^2/2=\mu_{0\uparrow}$. The global polarization P is the experimental parameter that determines the chemical potential difference $h=(\mu_{\uparrow}-\mu_{\downarrow})/2$, while r fixes the average local chemical potential $\mu=(\mu_{\uparrow}+\mu_{\downarrow})/2$, so we can interpret these diagrams as " $\mu-h$ " phase diagrams expressed in terms of experimentally measured quantities. The partially polarized phase occupying the part of the phase diagram between the balanced condensate and the fully polarized normal gas and depending on E_B/E_F may be a Sarma phase induced by quantum or thermal fluctuations, an FFLO phase or a Fermi liquid phase.

Unlike the 3D case [151], we have not observed discontinuities in the polarization or density profiles. Zero temperature phase diagrams in refs. [131, 132, 129] predict a first order phase transition between the superfluid and normal phases driven by the change in the average local chemical potential in the trap. This would be manifested by a sudden jump of the local polarization from zero in the superfluid to a finite polarization in the normal phase. In 3D, the first order transition only occurs for temperatures below the tricritical point [103]. If such a tricritical point exists in 2D, it is possible that the temperature of our clouds is not low enough to observe the first order transition or that the one-dimensional nature of the interface between the superfluid and normal phases makes it very susceptible to fluctuations that smear out discontinuities when averaging over trap contour lines. We also note that strong quantum fluctuations in 2D can in principle drive the superfluid to normal transition continuous [135].

Chapter 5

Quantum gas microscopy of an attractive Fermi–Hubbard system

5.1 The Fermi-Hubbard model

The Fermi-Hubbard model is a fundamental model in condensed matter physics that describes the behavior of strongly correlated fermions in a lattice [154, 155, 156]. It was originally formulated to describe electrons in solid state materials. The key features of this model are fermions in two spin states \uparrow and \downarrow , hopping between neighboring lattice sites (t) and an on-site interaction between fermions of opposite spins (U). To see how one arrives at the Hubbard Hamiltonian, one must start by trying to describe electrons in solids. These electrons have a kinetic energy given by their momentum \mathbf{p}_i , the periodic lattice potential V_L and the Coulomb interaction between them $V_C(\mathbf{r} - \mathbf{r}')$. We work under the assumption that the ionic lattice is stationary and only the electrons move. Then the Hamiltonian is given by

$$\mathcal{H} = \sum_{i=1}^{N} \left(\frac{\mathbf{p}_i^2}{2m} + V_L(\mathbf{r}_i) \right) + \sum_{\mathbf{r} \neq \mathbf{r}'} V_C(\mathbf{r} - \mathbf{r}')$$
 (5.1)

We first make a mean field approximation to the above Hamiltonian. In the limit of large N and adding one more electron to the system, this electron does not see the ionic background due to an effective screening by the rest of the electrons. In second quantized form in the basis of Wannier functions, the Hamiltonian can be written as

$$\mathcal{H} = \sum_{\alpha, \mathbf{r}, \mathbf{r}', \sigma} t^{\alpha}_{\mathbf{r}, \mathbf{r}'} c^{\dagger}_{\alpha \mathbf{r}, \sigma} c_{\alpha \mathbf{r}', \sigma} + \frac{1}{2} \sum_{\alpha, \beta, \gamma, \delta, \mathbf{r}, \mathbf{r}', \mathbf{r}'', \mathbf{r}'''} U^{\alpha, \beta, \gamma, \delta}_{\mathbf{r}, \mathbf{r}', \mathbf{r}'', \mathbf{r}'''} c^{\dagger}_{\alpha \mathbf{r}, \uparrow} c^{\dagger}_{\beta \mathbf{r}', \downarrow} c_{\gamma \mathbf{r}'', \downarrow} c_{\delta \mathbf{r}''', \uparrow} + h.c. \quad (5.2)$$

where, α, β, γ and δ are Bloch band indices, σ is the spin index that can be either \uparrow or \downarrow and $c_{\mathbf{r},\sigma}^{\dagger}$ and $c_{\mathbf{r},\sigma}$ are the fermionic creation and annihilation operators. Here we note that hopping matrix elements only exist within the same Bloch band and the interaction parameter $U_{\mathbf{r}..}^{\alpha}$ between bands and sites is given by an overlap integral and are similar to the ones described in appendix D. Next we consider a more practical

regime, when the interactions are strong but of a short range, a scenario characteristic for transition and rare earth metals. In addition, it is sufficient to describe physics in a single band $\alpha=1$ of the model knowing that the effect of higher bands can be taken into account later. Furthermore, we can assume that the system can be described in a tight binding approximation, where the electrons are strongly localized around a site. In that case, we can assume the hopping matrix element is only nearest neighbor. Under all these assumptions, we finally arive at the Fermi-Hubbard Hamiltonian

$$\mathcal{H} = -t \sum_{\langle \mathbf{r}, \mathbf{r}' \rangle, \sigma} c_{\mathbf{r}', \sigma}^{\dagger} c_{\mathbf{r}', \sigma} + h.c. + U \sum_{\mathbf{r}} n_{\mathbf{r}, \uparrow} n_{\mathbf{r}, \downarrow}$$
 (5.3)

where, $\langle ... \rangle$ means that the sum is over all nearest neighbors. This is the simplest model beyond band theory that includes many body effects and has shed light on many interesting phenomena, including the metal to Mott insulator transitions.

In a grand-canonical description of the model, one can introduce a chemical potential μ which describes the energy cost of adding an extra particle into the system. In addition, we can add a term corresponding to an external Zeeman field h which leads to an imbalance in spin.

$$\mathcal{H} = -t \sum_{\langle \mathbf{r} \mathbf{r}' \rangle, \sigma} \left(c_{\mathbf{r}, \sigma}^{\dagger} c_{\mathbf{r}', \sigma} + c_{\mathbf{r}', \sigma}^{\dagger} c_{\mathbf{r}, \sigma} \right) + U \sum_{\mathbf{r}} n_{\mathbf{r}, \uparrow} n_{\mathbf{r}, \downarrow} - \mu \sum_{\mathbf{r}, \sigma} n_{\mathbf{r}, \sigma} - h \sum_{\mathbf{r}} (n_{\mathbf{r}, \uparrow} - n_{\mathbf{r}, \downarrow})$$
 (5.4)

where, the density of spin σ on lattice site \mathbf{r} is given by the number operator $n_{\mathbf{r},\sigma} = c_{\mathbf{r},\sigma}^{\dagger} c_{\mathbf{r},\sigma}$. Despite its simplicity, the Fermi-Hubbard Hamiltonian is not tractable for physically relevant scenarios. In 1D, one can solve for the ground state exactly using the Bethe ansatz [40]. One finds that at exactly half filling (number of fermions equals the number of lattice sites), the 1D chain undergoes a metal-insulator transition for $U \geq 0$. In addition, for the 1D and 2D case, the Mermin-Wagner theorem [119] states that there cannot be long range order in the system. To numerically tackle the Hubbard model, many approaches have been used like mean-field theory [41], quantum Monte-Carlo [42, 43, 157], numerical linked cluster expansion [44] etc.

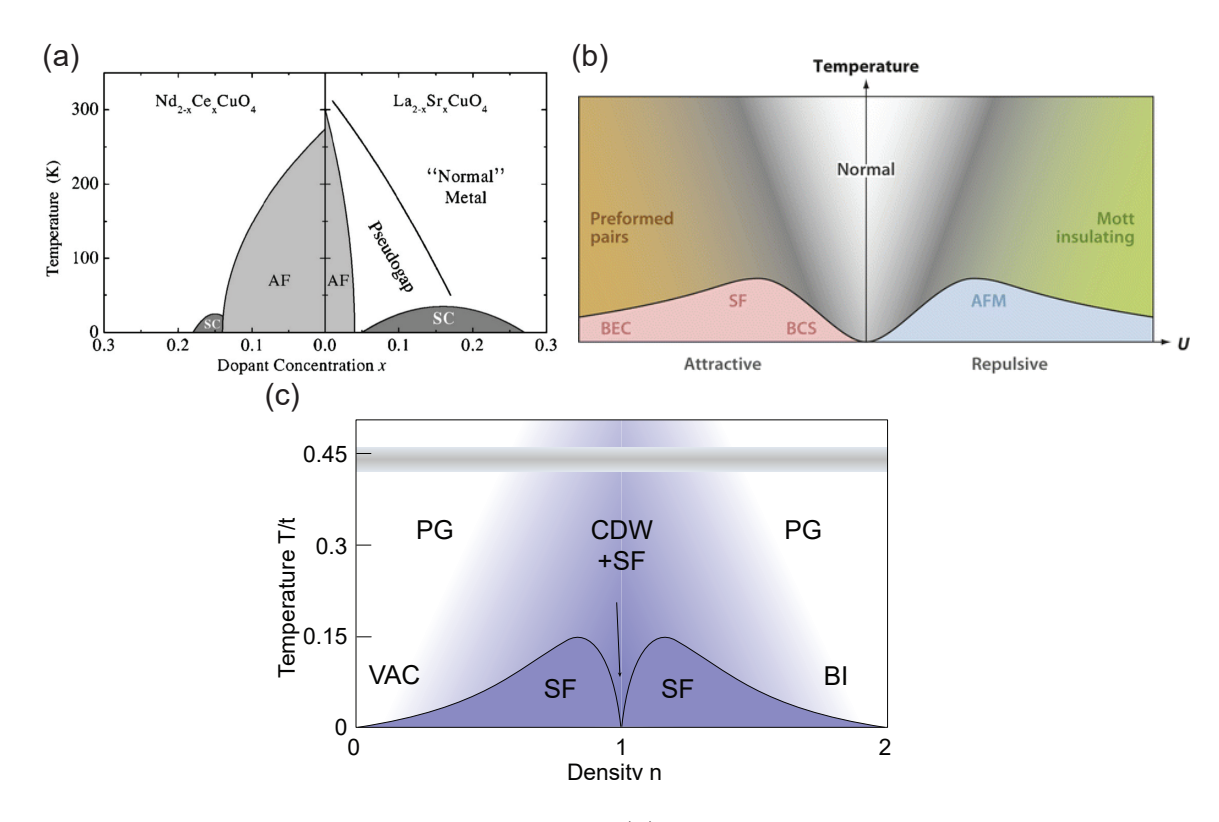


Figure 5.1: Fermi-Hubbard pase diagram. (a) The phase diagram of high T_c cuprate superconductors taken from [158]. As a function of doping (going away from half filling with electrons or holes), all cuprate superconductors behave similarly, i.e. are Mott insulating and have anti-ferromagnetic (AF) order when lightly doped and undergo a transition to a d-wave superconductor when sufficiently doped. (b) A sketch of the Fermi-Hubbard phase diagram for positive (repulsive) and negative (attractive) interactions (U) taken from [86]. On the repulsive side, one gets the physics of Mott insulators and anti-ferromagnetism while on the attractive side, one gets s-wave superfluidity and a BEC-BCS crossover. (c) Schematic phase diagram of the attractive Fermi-Hubbard model at intermediate interaction ($U/t \approx -5$), indicating pseudogap (PG), superfluid (SF), charge-density-wave (CDW) and band-insulating (BI) regimes. The critical temperature vanishes at n = 1. The temperatures achieved in the experiment (gray band) are above the BKT critical temperature but precursor correlations are present in the system.

The Fermi-Hubbard model is also one of the simplest models that is expected to contain the same phenomenology as high T_c cuprates. It was first suggested by P. W. Anderson that the Hubbard model (or the closely related t-J model) incorporates the strongly correlated nature of the 3d orbital electrons due to copper spins in CuO_2 planes [39]. The similarity between the phase diagrams can be seen in Fig. 5.1. More specifically, all cuprate superconductors seem to have similar traits like they are Mott insulating when undoped and show antiferromagnetism up to small dopings [159]. Away from half filling (doped), there is the emergence of a pseudogap regime which finally ends in a d-wave superconducting dome below T_c . The critical temperature T_c is maximum around an optimal doping. All these features are essentially present in the repulsive Fermi-Hubbard phase diagram, although d-wave superfluidity is only speculated and neither observed definitively in numerical simulations nor experiments [102]. The attractive Fermi-Hubbard model, however, is much more tractable theoretically because its not effected by the fermionic "sign problem" at low temperatures [160]. But the type of superfluidity it describes is s-wave and is not the same as is known for cuprates [161]. Nonetheless, it shares some phenomological features such as a pseudogap phase with anomalous properties [162].

Finally, the spin-imbalanced attractive gases described in the previous chapter can also be studied in a Hubbard setting. The FFLO state described in section 4.5 is expected to be enhanced in a 2D lattice geometry compared to 2D continuum [163]. The basic idea is still to find a pairing mechanism that can exist in a system with spin imbalance and attractive interactions. One of the reasons why the FFLO pairing mechanism, where Cooper pairs carry a finite center of mass momentum, can be enhanced in lattice geometries is due to Fermi surface nesting. The 2D continuum Fermi surface is a circle while it gets modified to a square near half-filling in the presence of a square lattice. It is believed that this modification increases the portion covered by the FFLO phase in the mean field phase diagram [164]. Phase diagrams for the attractive Hubbard model have been calculated and it has been established that the spin imbalanced Fermi liquid would be unstable towards the FFLO phase [165]. The current prediction is to have weak interactions $U \approx -4t$ and low temperatures T < 0.1t that have been very hard to achieve experimentally. In addition, its relation to a striped phase in the doped repulsive Fermi-Hubbard model has been established [166].

5.2 Attractive (U < 0) or Repulsive (U > 0)?

For the reasons mentioned above and many more, the attractive Fermi-Hubbard model would seem to be an ideal platform for studying pairing in lattice context and exotic pairing mechanisms. Although it has been theoretically studied quite extensively, it has not received much attention from the experimental community. So far only a few experiments with the attractive interactions have been performed. One example is the measurement of evidence of superfluidity in 3D optical lattices [61]. The evolution of a band insulator as the system is swept across the Feshbach resonance showed a continuous evolution into states occupying many bands [62]. The systems in these experiments do not fall in the category of the single band Hubbard model because of multi-band couplings and off-site interactions [167, 168, 169, 170, 171]. There have been a few experiments with single band attractive Hubbard systems. In one experiment, the displacement of the center-of-mass of a gas with attractive interactions in a 3D lattice was measured [63]. They observed that the oscillation frequency strongly depends on the formation of local pairs. Another experiment measured an anomalous expansion of the cloud with increasing attractive interactions [64]. Finally, out of equilibrium transport in Hubbard systems was measured for both attractive and repulsive interactions [172].

In contrast, the equilibrium repulsive Fermi-Hubbard model is very well studied experimentally. The first measurements were done with absorption imaging where the Mott insulator was observed as a reduction in double occupancy and a gap in the excitation spectrum [173]. The in-situ compressibility was measured in [174]. Nearest-neighbor antiferromagnetic correlations were measured by [175, 176]. Spin sensitive Bragg spectroscopy was further employed to reveal antiferromagnetic correlations [177]. The equation of state for a 2D repulsive Hubbard system was measured in [178]. With the first fermionic quantum gas microscopes a flurry of new developments followed like the direct observation of antiferromagnetic correlations in 2D [57, 58] and 1D chains [59]. More recently, long range antiferromagnetic order was observed in [179] and the effect of spin imbalance was measured by us [60].

There is, however, a mapping between the attractive and the repulsive Hubbard models which leads to a one-to-one correspondence between their properties and observed phenomena [180]. On a bipartite lattice, one can define a particle-hole transformation given by following mapping of the annihilation operators

$$c_{\mathbf{r},\downarrow} \leftrightarrow (-1)^{r_x + r_y} c_{\mathbf{r},\downarrow}^{\dagger}, \quad c_{\mathbf{r},\uparrow} \leftrightarrow c_{\mathbf{r},\uparrow}.$$
 (5.5)

Under this transformation, $n_{\uparrow} \leftrightarrow n_{\uparrow}$ and $n_{\downarrow} \leftrightarrow 1 - n_{\downarrow}$ and the Hubbard Hamiltonian (Eq. 5.4) transforms to (up to a constant energy offset)

$$\mathcal{H} \leftrightarrow -t \sum_{\langle \mathbf{r} \mathbf{r}' \rangle, \sigma} \left(c_{\mathbf{r}, \sigma}^{\dagger} c_{\mathbf{r}', \sigma} + c_{\mathbf{r}', \sigma}^{\dagger} c_{\mathbf{r}, \sigma} \right) - U \sum_{\mathbf{r}} n_{\mathbf{r}, \uparrow} n_{\mathbf{r}, \downarrow} - \mu' \sum_{\mathbf{r}, \sigma} n_{\mathbf{r}, \sigma} - h' \sum_{\mathbf{r}} (n_{\mathbf{r}, \uparrow} - n_{\mathbf{r}, \downarrow})$$

$$(5.6)$$

where, $\mu' = h - U/2$ and $h' = \mu - U/2$. So under this transformation, the kinetic term remains unchanged and the chemical potential μ swaps its role with the Zeeman field h. Most importantly, however, the sign associated with the interaction term changes. This implies that the negative U (attractive) Hubbard maps on to the positive U (repulsive) Hubbard.

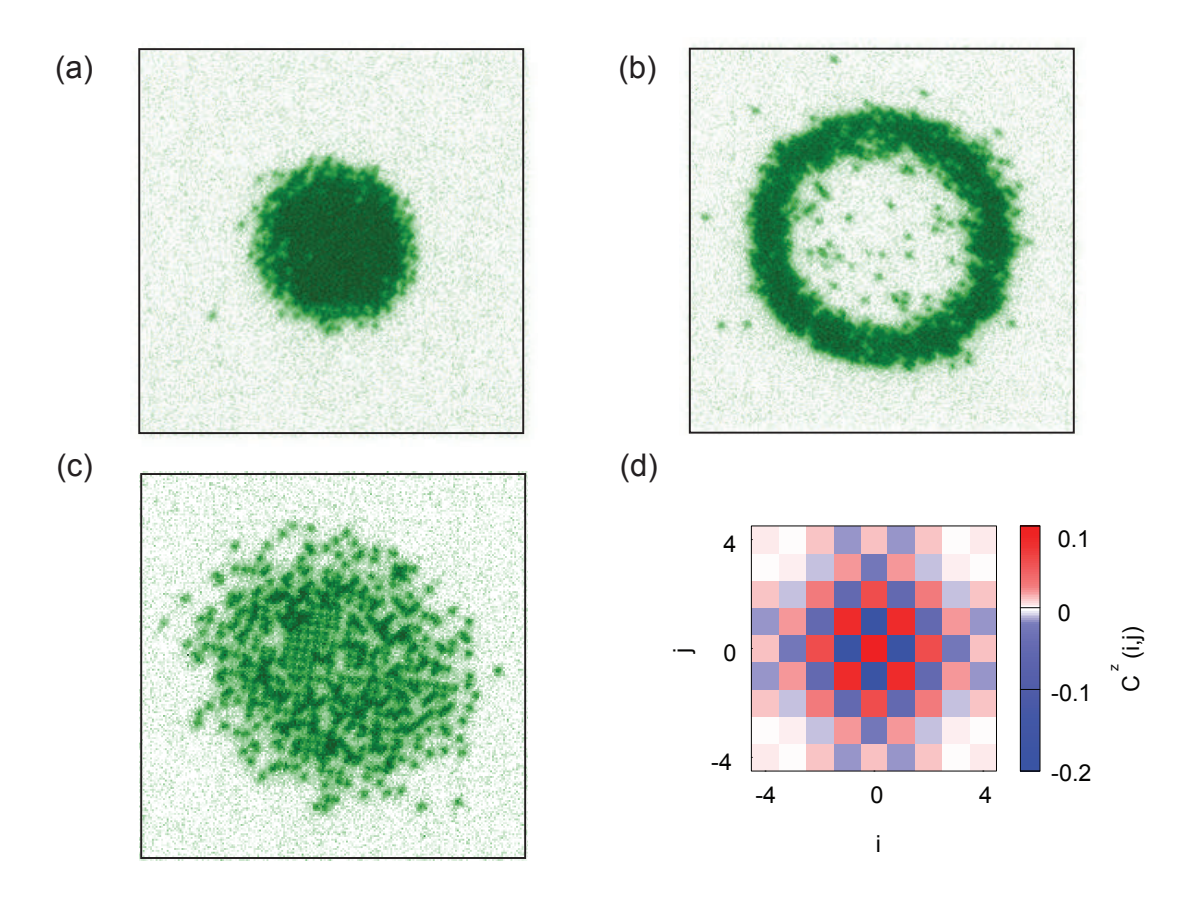


Figure 5.2: Single site images of a repulsive Fermi-Hubbard system. (a) Shows the image of a Mott insulator (MI) while (b) is when the filling has been increased such that the center of the trap becomes a band insulator (BI) with a Mott insulating ring around it. Due to parity imaging of the quantum gas microscope, all doubly occupied sites in the BI region are lost and appear empty. (c) Image of a single spin state \uparrow within a MI taken by removing all atoms in state \downarrow . The underlying short range antiferromagnetic (AFM) order can be seen as a region with a checkerboard. Image taken at U/t = 8 and T/t = 0.4. (d) Quantification of the AFM order in a spin balanced repulsive Hubbard system at half-filling. The quantity $C^z(i,j)$ is the two-point correlator of the projection of spin along the z-axis for spins at sites i and j.

For a spin-balanced system, h=0. Consider first the SU(2) spin symmetry of the problem for h=0. The vector spin operator on site \mathbf{r} is given by $(S_{\mathbf{r}}^x, S_{\mathbf{r}}^y, S_{\mathbf{r}}^z)$, where $S_{\mathbf{r}}^{\pm} = S_{\mathbf{r}}^x \pm i S_{\mathbf{r}}^y$. In terms of fermionic creation and annihilation operators, the generators of spin rotations are

$$S_{\mathbf{r}}^{-} = c_{\mathbf{r},\downarrow}^{\dagger} c_{\mathbf{r},\uparrow}$$

$$S_{\mathbf{r}}^{+} = (S_{\mathbf{r}}^{-})^{\dagger} = c_{\mathbf{r},\uparrow}^{\dagger} c_{\mathbf{r},\downarrow}$$

$$S_{\mathbf{r}}^{z} = \frac{1}{2} (c_{\mathbf{r},\uparrow}^{\dagger} c_{\mathbf{r},\uparrow} - c_{\mathbf{r},\downarrow}^{\dagger} c_{\mathbf{r},\downarrow}) = \frac{1}{2} (n_{\mathbf{r},\uparrow} - n_{\mathbf{r},\downarrow})$$
(5.7)

These operators obey the usual commutation relations

$$[S_{\mathbf{r}}^z, S_{\mathbf{r}}^{\pm}] = \pm S_{\mathbf{r}}^{\pm}, \quad [S_{\mathbf{r}}^+, S_{\mathbf{r}}^-] = 2S_{\mathbf{r}}^z$$
 (5.8)

In the absence of an effective Zeeman field, the operators $S^z = \sum_r S^z_{\mathbf{r}}$ and $S^{\pm} = \sum_r S^{\pm}_{\mathbf{r}}$ satisfy

$$[\mathcal{H}, S^{\pm}] = [\mathcal{H}, S^z] = 0 \tag{5.9}$$

implying the SU(2) spin-symmetry of the Hubbard model. In other words, the Hamiltonian is invariant under a global rotation of the spin degree of freedom. To demonstrate another "hidden" symmetry of the Hubbard model, we define a new set of generators for rotations of the "pseudo-spin" on a site given by

$$\eta_{\mathbf{r}}^{-} = (-1)^{r_{x}+r_{y}} c_{\mathbf{r},\uparrow} c_{\mathbf{r},\downarrow}
\eta_{\mathbf{r}}^{+} = (\eta_{\mathbf{r}}^{-})^{\dagger}
\eta_{\mathbf{r}}^{z} = \frac{1}{2} (n_{\mathbf{r}} - 1)$$
(5.10)

It can be easily verified [181] that they obey the following commutation relations

$$[\eta_{\mathbf{r}}^z, \eta_{\mathbf{r}}^{\pm}] = \pm \eta_{\mathbf{r}}^{\pm}, \quad [\eta_{\mathbf{r}}^+, \eta_{\mathbf{r}}^-] = 2\eta_{\mathbf{r}}^z. \tag{5.11}$$

The operators $\eta^z=\sum_r\eta^z_{\bf r}$ and $\eta^\pm=\sum_r\eta^\pm_{\bf r}$ satisfy

$$[\mathcal{H}, \eta^{\pm}] = \pm (U - 2\mu)\eta^{\pm}, \quad [\mathcal{H}, \eta^z] = 0.$$
 (5.12)

regardless of the sign of the interaction U. Exactly at half-filling, $\mu = U/2$ and all the pseudospin generators in Eq. 5.12 commute with \mathcal{H} similar to the spin generators in Eq. 5.9, meaning that the Hamiltonian is invariant under global rotations of the pseudo-spin giving rise to another SU(2) symmetry. So with the spin symmetry, the Hubbard model thus has a combined SU(2)×SU(2) = SO(4) symmetry [182]. Also notice that the pseudo-spin rotation generators map on to the regular spin rotation generators under the particle-hole transformation (Eq. 5.5):

$$\eta^{\pm} \leftrightarrow S^{\pm}, \quad \eta^z \leftrightarrow S^z$$
(5.13)

In other words, this transformation provides a mapping between the attractive and the repulsive Hubbard models, with the roles of doping and spin-imbalance interchanged [180]. The doped attractive Hubbard system studied in this work maps onto a spin-imbalanced repulsive Hubbard system. Therefore, the z-spin correlations we measured for repulsive interactions [60] are closely related to the density correlations I discuss here.

5.3 Quantum gas microscopy

Quantum gas microscopes (QGM) bring a new advantage in the study of the Hubbard model. The ability to directly detect occupation on a site, with spin resolution, implies that two point correlators can be directly measured. In addition this technique brings unprecedented signal to noise. The first QGM was actually achieved for bosonic Rb atoms in 2009 [47]. This led to direct measurements of the bosonic Mott insulator and the superfluid to Mott insulator transition [49]. QGMs of bosons were subsequently realized by groups in Germany [48] and Japan [183, 184]. The first QGM for fermionic atoms was demonstrated in 2015. They fall in two categories, the first where electromagnetically induced transparency (EIT) cooling is employed to cool the atoms while collecting scattered photons [50, 51]. The other category is where Raman sideband cooling is employed for imaging [52, 53, 59]. Our experiment falls in this latter category as described in section 3.3.

We realize the Fermi-Hubbard model using a spin-balanced degenerate mixture of two Zeeman states ($|1\rangle = |\uparrow\rangle$ and $|3\rangle = |\downarrow\rangle$) of ⁶Li in an optical lattice. To create the sample we evaporate near the 690 G Feshbach resonance. We stop the evaporation before Feshbach molecules form and transfer the atoms to the light sheet trap where the gas undergoes further evaporation to degeneracy at 305.4(1) G. At this field, the scattering length is $a_s = -889a_0$. Next we transfer the gas into the final trapping geometry where the bottom beam provides radial confinement and the accordion lattice with trapping frequency $\omega_z = 2\pi \times 21(1)$ kHz provides axial confinement. The spin populations are balanced to within 2.1(9)%. We then load the gas into a 2D square lattice with a 25 ms long ramp to varying depths from 4-7.5 E_r .

In addition to the scheme described above (scheme 1), we implemented another very different scheme for preparing a lithium gas with a negative scattering length, based on a different evaporation strategy commonly used in the lithium quantum gas community. In this scheme 2, we perform the entire evaporation at the Feshbach resonance. Three-body collisions lead to population of the molecular branch. Before loading into the lattice, the bias field is ramped to 907 G where the scattering length is -2800 a_0 . After pinning the atoms in a 55 E_R lattice, we ramp the field to 725 G where we perform a Landau-Zener sweep on an interaction-resolved transition to the 2-3 upper branch. In order to convert the 2-3 doubles to $|2\rangle$ -singles with high efficiency, we ramp to 641 G where we apply the resonant pulses to remove $|1\rangle$ and $|3\rangle$ atoms. This ramp is done quickly (within \sim 800 μs) to avoid atom losses due to the crossing of a narrow 2-3 Feshbach resonance around 714 G.

5.3.1 Calibrating Hubbard parameters

We calibrate our lattice depth by measuring the frequencies of the three d bands in a deep lattice using lattice depth modulation, and compare these with a 2D band structure calculation. This process is described in detail in Section 2.8.4. The inferred depth of the lattice at which our measurements are performed is 6.2(2) E_R , where $E_R = 14.66$ kHz. From that we obtain nearest-neighbor tunneling values $t_x = 1200$ Hz, $t_y = 1110$ Hz ($t_x/t_y = 1.08$). The reduction of the lattice depth across the cloud due to the Gaussian profile of the lattice beams leads to an increase in the tunneling by 10% at the edge of the cloud compared to the central value. We also calculate a non-zero but negligible diagonal tunneling $t_{11} = 42$ Hz = 0.04 t_x , due to the non-separability of the lattice.

We measure the interaction energy U at the lattice loading field of 305 G using radio frequency spectroscopy. We transfer atoms from state $|1\rangle$ to $|2\rangle$ and resolve the frequency shift between singly and doubly occupied sites. In the situation where a $|1\rangle$ atom is part of a bounded pair, then one must take into account the interaction between the $|2\rangle - |3\rangle$ pair that is formed. This final state interaction can be taken into account as

$$U_{13} = \delta U \frac{a_{13}}{a_{13} - a_{23}} \tag{5.14}$$

where δU is the measured difference between the singles and doublon peaks and a_{13} (a_{23}) is the scattering length at the spectroscopy field for a $|1\rangle - |3\rangle$ ($|2\rangle - |3\rangle$) mixture. The measured RF spectra are shown in Fig. 5.3. When the spectra are taken for deep lattices where tunneling is mostly supressed, we found good agreement with tight binding estimates. For example, in Fig. 5.3(e), a lattice depth of 15 E_R and at 305 G is expected to give U = -12.81 kHz. Taking into account the final state interaction of 2.05 for this field, we would expect $|\delta U| = 6.25$ kHz, which is very close to the measured value (6.3 kHz). For a shallow lattice depth of 6.6 E_R and 305 G (Fig. 5.3(b)), we would expect U = -6.4 kHz, leading to an expected $|\delta U| = 3.1$ kHz. However, we measure 2.2 kHz.

This indicates that for shallower lattices, many-body effects start influencing the RF spectra. In general, to obtain the correct two body interaction U, the best place to measure are isolated lattice sites. Once that condition is met, the tight binding estimate matches that of RF spectroscopy.

The value of U determined from band structure calculations can also be modified to include higher band corrections [185]. The resulting Hubbard interaction U is -5.9(1) kHz for our lattice depth of 6.2(2) E_R . Combining it with the tight binding tunneling average t = 1150(50) Hz, we obtain a $U/t \sim -5.4(3)$.

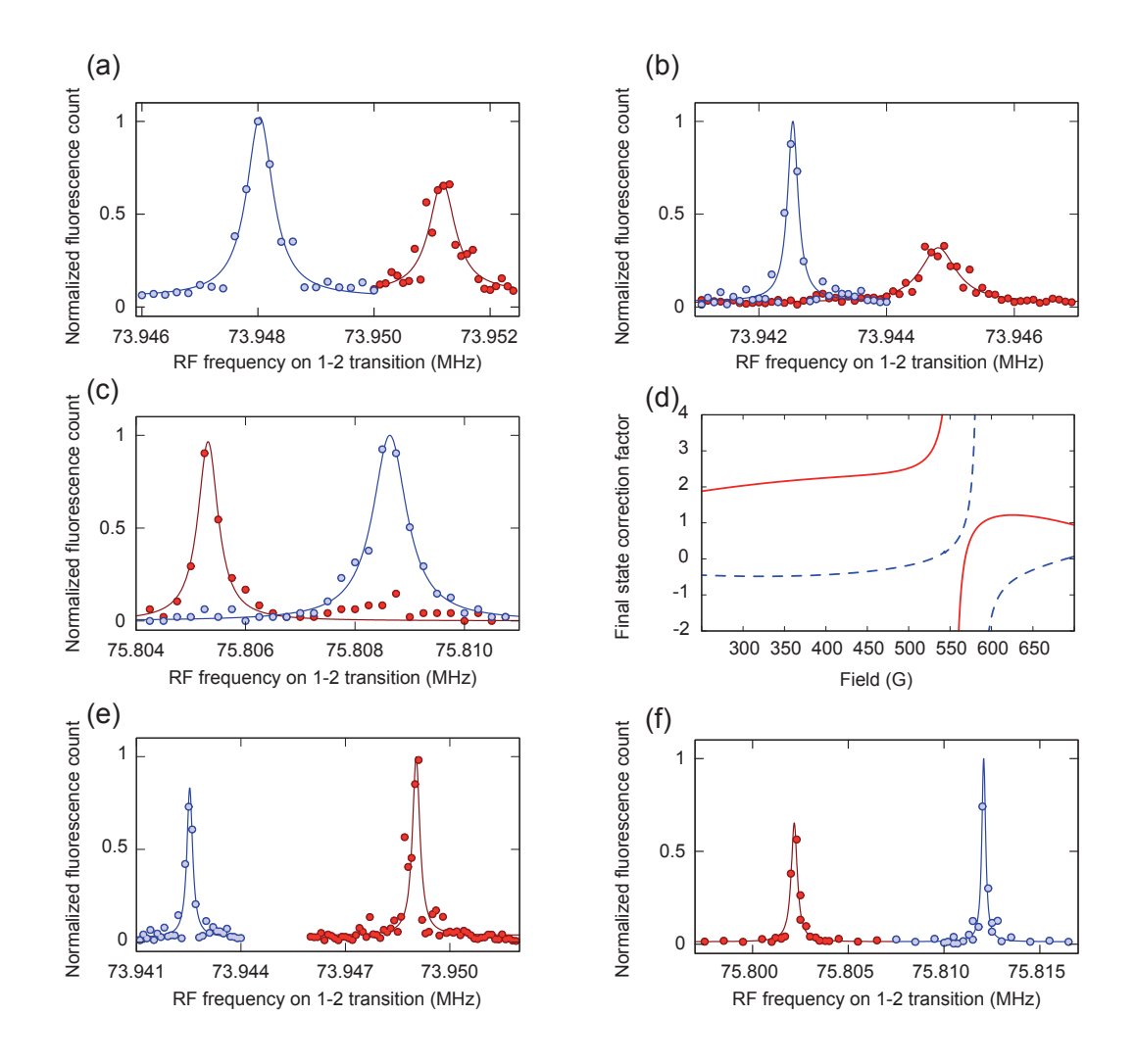


Figure 5.3: RF spectrosocopy of the Hubbard model. In all the spectra, red denotes doublons in states $|1\rangle$ and $|3\rangle$ while blue corresponds to single atoms in state $|1\rangle$. All RF spectra are taken by applying microwave pulses near the $|1\rangle - |2\rangle$ transition. (a) RF spectrosocpy at the lattice depth of V=6.2 E_R and a field of 305 G (scattering length $a_s=-889.3$ a_0). The spacing between the peaks is 3.2 kHz. (b) At a lattice depth of V=6.6 E_R and a field of 305 G. The spacing between the peaks is 2.2 kHz. (c) At a lattice depth of V=10.5 E_R and a field of 594 G ($a_s=448$ a_0). The spacing between the peaks is 3.3 kHz. (e) At a lattice depth of V=15 E_R and a field of 305 G. The spacing between the peaks is 6.3 kHz. (f) At a lattice depth of V=42 E_R and a field of 594 G. The spacing between the peaks is 10 kHz. (d) The final state correction factor to estimate the Hubbard U from the energy difference between singles and doubles as a function of field. Starting with a $|1\rangle - |3\rangle$ mixture and transfering from $|1\rangle$ to $|2\rangle$ (red solid line). Starting with a $|1\rangle - |2\rangle$ mixture and transfering from $|2\rangle$ to $|3\rangle$ (blue dashed line). At the field of 305 G, the correction factor in the former case is 2.05 while at 594 G, it is 1.08.

5.3.2 Measuring double occupancies

In the usual scheme of Raman imaging, a singly occupied lattice site produces a fluorescence signal while atoms in a doubly occupied site are lost due to light-assisted collisions. Thus we measure the singles density $n^s = n_{\uparrow} + n_{\downarrow} - 2n_{\uparrow}n_{\downarrow}$. To gain the full density information, one needs to measure the doubly occupied sites as well. To measure density correlations between doubly-occupied sites, we developed a new detection scheme (Fig. 5.4(a)). After the gas is loaded adiabatically into the optical lattice, we pin the atoms by increasing the lattice depth to 55(1) E_R in 100 μ s where tunnelling dynamics are frozen. The next step is to adiabatically ramp the field to 594 G where we perform an interaction resolved Landau-Zener sweep to selectively transfer $|1\rangle - |3\rangle$ doublons to $|2\rangle - |3\rangle$ doublons while not effecting the $|1\rangle$ singles [173, 178. Finally we ramp to a field of 641 G where the $|2\rangle - |3\rangle$ scattering length is 414 a_0 . We apply resonant pushing pulses of 30 μ s durations in the presence of a repulsive interaction to remove $|1\rangle$ and $|3\rangle$ atoms, leaving behind only $|2\rangle$ atoms on sites that originally had doublons. Since we have a relatively weak vertical confinement, the atoms feel a cigar-shaped on-site potential. The large relative wavefunction of the atoms on a site due to repulsive interactions and this weak vertical confinement significantly reduces the probability of light-assisted collisions during the resonant pulse. This procedure gives us access to the doublon density $n^d = n_{\uparrow} n_{\downarrow}$.

The pushing pulse duration is very critical to ensure that we do not remove other spin states with off-resonant light. Fig. 5.4(c) shows the effect of the pushing pulse duration, resonant on state $|1\rangle$. There is no effective pushing for pulses shorter than 10 μ s. But when the pulse is longer than $\sim 300~\mu$ s, we see off-resonant pushing of state $|3\rangle$ atoms. That is why we chose a 30 μ s duration for all our pushing pulses.

We can measure the efficiency of detecting doublons by analyzing the imaging fidelity of band insulating regions in the cloud (Fig. 5.4(d)). The filling in the trap center is saturated at two atoms per site. We perform the above-mentioned process to image only the doublons. We measure a combined fidelity (including RF-transfer efficiency and pushing efficiency) of $1 - \epsilon_d = 91(1)\%$ of imaging doublons, leading to an underestimation of our doublon density correlator by $(1 - \epsilon_d)^2 = 0.83$ which we correct for. We have also performed the same detection procedure on a Mott insulator, where we expect unit occupancy on the lattice sites. This allows us to extract the probability that a single atom in state $|1\rangle$ would get transferred to $|2\rangle$ and give a false positive signal of the presence of a doublon. We measure the probability of this process to be only 2.3(3)%. The average singles and doubles density profiles obtained from clouds prepared under identical conditions allow us to extract the total density profile $n = n^s + 2n^d$.

In addition, while holding the atoms in a deep lattice for doublon detection, we lose 2(1)% of the atoms, leading to a net detection efficiency of $\approx 95\%$ for singly occupied sites. The densities that we obtain are corrected for the above detection efficiency.

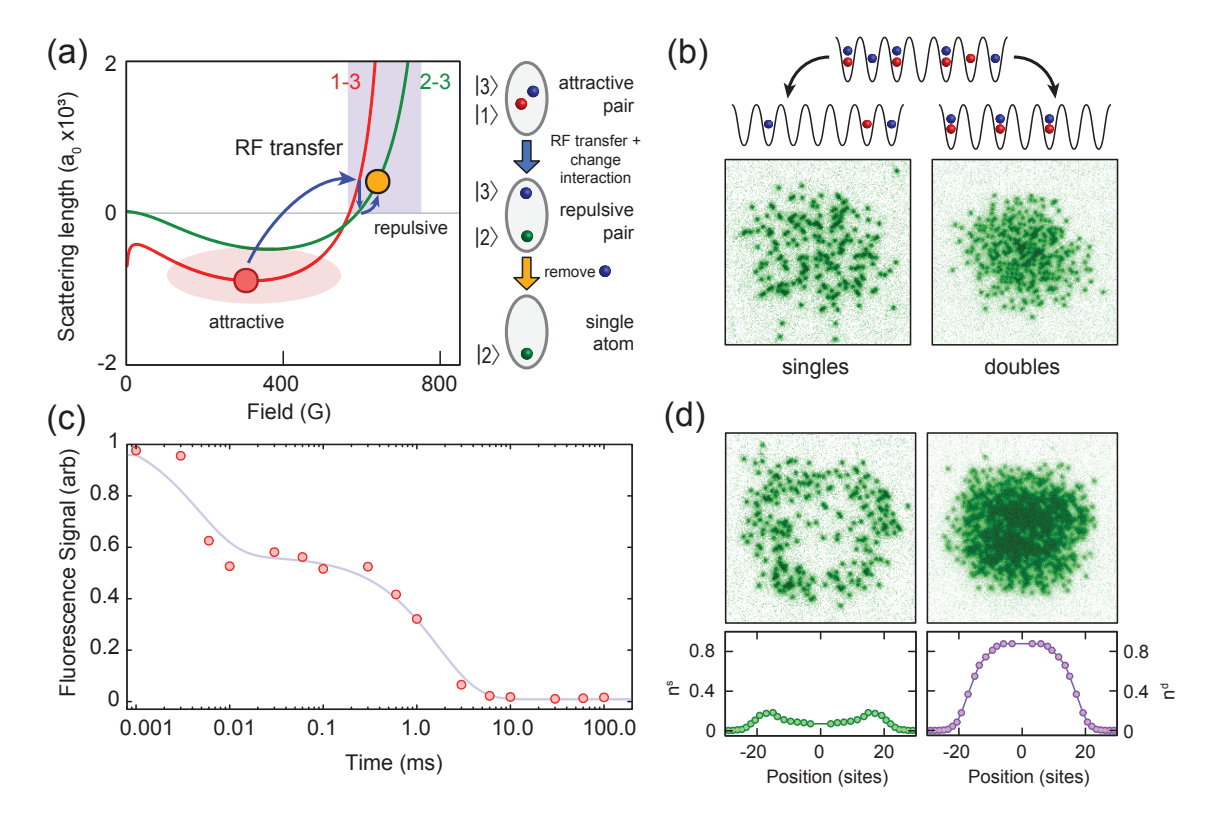


Figure 5.4: Detecting double occupancies. (a) Overview of magnetic fields and interactions used in the experimental sequence. Lines represent ⁶Li scattering length versus field for a $|1\rangle - |3\rangle$ mixture (red) and a $|2\rangle - |3\rangle$ mixture (green) [153]. We load the lattice at attractive interactions of $a_{13} = -889 \ a_0$ (red circle). After freezing the density distribution, we convert $|1\rangle - |3\rangle$ doublons to $|2\rangle - |3\rangle$ doublons of which the state $|3\rangle$ atom is pushed in a regime of repulsive interactions and we are left with only one atom per site (orange circle at $a_{23} = 414 a_0$). The diagram to the right illustrates the two steps of the doublon detection: First an interaction dependent transfer and switch to repulsive interactions and then the pushing of one state of the pair which only works efficiently at repulsive interactions. (b) Single-shot fluorescence images of the singles density n^s (left) and the doublon density n^d (right). In any single image, we can either detect atoms in the singly occupied sites of the lattice only or in the doubly occupied sites only. (c) Pushing pulse time series. We measure the effect of pushing $|1\rangle$ on atoms in $|3\rangle$ at the field 594 G. We notice that for pulses shorter than 10 μ s, we do not push any atoms. We start pushing out $|1\rangle$ atoms for pulses ranging up to 300 μ s. Beyond that, atoms in both spin states are ejected by the pushing pulse. (d) Calibration of the efficiency of the scheme to detect doublons in single-site imaging using a band insulating region in the center of the trap. Top, single image of singles (left) and doublons (right). Bottom, azimuthal average of 10 images of singles (left) and doubles (right). In the center, single occupancy is largely suppressed, while the double occupancy exhibits a plateau. Lines are atomic limit fits to the density profiles.

5.3.3 Charge density wave and s-wave pairing

So far I have discussed the Hamiltonian of the attractive Fermi-Hubbard model and discussed how we calibrate the Hubbard interaction U and tunelling t in the tight binding approximation of our lattice at a depth V. When a system is prepared, each lattice site can either be empty, contain a single atom of spin \uparrow or \downarrow or contain a doublon $\uparrow\downarrow$. I discussed how, by using interaction resolved RF spectroscopy, we can obtain the density of doubles n^d in an image. The usual Raman imaging gives us the singles density n^s and together we can obtain the total density as $n = n^s + 2n^d$.

The total density can vary from 0 near the tail of the cloud to at most 2 in a band insulating center. The density $n^{s,d} \equiv n^{s,d}(U/t,\mu/t,T/t)$. In other words, the density depends on the interaction, the chemical potential and the temperature. The chemical potential μ is defined such that at half-filling (number of particles = number of sites), $\mu = U/2$, for U of either sign. In addition, the density correlations C^{α} at a distance vector \mathbf{a} are defined as

$$C^{\alpha}(\mathbf{a}) = A(\langle n_{\mathbf{r}}^{\alpha} n_{\mathbf{r}+\mathbf{a}}^{\alpha} \rangle - \langle n_{\mathbf{r}}^{\alpha} \rangle \langle n_{\mathbf{r}+\mathbf{a}}^{\alpha} \rangle) = A \langle n_{\mathbf{r}}^{\alpha} n_{\mathbf{r}+\mathbf{a}}^{\alpha} \rangle_{c}$$
 (5.15)

where n^{α} could be singles, doubles or total density. $\langle ... \rangle$ denotes the ensemble average. The prefactor A is 1 for total and singles density while it is 4 for doubles and comes from the factor of 2 in $n = n^s + 2n^d$. The distance \mathbf{a} can be $(\pm 1, 0)$ or $(0, \pm 1)$ for nearest neighbor distance, (1,1) and (-1,-1) for next nearest neighbor and so on.

Determinantal quantum Monte Carlo

We perform determinantal quantum Monte Carlo (DQMC) simulations for the Hubbard model using a Fortran 90/95 package called QUantum Electron Simulation Toolbox (QUEST) developed and maintained by R. T. Scalettar et. al. [157]. For a spin-balanced system with attractive interactions (U/t < 0) the calculations do not suffer from a fermion sign problem. We can obtain the previously discussed correlators for a given value of U, T and $\bar{\mu} = \mu - U/2$. The simulations are performed on a square lattice of 8×8 sites with U/t = -5.7 and a chemical potential $\bar{\mu}$ varying from -3 to 1.5 with $\bar{\mu} = 0$ representing half filling. The inverse temperature $\beta = Ld\tau$ was split into L = 40 imaginary time slices, with an interval $d\tau$ given by L and T. To obtain higher statistics, the simulations were averaged over 10 runs, 50,000 passes each. The dependance of the correlators on n, U/t and T/t is shown in Fig. 5.5.

The main observation from the simulations is that both the total density n and the doubles density n^d exhibit checkerboard like correlations, i.e. the sign of $C^{\alpha}(\mathbf{a})$ oscillates between positive and negative with distance. This checkerboard correlation is caused by the underlying charge density wave (CDW) order in the system. Because it is energetically favored, atoms pair up on a lattice site. But if a doublon is next to an empty site, it can further reduce its energy by a superexchange process. In this process, an atom virtually tunnels to the empty site and back. The energy of the pair is reduced by $4t^2/U$. So it is more likely to find a double occupancy next to an empty site. These CDW correlators are maximal at half filling (n = 1) for any

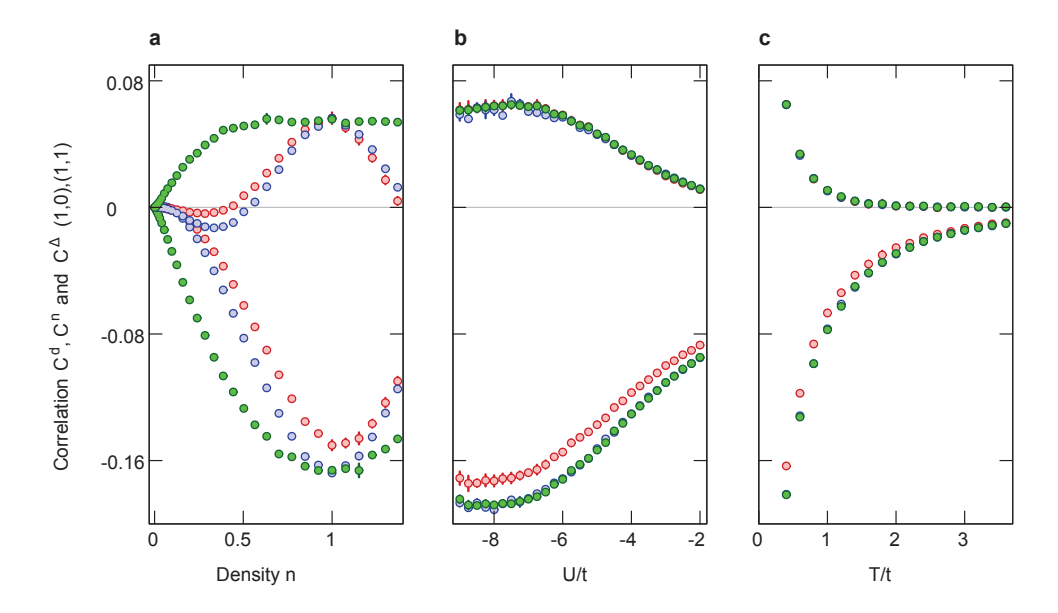


Figure 5.5: **DQMC** simulations of pairing, total density and doublon density correlators. (a) DQMC simulations for the nearest neighbor (1,0) and next-nearest neighbor (1,1) correlations of the doublon density ($C^d(\mathbf{a})$, red), total density ($C^n(\mathbf{a})$, blue) and pairing ($(-1)^{a_x+a_y}C^{\Delta}(\mathbf{a})$, green) as a function of density for U/t = -5.7 and T = 0.45t. (b) Same quantities as a function of U/t at half filling (n = 1) and T = 0.45t. (c) Same quantities as a function of T/t at half filling and for U/t = -5.7. Note that for both (1,0) and (1,1) correlators, $|C^{\Delta}| \geq |C^d|$.

temperature and U. Correlations initially grow with increasing |U|/t for a given n and T and saturate around U/t = -8. But with temperature, the correlators grow monotonically as T/t is lowered for the same n and U/t.

S-wave pairing correlations

In addition, simulations give us access to the s-wave pairing correlator C^{Δ} . In practice, measuring this correlator is hard because it is derived from a coherent superposition of a doublon and a hole on each site. To see how the correlations in density are related to pairing, consider the pseudo-spin operators introduced in Eq. 5.10. The pseudo-spin on a site can be visualized on the Bloch sphere like a regular spin. If it points up (down) the site contains a doublon (hole), while if it lies in the equatorial plane, the site contains an equal superposition of a doublon and hole with a complex relative phase determined by the azimuthal angle. In the limit of large attractive interactions, the spin-balanced Hubbard Hamiltonian can be approximated as a Heisenberg Hamiltonian with antiferromagnetic interactions between the pseudo-spins, leading to charge-density-wave and pairing correlations corresponding to z and x, y antiferromagnetic pseudo-spin correlations respectively. At half-filling, the pseudo-spin rotational symmetry implies

$$\left\langle \eta_{\mathbf{r}}^{z} \eta_{\mathbf{r}+\mathbf{a}}^{z} \right\rangle_{c} = \left\langle \eta_{\mathbf{r}}^{x} \eta_{\mathbf{r}+\mathbf{a}}^{x} \right\rangle_{c} \tag{5.16}$$

where $\eta_{\mathbf{r}}^x = (\eta_{\mathbf{r}}^+ + \eta_{\mathbf{r}}^-)/2$. Defining the s-wave pairing operator in the x direction as

$$\Delta_{\mathbf{r}}^{x} = c_{\mathbf{r},\uparrow} c_{\mathbf{r},\downarrow} + c_{\mathbf{r},\downarrow}^{\dagger} c_{\mathbf{r},\uparrow}^{\dagger}$$

$$(5.17)$$

one concludes that the density correlations $C^n(\mathbf{a}) = \langle n_{\mathbf{r}} n_{\mathbf{r}+\mathbf{a}} \rangle_c = 4 \langle \eta_{\mathbf{r}}^z \eta_{\mathbf{r}+\mathbf{a}}^z \rangle_c$ and pairing correlations $C^{\Delta}(\mathbf{a}) = \langle \Delta_{\mathbf{r}}^x \Delta_{\mathbf{r}+\mathbf{a}}^x \rangle_c = 4 \langle \eta_{\mathbf{r}}^x \eta_{\mathbf{r}+\mathbf{a}}^x \rangle_c$ are equal in magnitude at half-filling.

Deviation from half-filling introduces an effective Zeeman field along z that couples to the pseudo-spin. This leads to canted antiferromagnetic pseudo-spin correlations, with stronger correlations in the direction orthogonal to the field, i.e. the pairing correlations become stronger than the density correlations. Therefore, measurement of charge-density-wave density correlations in the attractive Hubbard model provides a lower bound on the pairing correlations at any filling. In our experiment we measure the more experimentally accessible quantity, the doublon density correlator $C^d(\mathbf{a}) = 4 \langle n_{\mathbf{r}}^d n_{\mathbf{r}+\mathbf{a}}^d \rangle_c$.

Relation between C^n and C^d

The doublon density and total density correlators become equal in the limit of low temperatures and large interactions. The two quantities are related by

$$C^{n}(\mathbf{a}) = C^{d}(\mathbf{a}) + C^{s}(\mathbf{a}) + C^{sd}(\mathbf{a})$$
(5.18)

where, $C^s = \langle n_{\mathbf{r}}^s n_{\mathbf{r}+\mathbf{a}}^s \rangle_c$ is the singles correlator and $C^{sd} = 4\langle n_{\mathbf{r}}^s n_{\mathbf{r}+\mathbf{a}}^d \rangle_c$ is the correlation between singles and doubles density. For typical parameters we have numerical evidence that only the doublon density correlations we measure in this experiment contribute to the checkerboard order in the total density correlations typically discussed in the attractive Hubbard model literature (Fig. 5.6). The C^s and C^{sd} terms show no checkerboard order.

However, the doublon density correlator C^d still provides a bound on the pairing correlator C^{Δ} as we verified numerically for the entire range of interactions, temperatures and fillings studied in the experiment (Fig. 5.5).

Corrections to the Hubbard model

We investigated the importance of corrections to the Hubbard model in our analysis of the experimental data. For this purpose, two effects were taken into account:

• Effects of next-nearest-neighbor tunneling From a tight-binding calculation, we obtain for a lattice depth of 6.2 E_R (used for gases prepared with scheme 1) tunnel couplings $t_{11}/t \sim 4\%$ and $t_{20}/t \sim -10\%$, where t_{ij} is the tunneling matrix element to the (1,1) and (2,0) neighboring site, respectively. We studied the effect of including these terms in the Hamiltonian on the doublon density

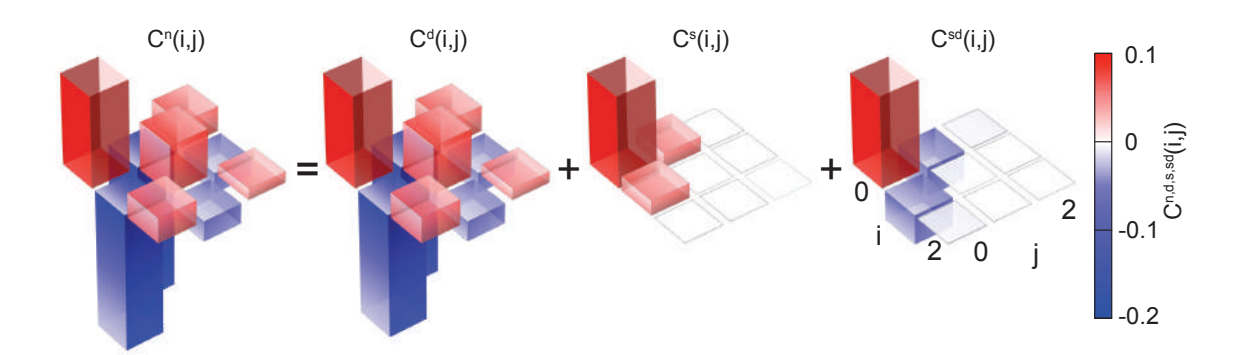


Figure 5.6: Contribution of different correlations to the total density correlator C^n . All DQMC results here are obtained at U/t = -5.7, T = 0.45t and half filling. Notice that the checkerboard order (alternating red and blue bars) is only present in C^n and C^d .

correlations (Fig. 5.7) and found it to be negligible within our experimental errors.

• Density-dependent tunneling The simple Hubbard model we use in this thesis assumes that the tunneling matrix element for an atom is independent of the occupancy of the site it is tunneling to. This approximation starts to break down as the scattering length a_s becomes large, and it may be expected that this effect is important in our system since most of the atoms are in pairs. The density-dependent hopping can be expressed in a tight-binding model as [186]

$$t_n = -\frac{4\pi\hbar^2 a_s}{m} \int d^3r w^*(\mathbf{r} - \mathbf{a}) w^*(\mathbf{r}) w^2(\mathbf{r})$$
(5.19)

where $w(\mathbf{r})$ is the Wannier function of an atom on a site and \mathbf{a} is the displacement vector to a neighboring site. For scheme 1 experiments, $t_n/t \sim -8\%$ and for scheme 2 experiments $t_n/t \sim -16\%$. To study the effect of the density-dependent tunneling on the measured doublon density correlations and singles fraction, we performed Numerical Linked Cluster Expansion (NLCE) simulations where the tunneling was replaced by $t_{\sigma,\mathbf{r},\mathbf{r}'} = t + (n_{-\sigma,\mathbf{r}} + n_{-\sigma,\mathbf{r}'})t_n$, where if $\sigma = \uparrow$, $-\sigma = \downarrow$ and vice versa. In other words, the tunneling of a spin σ from site \mathbf{r} to \mathbf{r}' depends on the total density of the opposite spin at the two sites between which the tunneling process is taking place. The strongest effect was about 10% on the singles fraction and that would change the fit value of the data in Fig. 5.12(b),(c) to U/t = -5.4 and T = 0.4t. Both this value of U/t and the one obtained without corrections to the Hubbard model fall within our experimental uncertainties.

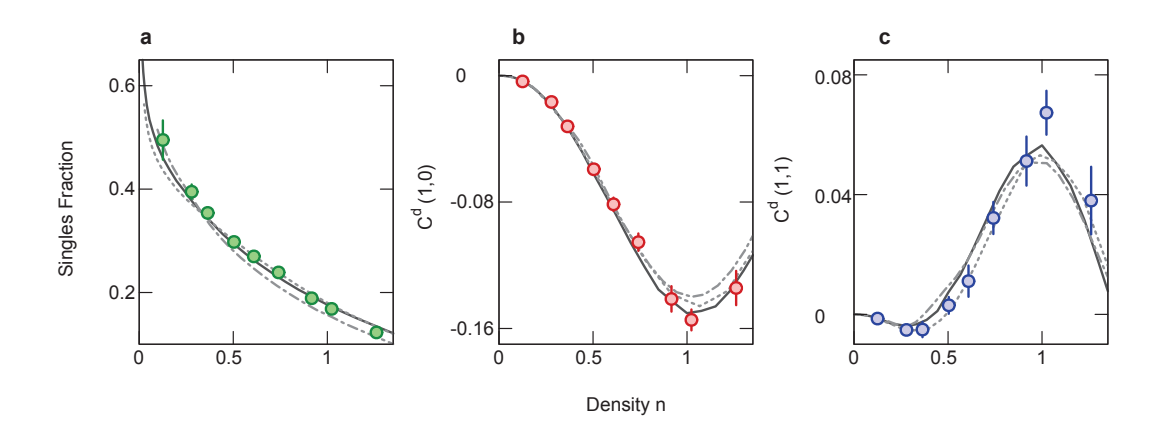


Figure 5.7: Fitting to DQMC and numerical study of effect of corrections to the Hubbard model. (a) Experimental singles fraction (green circles) as a function of filling for a 6.2(2) E_R lattice. (b) Experimental nearest neighbor doublon density correlator $C^d(1,0)$ (red circles) versus filling. (c) Experimental next-nearest neighbor doublon density correlator $C^d(1,1)$ (blue circles) versus filling. In all of the above, black line represents DQMC Hubbard model simulation results for U/t = -5.7 and T = 0.45t. Gray dotted line represents DQMC simulation results for the above U/t and T/t but including longer-range tunneling terms with $t_{11}/t = 4\%$ and $t_{20}/t = -10\%$. Gray dashed line represents NLCE simulation results with density-dependent hopping at the same U/t and T/t for $t_n/t = -8\%$.

5.3.4 Measuring correlations vs n

As was discussed in the last section, the correlator of the total density is not directly accessible from our data, so we extract a closely related quantity, the doublon density correlator $C^d(\mathbf{a}) = 4\langle n_{\mathbf{r}}^d n_{\mathbf{r}+\mathbf{a}}^d \rangle_c$. In a gas consisting mostly of on-site pairs, $C^d(\mathbf{a}) \approx C^n(\mathbf{a})$, and so it also exhibits checkerboard order. In the local density approximation, we obtain the doublon density correlator as a function of density naturally because of the harmonic trap.

As the attractive gas is compressible for any filling below unit filling (n=2), the local density varies across the harmonic trap. Fig. 5.8(a) shows the doublon density correlator versus density for the nearest-neighbor and the next-nearest-neighbor, obtained by azimuthally averaging the correlations over the trap. The corresponding trap density profile of the gas is depicted in Fig. 5.8(b). The nearest-neighbor doublon density correlator measured at half-filling, where the correlations are largest, is $C^d(1,0) = -0.155(6)$. An interesting feature of the next-nearest-neighbor correlator $C^d(1,1)$ is that it becomes negative as the average density falls below ~ 0.4 . This can be understood in the limit of large negative U, where the system can be treated as a gas of hardcore bosons with repulsive nearest-neighbor interactions, leading to negative correlations at distances less than the interparticle spacing. We observed similar behavior in the next-nearest-neighbor antiferromagnetic correlations of the z-projection of the spin in a spin-imbalanced repulsive Hubbard model [60]. This is a consequence of the mathematical mapping between the attractive and repulsive models.

We saw very good agreement between the experiment and DQMC fits for the doublon density correlators and density (Fig. 5.8). We simultaneously fit the singles fraction (n^s/n) , the nearest neighbor doublon density correlator $(C^d(1,0))$ and the next nearest neighbor doublon density correlator $(C^d(1,1))$ as a function of density (n) to the Hubbard model in local density approximation (LDA). In LDA, when the density varies slowly, the system can be approximated to be locally homogenous and is characterized by a local chemical potential. This local μ is then varied to simulate the trap effect. The fit parameters are thus only U/t and T/t, providing us with an alternate method to calibrate Hubbard parameters (section 5.3.1). An example of the fit can be found in Fig. 5.7.

From our fits, we get U/t = -5.7(2) and T/t = 0.45(3). The measured temperature is comparable to the temperatures (0.40(5)) we obtain for a gas in a repulsive Hubbard system [60]. The fact that the same temperature fits both the doublon density correlator and the density suggests that the system is in thermal equilibrium. In addition, we obtained the pairing correlations $C^{\Delta}(\mathbf{a})$ from DQMC as described in the previous section. As an example, we show the predicted pairing correlations versus density for the parameters above (Fig. 5.8(a)). We can see that $|C^d(\mathbf{a})| \leq |C^{\Delta}(\mathbf{a})|$ for all densities. At half-filling, we know that $C^n(\mathbf{a}) = C^{\Delta}(\mathbf{a})$ and $C^d(\mathbf{a}) \leq C^n(\mathbf{a})$. This implies that measuring the doublon density correlators indirectly gives us access to s-wave pairing correlations. Thus our measurement provides a first bound on s-wave pairing correlations in a cold atom lattice system.

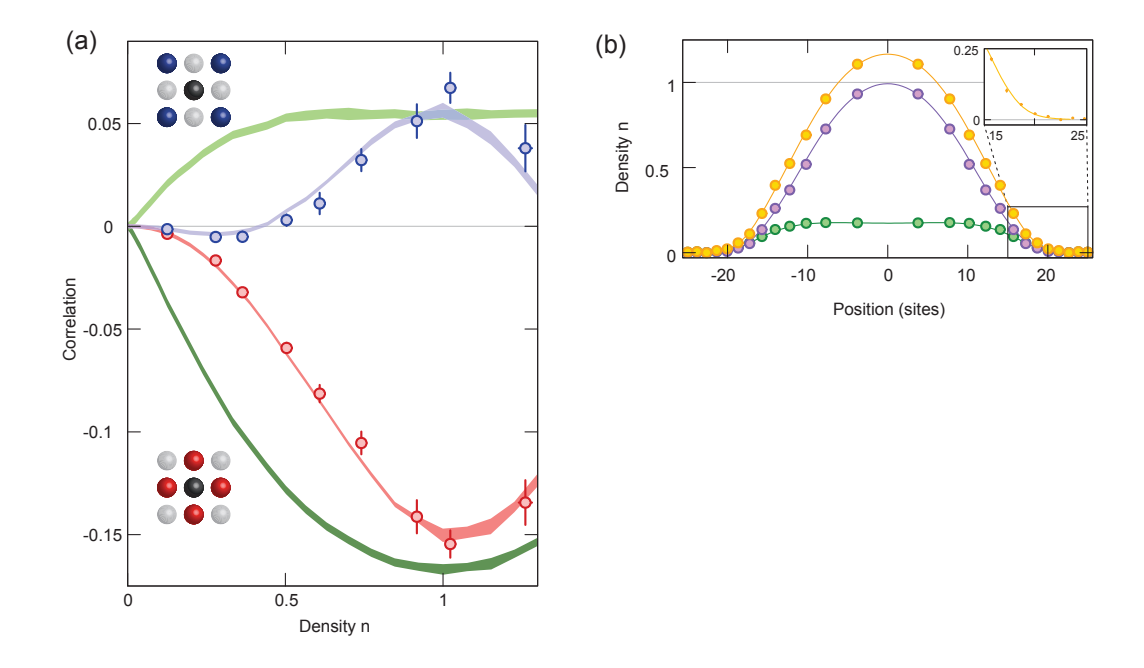


Figure 5.8: Observation of doublon density correlations. (a), Measured nearest-neighbor doublon density correlator $C^d(1,0)$ (red circles) and next-nearest-neighbor correlator $C^d(1,1)$ (blue circles) from an average of 60 repetitions. Error bars are s.e.m. DQMC results for $C^d(1,0)$ (red), $C^d(1,1)$ (blue), $-C^{\Delta}(1,0)$ (dark green) and $C^{\Delta}(1,1)$ (light green) at U/t=-5.7 and T/t=0.45 are shown for comparison (bands are s.e.m. of the numerics). (b) Density profiles. Density of singles $(n^s,$ green circles), density of doubles $(2n^d,$ purple circles) and total density $(n=n^s+2n^d,$ orange circles). Lines are a simultaneous local density approximation fit of DQMC data to the total and singles densities. Inset, zoom in on the tail of the density distribution. For this fit, we fix U/t and T/t at the values above and we obtain from the fit the central chemical potential $\mu(0)=0.46(2)U<0$ and the trap frequency $\omega=2\pi$ 202(5) Hz, in agreement with independent measurements of ω .

In addition to nearest and next nearest neighbors, we can measure longer distance correlations (Fig. 5.9). The applicability of LDA is not only limited by the finite temperature, but also by the variation of the density in the harmonic trap. Unlike repulsive interactions where the cloud becomes incompressible at half-filling in the Mott plateau, an attractively interacting cloud is always compressible for any filling other than unit filling. To obtain the longest-range correlations, the half filled region was created near the trap center, so it experiences the smallest potential gradient. Away from the center, the large potential gradients may be of concern when comparing to numerics due to a possible breakdown of LDA. For the above cloud profiles, we see doublon density correlations up to two sites on a diagonal shown in the correlation matrices $C^d(i, j)$. Again we can compare further neighbor correlations with DQMC, always assuming LDA. We find good agreement with DQMC calculations corresponding to the experimental densities, calculated using the same parameters as

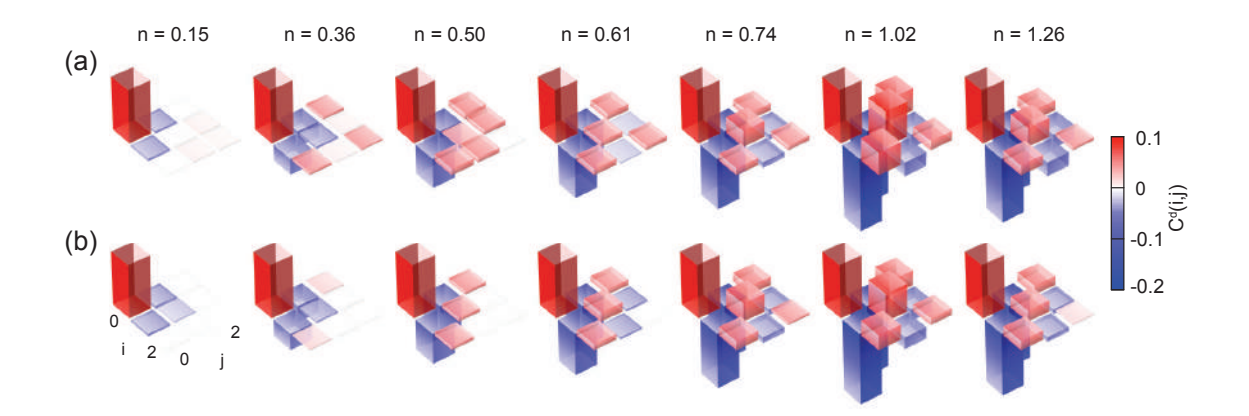


Figure 5.9: Doublon density correlation matrices for varying density. (a), Doublon density correlator $C^d(i,j)$ for average densities ranging from 0.15 to 1.26. Correlator values are averaged over 60 pictures. (b), DQMC matrices calculated for the same parameters as in Fig. 5.8.

above. We notice that the range of the correlation becomes maximal at half filling, as one would expect from theory where the correlations are also the strongest.

We also measured the doublon density correlators in scheme 2 (Fig. 5.10) described in the beginning of this section. The primary difference between the two schemes is the field where evaporation takes place. It is not clear a priori which evaporation method would yield a gas with a lower entropy. The least negative scattering length we can access with scheme 2 is $-2800a_0$, limited by the largest magnetic fields we can reach in our experiment, so we use a lower lattice depth of 4.1(1) E_R to reach the same value of U/t as for scheme 1 experiments. The advantage of that is shallower density gradient due to the trap. We obtain nearest-neighbor doublon density correlations of -0.172(5) at half filling, suggesting that we reach similar temperatures with both preparation schemes. The correlation matrices in Fig. 5.10 do not agree very well with theory, especially for larger site separations, which is expected since the onsite interaction energy is comparable to the vertical lattice confinement, leading to higher-band effects which modify the Hamiltonian. A precise determination of the temperature in this case requires taking these effects into account.

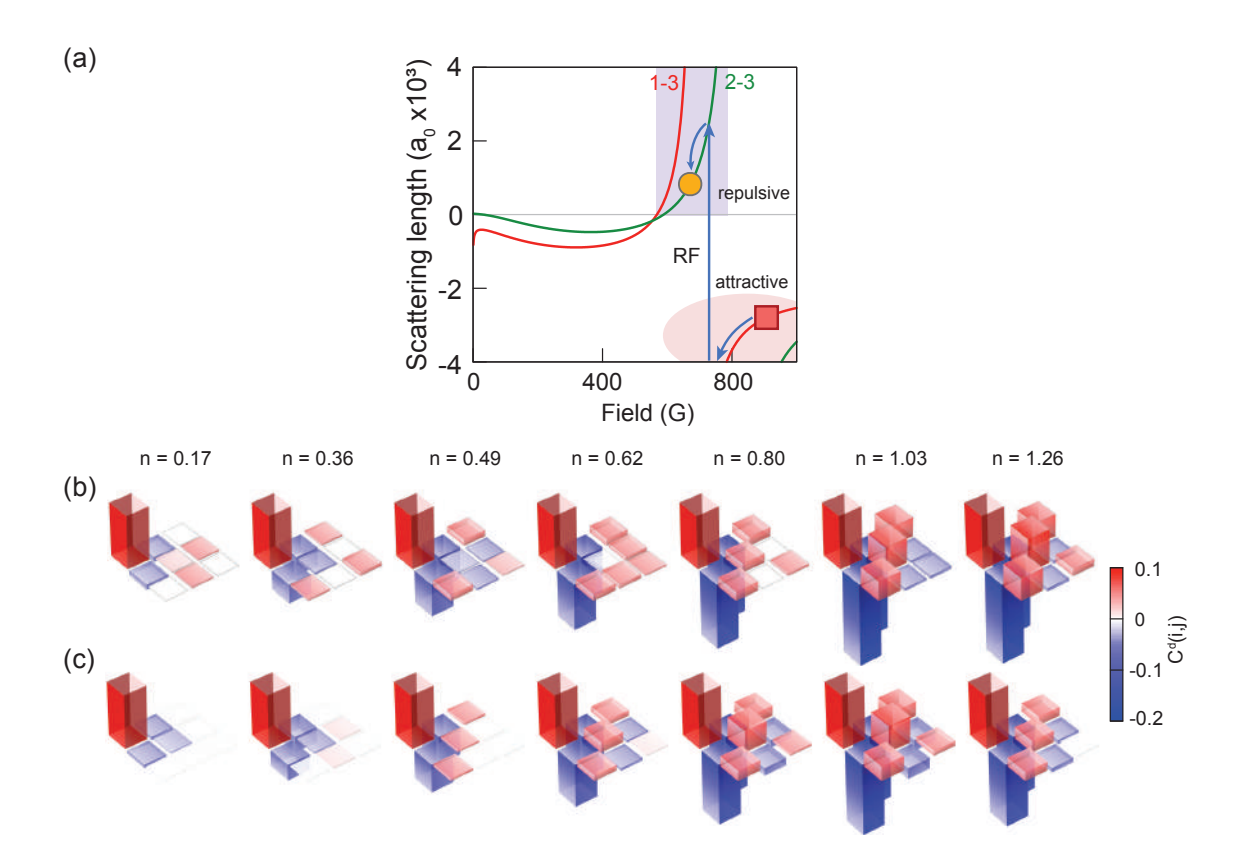


Figure 5.10: Observation of doublon density correlators in an attractive Hubbard system prepared using scheme 2. (a) The lattice is loaded at a scattering length $a_{13} = -2800 \ a_0$ (red square). After freezing the density distribution, we convert 1-3 doublons to 2-3 doublons of which the state $|3\rangle$ atom is pushed in a regime of repulsive interactions and we are left with only one atom per site (orange circle at $a_{23} = 414 \ a_0$). (b) Measured doublon density correlator for systems prepared using scheme 2 for varying filling. (c) Doublon density correlator obtained through DQMC simulations for experimental values of filling.

5.3.5 Measuring correlations vs U/t

In the previous section, we studied the dependance of the local density on charge density wave correlations. We saw that these correlations were maximized and had the longest range at half filling (n = 1). In addition, we found that these correlations are a lower bound for s-wave pairing correlations that one would expect in the attractive Hubbard model at our temperatures. So as a natural extension of the general study of the model, we next vary the interaction U/t. There are two ways to change U. The first one is to change the scattering length (a_s) by varying the magnetic field and the second is to change the lattice depth V. The disadvantage of the first method is that a_{13} is already the largest negative value reached for the 1-3 mixture away from the Feshbach resonance (for scheme 1) at 305 G. So we can only study lower U this way. The disadvantage of the second method is that changing V has an effect on both U and U. Another drawback is that the radial confinement changes with V.

The system was prepared with scheme 1 at a scattering length of $-889 \ a_0$ and U/t was varied by changing the lattice depth. Fig. 5.11 shows the nearest-neighbor and next-nearest-neighbor correlator versus density for different lattice depths. The data was fit to DQMC results with U/t and T/t used as fit parameters as described previously. We observed a slight increase in the temperature for larger lattice depths. The measured correlations initially increase as the lattice depth is increased, but do not show significant variation for lattice depths between 6.2 E_R and 7.4 E_R . This is expected from DQMC simulations as we saw in Fig. 5.5(b). At larger depths, it became experimentally difficult to obtain a half-filling condition near the center of the trap because of the increasing radial confinement from the lattice beams.

We also compared to DQMC in the presence of a spatially varying potential to reproduce the largest experimentally observed density gradients to verify that the LDA holds in our system. For data shown in Fig. 5.11, the density gradient at n = 1 varied from 0.07 atoms/(site)² for a depth of 4.1 E_R to 0.14 atoms/(site)² for a depth of 7.4 E_R . We performed DQMC simulations in the presence of a linearly varying chemical potential along one direction of the 2D Hubbard lattice to reproduce the maximal density gradients observed in the experiment. The results of this calculation showed that LDA holds to excellent approximation for our experimental parameters. However, we note that violation of the LDA had been predicted for such a system at much lower temperatures and higher gradients [187].

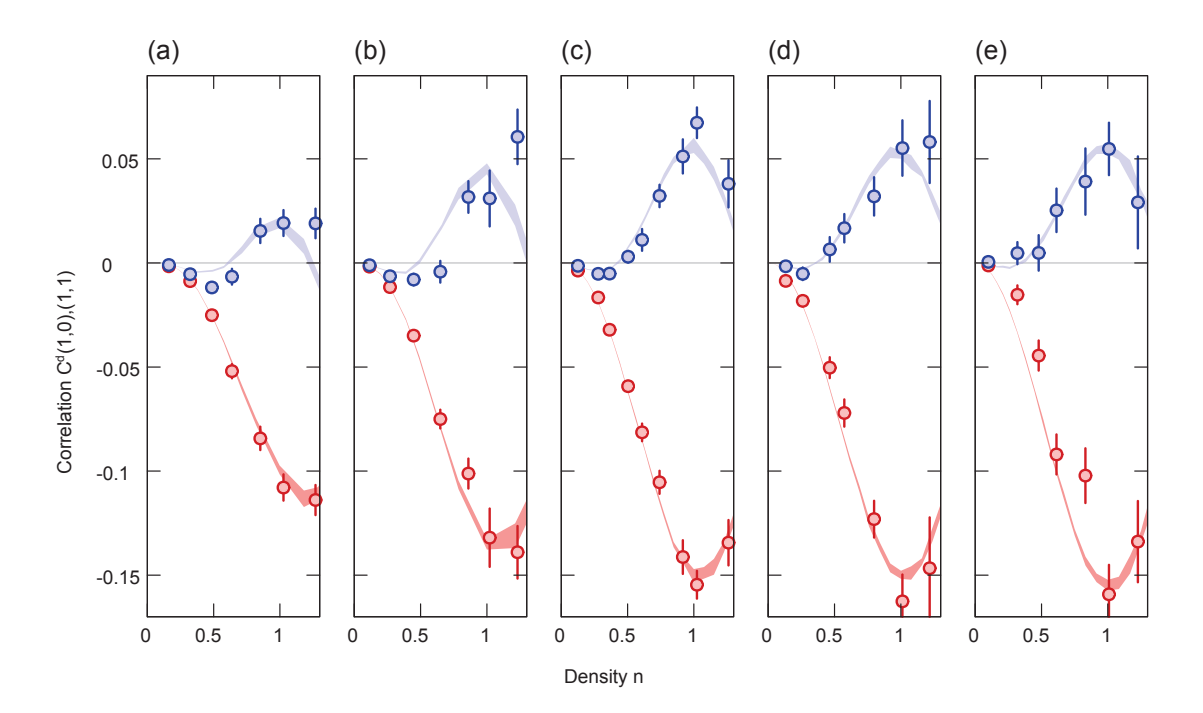


Figure 5.11: Nearest-neighbor and next-nearest neighbor doublon density correlators vs. filling as a function of lattice depth. $C^d(1,0)$ (red circles) and $C^d(1,1)$ (blue circles) obtained from different parts of the trap where filling varies from 0 to slightly above half-filling. (a) For lattice depth of 4.1(1) E_R , (b) 5.5(1) E_R , (c) 6.2(2) E_R , (d) 6.7(2) E_R , (e) 7.4(2) E_R . Shaded curves are DQMC fits for the data versus filling with U/t and T/t as fit parameters. (a) U/t = -2.75, T = 0.4t, (b) U/t = -4.5, T = 0.4t, (c) U/t = -5.7, T = 0.45t, (d) U/t = -6.75, T = 0.5t, (e) U/t = -7.5, T = 0.5t. The width of the shaded band is the s.e.m. of the simulation data.

5.3.6 Thermometry

In the last few sections, I have shown how quantum gas microscopy can effectively simulate the Hubbard model. But our consistency checks so far have been state-of-the-art numerical simulations. These simulations, however, suffer from issues like the fermion sign problem at low temperatures and with imbalanced spins and the inability to simulate large systems. So at some temperature scale it is expected that quantum gas microscopy will venture into numerically uncharted territory. One such territory is the FFLO phase which is expected to occur below temperatures of 0.1t [164]. The equivalent phase for the repulsive Hubbard model would be an incommensurate antiferromagnet at finite doping [86]. These phases are still out of reach of current experiments as the coldest Fermi Hubbard system so far has reached a temperature of $\sim 0.25t$ [179]. The development of new cooling techniques to reach lower temperatures will need to be accompanied by the development of low temperature thermometry techniques.

Both the doublon fraction and doublon density correlations may be used as thermometers in an attractive Hubbard system. To investigate their sensitivity as thermometers, we heated the system in a controlled fashion by holding it for variable times in the lattice before imaging. Technical noise leads to a linear increase in the temperature. We observe a slight reduction in doublon fraction in the half filled region for long hold times (Fig. 5.12(a)), while the doublon density correlators $C^d(1,0)$ and $C^{d}(1,1)$ show a significant change during the same time. These observations illustrate that the doublon fraction is a good thermometer for temperatures on the order of U, where doublon density correlations are small, while the latter are a more sensitive thermometer for temperatures on the order of the exchange energy $4t^2/U$. This is similar to the case of repulsive interactions, where spin correlations have been found to be a more sensitive thermometer than density [176]. Fig. 5.12(b) and (c) show the nearest-neighbor and next-nearest-neighbor doublon density correlators versus the singles fraction at half-filling. Plotting the data this way allows a temperatureindependent comparison to DQMC with a single free-parameter (U/t), and we obtain good agreement for U/t = -5.7.

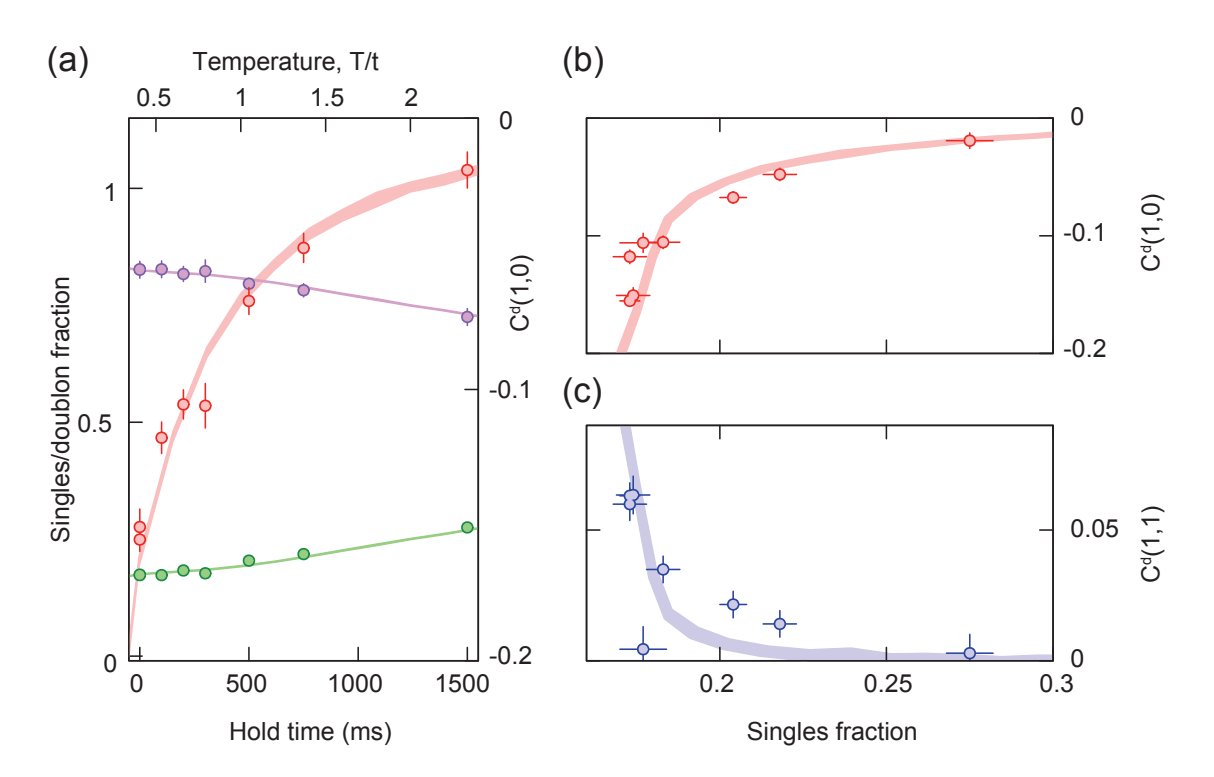


Figure 5.12: Thermometry of an attractive Hubbard system. (a) Temperature dependence of the paired fraction and nearest-neighbor doublon density correlations. Shown are the fraction of singles (green circles) and doubles (purple circles) at half-filling on the left axis as a function of hold time in the lattice. On the right axis is the doublon density correlator $C^d(1,0)$ (red circles) at half-filling measured for the same hold times. The upper x-axis are temperatures obtained from comparison to DQMC, giving a linear heating rate of 1.3(1) t/s. (b) $C^d(1,0)$ as a function of singles fraction. Each data point corresponds to a single hold time. (c) The next-nearest neighbor doublon density correlator $C^d(1,1)$ as function of singles fraction. Bands correspond to DQMC results for U/t = -5.7 and half filling in all of the above. Each point is averaged over 60 pictures. Error bars and bands are s.e.m.

5.4 Mapping and further work

In this section, we compare the results of this chapter on attractive Hubbard model at finite doping with the results of our previous work on the spin-imbalanced repulsive Hubbard model [60]. We described in section 5.2 a particle-hole transformation under which $U \leftrightarrow -U$, $\mu \leftrightarrow h$ and $\eta^{\pm,z} \leftrightarrow S^{\pm,z}$. In other words, a doped attractive system maps on to a spin polarized repulsive system. In addition, the charge density wave and s-wave superfluid order in the attractive system maps on to an isotropic antiferromagnet in the repulsive system (Fig. 5.13). We see that the in-plane spin correlator $C^{\perp}(\mathbf{a})$ follows the same trend as the s-wave pairing correlator $C^{\Delta}(\mathbf{a})$. Similarly, the out-of-plane spin correlator $C^z(\mathbf{a})$ should map on to the density correlator $C^n(\mathbf{a})$. We measure the doubles density correlator $C^d(\mathbf{a})$ which is similar to $C^n(\mathbf{a})$ and we see similar behavior between the two.

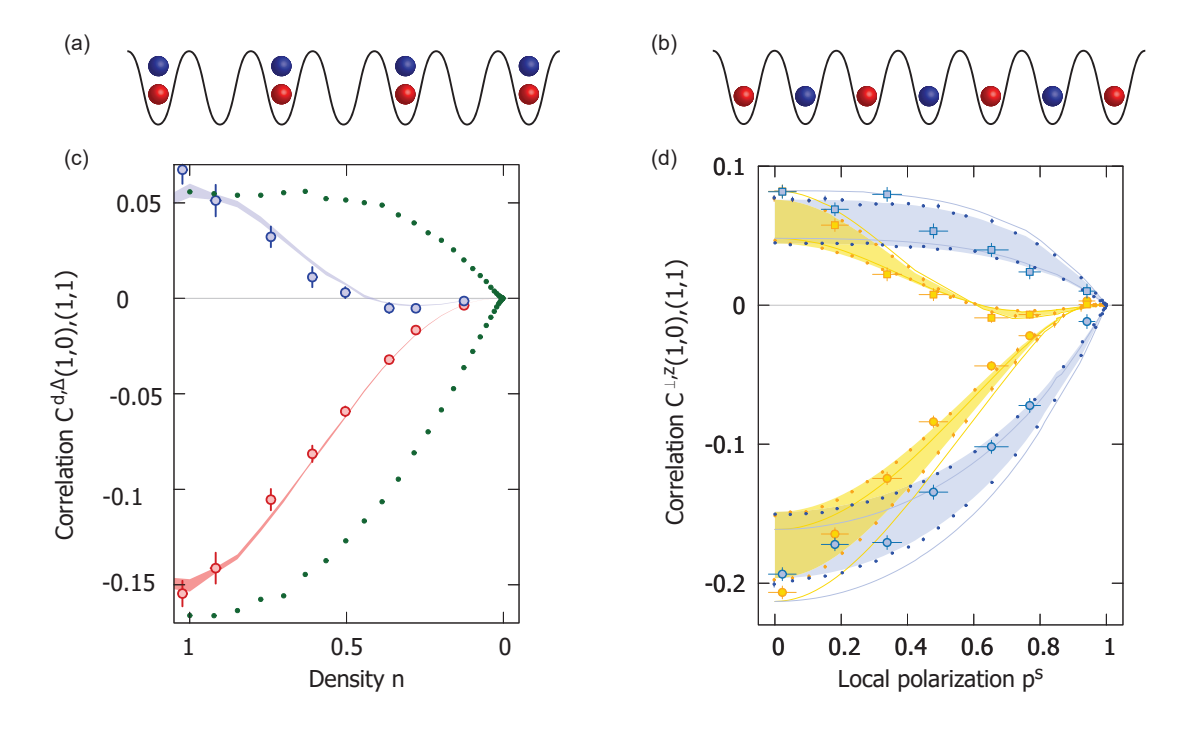


Figure 5.13: Mapping between the attractive and repulsive Hubbard model. (a) A charge density wave for negative U transforms to an antiferromagnet (b) for positive U under the particle-hole transformation. Red and blue circles denote spin \uparrow and \downarrow . (c) Doublon density correlator (C^d) for nearest neighbor (red) and next nearest neighbor (blue) plotted versus density n. In addition, the s-wave pairing correlator C^{Δ} computed using DQMC for identical parameters (green). (d) Spin correlations in-plane C^{\perp} (blue) and out-of-plane C^z (yellow) as a function of polarization taken from [60]. Notice that under the particle-hole transformation, the chemical potential μ (hence density n) switches roles with the Zeeman field n (hence polarization n), n0, n1. Since n2 and n3 and n4 and n5 are n5 and n5 and n6 and n6 are n6 and n6 and n7 and n8 are n9 are n9 and n9 are n9 are n9 and n9 are n9 are n9 are n9 and n9 are n9 are n9 and n9 are n9 and n9 are n9 are n9 and n9 are n9 are n9 and n9 are n9 and n9 are n9 are n9 and n9 are n9 and n9 are n9 and n9 are n9 are n9 and n9 are n9 and n9 are n9 and n9 are n9 are n9 are n9 and n9 are n9 are n9 are n9 and n9 are n9 and n9 are n9 and n9 are n9 are n9 and n9 are n9 a

Another related experiment that we have taken steps towards is to study the collective modes of the Hubbard model. For repulsive interactions, spin-waves would be generated in the system when it is excited through a Zeeman field, as is done in neutron scattering experiments [188]. Such a measurement is expected to be difficult for lithium because it requires a spin-dependent potential. For attractive interactions, however, chemical potential modulations couple to a new class of collective excitations [181].

To see the nature of these modes, consider the pseudo-spin operators defined in Eq. 5.10 in momentum space

$$\eta^{-} = \sum_{\mathbf{k}} c_{\mathbf{k}+\mathbf{Q},\uparrow} c_{-\mathbf{k},\downarrow}$$

$$\eta^{+} = (\eta^{-})^{\dagger}$$

$$\eta^{z} = \frac{1}{2}(n-1)$$
(5.20)

where $\mathbf{Q} = (\pi, \pi)$ is the largest reciprocal lattice vector and n is the filling of the lattice. When the operator η^+ acts on vacuum, we get a state $|\eta\rangle = \eta^+|0\rangle$, known as an η -excitation. It can be shown through the commutation relations (Eq. 5.12) that

$$\mathcal{H}|\eta\rangle = (U - 2\mu)|\eta\rangle \tag{5.21}$$

So the η -excitation that is created from vacuum is an eigenstate of the Hubbard Hamiltonian and thus propagates without scattering. This η -excitation is of finite energy away from half-filling and has a momentum \mathbf{Q} . This is the new collective excitation of the Hubbard model.

This excitation, however is particle-particle like and most experimental probes can not directly access it. But particle-hole (or density $\rho_{\bf q}$) excitations can lead to particle-particle excitations via interactions with a superconducting ground state in a process similar to Andreev reflection [189]. We can generate particle-hole excitations by adding a time dependent modulation to the chemical potential μ of the form $\delta \mu e^{i(qr+\omega\tau)}$, where q is the wave-vector of the modulation and ω is its frequency. then the perturbative term in the Hamiltonian (Eq. 5.4) will be of the form

$$\mathcal{H}_{pert} = \sum_{j,\sigma} n_{j,\sigma} \delta \mu_j = \delta \mu \sum_{j,\sigma} c_{j,\sigma}^{\dagger} c_{j,\sigma} e^{i(qr_j + \omega \tau)}$$
 (5.22)

If we perform the Fourier transform of the above expression, we get

$$\mathcal{H}_{pert} = \delta \mu e^{i\omega\tau} \sum_{\mathbf{k},\sigma} c_{\mathbf{k},\sigma}^{\dagger} c_{\mathbf{k}+\mathbf{q},\sigma} = \delta \mu e^{i\omega\tau} \rho_{\mathbf{q}}$$
 (5.23)

Where $\rho_{\mathbf{q}} = \sum_{\mathbf{k},\sigma} c_{\mathbf{k},\sigma}^{\dagger} c_{\mathbf{k}+\mathbf{q},\sigma}$ is the density operator. We are capable of creating these modulations up to the largest k-vector (π,π) by projecting a travelling sinudoidal

wave using a digital micromirror device (DMD) through our high NA objective (Fig. 5.14).

Although our experiments are significantly over T_c for the s-wave BKT transition in 2D, expected around 0.15-0.2t for our parameters [190], we would expect a measurable effect in the density spectral function at our temperatures because of strong superconducting fluctuations in the pseudogap regime above T_c [191].

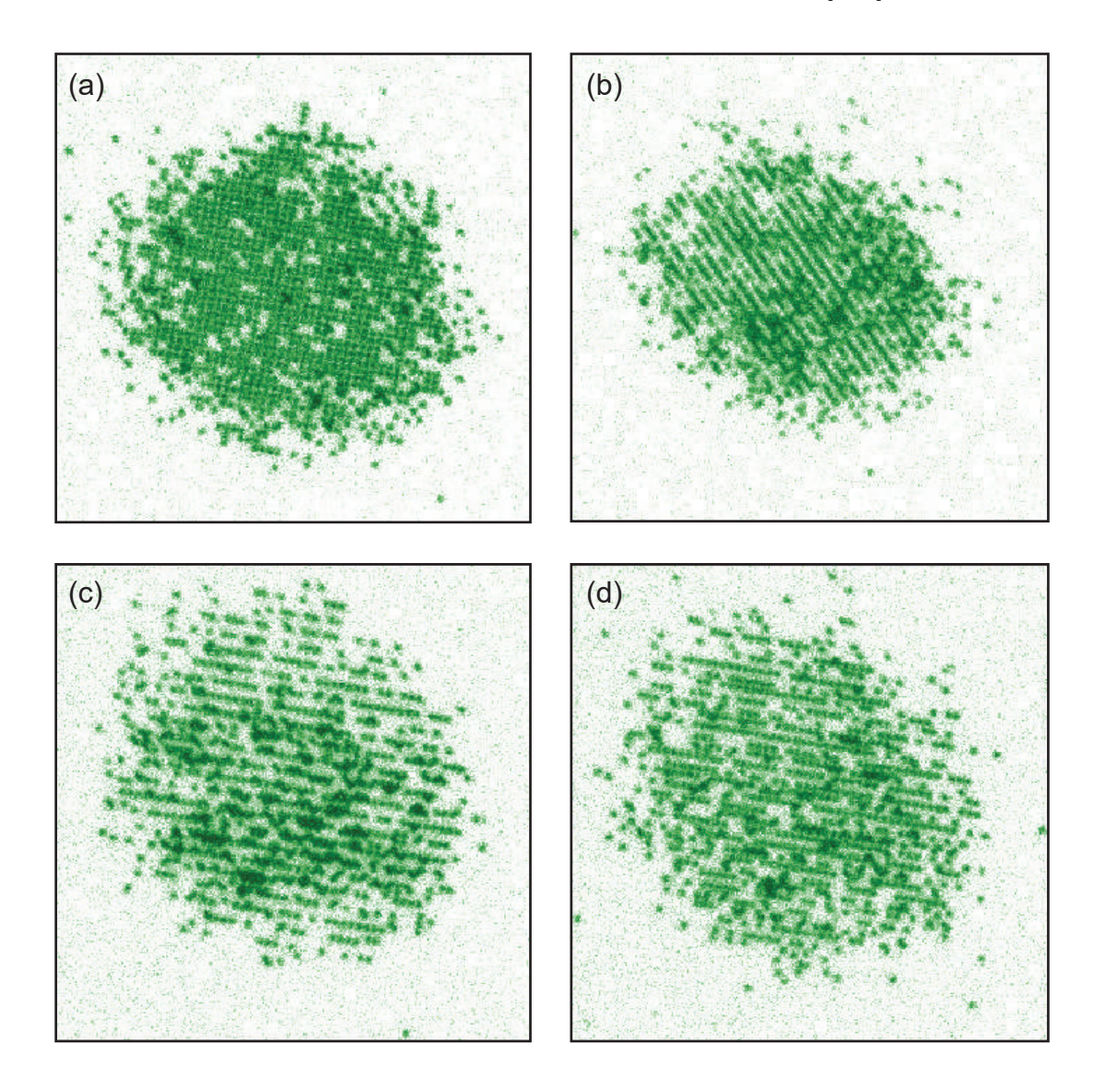


Figure 5.14: Single atom resolution images of the modulated lattice produced by projecting a sinusoidal pattern generated by a DMD. (a) Modulation at wave-vector (π,π) . (b) At wave-vector $(\pi,0)$. (c) At wave-vector $(\pi/2,\pi/2)$. (d) At wave-vector $(3\pi/4,3\pi/4)$.

Chapter 6

Conclusion

In conclusion, I have described the process of building a fermionic lithium quantum gas microscope in this thesis. We used the experimental setup to explore the physics of strongly interacting fermions with a focus on attractive interactions. In the next few paragraphs I will summarize the main scientific achievements of this thesis.

In chapter 4, I described in detail our study of pair condensation in "quasi" 2D across the BEC-BCS crossover [35]. We studied a spin imbalanced "quasi" 2D Fermi gas across the BEC-BCS crossover. We found that phase separation persists up to an interaction-dependent critical polarization P_c . This critical polarization decreases as one goes from the BEC regime, with high binding energy, to the BCS regime with weak attractive interactions. In addition, we discovered that the condensate does not vanish with phase separation, pointing to the existence of a polarized condensate. Finally we mapped the phase diagram of the 2D interacting Fermi gas. We note the existence of three phases, a balanced condensate, a partially polarized phase and a fully polarized Fermi gas. The results are a step towards measuring exotic pairing mechanisms in the presence of spin imbalance.

In chapter 5, I described our exploration of charge density wave correlations in the attractive Hubbard model [65]. We performed the first quantum gas microscopy of the attractive Fermi-Hubbard model. We measured the doublon density correlator $C^d(\mathbf{a})$. We measured the interaction U/t and the temperature T/t by simultaneously fitting the singles fraction, the nearest neighbor $C^d(1,0)$ and the next nearest neighbor $C^d(1,1)$ correlators. By measuring the sensitivity of the correlators and the density to temperature, we concluded that the correlators are a better thermometer at the exchange scale $4t^2/U$ while the densities are more sensitive at the scale of U. Finally, by employing DQMC simulations, we placed a lower bound on s-wave pairing in the system.

6.1 Future Work

What I have described in this thesis is just a glimpse of the physics of correlated fermionic systems that can be explored with quantum gas microscopes. Further work is required to shed light on many more poorly understood properties of the Hubbard model. One of the immediate challenges is to lower the temperature in our systems to access the critical temperature for d-wave superconductivity and the FFLO phase. One promising technique is entropy redistribution that has led to the lowest Hubbard temperature to date [179]. But even at our current temperatures, there remain many interesting aspects to explore.

One aspect is to measure the pseudogap regime in the attractive model at intermediate interactions. Measuring spin susceptibility χ_s is one such route [167]. One would expect χ_s to start descreasing as pairs begin to form. Another interesting direction is to perform RF spectrosocpy in a regime where many-body effects are important. For example, I showed in section 5.3.1 that there is good agreement between RF spectra and the expected tight-binding U in a deep lattice but deviations start occurring when the lattice is shallow and tunneling is non-negligible. However, these measurements are plagued by final state interactions. To circumvent the problem, one can either work at a field where the final state is non-interacting or take them into account numerically. The measurement of the spectral function of the Hubbard model will shed light on the pairing mechanisms, including a crossover from BEC-like to BCS-like pairing [192].

Another interesting direction lies in the study of Fermi gases with long-range interactions. We have been working on the implementation of Rydberg dressing in our experiments. When an atom is excited to a Rydberg state, dipolar interactions can be induced. Recently we studied quench dynamics in a 2D transverse Ising system using a UV laser to transfer atoms to the Rydberg state [193]. But the Rydberg atoms suffer from very short lifetimes. So the idea is to dress a ground state atom with a small admixture of the Rydberg state [194, 195]. One can study spin systems with long range interactions [196] or go beyond the frozen gas regime, i.e. when the fermions are free to tunnel in the lattice.

The study of dynamical properties of the Hubbard model poses a new set of challenges for numerical simulations [197]. We have measured charge transport in the repulsive Hubbard model [71]. But the same technique could be extended to measure transport in the superfluid phase of the attractive Hubbard model. There, one would expect an enhancement of conductivity as one crossed the pairing temperature scale.

The study of collective modes of the Hubbard model, as described in section 5.4, would enable further study of the dynamics of the Hubbard model. Observation of the conjectured η mode above T_c would be evidence of strong superconducting fluctuations [191].

Recent experiments have explored the Hubbard model under a Floquet drive [198]. In these driven lattices, the effective Hubbard parameters can be thought of as renormalized by the drive and can lead to enhancement of antiferromagnetic correlations or even their transformation to ferromagnetic correlations. They can be used to realize the t-J model with independent control over t and J such that the large J/t regime becomes accessible. This may lead to an enhancement of the superconducting critical temperature. Such driven Floquet Hamiltonians can be easily generated in our experiments and it would be interesting to study the microscopic spin correlations in such a system with a quantum gas microscope.

Appendix A Properties of ⁶Li

A.1 Atomic properties

Table A.1: Properties of ⁶Li [199]

Property	Symbol	Value	Units
Mass	$\frac{1}{m}$	1.0020×10^{-26}	Kg
D1 transition	λ_{D1}	670.992421	nm
D2 transition	λ_{D2}	670.977338	nm
Natural linewidth	Γ	5.8724	MHz
Electron spin g-factor	g_s	2.0023	
Electron orbital g-factor	g_L	0.999996	
Total Nuclear g-factor	g_I	-0.000448	
Total Electronic g-factor $(2^2S_{1/2})$	g_J	2.0023	
Total Electronic g-factor $(2^2P_{1/2})$	g_J	0.6668	
Total Electronic g-factor $(2^2P_{3/2})$	g_J	1.335	
$2^2S_{1/2}$ Magnetic Dipole Constant	$A_{2^2S_{1/2}}$	152.13684	MHz
$2^2 P_{1/2}$ Magnetic Dipole Constant	$A_{2^2P_{1/2}}$	17.386	MHz
$2^2 P_{3/2}$ Magnetic Dipole Constant	$A_{2^2P_{3/2}}$	-1.155	MHz
$2^2P_{3/2}$ Electric Quadrupole Constant	$B_{2^2P_{3/2}}$	-0.10	MHz
D1 Saturation Intensity	I_{sat}	7.59	$\mathrm{mW/cm^2}$
D2 Saturation Intensity	I_{sat}	2.54	$ \text{mW/cm}^2 $

A.2 Zeeman shifts

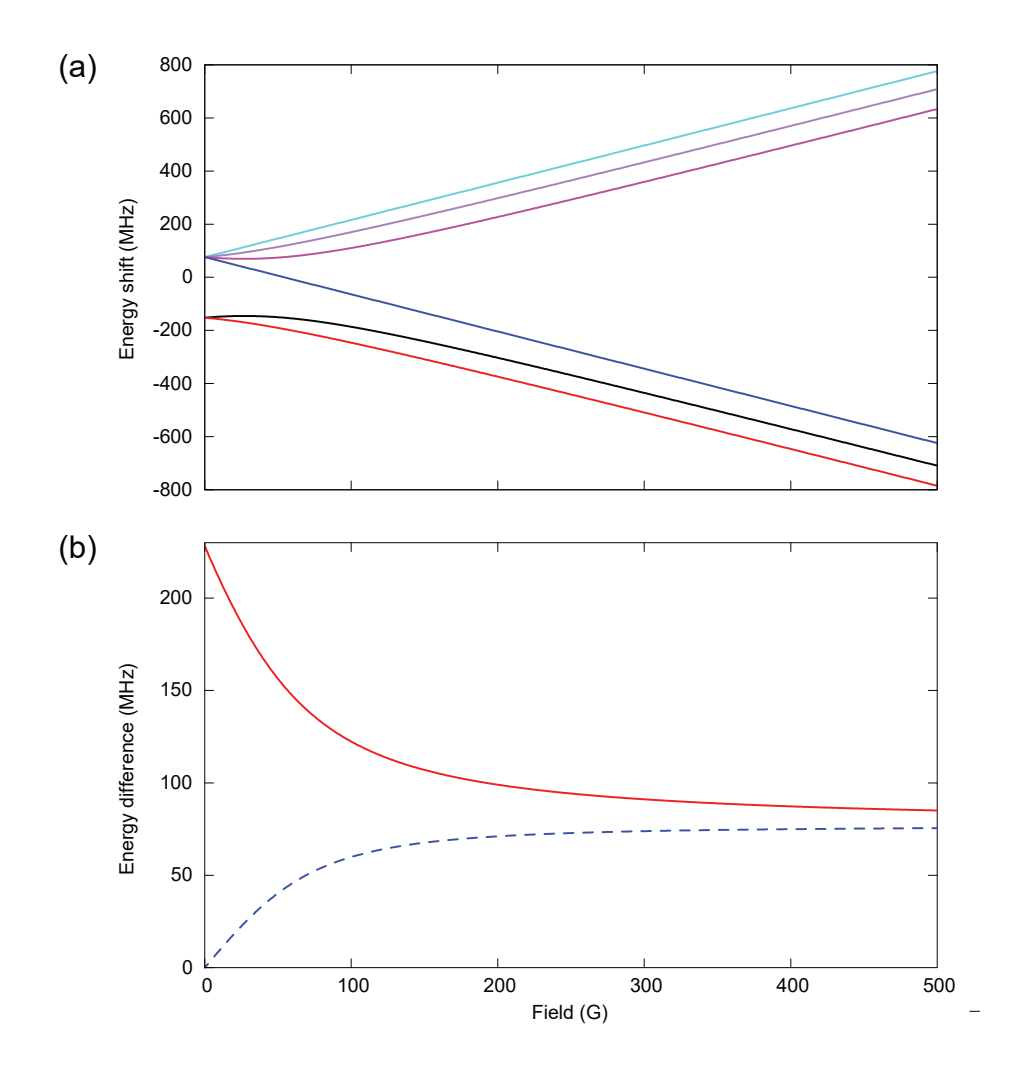


Figure A.1: (a) Zeeman shift for energy of the hyperfine sublevels of the ground state $2S_{1/2}$ of ^6Li as a function of B-field. The states are numbered as follows from bottom to top: $|1\rangle = [2S_{1/2}, \, F = 1/2, \, m_F = 1/2], \, |2\rangle = [2S_{1/2}, \, F = 1/2, \, m_F = -1/2], \, |3\rangle = [2S_{1/2}, \, F = 3/2, \, m_F = -3/2], \, |4\rangle = [2S_{1/2}, \, F = -1/2, \, m_F = 1/2, \, |5\rangle = 2S_{1/2}, \, F = 3/2, \, m_F = 1/2 \, \text{and} \, |6\rangle = [2S_{1/2}, \, F = 3/2, \, m_F = 3/2].$ Above a field of $\sim 200 \, \text{G}$, the splitting becomes effectively linear in the Paschen-Back limit. (b) Energy difference between states $|1\rangle$ and $|2\rangle$ (blue dashed line) and states $|2\rangle$ and $|3\rangle$ (red solid line) as a function of field. Due to the effective saturation at high fields, the RF antennas we use are resonant around 76 MHz for $|1\rangle - |2\rangle$ and around 85 MHz for $|2\rangle - |3\rangle$.

A.3 Scattering lengths

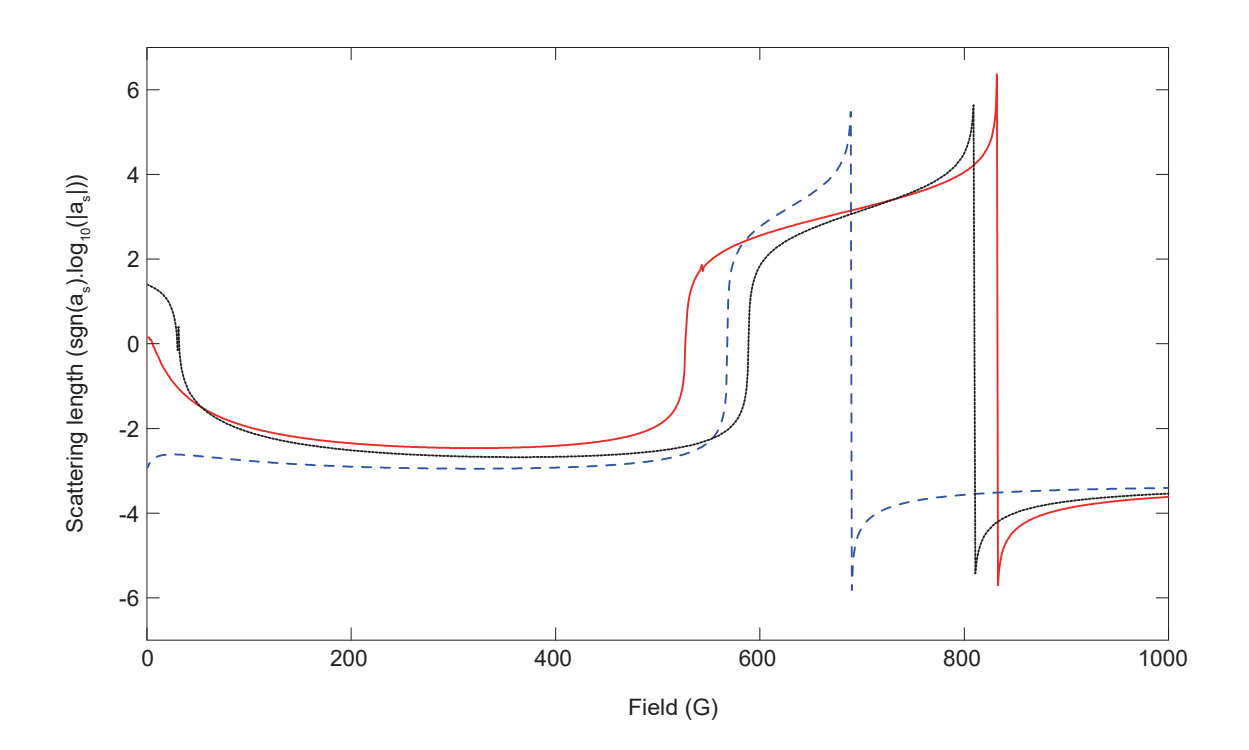


Figure A.2: Scattering lengths for ⁶Li as a function of B-field taken from [153]. Y-axis is $\operatorname{sgn}(a_s)\operatorname{log}_{10}(|a_s|)$, where a_s is the scattering length in units of the Bohr radius $(a_0 = 5.29 \times 10^{-11} \mathrm{m})$. Curves shown for the combination of the three lowest Zeeman sublevels of the hyperfine ground state $(2S_{1/2})$ of ⁶Li. The states are numbered as state $|1\rangle = [2S_{1/2}, F = 1/2, m_F = 1/2]$, $|2\rangle = [2S_{1/2}, F = 1/2, m_F = -1/2]$ and $|3\rangle = [2S_{1/2}, F = 3/2, m_F = -3/2]$. The broad Feshbach resonance for a $|1\rangle - |2\rangle$ mixture (red solid line) is located at 832 G. The broad Feshbach resonance for a $|2\rangle - |3\rangle$ mixture (black dotted line) is located at 809 G. The broad Feshbach resonance for a $|1\rangle - |3\rangle$ mixture (blue dashed line) is located at 689 G. The zero-crossings of the curves are also useful for radio frequency spectroscopy. They are located at 527 G for the $|1\rangle - |2\rangle$ mixture, at 589 G for the $|2\rangle - |3\rangle$ mixture and at 568 G for the $|1\rangle - |3\rangle$ mixture. Beyond 1200 G, the scattering length for all three mixtures saturates to a value of \sim -2210 a_0 .

Appendix B

Reentrant vacuum viewport design

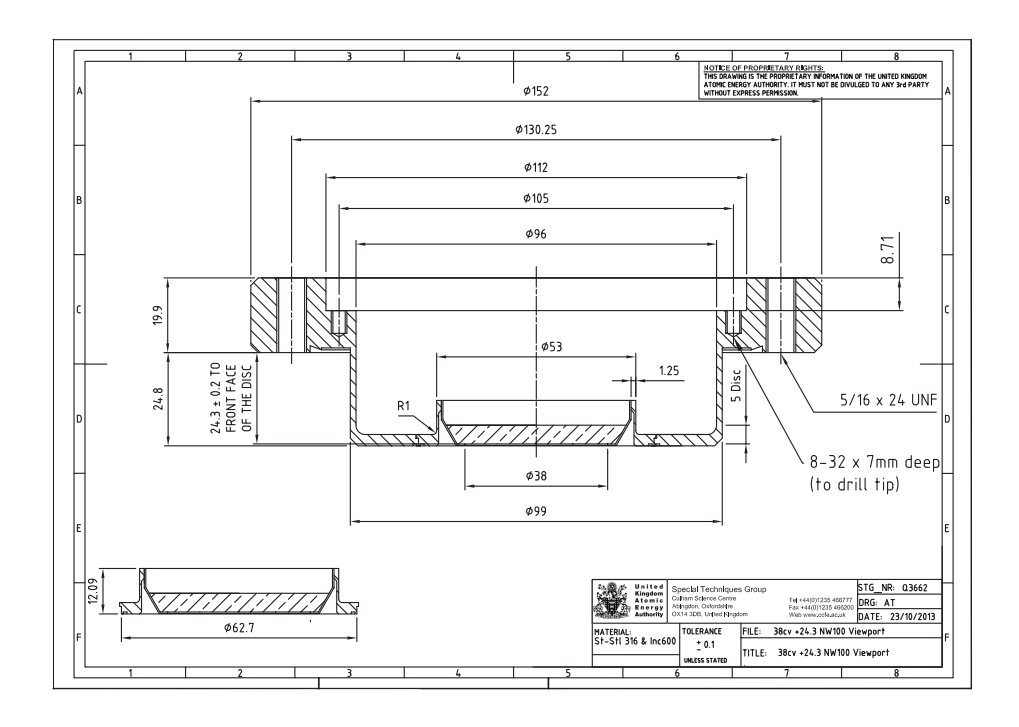


Figure B.1: Reentrant vaccum viewport. Note that per this drawing, all the holes in the reentrant viewport assembly are tapped. To be able to attach the viewport to the spherical octagon, we had to machine out the threads of $32 \text{ mm} \log 1/4-28$ bolts 24 mm from the head to be sufficiently clear of the 20 mm flange thickness and a washer.

Appendix C

AR/HR coatings

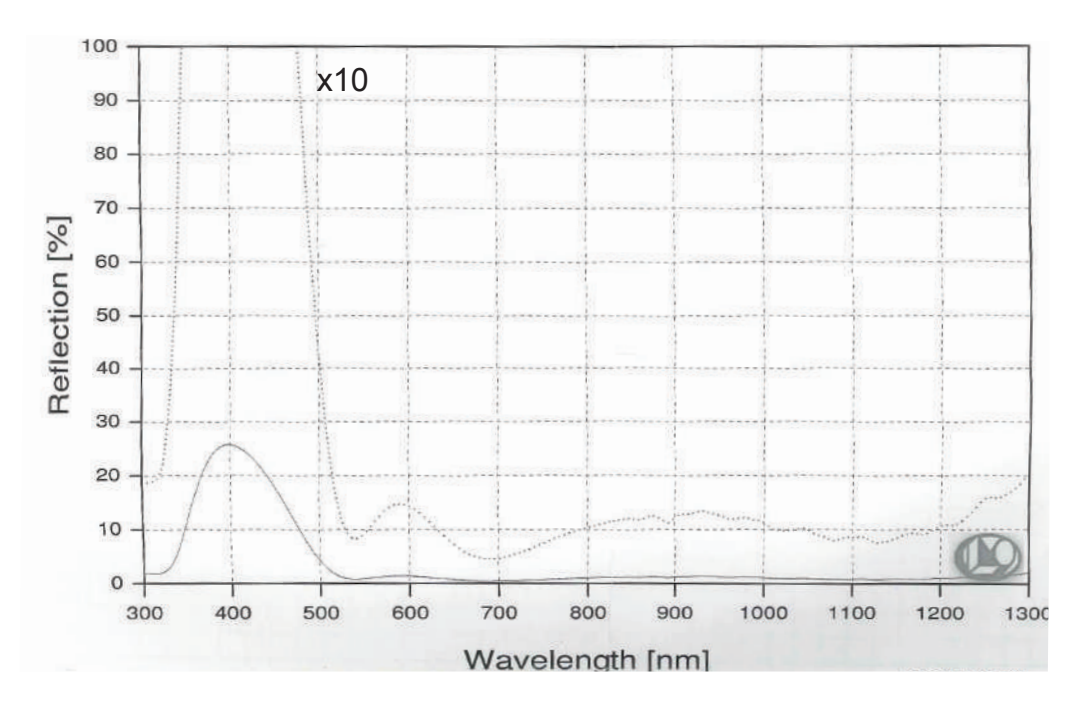


Figure C.1: Anti-reflection coating curve for all CF40 viewports for an angle of incidence of 0°

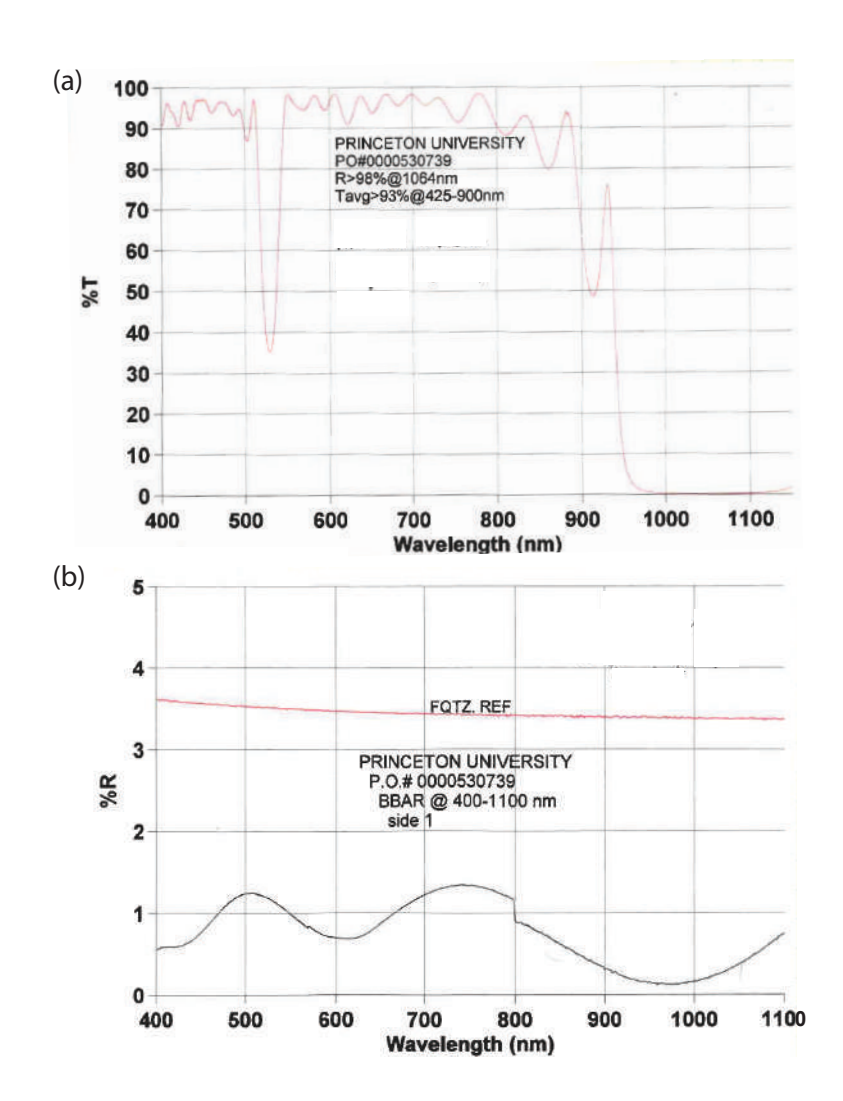


Figure C.2: High-reflection (a) and Anti-reflection (b) coating curves for reentrant vacuum viewports and for an angle of incidence of 0°

Appendix D

Lattice description

D.1 Lattice potential

In this section, we derive the expression for the lattice potential. First consider the case of a 4-fold interference (vertical polarization) of equal magnitude electric fields E_0 . Let us consider that the lattice principle axes are the x and y-axis. Let us define the origin as the point where the interference occurs and take time t=0. The magnitude of the electric fields are:

$$E_{1} = E_{0}e^{ik(x\sin(\theta/2)+y\cos(\theta/2))}$$

$$E_{2} = E_{0}e^{ik(x\sin(\theta/2)-y\cos(\theta/2))}$$

$$E_{3} = E_{0}e^{-ik(x\sin(\theta/2)+y\cos(\theta/2))}$$

$$E_{4} = E_{0}e^{-ik(x\sin(\theta/2)+y\cos(\theta/2))}$$
(D.1)

where k is the wave-vector given by $2\pi/\lambda$ and θ is the angle between the beams. The potential due to the interference of the 4 beams would be proportional to $|\sum E_i|^2$, which gives:

$$V^{\perp}(x,y) \propto 4|E_{0}|^{2}(\cos(kx\sin(\theta/2) + ky\cos(\theta/2)) + \cos(kx\sin(\theta/2) - ky\cos(\theta/2)))^{2}$$

$$\propto 16|E_{0}|^{2}\cos^{2}(kx\sin(\theta/2))\cos^{2}(ky\cos(\theta/2))$$

$$\propto 4|E_{0}|^{2}(1 + \cos(2kx\sin(\theta/2)))(1 + \cos(2ky\cos(\theta/2))) \tag{D.2}$$

Now consider the case where only two pairs of beams interfere (horizontal polarization), then the total potential is proportional to $|E_1 + E_3|^2 + |E_2 + E_4|^2$ giving

$$V^{\parallel}(x,y) \propto 4|E_0|^2(\cos^2(kx\sin(\theta/2) + ky\cos(\theta/2)) + \cos^2(kx\sin(\theta/2) - ky\cos(\theta/2))$$

$$= 4|E_0|^2\left(\frac{1 + \cos(2kx\sin(\theta/2) + 2ky\cos(\theta/2))}{2} + \frac{1 + \cos(2kx\sin(\theta/2) - 2ky\cos(\theta/2))}{2}\right)$$

$$= 4|E_0|^2(1 + \cos(2kx\sin(\theta/2))\cos(2ky\cos(\theta/2))) \tag{D.3}$$

In order to compare the two potentials, they need to be referenced with respect to a standard energy scale of the system, which is the recoil energy. For the perpendular configuration, lattice spacing is $a = \lambda/\sqrt{2}$. So we define $E_R = E_R^{\perp} = \hbar^2 (\pi/a)^2/2m = \hbar^2 k^2/4m$. So the maximum depth is $V_0 = 16|E_0|^2/E_R$. But for the parallel configuration, the spacing is $a = \lambda/2$ and so $E_R^{\parallel} = \hbar^2 k^2/2m = 2E_R$. Hence the maximum depth in this case is $4|E_0|^2/E_R$. Hence the first configuration gives a lattice that is 4 times deeper than the second.

Next, we can calculate the 4-fold interference but with an attenuation r in the retro-reflected beams,

$$E_{1} = E_{0}e^{ik(x\sin(\theta/2)+y\cos(\theta/2))}$$

$$E_{2} = E_{0}e^{ik(x\sin(\theta/2)-y\cos(\theta/2))}$$

$$E_{3} = rE_{0}e^{-ik(x\sin(\theta/2)+y\cos(\theta/2))}$$

$$E_{4} = rE_{0}e^{-ik(x\sin(\theta/2)+y\cos(\theta/2))}$$
(D.4)

The resulting potential is proportional to

$$V_r^{\perp}(x,y) \propto 4|E_0|^2\cos^2(ky\cos(\theta/2))(1+r^2+2r\cos(2kx\sin(\theta/2)))$$

 $\propto 2|E_0|^2(1+\cos(2ky\cos(\theta/2)))(1+r^2+2r\cos(2kx\sin(\theta/2)))$ (D.5)

We can rewrite the above potential in a normalized form, knowing that the maximum value possible is $4|E_0|^2(1+r^2+2r)$.

$$V(x,y) = V_0 \left(1 - \frac{(1 + \cos(2ky\cos(\theta/2)))}{2} \frac{(1 + r^2 + 2r\cos(2kx\sin(\theta/2)))}{1 + r^2 + 2r} \right)$$
(D.6)

One can easily verify that in the case without attenuation (r=1), the potential $V(x,y) = V^{\perp}(x,y)$.

D.2 Band structure calculation

The simplest method of numerical single particle band structure calculation is by using the plane wave expansion. In this method, we expand the bloch wavefunctions in the basis of plane waves

$$\psi_q(x,y) = \sum_{m,n} a_{m,n} e^{i(q_x + 2\pi m/a)x + i(q_y + 2\pi n/a)y}$$
(D.7)

where (m, n) are integers and $a_{m,n}$ are complex coefficients. Consider first the kinetic term of a Hamiltonian $\hbar^2 k^2/2m$. If we want to write this term in the basis of (m, n) then the matrix will be diagonal. But the lattice potential V(x, y) has terms of the form $e^{ikx} + e^{-ikx}$ which would hybridize plane waves with different n and m.

The number N of plane waves to include in the sum depends on the number of bands to calculate. It leads to a Hilbert space of size $(2N+1)^2 \times (2N+1)^2$). For the lowest energy bands, $N \sim 10$ is enough. The Hamiltonian that one generates at a given value of q is:

$$\mathcal{H}_{q}((n,m),(n',m')) =$$

$$= V_{0} \frac{1 + r(4+r)}{2(1+r)^{2}} r + (q_{x} + 2n\cos(\theta/2))^{2} + (q_{y} + 2m\sin(\theta/2))^{2}, n = n'; m = m'$$

$$= -V_{0} \frac{r}{2(1+r)^{2}}, n = n' \pm 1; m = m'$$

$$= -V_{0} \frac{1+r^{2}}{4(1+r)^{2}}, n = n'; m = m' \pm 1$$

$$= -V_{0} \frac{r}{4(1+r)^{2}}, n = n' \pm 1; m = m' \pm 1$$
(D.8)

So the eigenvalues of this Hamiltonian at a given q gives the energy of the different bands and the eigenvectors give the Bloch wavefunction $\psi_q(x, y)$. The value of q varies between the edges of the Brilluoin zone. An example of the calculated band structure is shown in Fig. D.1(b) for a lattice depth of $10 E_R$ and r = 0.5.

From the Bloch wavefunctions, one can calculate the maximally localized Wannier functions in the n^{th} band as

$$w_n(x,y) = \frac{1}{\sqrt{N}} \sum_k \psi_k(x,y) e^{ikR}$$
 (D.9)

These Wannier functions can also be obtained from other projection techniques directly in real space [87]. From the knowledge of the Wannier functions, one can calculate the hopping which is an overlap integral of two Wannier functions on neighboring sites with the Hamiltonian. The reason for that is Wannier functions are not eigen states of the Hamiltonian. So if an atom were prepared in a Wannier state, it would tunnel to other Wannier states over time. The tunelling (J) between two sites is characterized by the matrix elements between respective Wannier states at those sites [200]

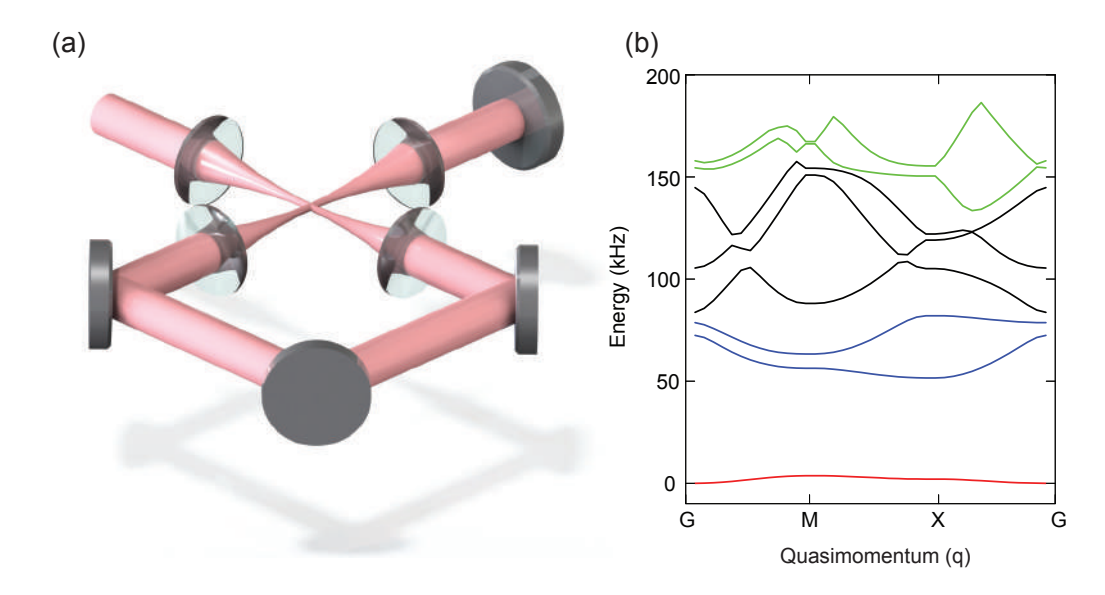


Figure D.1: Lattice band structure. (a) Schematic of the lattice formed due to 4-fold interference. (b) Band structure of the lattice calculated for $V_0 = 10E_R$ and r = 0.5. The three bands in black are the three d-bands that are used to fit the experimental measurement of lattice depth using amplitude modulation spectroscopy.

$$J = \int d\mathbf{r} \overline{w}_0(\mathbf{r}) \mathcal{H} w_0(\mathbf{r} - \mathbf{1})$$
 (D.10)

Similarly, the on-site interaction U can be obtained from the integration over two Wannier functions localized on the same site. This is valid under the assumption that the presence of one atom does not effect the Wannier functions of both atoms. The Wannier function in the third (z) direction is a harmonic oscillator. So the integral along z just introduces a multiplicative factor

$$U = \frac{4\pi\hbar^2 a_s}{m} \sqrt{\frac{m\omega_z}{h}} \int |w_0(x,y)|^4 dx dy$$
 (D.11)

where ω_z is the confinement in the third direction.

Appendix E

Objective specifications

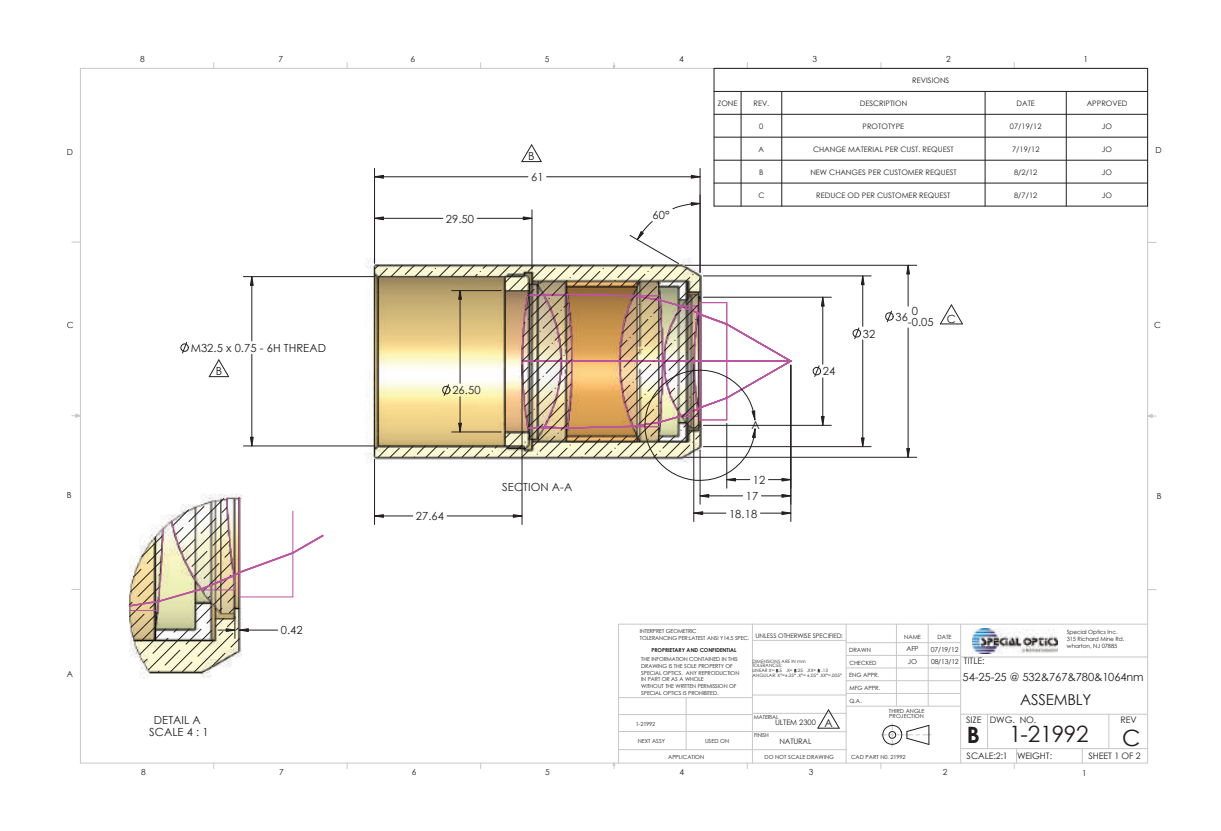


Figure E.1: Objective Design

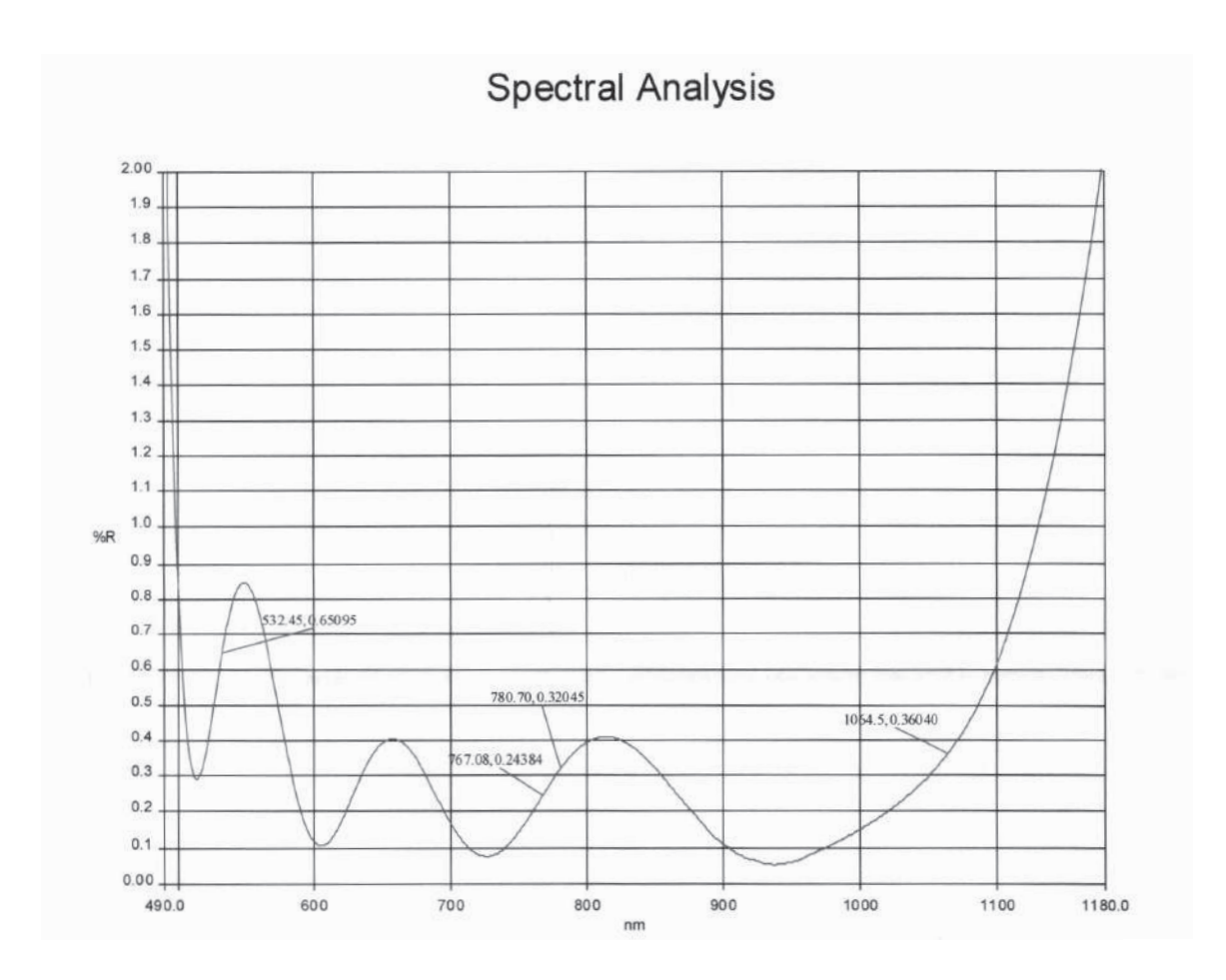


Figure E.2: AR coating on objective

Bibliography

- [1] V. Ginzburg and L. Landau. Toward the superconductivity theory. Zh. Eksp. Teor. Fiz., 29:1064, 1950.
- [2] J. Bardeen, L. N. Cooper, and J. R. Schrieffer. Theory of Superconductivity. *Phys. Rev.*, 108:1175–1204, 1957.
- [3] M. H. Anderson, J. R. Ensher, M. R. Matthews, C. E. Wieman, and E. A. Cornell. Observation of Bose-Einstein Condensation in a Dilute Atomic Vapor. *Science*, 269(5221):198–201, 1995.
- [4] K. B. Davis, M. O. Mewes, M. R. Andrews, N. J. van Druten, D. S. Durfee, D. M. Kurn, and W. Ketterle. Bose-Einstein Condensation in a Gas of Sodium Atoms. *Phys. Rev. Lett.*, 75:3969–3973, 1995.
- [5] B. DeMarco and D. S. Jin. Onset of Fermi Degeneracy in a Trapped Atomic Gas. *Science*, 285(5434):1703–1706, 1999.
- [6] Cheng Chin, Rudolf Grimm, Paul Julienne, and Eite Tiesinga. Feshbach resonances in ultracold gases. *Rev. Mod. Phys.*, 82:1225–1286, 2010.
- [7] Immanuel Bloch. Ultracold quantum gases in optical lattices. *Nature Physics*, 1:23–30, 2005. Review Article.
- [8] Ketterle W., M. Inguscio, and C. Salomon. Ultracold fermi gases. In *Proceedings* of the Varenna 'Enrico Fermi' Summer School, volume 164, 2007.
- [9] C. Chin, M. Bartenstein, A. Altmeyer, S. Riedl, S. Jochim, J. Hecker Denschlag, and R. Grimm. Observation of the Pairing Gap in a Strongly Interacting Fermi Gas. *Science*, 305(5687):1128–1130, 2004.
- [10] G. B. Partridge, K. E. Strecker, R. I. Kamar, M. W. Jack, and R. G. Hulet. Molecular Probe of Pairing in the BEC-BCS Crossover. *Phys. Rev. Lett.*, 95:020404, 2005.
- [11] M. W. Zwierlein, J. R. Abo-Shaeer, A. Schirotzek, C. H. Schunck, and W. Ketterle. Vortices and superfluidity in a strongly interacting Fermi gas. *Nature*, 435:1047–1051, 2005. Article.

- [12] Munekazu Horikoshi, Shuta Nakajima, Masahito Ueda, and Takashi Mukaiyama. Measurement of Universal Thermodynamic Functions for a Unitary Fermi Gas. *Science*, 327(5964):442–445, 2010.
- [13] N. Navon, S. Nascimbène, F. Chevy, and C. Salomon. The Equation of State of a Low-Temperature Fermi Gas with Tunable Interactions. *Science*, 328(5979):729–732, 2010.
- [14] Mark J. H. Ku, Ariel T. Sommer, Lawrence W. Cheuk, and Martin W. Zwierlein. Revealing the Superfluid Lambda Transition in the Universal Thermodynamics of a Unitary Fermi Gas. *Science*, 335(6068):563–567, 2012.
- [15] Tarik Yefsah, Ariel T. Sommer, Mark J. H. Ku, Lawrence W. Cheuk, Wenjie Ji, Waseem S. Bakr, and Martin W. Zwierlein. Heavy solitons in a fermionic superfluid. *Nature*, 499:426–430, 2013. Article.
- [16] Kenneth Günter, Thilo Stöferle, Henning Moritz, Michael Köhl, and Tilman Esslinger. p-Wave Interactions in Low-Dimensional Fermionic Gases. Phys. Rev. Lett., 95:230401, 2005.
- [17] Kirill Martiyanov, Vasiliy Makhalov, and Andrey Turlapov. Observation of a Two-Dimensional Fermi Gas of Atoms. *Phys. Rev. Lett.*, 105:030404, 2010.
- [18] Bernd Fröhlich, Michael Feld, Enrico Vogt, Marco Koschorreck, Wilhelm Zwerger, and Michael Köhl. Radio-Frequency Spectroscopy of a Strongly Interacting Two-Dimensional Fermi Gas. *Phys. Rev. Lett.*, 106:105301, 2011.
- [19] P. Dyke, E. D. Kuhnle, S. Whitlock, H. Hu, M. Mark, S. Hoinka, M. Lingham, P. Hannaford, and C. J. Vale. Crossover from 2D to 3D in a Weakly Interacting Fermi Gas. *Phys. Rev. Lett.*, 106:105304, 2011.
- [20] Ariel T. Sommer, Lawrence W. Cheuk, Mark J. H. Ku, Waseem S. Bakr, and Martin W. Zwierlein. Evolution of Fermion Pairing from Three to Two Dimensions. *Phys. Rev. Lett.*, 108:045302, 2012.
- [21] P. A. Murthy, I. Boettcher, L. Bayha, M. Holzmann, D. Kedar, M. Neidig, M. G. Ries, A. N. Wenz, G. Zürn, and S. Jochim. Observation of the Berezinskii-Kosterlitz-Thouless Phase Transition in an Ultracold Fermi Gas. *Phys. Rev. Lett.*, 115:010401, 2015.
- [22] C. A. Regal, M. Greiner, and D. S. Jin. Observation of Resonance Condensation of Fermionic Atom Pairs. *Phys. Rev. Lett.*, 92:040403, 2004.
- [23] Christian H. Schunck, Yong-il Shin, André Schirotzek, and Wolfgang Ketterle. Determination of the fermion pair size in a resonantly interacting superfluid. *Nature*, 454:739–743, 2008.

- [24] Michael Feld, Bernd Fröhlich, Enrico Vogt, Marco Koschorreck, and Michael Köhl. Observation of a pairing pseudogap in a two-dimensional Fermi gas. Nature, 480:75–78, 2011.
- [25] André Schirotzek, Cheng-Hsun Wu, Ariel Sommer, and Martin W. Zwierlein. Observation of Fermi Polarons in a Tunable Fermi Liquid of Ultracold Atoms. *Phys. Rev. Lett.*, 102:230402, 2009.
- [26] Y. Zhang, W. Ong, I. Arakelyan, and J. E. Thomas. Polaron-to-Polaron Transitions in the Radio-Frequency Spectrum of a Quasi-Two-Dimensional Fermi Gas. *Phys. Rev. Lett.*, 108:235302, 2012.
- [27] Marco Koschorreck, Daniel Pertot, Enrico Vogt, Bernd Fröhlich, Michael Feld, and Michael Köhl. Attractive and repulsive Fermi polarons in two dimensions. *Nature*, 485:619–622, 2012.
- [28] Giacomo Valtolina, Alessia Burchianti, Andrea Amico, Elettra Neri, Klejdja Xhani, Jorge Amin Seman, Andrea Trombettoni, Augusto Smerzi, Matteo Zaccanti, Massimo Inguscio, and Giacomo Roati. Josephson effect in fermionic superfluids across the BEC-BCS crossover. Science, 350(6267):1505–1508, 2015.
- [29] Martin W. Zwierlein, André Schirotzek, Christian H. Schunck, and Wolfgang Ketterle. Fermionic Superfluidity with Imbalanced Spin Populations. *Science*, 311(5760):492–496, 2006.
- [30] Y. Shin, M. W. Zwierlein, C. H. Schunck, A. Schirotzek, and W. Ketterle. Observation of Phase Separation in a Strongly Interacting Imbalanced Fermi Gas. *Phys. Rev. Lett.*, 97:030401, 2006.
- [31] G. B. Partridge, Wenhui Li, Y. A. Liao, R. G. Hulet, M. Haque, and H. T. C. Stoof. Deformation of a Trapped Fermi Gas with Unequal Spin Populations. *Phys. Rev. Lett.*, 97:190407, 2006.
- [32] Yean-an Liao, Ann Sophie C. Rittner, Tobias Paprotta, Wenhui Li, Guthrie B. Partridge, Randall G. Hulet, Stefan K. Baur, and Erich J. Mueller. Spinimbalance in a one-dimensional Fermi gas. *Nature*, 467:567–569, 2010.
- [33] S. Nascimbène, N. Navon, K. J. Jiang, F. Chevy, and C. Salomon. Exploring the thermodynamics of a universal Fermi gas. *Nature*, 463:1057–1060, 2010.
- [34] W. Ong, Chingyun Cheng, I. Arakelyan, and J. E. Thomas. Spin-Imbalanced Quasi-Two-Dimensional Fermi Gases. *Phys. Rev. Lett.*, 114:110403, 2015.
- [35] Debayan Mitra, Peter T. Brown, Peter Schauß, Stanimir S. Kondov, and Waseem S. Bakr. Phase Separation and Pair Condensation in a Spin-Imbalanced 2D Fermi Gas. *Phys. Rev. Lett.*, 117:093601, 2016.

- [36] O. Morsch, J. H. Müller, M. Cristiani, D. Ciampini, and E. Arimondo. Bloch Oscillations and Mean-Field Effects of Bose-Einstein Condensates in 1D Optical Lattices. *Phys. Rev. Lett.*, 87:140402, 2001.
- [37] Marcos Atala, Monika Aidelsburger, Julio T. Barreiro, Dmitry Abanin, Takuya Kitagawa, Eugene Demler, and Immanuel Bloch. Direct measurement of the Zak phase in topological Bloch bands. *Nature Physics*, 9:795–800, 2013.
- [38] M. Aidelsburger, M. Lohse, C. Schweizer, M. Atala, J. T. Barreiro, S. Nascimbène, N. R. Cooper, I. Bloch, and N. Goldman. Measuring the Chern number of Hofstadter bands with ultracold bosonic atoms. *Nature Physics*, 11:162–166, 2014.
- [39] P. W. Anderson. The Resonating Valence Bond State in La₂CuO₄ and Superconductivity. *Science*, 235(4793):1196–1198, 1987.
- [40] Elliott H. Lieb and F. Y. Wu. Absence of Mott Transition in an Exact Solution of the Short-Range, One-Band Model in One Dimension. *Phys. Rev. Lett.*, 20:1445–1448, 1968.
- [41] J. E. Hirsch. Two-dimensional Hubbard model: Numerical simulation study. *Phys. Rev. B*, 31:4403–4419, 1985.
- [42] A. Moreo and D. J. Scalapino. Two-dimensional negative-U Hubbard model. *Phys. Rev. Lett.*, 66:946–948, 1991.
- [43] Thereza Paiva, Raimundo R. dos Santos, R. T. Scalettar, and P. J. H. Denteneer. Critical temperature for the two-dimensional attractive Hubbard model. *Phys. Rev. B*, 69:184501, 2004.
- [44] Marcos Rigol, Tyler Bryant, and Rajiv R. P. Singh. Numerical Linked-Cluster Approach to Quantum Lattice Models. *Phys. Rev. Lett.*, 97:187202, 2006.
- [45] Matthias Troyer and Uwe-Jens Wiese. Computational Complexity and Fundamental Limitations to Fermionic Quantum Monte Carlo Simulations. *Phys. Rev. Lett.*, 94:170201, 2005.
- [46] Richard P. Feynman. Simulating physics with computers. *International Journal of Theoretical Physics*, 21(6):467–488, 1982.
- [47] Waseem S. Bakr, Jonathon I. Gillen, Amy Peng, Simon Fölling, and Markus Greiner. A quantum gas microscope for detecting single atoms in a Hubbard-regime optical lattice. *Nature*, 462:74–77, 2009.
- [48] Jacob F. Sherson, Christof Weitenberg, Manuel Endres, Marc Cheneau, Immanuel Bloch, and Stefan Kuhr. Single-atom-resolved fluorescence imaging of an atomic Mott insulator. *Nature*, 467:68–72, 2010.

- [49] W. S. Bakr, A. Peng, M. E. Tai, R. Ma, J. Simon, J. I. Gillen, S. Fölling, L. Pollet, and M. Greiner. Probing the Superfluid—to—Mott Insulator Transition at the Single-Atom Level. *Science*, 329(5991):547–550, 2010.
- [50] Elmar Haller, James Hudson, Andrew Kelly, Dylan A. Cotta, Bruno Peaudecerf, Graham D. Bruce, and Stefan Kuhr. Single-atom imaging of fermions in a quantum-gas microscope. *Nature Physics*, 11:738 – 742, 2015.
- [51] G. J. A. Edge, R. Anderson, D. Jervis, D. C. McKay, R. Day, S. Trotzky, and J. H. Thywissen. Imaging and addressing of individual fermionic atoms in an optical lattice. *Phys. Rev. A*, 92:063406, 2015.
- [52] Ahmed Omran, Martin Boll, Timon A. Hilker, Katharina Kleinlein, Guillaume Salomon, Immanuel Bloch, and Christian Gross. Microscopic Observation of Pauli Blocking in Degenerate Fermionic Lattice Gases. *Phys. Rev. Lett.*, 115:263001, 2015.
- [53] Maxwell F. Parsons, Florian Huber, Anton Mazurenko, Christie S. Chiu, Widagdo Setiawan, Katherine Wooley-Brown, Sebastian Blatt, and Markus Greiner. Site-Resolved Imaging of Fermionic ⁶Li in an Optical Lattice. *Phys. Rev. Lett.*, 114:213002, 2015.
- [54] Lawrence W. Cheuk, Matthew A. Nichols, Melih Okan, Thomas Gersdorf, Vinay V. Ramasesh, Waseem S. Bakr, Thomas Lompe, and Martin W. Zwierlein. Quantum-Gas Microscope for Fermionic Atoms. *Phys. Rev. Lett.*, 114:193001, 2015.
- [55] Daniel Greif, Maxwell F. Parsons, Anton Mazurenko, Christie S. Chiu, Sebastian Blatt, Florian Huber, Geoffrey Ji, and Markus Greiner. Site-resolved imaging of a fermionic Mott insulator. *Science*, 351(6276):953–957, 2016.
- [56] Lawrence W. Cheuk, Matthew A. Nichols, Katherine R. Lawrence, Melih Okan, Hao Zhang, and Martin W. Zwierlein. Observation of 2D Fermionic Mott Insulators of ⁴⁰K with Single-Site Resolution. *Phys. Rev. Lett.*, 116:235301, 2016.
- [57] Maxwell F. Parsons, Anton Mazurenko, Christie S. Chiu, Geoffrey Ji, Daniel Greif, and Markus Greiner. Site-resolved measurement of the spin-correlation function in the Fermi-Hubbard model. *Science*, 353(6305):1253–1256, 2016.
- [58] Lawrence W. Cheuk, Matthew A. Nichols, Katherine R. Lawrence, Melih Okan, Hao Zhang, Ehsan Khatami, Nandini Trivedi, Thereza Paiva, Marcos Rigol, and Martin W. Zwierlein. Observation of spatial charge and spin correlations in the 2D Fermi-Hubbard model. *Science*, 353(6305):1260–1264, 2016.
- [59] Martin Boll, Timon A. Hilker, Guillaume Salomon, Ahmed Omran, Jacopo Nespolo, Lode Pollet, Immanuel Bloch, and Christian Gross. Spin- and density-resolved microscopy of antiferromagnetic correlations in Fermi-Hubbard chains. *Science*, 353(6305):1257–1260, 2016.

- [60] Peter T. Brown, Debayan Mitra, Elmer Guardado-Sanchez, Peter Schauß, Stanimir S. Kondov, Ehsan Khatami, Thereza Paiva, Nandini Trivedi, David A. Huse, and Waseem S. Bakr. Spin-imbalance in a 2D Fermi-Hubbard system. Science, 357(6358):1385–1388, 2017.
- [61] J. K. Chin, D. E. Miller, Y. Liu, C. Stan, W. Setiawan, C. Sanner, K. Xu, and W. Ketterle. Evidence for superfluidity of ultracold fermions in an optical lattice. *Nature*, 443:961–964, 2006.
- [62] Michael Köhl, Henning Moritz, Thilo Stöferle, Kenneth Günter, and Tilman Esslinger. Fermionic Atoms in a Three Dimensional Optical Lattice: Observing Fermi Surfaces, Dynamics, and Interactions. *Phys. Rev. Lett.*, 94:080403, 2005.
- [63] Niels Strohmaier, Yosuke Takasu, Kenneth Günter, Robert Jördens, Michael Köhl, Henning Moritz, and Tilman Esslinger. Interaction-Controlled Transport of an Ultracold Fermi Gas. Phys. Rev. Lett., 99:220601, 2007.
- [64] Lucia Hackermüller, Ulrich Schneider, Maria Moreno-Cardoner, Takuya Kitagawa, Thorsten Best, Sebastian Will, Eugene Demler, Ehud Altman, Immanuel Bloch, and Belén Paredes. Anomalous Expansion of Attractively Interacting Fermionic Atoms in an Optical Lattice. Science, 327(5973):1621–1624, 2010.
- [65] Debayan Mitra, Peter T. Brown, Elmer Guardado-Sanchez, Stanimir S. Kondov, Trithep Devakul, David A. Huse, Peter Schauß, and Waseem S. Bakr. Quantum gas microscopy of an attractive Fermi-Hubbard system. *Nature Physics*, 14:173–177, 2017.
- [66] Jean-Philippe Brantut, Jakob Meineke, David Stadler, Sebastian Krinner, and Tilman Esslinger. Conduction of Ultracold Fermions Through a Mesoscopic Channel. *Science*, 337(6098):1069–1071, 2012.
- [67] Martin Lebrat, Pjotrs Grišins, Dominik Husmann, Samuel Häusler, Laura Corman, Thierry Giamarchi, Jean-Philippe Brantut, and Tilman Esslinger. Band and Correlated Insulators of Cold Fermions in a Mesoscopic Lattice. *Phys. Rev.* X, 8:011053, 2018.
- [68] H. Ott, E. de Mirandes, F. Ferlaino, G. Roati, G. Modugno, and M. Inguscio. Collisionally Induced Transport in Periodic Potentials. *Phys. Rev. Lett.*, 92:160601, 2004.
- [69] Wenchao Xu, William McGehee, William Morong, and Brian DeMarco. Bad Metal in a Fermi Lattice Gas. arXiv:1606.06669, 2016.
- [70] Rhys Anderson, Fudong Wang, Peihang Xu, Vijin Venu, Stefan Trotzky, Frédéric Chevy, and Joseph H. Thywissen. Optical conductivity of a quantum gas. arXiv:1712.09965, 2017.

- [71] Peter T. Brown, Debayan Mitra, Elmer Guardado-Sanchez, Reza Nourafkan, Alexis Reymbaut, Simon Bergeron, A. M. S. Tremblay, Jure Kokalj, David A. Huse, Peter Schauss, and Waseem S. Bakr. Bad metallic transport in a cold atom Fermi-Hubbard system. arXiv:1802.09456, 2018.
- [72] N. F. Mott. Conduction in non-crystalline systems IX. the minimum metallic conductivity. The Philosophical Magazine: A Journal of Theoretical Experimental and Applied Physics, 26(4):1015–1026, 1972.
- [73] A.F. Ioffe and A.R. Regel. Prog. Semicond., 4:237, 1960.
- [74] Friedhelm Serwane. The setup of a Magneto Optical Trap for the preparation of a mesoscopic degenerate Fermi gas. Master's thesis, University of Heidelberg, 2007.
- [75] Scientific Software Developed by the ID Group. Radia, Version 4.1, 2017.
- [76] R. K. Raj, D. Bloch, J. J. Snyder, G. Camy, and M. Ducloy. High-Frequency Optically Heterodyned Saturation Spectroscopy Via Resonant Degenerate Four-Wave Mixing. *Phys. Rev. Lett.*, 44:1251–1254, 1980.
- [77] F. Huber. Site-Resolved Imaging with the Fermi Gas Microscope. PhD thesis, Harvard University, 2014.
- [78] Eryn C. Cook, Paul J. Martin, Tobias L. Brown-Heft, Jeffrey C. Garman, and Daniel A. Steck. High passive-stability diode-laser design for use in atomicphysics experiments. *Review of Scientific Instruments*, 83(4):043101, 2012.
- [79] Rudolf Grimm, Matthias Weidemüller, and Yurii B. Ovchinnikov. Optical Dipole Traps for Neutral Atoms. 42:95–170, 2000.
- [80] S. Al-Assam, R. A. Williams, and C. J. Foot. Ultracold atoms in an optical lattice with dynamically variable periodicity. *Phys. Rev. A*, 82:021604, 2010.
- [81] Zhang Bai-Gang, Yao Jian-Quan, Lu Yang, Xu De-Gang, Ding Xin, Wang Peng, Zhang Tie-Li, and Ji Feng. High-efficiency single-pass cw quasi-phase-matched frequency doubling based on PP-MgO:SLT. *Chinese Physics B*, 14:353, 2005.
- [82] Hwan Hong Lim, Toshio Katagai, Sunao Kurimura, Noriaki Ohmae, Norikatsu Mio, Takahiro Shimizu, and Ichiro Shoji. Thermal Management in High Power CW SHG Characterized by PMC. In *Nonlinear Optics*. Optical Society of America, 2011.
- [83] J. Sebby-Strabley, M. Anderlini, P. S. Jessen, and J. V. Porto. Lattice of double wells for manipulating pairs of cold atoms. *Phys. Rev. A*, 73:033605, 2006.
- [84] Immanuel Bloch, Jean Dalibard, and Wilhelm Zwerger. Many-body physics with ultracold gases. Rev. Mod. Phys., 80:885–964, 2008.

- [85] Wilhelm Zwerger. Mott-Hubbard transition of cold atoms in optical lattices. Journal of Optics B: Quantum and Semiclassical Optics, 5(2):S9, 2003.
- [86] Tilman Esslinger. Fermi-Hubbard Physics with Atoms in an Optical Lattice. Annual Review of Condensed Matter Physics, 1(1):129–152, 2010.
- [87] Nicola Marzari, Arash A. Mostofi, Jonathan R. Yates, Ivo Souza, and David Vanderbilt. Maximally localized Wannier functions: Theory and applications. Rev. Mod. Phys., 84:1419–1475, 2012.
- [88] Thomas Uehlinger, Gregor Jotzu, Michael Messer, Daniel Greif, Walter Hofstetter, Ulf Bissbort, and Tilman Esslinger. Artificial Graphene with Tunable Interactions. *Phys. Rev. Lett.*, 111:185307, 2013.
- [89] P. M. Duarte, R. A. Hart, J. M. Hitchcock, T. A. Corcovilos, T.-L. Yang, A. Reed, and R. G. Hulet. All-optical production of a lithium quantum gas using narrow-line laser cooling. *Phys. Rev. A*, 84:061406, 2011.
- [90] H.J. Metcalf and P. van der Straten. Laser Cooling and Trapping. Springer, 1999.
- [91] Amar C Vutha. A simple approach to the Landau–Zener formula. *European Journal of Physics*, 31(2):389, 2010.
- [92] Bryce Gadway, Daniel Pertot, René Reimann, Martin G. Cohen, and Dominik Schneble. Analysis of Kapitza-Dirac diffraction patterns beyond the Raman-Nath regime. *Opt. Express*, 17(21):19173–19180, 2009.
- [93] Giovanna Morigi, Jürgen Eschner, and Christoph H. Keitel. Ground State Laser Cooling Using Electromagnetically Induced Transparency. *Phys. Rev. Lett.*, 85:4458–4461, 2000.
- [94] C. Monroe, D. M. Meekhof, B. E. King, S. R. Jefferts, W. M. Itano, D. J. Wineland, and P. Gould. Resolved-Sideband Raman Cooling of a Bound Atom to the 3D Zero-Point Energy. *Phys. Rev. Lett.*, 75:4011–4014, 1995.
- [95] Vladan Vuletić, Cheng Chin, Andrew J. Kerman, and Steven Chu. Degenerate Raman Sideband Cooling of Trapped Cesium Atoms at Very High Atomic Densities. *Phys. Rev. Lett.*, 81:5768–5771, 1998.
- [96] P. Schauß. High-resolution imaging of ordering in Rydberg many-body systems. PhD thesis, LMU München, 2014.
- [97] E. Fermi. Zur Quantelung des idealen einatomigen Gases. Zeitschrift für Physik, 36(11):902–912, 1926.
- [98] W. Pauli. Über den Zusammenhang des Abschlusses der Elektronengruppen im Atom mit der Komplexstruktur der Spektren. Zeitschrift für Physik, 31(1):765–783, 1925.

- [99] D. A. Butts and D. S. Rokhsar. Trapped Fermi gases. Phys. Rev. A, 55:4346–4350, 1997.
- [100] R. B. Laughlin. Quantized Hall conductivity in two dimensions. *Phys. Rev. B*, 23:5632–5633, 1981.
- [101] F. D. M. Haldane. Model for a Quantum Hall Effect without Landau Levels: Condensed-Matter Realization of the "Parity Anomaly". *Phys. Rev. Lett.*, 61:2015–2018, 1988.
- [102] Elbio Dagotto. Correlated electrons in high-temperature superconductors. Rev. Mod. Phys., 66:763–840, 1994.
- [103] Meera M. Parish, Stefan K. Baur, Erich J. Mueller, and David A. Huse. Quasi-One-Dimensional Polarized Fermi Superfluids. *Phys. Rev. Lett.*, 99:250403, 2007.
- [104] T K Koponen, T Paananen, J-P Martikainen, M R Bakhtiari, and P Törmä. FFLO state in 1-, 2- and 3-dimensional optical lattices combined with a non-uniform background potential. *New Journal of Physics*, 10(4):045014, 2008.
- [105] W. C. Ong. Spin Imbalanced Quasi-Two-Dimensional Fermi Gases. PhD thesis, Duke University, 2015.
- [106] Sadhan K. Adhikari. Quantum scattering in two dimensions. *American Journal of Physics*, 54(4):362–367, 1986.
- [107] Jesper Levinsen and Meera M. Parish. Strongly interacting two-dimensional Fermi gases, chapter 1, pages 1–75.
- [108] Mohit Randeria, Ji-Min Duan, and Lih-Yir Shieh. Superconductivity in a twodimensional Fermi gas: Evolution from Cooper pairing to Bose condensation. *Phys. Rev. B*, 41:327–343, 1990.
- [109] D. S. Petrov and G. V. Shlyapnikov. Interatomic collisions in a tightly confined Bose gas. *Phys. Rev. A*, 64:012706, 2001.
- [110] Vasiliy Makhalov, Kirill Martiyanov, and Andrey Turlapov. Ground-State Pressure of Quasi-2D Fermi and Bose Gases. *Phys. Rev. Lett.*, 112:045301, 2014.
- [111] Chingyun Cheng, J. Kangara, I. Arakelyan, and J. E. Thomas. Fermi gases in the two-dimensional to quasi-two-dimensional crossover. *Phys. Rev. A*, 94:031606, 2016.
- [112] P. Dyke, K. Fenech, T. Peppler, M. G. Lingham, S. Hoinka, W. Zhang, S.-G. Peng, B. Mulkerin, H. Hu, X.-J. Liu, and C. J. Vale. Criteria for two-dimensional kinematics in an interacting Fermi gas. *Phys. Rev. A*, 93:011603, 2016.

- [113] T. Bourdel, L. Khaykovich, J. Cubizolles, J. Zhang, F. Chevy, M. Teichmann, L. Tarruell, S. J. J. M. F. Kokkelmans, and C. Salomon. Experimental Study of the BEC-BCS Crossover Region in Lithium 6. *Phys. Rev. Lett.*, 93:050401, 2004.
- [114] I. Boettcher, L. Bayha, D. Kedar, P. A. Murthy, M. Neidig, M. G. Ries, A. N. Wenz, G. Zürn, S. Jochim, and T. Enss. Equation of State of Ultracold Fermions in the 2D BEC-BCS Crossover Region. *Phys. Rev. Lett.*, 116:045303, 2016.
- [115] D. S. Petrov, M. A. Baranov, and G. V. Shlyapnikov. Superfluid transition in quasi-two-dimensional Fermi gases. *Phys. Rev. A*, 67:031601, 2003.
- [116] D. S. Petrov, C. Salomon, and G. V. Shlyapnikov. Weakly Bound Dimers of Fermionic Atoms. *Phys. Rev. Lett.*, 93:090404, 2004.
- [117] Mohit Randeria and Edward Taylor. Crossover from Bardeen-Cooper-Schrieffer to Bose-Einstein Condensation and the Unitary Fermi Gas. *Annual Review of Condensed Matter Physics*, 5(1):209–232, 2014.
- [118] M. Bartenstein, A. Altmeyer, S. Riedl, S. Jochim, R. Geursen, C. Chin, J. Hecker Denschlag, and R. Grimm. Exploring the BEC-BCS Crossover with an Ultracold Gas of ⁶Li Atoms. AIP Conference Proceedings, 770(1):278–288, 2005.
- [119] N. D. Mermin and H. Wagner. Absence of Ferromagnetism or Antiferromagnetism in One- or Two-Dimensional Isotropic Heisenberg Models. *Phys. Rev. Lett.*, 17:1133–1136, 1966.
- [120] P. C. Hohenberg. Existence of Long-Range Order in One and Two Dimensions. *Phys. Rev.*, 158:383–386, 1967.
- [121] J. W. Kane and L. P. Kadanoff. Long-Range Order in Superfluid Helium. *Phys. Rev.*, 155:80–83, 1967.
- [122] V.L. Berezinskii. Destruction of Long-range Order in One-dimensional and Two-dimensional Systems Possessing a Continuous Symmetry Group. II. Quantum Systems. Sov. Phys. JETP, 34:610, 1971.
- [123] J M Kosterlitz and D J Thouless. Ordering, metastability and phase transitions in two-dimensional systems. *Journal of Physics C: Solid State Physics*, 6(7):1181, 1973.
- [124] J M Kosterlitz. The critical properties of the two-dimensional XY model. *Journal of Physics C: Solid State Physics*, 7(6):1046, 1974.
- [125] David R. Nelson and J. M. Kosterlitz. Universal Jump in the Superfluid Density of Two-Dimensional Superfluids. *Phys. Rev. Lett.*, 39:1201–1205, 1977.

- [126] Zoran Hadzibabic, Peter Krüger, Marc Cheneau, Baptiste Battelier, and Jean Dalibard. Berezinskii-Kosterlitz-Thouless crossover in a trapped atomic gas. *Nature*, 441:1118–1121, 2006.
- [127] Peter Fulde and Richard A. Ferrell. Superconductivity in a Strong Spin-Exchange Field. *Phys. Rev.*, 135:A550–A563, 1964.
- [128] A.I. Larkin and Y.N. Ovchinnikov. Nonuniform state of superconductors. Sov. Phys. JETP, 20:762, 1965.
- [129] Daniel E. Sheehy. Fulde-Ferrell-Larkin-Ovchinnikov state of two-dimensional imbalanced Fermi gases. *Phys. Rev. A*, 92:053631, 2015.
- [130] M. M. Parish, F. M. Marchetti, A. Lamacraft, and B. D. Simons. Finite-temperature phase diagram of a polarized Fermi condensate. *Nature Physics*, 3:124–128, 2007.
- [131] G. J. Conduit, P. H. Conlon, and B. D. Simons. Superfluidity at the BEC-BCS crossover in two-dimensional Fermi gases with population and mass imbalance. *Phys. Rev. A*, 77:053617, 2008.
- [132] Lianyi He and Pengfei Zhuang. Phase diagram of a cold polarized Fermi gas in two dimensions. *Phys. Rev. A*, 78:033613, 2008.
- [133] Andrea M. Fischer and Meera M. Parish. Quasi-two-dimensional Fermi gases at finite temperatures. *Phys. Rev. B*, 90:214503, 2014.
- [134] Shaoyu Yin, J.-P. Martikainen, and P. Törmä. Fulde-Ferrell states and Berezinskii-Kosterlitz-Thouless phase transition in two-dimensional imbalanced Fermi gases. *Phys. Rev. B*, 89:014507, 2014.
- [135] Philipp Strack and Pawel Jakubczyk. Fluctuations of Imbalanced Fermionic Superfluids in Two Dimensions Induce Continuous Quantum Phase Transitions and Non-Fermi-Liquid Behavior. *Phys. Rev. X*, 4:021012, 2014.
- [136] Martin W. Zwierlein, Christian H. Schunck, André Schirotzek, and Wolfgang Ketterle. Direct observation of the superfluid phase transition in ultracold Fermi gases. *Nature*, 442:54–58, 2006.
- [137] Ben A. Olsen, Melissa C. Revelle, Jacob A. Fry, Daniel E. Sheehy, and Randall G. Hulet. Phase diagram of a strongly interacting spin-imbalanced Fermi gas. *Phys. Rev. A*, 92:063616, 2015.
- [138] Paulo F. Bedaque, Heron Caldas, and Gautam Rupak. Phase Separation in Asymmetrical Fermion Superfluids. Phys. Rev. Lett., 91:247002, 2003.
- [139] J. Carlson and Sanjay Reddy. Asymmetric Two-Component Fermion Systems in Strong Coupling. *Phys. Rev. Lett.*, 95:060401, 2005.

- [140] Daniel E. Sheehy and Leo Radzihovsky. BEC-BCS Crossover in "Magnetized" Feshbach-Resonantly Paired Superfluids. *Phys. Rev. Lett.*, 96:060401, 2006.
- [141] Daniel E. Sheehy and Leo Radzihovsky. BEC–BCS crossover, phase transitions and phase separation in polarized resonantly-paired superfluids. *Annals of Physics*, 322(8):1790 1924, 2007.
- [142] G. Sarma. On the influence of a uniform exchange field acting on the spins of the conduction electrons in a superconductor. *Journal of Physics and Chemistry of Solids*, 24(8):1029–1032, 1963.
- [143] K. B. Gubbels, M. W. J. Romans, and H. T. C. Stoof. Sarma Phase in Trapped Unbalanced Fermi Gases. *Phys. Rev. Lett.*, 97:210402, 2006.
- [144] A. M. Clogston. Upper Limit for the Critical Field in Hard Superconductors. *Phys. Rev. Lett.*, 9:266–267, 1962.
- [145] I. Bausmerth, A. Recati, and S. Stringari. Chandrasekhar-Clogston limit and phase separation in Fermi mixtures at unitarity. *Phys. Rev. A*, 79:043622, 2009.
- [146] A V Turlapov and M Yu Kagan. Fermi-to-Bose crossover in a trapped quasi-2D gas of fermionic atoms. *Journal of Physics: Condensed Matter*, 29(38):383004, 2017.
- [147] Vudtiwat Ngampruetikorn, Jesper Levinsen, and Meera M. Parish. Pair Correlations in the Two-Dimensional Fermi Gas. *Phys. Rev. Lett.*, 111:265301, 2013.
- [148] M. G. Ries, A. N. Wenz, G. Zürn, L. Bayha, I. Boettcher, D. Kedar, P. A. Murthy, M. Neidig, T. Lompe, and S. Jochim. Observation of Pair Condensation in the Quasi-2D BEC-BCS Crossover. *Phys. Rev. Lett.*, 114:230401, 2015.
- [149] K. Fenech, P. Dyke, T. Peppler, M. G. Lingham, S. Hoinka, H. Hu, and C. J. Vale. Thermodynamics of an Attractive 2D Fermi Gas. *Phys. Rev. Lett.*, 116:045302, 2016.
- [150] H. P. Büchler and G. Blatter. Phase separation of atomic Bose-Fermi mixtures in an optical lattice. *Phys. Rev. A*, 69:063603, 2004.
- [151] Yong-il Shin, André Schirotzek, Christian H. Schunck, and Wolfgang Ketterle. Realization of a Strongly Interacting Bose-Fermi Mixture from a Two-Component Fermi Gas. *Phys. Rev. Lett.*, 101:070404, 2008.
- [152] G. V. Skorniakov and K. A. Ter-Martirosian. Three Body Problem for Short Range Forces. I. Scattering of Low Energy Neutrons by Deuterons. Sov. Phys. JETP, 4:648, 1957.

- [153] G. Zürn, T. Lompe, A. N. Wenz, S. Jochim, P. S. Julienne, and J. M. Hutson. Precise Characterization of ⁶Li Feshbach Resonances Using Trap-Sideband-Resolved RF Spectroscopy of Weakly Bound Molecules. *Phys. Rev. Lett.*, 110:135301, 2013.
- [154] Electron correlations in narrow energy bands. Proceedings of the Royal Society of London A: Mathematical, Physical and Engineering Sciences, 276(1365):238–257, 1963.
- [155] R. Micnas, J. Ranninger, and S. Robaszkiewicz. Superconductivity in narrow-band systems with local nonretarded attractive interactions. Rev. Mod. Phys., 62:113–171, 1990.
- [156] A. Auerbach. Interacting Electrons and Quantum Magnetism. Springer, 1994.
- [157] C. N. Varney, C.-R. Lee, Z. J. Bai, S. Chiesa, M. Jarrell, and R. T. Scalettar. Quantum Monte Carlo study of the two-dimensional fermion Hubbard model. *Phys. Rev. B*, 80:075116, 2009.
- [158] Andrea Damascelli, Zahid Hussain, and Zhi-Xun Shen. Angle-resolved photoe-mission studies of the cuprate superconductors. *Rev. Mod. Phys.*, 75:473–541, 2003.
- [159] Patrick A. Lee, Naoto Nagaosa, and Xiao-Gang Wen. Doping a Mott insulator: Physics of high-temperature superconductivity. Rev. Mod. Phys., 78:17–85, 2006.
- [160] Mohit Randeria, Nandini Trivedi, Adriana Moreo, and Richard T. Scalettar. Pairing and spin gap in the normal state of short coherence length superconductors. *Phys. Rev. Lett.*, 69:2001–2004, 1992.
- [161] Nandini Trivedi and Mohit Randeria. Deviations from Fermi-Liquid Behavior above T_c in 2D Short Coherence Length Superconductors. *Phys. Rev. Lett.*, 75:312–315, 1995.
- [162] B. Kyung, S. Allen, and A.-M. S. Tremblay. Pairing fluctuations and pseudogaps in the attractive Hubbard model. *Phys. Rev. B*, 64:075116, 2001.
- [163] Yen Lee Loh and Nandini Trivedi. Detecting the Elusive Larkin-Ovchinnikov Modulated Superfluid Phases for Imbalanced Fermi Gases in Optical Lattices. Phys. Rev. Lett., 104:165302, 2010.
- [164] Dong-Hee Kim and Päivi Törmä. Fulde-Ferrell-Larkin-Ovchinnikov state in the dimensional crossover between one- and three-dimensional lattices. *Phys. Rev. B*, 85:180508, 2012.
- [165] Jan Gukelberger, Sebastian Lienert, Evgeny Kozik, Lode Pollet, and Matthias Troyer. Fulde-Ferrell-Larkin-Ovchinnikov pairing as leading instability on the square lattice. *Phys. Rev. B*, 94:075157, 2016.

- [166] Adriana Moreo and D. J. Scalapino. Cold Attractive Spin Polarized Fermi Lattice Gases and the Doped Positive *U* Hubbard Model. *Phys. Rev. Lett.*, 98:216402, 2007.
- [167] J. M. Singer, M. H. Pedersen, T. Schneider, H. Beck, and H.-G. Matuttis. From BCS-like superconductivity to condensation of local pairs: A numerical study of the attractive Hubbard model. *Phys. Rev. B*, 54:1286–1301, 1996.
- [168] L.-M. Duan. Effective Hamiltonian for Fermions in an Optical Lattice across a Feshbach Resonance. *Phys. Rev. Lett.*, 95:243202, 2005.
- [169] L. D. Carr and M. J. Holland. Quantum phase transitions in the Fermi-Bose Hubbard model. *Phys. Rev. A*, 72:031604, 2005.
- [170] Fei Zhou. Mott states under the influence of fermion-boson conversion. *Phys. Rev. B*, 72:220501, 2005.
- [171] Roberto B. Diener and Tin-Lun Ho. Fermions in Optical Lattices Swept across Feshbach Resonances. *Phys. Rev. Lett.*, 96:010402, 2006.
- [172] Ulrich Schneider, Lucia Hackermüller, Jens Philipp Ronzheimer, Sebastian Will, Simon Braun, Thorsten Best, Immanuel Bloch, Eugene Demler, Stephan Mandt, David Rasch, and Achim Rosch. Fermionic transport and out-of-equilibrium dynamics in a homogeneous Hubbard model with ultracold atoms. *Nature Physics*, 8:213–218, 2012.
- [173] Robert Jördens, Niels Strohmaier, Kenneth Günter, Henning Moritz, and Tilman Esslinger. A Mott insulator of fermionic atoms in an optical lattice. Nature, 455:204–207, 2008.
- [174] U. Schneider, L. Hackermüller, S. Will, Th. Best, I. Bloch, T. A. Costi, R. W. Helmes, D. Rasch, and A. Rosch. Metallic and Insulating Phases of Repulsively Interacting Fermions in a 3D Optical Lattice. *Science*, 322(5907):1520–1525, 2008.
- [175] Daniel Greif, Thomas Uehlinger, Gregor Jotzu, Leticia Tarruell, and Tilman Esslinger. Short-Range Quantum Magnetism of Ultracold Fermions in an Optical Lattice. *Science*, 340(6138):1307–1310, 2013.
- [176] J. H. Drewes, L. A. Miller, E. Cocchi, C. F. Chan, N. Wurz, M. Gall, D. Pertot, F. Brennecke, and M. Köhl. Antiferromagnetic Correlations in Two-Dimensional Fermionic Mott-Insulating and Metallic Phases. *Phys. Rev. Lett.*, 118:170401, 2017.
- [177] Russell A. Hart, Pedro M. Duarte, Tsung-Lin Yang, Xinxing Liu, Thereza Paiva, Ehsan Khatami, Richard T. Scalettar, Nandini Trivedi, David A. Huse, and Randall G. Hulet. Observation of antiferromagnetic correlations in the Hubbard model with ultracold atoms. *Nature*, 519:211–214, 2015.

- [178] Eugenio Cocchi, Luke A. Miller, Jan H. Drewes, Marco Koschorreck, Daniel Pertot, Ferdinand Brennecke, and Michael Köhl. Equation of State of the Two-Dimensional Hubbard Model. *Phys. Rev. Lett.*, 116:175301, 2016.
- [179] Anton Mazurenko, Christie S. Chiu, Geoffrey Ji, Maxwell F. Parsons, Márton Kanász-Nagy, Richard Schmidt, Fabian Grusdt, Eugene Demler, Daniel Greif, and Markus Greiner. A cold-atom Fermi-Hubbard antiferromagnet. *Nature*, 545:462–466, 2017.
- [180] A. F. Ho, M. A. Cazalilla, and T. Giamarchi. Quantum simulation of the Hubbard model: The attractive route. *Phys. Rev. A*, 79:033620, 2009.
- [181] Shoucheng Zhang. Pseudospin symmetry and new collective modes of the Hubbard model. *Phys. Rev. Lett.*, 65:120–122, 1990.
- [182] Chen Ning Yang and S.C. Zhang. SO₄ symmetry in a Hubbard model. *Modern Physics Letters B*, 04(11):759–766, 1990.
- [183] Ryuta Yamamoto, Jun Kobayashi, Takuma Kuno, Kohei Kato, and Yoshiro Takahashi. An ytterbium quantum gas microscope with narrow-line laser cooling. *New Journal of Physics*, 18(2):023016, 2016.
- [184] Martin Miranda, Ryotaro Inoue, Yuki Okuyama, Akimasa Nakamoto, and Mikio Kozuma. Site-resolved imaging of ytterbium atoms in a two-dimensional optical lattice. *Phys. Rev. A*, 91:063414, 2015.
- [185] Z. Idziaszek and T. Calarco. Two atoms in an anisotropic harmonic trap. *Phys. Rev. A*, 71:050701, 2005.
- [186] Ole Jürgensen, Florian Meinert, Manfred J. Mark, Hanns-Christoph Nägerl, and Dirk-Sören Lühmann. Observation of Density-Induced Tunneling. *Phys. Rev. Lett.*, 113:193003, 2014.
- [187] E. Assmann, S. Chiesa, G. G. Batrouni, H. G. Evertz, and R. T. Scalettar. Superconductivity and charge order of confined Fermi systems. *Phys. Rev. B*, 85:014509, 2012.
- [188] H. A. Mook, M. Yethiraj, G. Aeppli, T. E. Mason, and T. Armstrong. Polarized neutron determination of the magnetic excitations in YBa₂Cu₃O₇. Phys. Rev. Lett., 70:3490–3493, 1993.
- [189] Shoucheng Zhang. SO(4) Symmetry of the Hubbard Model and its Experimental Consequences. *International Journal of Modern Physics B*, 5(1&2):153–168, 1991.
- [190] Thereza Paiva, Richard Scalettar, Mohit Randeria, and Nandini Trivedi. Fermions in 2D Optical Lattices: Temperature and Entropy Scales for Observing Antiferromagnetism and Superfluidity. Phys. Rev. Lett., 104:066406, 2010.

- [191] Eugene Demler, Shou-Cheng Zhang, Nejat Bulut, and Douglas J. Scalapino. A class of collective excitations of the Hubbard model: η excitation of the negative-U model. *International Journal of Modern Physics B*, 10(17):2137–2166, 1996.
- [192] Singer, J. M., Schneider, T., and Meier, P. F. Spectral properties of the attractive Hubbard model. Eur. Phys. J. B, 7(1):37–51, 1999.
- [193] Elmer Guardado-Sanchez, Peter T. Brown, Debayan Mitra, Trithep Devakul, David A. Huse, Peter Schauß, and Waseem S. Bakr. Probing the Quench Dynamics of Antiferromagnetic Correlations in a 2D Quantum Ising Spin System. Phys. Rev. X, 8:021069, 2018.
- [194] N. Henkel, R. Nath, and T. Pohl. Three-Dimensional Roton Excitations and Supersolid Formation in Rydberg-Excited Bose-Einstein Condensates. *Phys. Rev. Lett.*, 104:195302, 2010.
- [195] G. Pupillo, A. Micheli, M. Boninsegni, I. Lesanovsky, and P. Zoller. Strongly Correlated Gases of Rydberg-Dressed Atoms: Quantum and Classical Dynamics. *Phys. Rev. Lett.*, 104:223002, 2010.
- [196] Johannes Zeiher, Rick van Bijnen, Peter Schauß, Sebastian Hild, Jae-yoon Choi, Thomas Pohl, Immanuel Bloch, and Christian Gross. Many-body interferometry of a Rydberg-dressed spin lattice. *Nature Physics*, 12:1095–1099, 2016.
- [197] Edward Perepelitsky, Andrew Galatas, Jernej Mravlje, Rok Žitko, Ehsan Khatami, B. Sriram Shastry, and Antoine Georges. Transport and optical conductivity in the Hubbard model: A high-temperature expansion perspective. *Phys. Rev. B*, 94:235115, 2016.
- [198] Frederik Görg, Michael Messer, Kilian Sandholzer, Gregor Jotzu, Rémi Desbuquois, and Tilman Esslinger. Enhancement and sign change of magnetic correlations in a driven quantum many-body system. *Nature*, 553:481–485, 2018.
- [199] E. Arimondo, M. Inguscio, and P. Violino. Experimental determinations of the hyperfine structure in the alkali atoms. *Rev. Mod. Phys.*, 49:31–75, 1977.
- [200] P Blair Blakie and Charles W Clark. Wannier states and Bose–Hubbard parameters for 2D optical lattices. *Journal of Physics B: Atomic, Molecular and Optical Physics*, 37(7):1391, 2004.